



**Universitatea "Politehnica" din Timișoara
Facultatea de Electronică și Telecomunicații**

Aldo De Sabata

**Habilitation Thesis
Teză de Abilitare**

2012

Contents

1. Abstract	3
1.1 Abstract	3
1.2. Rezumat	5
2. Technical Presentation	7
2.1. Overview of Activity and Results, 1993-2012	7
2.2. Applied Electromagnetics: Metamaterials	12
<i>A. Metamaterials: Literature Review</i>	12
<i>B. Fixed Surfaces</i>	18
<i>C. Switched Surfaces</i>	50
2.3. Magnetic Fluid Bearings	66
<i>A. Rotor with Alternating Poles, Plane-Parallel Approximation</i>	66
<i>B. Poles on the Stator, Plane-Meridian Model</i>	73
<i>C. Poles on the Shaft, Plane-Meridian Model</i>	80
2.4. Spectral Analysis	86
<i>A. Closed Form Expression of the Small Sample Variance of a Frequency Estimator</i> ...	86
<i>B. Two-Step Procedure for Reducing Variance in Single Tone Frequency Estimation</i> ..	95
<i>C. Frequency Estimation by an Iterative Procedure</i>	103
<i>D. Analysis of the Iterative Frequency Estimation Algorithm</i>	107
2.5. Sampling Theory for Multidimensional Signals	112
<i>A. Sampling Theorem for 2D Periodic Signals</i>	112
<i>B. Sampling Expansion for 2D Band-Limited, Finite Energy Signals with Gaps in the Spectrum</i>	116
<i>C. Sampling Expansion on Lattices for Multidimensional, Multi-Band Signals</i>	123
2.6. Development	130
3. References	133
3.1. General References	133
3.2. List of Publications 1993-2012	141

1. Abstract

1.1 Abstract

Personal work and research results in the period 1993-2012 are presented. This period follows the public presentation of my doctoral thesis in 1992.

Three main research areas have been approached: Applied Electromagnetics, Signal Processing and Solar Energy. The same domains constitute my education related interests.

Activity in the field of Applied Electromagnetics has been directed to (i) applications of Metamaterials with electromagnetic band-gap (ii) calculation of forces in magnetic fluids environment and (iii) education.

The history of Metamaterials is about a decade long. Our team has recently approached this direction of research, in 2009. We have devised many fixed and switched planar structures with potential applications in filtering and signal integrity. We have published 3 articles in international peer-reviewed journals, 18 papers in conference proceedings on four continents and 4 articles in other national and international journals.

Our team has calculated restoring forces in magnetic fluids bearings by using several models and approximations in view of validation. We have published 3 articles in peer-reviewed journals, one paper in conference proceedings and other 2 papers in national journals.

I have taught disciplines related to Microwaves and Optical Electronics since these fields have been considered to be related at educational level by the responsible department in the University. I taught 5 disciplines related to the field, out of which 3 have been newly introduced. I wrote 3 textbooks and co authored 2 monographs. I coauthored 2 education related papers published in international peer-reviewed journals participated to two international conferences and coauthored other 5 papers with educational content published in international and national journals. I coauthored other 4 papers presented at international conferences with various topics from Microwaves. I have also approached applications of holograms in dentistry.

I participated to 7 national programs and grants related to Microwaves and Optical Electronics and conducted a direct contract with a local subsidiary of a multinational enterprise for course delivery.

In Signal Processing, work and results can be grouped in two categories (i) spectral analysis and (ii) sampling theory.

I have been member of a team that has tackled the problem of frequency estimation of real sinusoids embedded in additive, white, Gaussian noise in 2006. I have participated to devising two new procedures of spectral estimation that significantly improved existing ones and kept the same level of complexity of algorithms. Results have been published in 4 papers in national and international peer reviewed journals and 4 papers have been presented at international conferences. Other 2 papers have been published in the Scientific Bulletin of my institution.

The results obtained in Sampling theory are a continuation of my doctoral work. The selected signal model consisted of complex, multidimensional, band-limited periodic and finite energy signals sampled along non-orthogonal axes. I proposed several sampling procedures at the minimum sampling density and the corresponding reconstruction methods. I authored 15 journal papers and participated to 4 international conferences.

In the field of Signal Processing, I participated to 3 national grants, conducted one as a director and conducted an European Tempus grant as contractor. I authored 2 educational books and taught 4 disciplines out of which 2 have been newly introduced.

Solar Energy applications have been approached in 2006 following an administrative decision of the University. The field has a long history at the "Politehnica" University of Timișoara (from 1976) and notable achievements. However, work has stagnated after 1990. The activity has been resumed by organizing and equipping a network of laboratories and a Solar House, by restarting research, by disseminating information on the historical applications and publication record and by organizing a master level degree in Solar Energy. This has been possible by attracting funds through a Platform of Solar Energy at the University level, where I have acted as a scientific director. I have introduced a new discipline at the master level. I have coauthored 6 papers published in international peer-reviewed journals, 10 papers published in university and national journals and 3 papers presented at international conferences. I have also co-authored a review book and a chapter in a book issued by an international publisher. Besides the Platform, I conducted 3 contracts with partners from industry and I have been member of a team in a national grant. I participated to an intense activity of mass-media dissemination of solar application at the "Politehnica" University of Timișoara.

The second part of this work is structured in four sections. It starts with an account of relevant facts and achievements from my career. The section on Applied Electromagnetics contains a review of the field of metamaterials introduced in order to motivate the framework of my related interests and activity. A selection of relevant results in fixed, planar structured surfaces acting like Metamaterials with electromagnetic band-gaps is presented, followed by another subsection containing results on switched surfaces. The second part of the section on Applied Electromagnetics is dedicated to results obtained in calculation of restoring force in magnetic fluid bearings with poles on the stator and on the rotor (shaft). Plane-parallel and plane-meridian models for the magnetic field are used in order to compare the predictions in view of validation of results concerning the evaluation of the restoring force.

In the section concerning Signal Processing, two algorithms that significantly improve the frequency estimation of sinusoids embedded in white, Gaussian noise are presented. The algorithms are evaluated in the small sample case and asymptotically and results of computer experiments are reported in order to demonstrate the effectiveness of the proposed methods.

Results in Sampling Theory of multi-dimensional signals are then reviewed. A sampling theorem for band-limited, complex periodic signals is stated and demonstrated. Sampling is performed on non-orthogonal directions. Finite-energy, complex, band-limited signals with spectrums containing gaps have been considered in view of finding sampling procedures at the minimum Shannon-Landau sampling density. Examples in the cases of derivative sampling and delay-systems sampling are provided. The aliasing error is evaluated and aliasing error bounds are reported.

The second part of this reports ends with perspectives on future work in the newly equipped Laboratory of Microwaves, Antennas and Electromagnetic Compatibility.

A list of references and a complete list of my publications in the time period 1993-2012 are attached at the end.

1.2. Rezumat

Se prezintă activitatea și rezultatele cercetării din perioada 1993-2012. Această perioadă urmează susținerea publică a tezei de doctorat în 1992.

Au fost abordate trei domenii de cercetare principale: Electromagnetism, Prelucrarea Semnalelor și Energie Solară. Aceleași domenii constituie și preocupările educaționale ale autorului.

Activitatea în domeniul Electromagnetismului a fost direcționată către: (i) aplicații ale metamaterialelor cu bandă interzisă electromagnetică; (ii) calculul forței de sustentație în fluide magnetice și (iii) educație.

Istoria metamaterialelor nu e mai lungă de un deceniu. Echipa noastră a abordat această direcție de cercetare în 2009. Am conceput mai multe structuri planare fixe și comutate cu aplicații potențiale în filtrare și intergritatea semnalelor. Am publicat 3 articole în reviste internaționale cu evaluare colegială, 18 lucrări la conferințe internaționale desfășurate pe patru continente și 4 articole în alte reviste. Echipa noastră a calculat forța de readucere în lagărele cu fluid magnetic folosind diverse modele în vederea validării rezultatelor. Am publicat 3 articole în reviste cu evaluare colegială, am participat la o conferință internațională și am publicat alte 2 articole în periodice naționale.

Am predat discipline legate de Microunde și Electronică Optică deoarece aceste domenii au fost considerate înrudite la nivel educațional de către conducerea departamentului de resort.

Am predat 5 discipline din domeniu, dintre care 3 au fost nou introduse. Am scris 3 manuale și am participat la scrierea a 2 monografii. Am mai publicat în colaborare două lucrări pe teme educaționale în reviste internaționale cu evaluare colegială, am participat la două conferințe internaționale și am participat la publicarea a altor 5 lucrări cu conținut educațional în periodice. Am mai colaborat la alte 4 lucrări cu conținut de Microunde prezentate la conferințe internaționale și am lucrat la aplicarea tehnicilor holografice în Stomatologie.

Am participat la 7 programe și granturi naționale legate de Microunde și Electronică Optică și am condus un contract direct cu o filială a unei multinaționale pentru furnizare de cursuri.

În domeniul Prelucrării Semnalelor, activitatea poate fi grupată în două categorii: (i) analiză spectrală și (ii) teoria eșantionării.

Am făcut parte dintr-o echipă care a abordat problema estimării frecvenței sinusoidelor acoperite de zgomot alb, gaussian în 2006. Am participat la concepția a două noi proceduri de estimare spectrală care au îmbunătățit semnificativ procedurile existente păstrând același nivel de complexitate a algoritmilor. Rezultatele au fost publicate în 4 lucrări în reviste cu evaluare colegială și 4 lucrări au fost prezentate la conferințe internaționale. Alte două lucrări au fost publicate în Buletinul Științific al UPT.

Rezultatele obținute în teoria eșantionării sunt o continuare a activității doctorale. Modelul ales a fost cel al semnalelor complexe, multidimensionale, de bandă limitată, periodice sau de energie finită, eșantionate paralel cu axe neapărat ortogonale. Am propus diverse proceduri de eșantionare la densitate minimă, precum și metodele corespunzătoare de reconstrucție. Am publicat 15 articole în periodice și am participat la 4 conferințe internaționale.

În domeniul Prelucrării Semnalelor, am participat la 3 granturi naționale și am condus un astfel de grant ca director. Am fost contractor la un program Tempus. Am publicat două cărți având conținut educațional și am predat 4 discipline, dintre care două au fost nou introduse.

Aplicațiile Energiei Solare au fost abordate în 2006 în urma unei decizii administrative la nivel de Universitate. Domeniul are o istorie lungă la Universitatea "Politehnica" din Timișoara (din 1976) și realizări notabile. Din păcate, activitatea a stagnat după 1990. A fost

reluată prin organizarea echiparea unei rețele de laboratoare și a unei Case Solare, prin redemararea cercetării, prin diseminarea informațiilor asupra aplicațiilor puse la punct în trecut și a publicațiilor aferente și prin organizarea unei direcții de master în Energetică Solară. Acestea au fost posibile datorită atragerii de fonduri printr-o Platformă de Energie Solară la care am participat ca Director Științific. Am introdus o nouă disciplină la nivel de master. Am publicat în colaborare 6 lucrări în reviste internaționale cu evaluare colegială, 10 lucrări în periodice naționale și 3 lucrări la conferințe internaționale. Am colaborat la scrierea unei cărți de sinteză a rezultatelor de cercetare și la un capitol dintr-o carte publicată la o editură din străinătate. În afara Platformei, am condus 3 contracte directe și am fost membru al echipei unui grant național.

Partea a doua acestei teze este structurată în patru secțiuni. Începe cu o dare de seamă asupra realizărilor și rezultatelor din carieră. Secțiunea dedicată Electromagnetismului Aplicat conține o sinteză a domeniului Metamaterialelor introdusă cu scopul de a motiva și încadra preocupările mele din acest domeniu. Este prezentată o selecție a rezultatelor personale relevante obținute în legătură cu structurile planare fixe care se comportă ca Metamateriale cu bandă electromagnetică interzisă, urmată de o altă subsecțiune conținând rezultate în legătură cu suprafețele comutate. A doua parte a secțiunii consacrate Electromagnetismului este dedicată rezultatelor obținute în calculul forței de readucere în lagărele cu lichid magnetic cu poli pe stator sau rotor. Sunt folosite atât modele plan-paralele cât și plan-meridiane pentru câmpul magnetic cu scopul de a compara predicțiile celor două în vederea validării rezultatelor.

În secțiunea dedicată Prelucrării Semnalelor sunt prezentați doi algoritmi care îmbunătățesc semnificativ estimarea frecvenței sinusoidelor acoperite de zgomot alb, gaussian. Algoritmii sunt evaluați în ipoteza unui număr mic de eșantioane, dar și asimptotic. Rezultate ale experimentelor efectuate pe calculator demonstrează eficiența metodelor propuse.

Este prezentată apoi o sinteză a rezultatelor obținute în teoria eșantionării semnalelor multidimensionale. Se enunță și se demonstrează o teoremă de eșantionare a semnalelor complexe, periodice, de bandă limitată. Eșantionarea este realizată pe direcții neortogonale. Au fost apoi considerate semnale complexe, de energie finită, de bandă limitată ale căror spectre conțin lacune în vederea găsirii de proceduri de eșantionare la densitatea minimă Shannon-Landau. Sunt date exemple în cazul eșantionării semnalului și derivatelor sale, precum și a unor variante întârziate ale semnalului. Se prezintă o evaluare a erorii de aliere și se propun margini pentru aceste erori.

A doua parte a tezei se încheie cu perspective ale dezvoltării viitoare în Laboratorul de Microunde, Antene și Compatibilitate Electromagnetică, proaspăt echipat.

La sfârșit, sunt atașate o listă a referințelor bibliografice și o listă completă a publicațiilor autorului din perioada 1993-2012.

Technical Presentation

2.1. Overview of Activity and Results, 1993-2012

The title of my PhD thesis was *Adaptive Sampling for Data Compression* and I presented it publicly at the "Politehnica" University of Bucharest in 1992. Therefore the following overview of my scientific interests and work starts from 1993.

I have worked in three fields of research: Signal Processing, Applied Electromagnetics and Solar Energy. My teaching interests are also related to these fields and the list of publications reflects this situation. In the list the first topic is identified by an "S", the second one by an "M" and the third one by "E".

In Signal Processing I tackled two different topics: sampling theory and spectral analysis of real sinusoidal signals. Sampling theory has been also the subject of my PhD thesis and I continued the research in this field until 2006 when I began working in Spectral Analysis. I have published 21 papers related to sampling of signals and 10 papers in Spectral Analysis.

My scientific interest in Sampling Theory has been related to finding sampling expansions for multidimensional signals having finite support spectrums that contained gaps. A well-known result states that a minimum sampling density that ensures possibility of reconstruction for the signal is given by the reciprocal of the measure of the spectrum (Shannon-Landau). However sampling strategies do not exist in general. I considered both finite energy signals and band-limited periodic signals in my work and found the above-mentioned sampling strategies and expansions under various hypotheses on the supports of the spectra. The most significant results are reviewed in the section devoted to this subject.

The work in Spectral Analysis has targeted algorithms for recovery of frequency of sinusoids embedded in white, additive noise in the small sample case. The team I worked with proposed two novel algorithms that significantly reduced the mean square error of the estimate with respect to known procedures but still keeping complexity of the same order of magnitude. A first two-step solution relies on finding a rough estimate of the frequency in a first step, by using a known method, estimating then a multiple of the unknown frequency and resolving the induced aliasing through the information from the first step. A second method consists of an iterative procedure: a rough frequency estimate is found at the first iteration and the result is filtered at each iteration with a linear system whose frequency response depends on the first estimate. It has been shown experimentally that the mean square error of the estimate approached the Cramer-Rao bound after a few iterations. All algorithms have been analyzed theoretically in the small sample case and asymptotically. The results are reviewed in one of the next sections.

At the same time I participated to national research programs and grants as follows: 1. *Research concerning time-frequency and time-scale representations of 1- and 2D signals with applications to devising new multi-resolution analysis algorithms* (1995, 1996); 2. *Construction of statistical mathematical morphology operators through hierarchic random processes with applications to digital processing of 1- and 2D signals* (1996); 3. *Time frequency representations for signal analysis and processing* (1996). I have conducted as a director the national research grant *New methods of non-uniform sampling with applications to spectral analysis* (2000-2002). I have also conducted as a contractor a Tempus program *Restructuring post-university DSP course* (1999-2001). Besides restructuring courses, the purpose of the program has been to re-equip laboratories with modern DSP instruments and to publish a series of courses written by the participants to the program. My contribution has been a book on applications of adaptive filtering to measurements (*Adaptive Methods for Measurements Technique* [01_06_S]).

I had also a long-run teaching activity in the field of Signal Processing. I have taught the following undergraduate and graduate courses: "Signals, Circuits and Systems", "Time-Frequency Representations" (in French), "Adaptive Measurements Techniques" and "Spectral Analysis". I wrote several series of lecture and applications notes.

The development of Signal Processing took inputs from a wide range of disciplines and consequently its concepts, methods and algorithms have a wide range of applications. Therefore the experience I have gained in this field has been very useful for the research in the other fields I have approached.

The second subject for research has been Applied Electromagnetics. I approached this field for two reasons: by personal interest and by the shift in main teaching domain from Signal Processing to Microwave and Optical Electronics in 1997. My first published technical contributions tackled educational issues: wave propagation and power transfer on transmission lines. I have continued by devising a measurement setup for determining the constitutive parameters of various types of seeds in view of food processing by microwave heating. The first substantial subject of research that resulted in significant results concerned theoretical evaluation of restoring force in magnetic fluid bearings. This topic has been approached following a long-term cooperation of one of the authors with the research team on magnetic fluids, belonging to the Romanian Academy and the "Politehnica" University of Timișoara. Several theoretical models have been conceived and results have been compared in view of validation. This subject is covered in one of the next sections. The third considered field has been the recently introduced one concerning metamaterials. Scientific interest on metamaterials is about one decade long, so that the subject is dynamic. I consider this my main scientific field of activity. I have approached research in connection to metamaterials in 2009 and published over 20 papers since, in refereed journals and in proceedings of international conferences held on four continents (according to my publication list). These publications deal mainly with fixed and tunable filtering applications and with Electromagnetic Compatibility and Signal Integrity ones. In parallel with further research on metamaterials, a closely related direction occurred recently, namely an opportunity to approach again the field of magnetic fluids, only this time at a much higher frequency. Preliminary results of waveguide measurement of constitutive parameters of nano-structured magnetite particles embedded in a support material, by means of S parameters, showed promising results.

The disciplines related to Microwaves and Optical Electronics are considered related at Department of Measurement and Optical Electronics. The part of my research activity pertaining to Optics concerned mainly production of holograms. The holograms produced in our laboratory have been used in Dentistry applications [09_02_M]. Experience in optical devices triggered our interest in photovoltaic cells and consequently in Solar Energy. This field of research will be covered at a later point below.

Apart from journal articles and conference proceeding publications, I have co-authored two monographs treating subjects from high frequencies domain: *Antennas and Propagation* [02_02_M] and *Aspects Concerning Monitoring of Perturbations in a Site* [06_01_M].

Education in Microwaves and Optical Electronics involved teaching several disciplines both at an undergraduate and graduate level: *Microwaves, High Frequency Techniques, Optical Electronics, Electronic and Optoelectronic Devices, Optoelectronics and Microwaves Measurements* and *Antennas and Waves Propagation* (in English). I have authored a book *High Frequency Techniques* [01_02_M] and the first part of a university course *Optoelectronics and Microwaves Measurements* [96_01_M]. The published part concerned microwave measurements and has been the first publication devoted entirely to this topic at the university. Besides publications, I have written several hundreds of pages of lecture notes for all the aforementioned disciplines, which are available from the web-site of the Faculty of Electronics and Telecommunications.

The research activity in the field of metamaterials has been realized in an informal way in cooperation with a small group from the Laboratory of Antennas and Electromagnetic Compatibility with the Politecnico di Torino, Italy. However, these contacts have not been restricted to research: we had teaching exchanges every year in the period 2003-2009 and the exchanges will be resumed this year under the framework of the Socrates / Erasmus program. From my part, I sustained 8-hour courses at the third year of Electronics Engineering each year in the above referred period and I have written 60 pages of lecture notes with the subject *S parameters*. The notes are available from the web-site of the Italian institution. My colleague from Torino taught 8-hour courses with topics from the *Applications of the Smith Chart* and *Constitutive Parameters* to our students from the second year, undergraduate level.

I have participated as member of the team to several national research programs and grants: *Research on magneto-optic electro-optic and electro-luminiscent effects with applications to sensor construction* (1997), *Research on magneto-optic, electro-optic, piezo-electric and optoelectronic sensors and their interface with computers* (1998), *Monitoring system of bone tissues and study of healing of fractures and bone-implant interface through vibration-related techniques* (2001), *Antenna calibration by means of the auto-reciprocity method* (2000-2002), *Modern techniques for biomedical*

signal processing and hypermedia transmission (2006), *Electromagnetic monitoring of the "Județean" Hospital, Timișoara* (2004), *Foresight Scenarios for the Romanian Economical Sectors with Inovetion Potential in the View of the Year 2020, "INOVFOR"* (CEEX 2005, 2006) and *Inter-laboratory tests for evaluation of measuring uncertainty in Electromagnetic Compatibility* (PNCDI-INFRA 2004-2006).

I have also participated as a coordinator of the team from the "Politehnica" University of Timișoara to the COST 289 action *Spectrum and Power Efficient Broadband Communications* (2004-2006).

Electronics industry developed in the last years in the region of Timișoara. Cooperation between industry and university is advisable for both sides. I have started a cooperation with Flextronics, a local producer of electronic boards and equipment by signing a *contract on education provided for the employees*. I sustained courses under this contract with topics from Optical Communications, Transmission lines, Microwaves devices, systems and measurements.

A constant concern has been procurement of modern microwave and optical equipment, since no modern research activity can be conceived without experimental facilities. The instruments that are used in these fields are notoriously costly. Due to favorable opportunities offered by the programs I participated in or coordinated, to be presented at a later point below, it has been possible to purchase equipment that allow a wide range of measurements and experiments for the Microwaves and Electromagnetic Compatibility Laboratory: a 24 GHz vector network analyzer, a high frequency programable signal generator, a high performance and two average performance spectrum analyzers. These acquisitions made the laboratory functional. For the Optical Electronics Laboratory, I contributed to the acquisition of an optical kit and of an optical communications kit to be used in education and research. I have also contributed to the acquisition of a wide range of general purpose electronic instruments and tools and computers.

The third field of research I have contributed to is Solar Energy. Solar Energy has a long tradition at the "Politehnica" University of Timișoara since research started back in 1976. After some pioneering achievements in industrial and home applications, the work has stagnated after 1990. An administrative decision has been taken in 2006 to revigorate this research field in order to take advantage of the still existing experience. I have been personally involved in this initiative, so that I concentrated on several actions: i) document and spread worldwide information on the research results and practical implementations obtained by the university in this field in the last 35 years; ii) procure modern equipment for supporting research and education; iii) revigorate publication activity; iv) introduce Solar Energy in the education offer of the university by creating a new master level program; v) cooperate with local authorities and industry for finding common interests in view of finding financment opportunities; and vi) public and mass-media dissemination of information regarding Solar Energy expertise existing in the university.

Information on Solar Energy related activity at the university has been disseminated by means of publications in international peer-review journals. Several new measurement results on solar radiation and climatic data and feasibility studies for solar applications relying upon have been presented at international conferences and published in the proceedings (according to the list of publications). In order to document the past activity we have published a book (*Tradition and Perspectives in Solar Energy at the Politehnica University of Timișoara* [10_08_E]) and current and past research results have been reported in a chapter of an international book (*Applications Oriented Research on Solar Collectors at the "Politehnica" University of Timișoara* [10_06_E]).

The means for equipment procurement have been provided by a *Platform for Solar Energy* (2006-2009), a grant won by competition where I have acted as a scientific director. Six new laboratories and a Solar House have been equiped with research instruments and tools. Following the activity of the Platform, the following research areas have been approached at the university: measurements and local models for solar radiation, energy and air conditioning for residences, simulation and measurements of photovoltaic cells, measurement and conception of materials for solar applications, system integration of solar energy applications, greenhouse effect applications, data acquisition, automation and control of solar applications and systems, solar collectors and concentrators, fuel cells, hydrogen production and storage and solar architecture.

A new master level program has been created with the Department of Physics Foundations of Engineering under the same framework, where I teach a course in "Optical Electronics". I have elaborated the necessary teaching material.

The connection with local authorities led to several participations to meetings and cooperation, one of which has been formally finalised by a contract with the mayor office of the town of Jimbolia where I acted as director (*Assessment of renewable energies potential of the Timiș Department – charge book*, a PHARE CBC Ro-Hu 2006, contract). Another cooperation activity with local authorities has been personal participation through direct contract to the elaboration of a charge book for a *Renewable Energies Industrial Parc at Covaci, department of Timiș*. The beneficiary has been the Development Agency of the Timiș Department – ADETIM.

I have participated to several press conferences and at a television round table dedicated to solar energy, at national and international energy fairs with presentations aimed to disseminate the experience and current research interests existing at the "Politehnica" University of Timișoara: *Energia viitorului (The Energy of Future)* – 2007, 2008, 2009, 2010, *Săptămâna calității Timișorene (Week Dedicated to Quality in Timișoara)* – 2008, 2009. I have written a study for the Commerce and Industry Chamber of Timișoara entitled *Studiu privind sursele alternative de energie în regiunea transfrontalieră România - Ungaria, județele Timiș și Csongrád (Study on alternative sources of energy in the frontier region Romania – Hungary, Departments of Timiș and Csongrád)*, 47 pages, 2009.

I have benefited of several mobilities abroad. The first one has been a nine-month postdoctoral grant at the Institut National Polytechnique de Lorraine, Center de Recherche en Informatique, France, 1993-94. In the framework of the Tempus program where I acted as a contractor, I benefited of short term (two-week) mobilities at the University of Granada, Spain, National Technical University of Athens, Greece and Fachhochschule Karlsruhe, Germany (1999-2000). I participated to a one-week course in Digital Radio and TV at Kathrein Werke in Rosenheim, Germany, 1999 and a Tempus mobility at ITAL TBS SpA, Trieste, Italy, for education in Medical Electronics (1997).

I sustained lectures of Electronics for four months with IUT Rennes, France, 2001 as PAST. And, as already mentioned, I sustained lectures with topics from Microwaves at the Politecnico di Torino, Italy for seven consecutive years (2003-2009) and this activity will be resumed next year in the framework of the Socrates / Erasmus program.

As a Scientific Secretary of the Faculty of Electronics and Telecommunications I have organized four editions of the *International Symposium of Electronics and Telecommunications*, 2001-2008.

In the next section, some of the relevant research results I have obtained in the course of my career are presented. Since I consider Applied Electromagnetics and Signal Processing as the research fields that best define my activity, the selected topics are taken from these fields. Nevertheless, publications in the field of Solar Energy are also relevant (four papers published in peer-reviewed journals abroad), despite the fact that I have approached this field of research only in 2006. Sample papers focusing on Solar Energy are attached.

The next two sections present results from Applied Electromagnetics, from low frequencies, which allows neglect of radiation to microwave frequencies, where focus is on radiation and wave propagation. Section 2.2 contains results for the field of Metamaterials. It is divided into three subsections. The first one is entirely dedicated to a survey of the results that are relevant to my work. The presence of the survey is motivated by the novelty of the field, about one decade old. Furthermore, it provides the framework of my results. The results are of exploratory type and are devoted to finding new structures and devices with favorable properties for applications by simulation and experiments. The next two subsection deal with conception of fixed and switched electromagnetic band-gap structures in view of applications to filtering and signal integrity. For space limitation, the mathematical model concerning wave propagation and consequently issues like Bloch waves, Floquet theorem and Bloch harmonics are not tackled. This part is very well covered in classic literature e.g. [bri_53], [collin_92], [kittel_96] etc.

Section 2.3 presents a series of three works where a thorough study of restoring forces acting on bearings built with magnetic fluids is reported. Here the emphasis is on mathematical modelling, since several models have been constructed and the prediction compared in view of validation of results. Therefore this section is more mathematically involved.

In Sections 2.4 and 2.5, results from Signal Processing are presented. In Section 2.4, two novel procedures for spectral analysis of real sinusoids embedded in white, gaussian noise are reviewed. The algorithms are described and low sample analysis and asymptotic analysis are performed. The effectiveness of the novel algorithms is demonstrated by computer experiments. Sampling theory is the subject of the last section. Both multi-dimensional band-limited periodic signals and finite energy signals are considered. Sampling strategies and sampling expansions on general, non-orthogonal grids, targeting the minimum Shannon-Landau sampling density are presented. Aliasing error bounds are provided. References and the author's list of publications are grouped in the third Chapter.

2.2. Applied Electromagnetics: Metamaterials

A. Metamaterials: Literature Review

Interest on microstrip boards having impressed a periodic metal pattern on the face opposite to the ground plane has been raised to the microwave and antenna community by the works of Sievenpiper published at the end of the last decade of the last century [siev_98, 99_a, 99_b]. A periodic pattern consisting of square shaped unit cells that contained a square metal patch positioned symmetrically with respect to the center of the unit cell and connected around the same point to the ground plane through a via with metal walls has been proposed. This arrangement is now known as "Sievenpiper's mushroom structure". It has been demonstrated that the structure could carry surface waves, except for some frequency bands called electromagnetic band-gaps (EBGs). Guided waves have been classified in slow and fast following a comparison with the speed of light. Fast waves have been proven to be leaky, so that the device became useful as a controllable leaky-wave antenna, a topic that will be considered at a latter point.

In order to describe theoretically the mushroom structure, an effective impedance model for the surface has been developed in the cited publications. Such a model works properly when the wavelength is much larger than the dimension of the unit cell, which means low frequency and small wave-numbers. The surface presents a distributed impedance that can be modeled by a parallel L - C circuit with typical parameters values of $C=0.5-10$ pF/square and $L=1-2$ nH/square (the reported unit cell had an edge of 2.4 mm, a distance between metal plates of 0.15 mm, a radius of the vias of 0.36 mm, a thickness of the board of 1.6 mm and a dielectric constant of the substrate of 2.2). The resonance frequency is around 10 GHz and the surface impedance has an inductive behavior below and a capacitive one above the resonance frequency. It has been demonstrated that the surface impedance is very high in the vicinity of the resonance frequency; therefore, the surface acts like an artificial magnetic conductor in the considered frequency band. The structure radiates at an angle determined by the condition of continuity of the tangential wave vectors of the surface waves and plane waves propagating through free space surrounding the device. The resonance frequency is $1/\sqrt{LC}$ and the relative bandwidth is proportional to $\sqrt{L/C}$. The reflecting properties of the surface are those of a magnetic conductor inside this bandwidth. These results suggested the name of "high impedance surfaces" (HISs) for the considered structures.

Several applications have been proposed: enhancing the radiated power by using a reflective plane near the antenna, due to the magnetic conductor behavior of the surface around the resonance frequency, reduction of ground plane currents in antenna arrays sharing a common ground plane and consequently reduction of speckle related effects etc.

The frequency related properties of the surface have been presented in terms of dispersion diagrams (DDs) that consist of representations of frequencies versus wave-numbers [bri_53]. Electromagnetic waves interact with the periodic structure in a way that is analog to the one in which crystal lattices in solids interact with de Broglie waves associated to electrons. DDs display various modes of propagations and one or several EBGs. Following such an analogy, microstrip boards printed with a periodic metal pattern have been associated later to the field of metamaterials [lapine_07].

The present time interest in metamaterials has a history of about one decade [elef_11_a]. This interest has been raised mainly by the possibility to synthesize materials with user-defined constitutive parameters. Electromagnetic waves that interact with an array of small-sized scatterers (much smaller than the wavelength) can be considered to propagate through a homogeneous medium with appropriately defined effective permittivity and permeability. This idea, inspired from the propagation of light is not new in the Applied Electromagnetics community, since "artificial dielectrics" relying on the same principle have been created in the WW2 period and in the aftermath. A brief discussion of the history of the concept of effective medium can be found in the review article [elef_12_b]. However, a major excitement has been triggered by the demonstration of existence of materials with negative index of refraction [shelby_01]. This opened a new perspective for the pioneering work of Veselago [veselago_68] who derived theoretically the wave-related properties of such media.

A material with a negative index of refraction must have a negative permittivity and a negative permeability (see e.g. [elef_02]). A medium with negative permeability has been proposed in [pendry_99], relying on a periodic network of loosely-coupled split-ring resonators. The 3D medium with negative index of refraction reported in [shelby_01] has been obtained by alternating split-ring

resonators and wires. The medium filled with wires presents a negative permittivity for electric fields polarized along the wires, while the split-ring resonators provide the negative permeability [elef_2012_b].

The negative permittivity and permeability are achieved in some frequency bands and are components of tensors. The other components of the tensors are positive, so that negative index of refraction can be obtained only for appropriately polarized fields [dong_12].

Media with negative index of refraction exhibit negative refraction i.e. a negative angle of refraction when electromagnetic waves are incident from a usual medium on the boundary of the metamaterial. This property gave rise to a large palette of dispersion engineering applications such as self-collimation [matt_07], super lens, super prisms [enoch_03] and propagation control [notomi_00].

Another interesting feature of materials with a negative index of refraction is that the phase and group velocities are opposite directed vectors in some frequency bands i.e. the phase of the wave and the energy (or narrow band signals) propagate in opposite directions. In fact, signals in periodic media are Bloch waves, with an infinite number of spatial harmonics. It has been known for long that some harmonics have positive group velocities while other harmonics have negative ones [collin_92]. However, in the case of negative refractive index materials, the first (fundamental) harmonic enjoys of this interesting property.

In our work we have considered devices based on microstrip boards with a 2D periodic pattern impressed on one side. The metal patches have been connected to the ground plane through one or several vias. Such structures have also been considered by many research groups in the last decade and an extensive literature is available, as reviewed below. Radiation properties of the HISs have been exploited in the conception of steerable and electronically tunable antennas. The EBG structure led to filtering applications, while the presence of a large fundamental (low frequency) EBG has been taken advantage of in suppression of switching noise in power planes for fast digital or mixed signal circuits. Reflectarrays, holographic surfaces and active configurations represent important challenges for the present-day research activity. In the considered applications, the interest in DDs is not restricted to zones where an effective medium model can be applied. Therefore, generally the DDs are calculated and exploited for a wider range of parameters, including high frequencies and large wave-numbers.

As mentioned above, one of the simplest ways for realizing HIS structures is employing microstrip technology. Periodic microwave structures can be obtained by impressing a basic pattern periodically on one face of a microstrip board. It can be floating as for Peano [mcvay_05] or Hilbert [mcvay_04] surfaces, the fish-like solution [matek_08] or other shapes or connected to the continuous metallic ground plane on the other side of the board through one or several vias. This second solution has been spread out following their introduction by Sivenpiper. Fabry-Perot like resonators used e.g. to increase antenna performances require partially reflective surfaces. This can be done by impressing different patterns on both sides of the dielectric support [vall_09]. Other applications of HIS include surfaces transparent for the magnetic field [teix_07] and holographic surfaces [siev_05_a].

Our main topics of interest in this field has been related to filtering properties of HISs, including conception of switched filters and to applications to parallel-plate noise mitigation in digital and mixed-signal high-speed circuits. Therefore, literature related to these topics will be covered in detail. Nevertheless, present-day research challenges from other applications domains will be also tackled below.

The physics governing electromagnetic phenomena is well known and understood. However, analytical solutions to equations can be found only in some simplified situations, and therefore computer simulations have to be relied upon. This issue applies to wave propagation in periodic planar structures too. Fortunately, the development of specialized electromagnetic simulation and design software in the last two decades provided means for parametric characterization of the devices that constitute the subject of our work [gupta_02].

When only the low frequency, low wave-number part of DDs are of interest, circuit models predicting the limits of the first EBG can be elaborated and used [elek_04]. These models, relying on transmission line theory and related to the physical parameters of the periodic structure are more or less precise but greatly reduce the computation time since circuit models run much faster on computers than full-wave electromagnetic simulations. However, when the DDs are needed for a large range of frequencies and wave-numbers, in 1D or 2D, then full-wave simulation becomes irreplaceable. In order to provide design guidelines, parametric studies have to be performed by

varying the geometrical parameters of the structure or the constitutive parameters of the materials entering the composition of the structure [rajo_07], [rajo_09]. The constitutive parameters can take values from a wide range due to present-day achievements in materials synthesis [she_05].

The possibility of controlling analytically the band limits of the first EBG exhibited by a HIS has been proven for an array of width-modulated microstrip transmission lines [matek_08]. In the same paper, an example of HIS exhibiting EBG in the absence of vias has been reported. This situation can occur in open structures, but presence of vias is mandatory in closed structures, such as parallel-plate waveguides (PPWs), in order for EBGs to be present [pau_10].

Another solution for unit cells with analytically expressed DDs has been proposed in [matek_10] in connection to holographic surfaces obtained by cascading unit cells with sinusoidal modulated effective dielectric constant and different modulation parameters.

EBG structures, initially introduced in [siev_99_a] in connection to low profile antennas, has gained attention for application in power distribution networks of high-speed digital and mixed-signal electronic circuits in view of switching noise suppression. Fast signal edges and fast varying conduction currents through vias give rise in the PPW environment of multilayered printed circuit boards (PCBs) to simultaneous switching noise, also termed ground bounce or power/ground noise that can cause signal integrity problems and malfunctioning of analog and digital circuits. The spurious signals are deterministic in nature; nevertheless, the term "noise" is motivated by their harmful effects. Once they reach the edges of the PCBs, PPW noise causes additional problems by radiation into the surroundings. The inclusion of EBG structures into the multilayered structures mitigates these problems since EBG structures are patterned surfaces that propagate surface electromagnetic waves in some frequency bands and prevent their propagation in other bands. To be effective for PPW noise suppression, the stopbands have to be wide enough in the low frequency range of the spectrum and the low cut-off frequency should be as small as possible. An obvious solution for these issues is to increase the size of the unit cell of the EBG structure. However, this solution is in contradiction with miniaturization of present-day circuits, since several unit cells must be present in 2D in order for the finite-size surface to appropriately function similarly to the infinite one. Therefore this solution has to be combined to other ones, such as enhancing the distributed inductance and capacitance by connection of additional lumped components, increasing the number of vias and finding new shapes for the metallization in order to increase the number of resonances.

An early work in suppression of parallel plate power leakage by using a 1D periodic structure has been [das_96]. A solution based on two rows of shorting pins placed parallel to the central conductor of a conductor backed coplanar waveguide has been proposed among others.

Suppression of parallel-plate modes can be achieved by inserting a HIS in between two dielectric materials contained in the space bordered by the plates of a PPW. The HIS consists of square shaped unit cells with square metal patches. Each patch is connected to the ground plane by vias with metal walls [abhari_03]. Through an appropriate design, the EBG covers the most part of the PPW noise spectrum which extends from DC to around 6 GHz. In the cited reference, the transverse resonance method for transmission lines is used for predicting the limits of the first EBG with a certain degree of approximation in order to alleviate the design. A similar idea is developed in [rogers_05], where a circuit model for the structure is derived. The circuit model has several limitations but it drastically reduces the computation time since the correct results can be obtained only by solving an eigenmode equation in a full-wave simulator software environment.

A low-period coplanar EBG structure is proposed in [wu_05] in view of ground bounce noise elimination. The novel design is incorporated in the power plane, while the ground plane is kept continuous. A transmission line model providing stop-band prediction is also proposed. The edge of the unit cell has been chosen as 18 and 30 mm in two reported experiments. Stop-band widths of 4–6 GHz have been measured, starting from low cut-off frequencies of 1–2 GHz on finite dimension boards. It has been demonstrated by EMI measurements that the board does not suffer from radiation problems, although the upper metal plane is not contiguous.

The problem of finding a more precise circuit model for HISs embedded in power planes has been approached in [kam_05]. The authors report the results of a large number of simulations performed in order to find the influence of various geometrical parameters on the band-width of the first EBG. A circuit model is extracted, which is quite complicated, contrarily to the ones reported before. However,

a claimed reduction of computation time for finding EBG limits from 1–2 days with a commercial EM solver to 1 min has been obtained.

A further extension of the conventional solution to the parallel-plate noise mitigation problem has been to embed two HIS layers, with different low frequency EBGs, between the upper and lower metal walls of the power distribution network [park_06]. The solution has been applied to low-temperature co-fired ceramic system-in-package products. 100 μm thick dielectrics and 10 μm thick gold conductors have been used for constructing the device. Unit cells with edge dimensions of 3.8 and 1.8 mm have been tested. One or two EBGs in the GHz frequency range have been experimentally determined.

The problem of 2D transmission-line models for the mushroom structure embedded in PPW configuration has been revisited in [tav_07]. Transmission line based eigenvalue dispersion equations giving approximate limits for the low-frequency EBGs have been proposed.

In [zhang_07] it has been shown that increasing the number of vias per unit cell in the embedded mushroom structure widens the bandwidth of the EBG with favorable effects on parallel-plate noise suppression when appropriately placed.

A fundamental limitation of planar EBG structures, namely the difficulty to obtain a low cut-off frequency with reasonable dimensions of the unit cell, is tackled in [kim_08]. The authors propose the use of hybrid planar-type EBG structures that contain lumped passive components in order to increase the capacitances and inductances, with the favorable consequence of decreasing the lowest cut-off frequency. A 1D model is provided and a feasibility study for application of the hybrid EBG structure is conducted. The same issue is addressed in [kam_08]. The proposed solution relies on planar structures containing unit cells with spiral metallizations, called spiral-based inductance-enhanced EBG surfaces.

Results concerning the impact on signal integrity of planar EBG structures embedded in transmission media such as strip-lines and of the placement of vias in multi-layered circuit boards are reported in [pau_09] and [pau_10].

An EBG surface based on square unit-cells with multiple slits in the upper metal plane is introduced in [rao_11] for noise mitigation. With a cell edge of 15.2 mm, a stop-band in the range 0.9–3.5 GHz has been obtained. A circuit model is proposed for predicting the band limits.

Leaky wave antennas can be built starting from a high impedance surface exploited in the region of fast surface waves, when the structure radiates and consequently the propagation constant corresponding to surface waves is complex. As mentioned above, radiation steering is explained by the continuity of the tangent component of the wave vector when surface waves couple with plane waves that propagate in the medium surrounding the surface. The literature treating leaky wave antennas inspired from metamaterial technology is very large and will not be covered here in detail. Only some examples will be provided instead. Rather, the topic concerning switched and tunable radiating structures will be referred more thoroughly since it has constituted a starting point for a part of our own work.

An application of EBG structures to antenna construction has been reported in the same issue of the journal where the first work of Sievenpiper on HISs has been published [shum_99]. An EBG structure in a PPW has been used for construction of a Luneburg lens in antenna feeding [park_01].

Finding new shapes for the metal pattern in the unit cell of periodic surfaces based on microstrip boards in view of improving various features have been a constant subject of research. A proposed fork-like pattern has reduced the covered area by 40% with respect to the mushroom structure [yang_05] The device has been used for a double-element microstrip antenna array, a notch-type antenna duplexer etc.

When the geometry of the surface is altered, the effective parameters change and so does the tangent component of the wave vector. Consequently, signals can be steered by taking advantage of this property. A mechanical solution for beam-steering of radiation from a HIS has been proposed in [siev_02]. The modification of surface parameters of the HIS is achieved by translating a second tuning layer at a certain distance above the surface. The tuning layer consists of square metal patches and changes the capacitance of the HIS with the effect of modifying the steering angle for a given frequency. A claimed 45° scan is obtained for a movement of the tuning layer of 1/500 of a wavelength.

Electronic solutions when exist are in general more reliable and controllable than mechanical ones. Tunable surfaces can be obtained by incorporating electronic control devices, such as MEMS, diodes or FETs, into the geometry of the HIS. A solution that relies on varactor diodes connecting the patches of the mushroom structure is presented in [siev_03]. A bias voltage modifies the capacitances of the varactors and consequently the resonance frequency of the surface. A $\pm 40^\circ$ range of modifiable steering has been obtained in two dimensions. The device can function as a reflectarray with greater bandwidth than conventional solutions and offer a low-cost alternative to generally used phased arrays. However, the array of varactors needs a biasing network that could alter the propagation of the electromagnetic field.

A tunable HIS also based on the mushroom structure and varactor diodes has been used for the realization of an electronically steerable leaky wave antenna [siev_05-b]. By tuning the surface, the radiated beam could be scanned over a wide range in both forward and backward directions. An optimization algorithm has been applied for finding the bias voltage of individual varactors in order to provide a convenient beam steering.

A solution for tunable and steerable S-band low-profile antenna based on varactor diodes mounted between patches of a HIS has been proposed in [costa_08]. A bow-tie radiating element has been placed above the FSS which acted like an artificial magnetic conductor due to the high impedance. Beam scanning for each working frequency has been achieved by appropriately biasing the diodes and changing in this way the capacity between patches. The proposed biasing solution is simple, involving two potentials, one applied to the patch plane and one to the ground plane. However, the biasing network must be present on the face of the board containing the patches.

A tunable surface based on periodic arrays of metallic loops impressed on either side of a thin dielectric substrate has been proposed, discussed and tested in [baya_09]. Tuning has been achieved again by means of varactor diodes mounted between metallizations of the unit cells and by modifying the value of the bias voltage. The solution has been assessed by simulation and then tested in a waveguide measurement setup. The difficulties for biasing the diodes inside the waveguide have been circumvented by using different values of fixed capacitors in the experiments.

A 1D tunable structure using FET devices has been proposed in [matek_09]. The device consisted of a 1D periodic structure positioned between the ground plane and the microstrip line. The unit cell contained one metal patch of rectangular shape. The patches could be selectively connected to the ground plane by individually controlled FETs. The technology (GaAs substrate) allowed for very small dimensions of the unit cell (tenths of mm). Variation of the effective dielectric constant of the material from small values up to 100 has been obtained in a frequency range from low values up to 150 GHz.

An improved device, relying on the same principles has been proposed in [matek_11]. This time, the device has been aimed to function in the leaky region for antenna-on-chip or system-on-chip millimeter-wave applications. The possibility to digitally program the device allowed for changing the radiation pattern for a given frequency and for obtaining nearly identical radiation patterns for different frequencies. Dynamic shifting of the EBG by 80 GHz has been demonstrated.

The problem of modeling of switching devices for use in electromagnetic simulators has been raised in [thala_11]. It has been demonstrated that replacing reverse biased varactor diodes by capacities is not enough. Complete S parameters model should be used instead. Furthermore, placement of switching elements has an significant impact on the frequency characteristics of the system because of their transmission characteristics.

Switched and tunable frequency selective surfaces (FSSs) to be used in indoor environment for modification of electromagnetic architecture in view of facilitating propagation of mobile and wireless technology related signals has been proposed in [sanz_09]. The FSS consisted of slot dipoles and has been placed on one side of a flexible dielectric layer, while the active elements and the biasing network have been mounted on the other side. Switching between reflecting and transmitting modes has been demonstrated with *pin* diodes as control elements. Control of the pass-band has been achieved through varactor diodes.

A similar switching technique has been applied to substrate integrated waveguides (SIW) [xu_11]. SIWs are waveguides realized in microstrip technology that represent a low-cost and low-profile alternative to rectangular waveguides. The lateral walls are obtained by drilling two parallel rows of aligned vias along the conducting strip in the microstrip board. A fundamental high-pass mode of

propagation exists, like in a waveguide with metal walls. The switching solution involves a slot in the upper wall, parallel to the direction of propagation, which can be short-circuited by means of transversally mounted *pin* diodes. The diodes are placed on metal pads, separated from the upper wall of the waveguide by a thin insulating layer. The waveguide can be switched between conduction and 50 dB isolation with a 3 dB insertion loss.

When building a tunable FSS, at least one tuning element must be considered per unit cell. If the number of unit cells is large, the cost of the final product becomes prohibitive. A solution to reduce the number of varactors has been proposed in [costa_11]. Square metal patches impressed on one side of a board have been connected through vias to a layer placed beneath and insulated from the ground plane, containing a network of segments of transmission lines which connected several patches (eight) to one diode. Waveguide measurements of reflection phase demonstrated tuning capabilities controlled by the bias voltage of the diode.

Filtering is a natural application of EBG materials due to the band-structure. Multi-band and broad-band filters in microstrip and suspended strip-line technology are current subject of research (see e.g. [menzel_03]). In microstrip filter design, patterns introduced as defects in the ground plane are known as a solution for frequency response shaping [ahn_01].

A non-uniform series of circular slots or annular rings in the ground plane parallel to the signal line of a microstrip board, with dimensions proportional to coefficients of binomial and Chebyshev polynomials, have been shown to provide low pass-band ripples and distinct stop-bands [karm_03].

A repeated pattern of resonant loads etched in the ground plate below a microstrip line has been proposed as a 1D structure of filter inspired from EBG materials [gao_06]. A design methodology, including control of ripples in pass-bands has been devised.

Filtering applications of 1D periodic structures realized in ridge waveguide technology have also been reported [gouss_06].

A dual-band filter has been devised for applications in the wireless communications area, such as multi-antennas, by using a 2D periodic structure in microstrip technology obtained by cascading mushroom-like unit cells that operate at different frequencies [zhang_08]. The modification of the frequencies defining the filter bands has been achieved by changing the positions of the vias within the rectangular patches in the unit cells.

Filters with multiple notch bands, fabricated in multi-layer liquid-crystal polymer lamination technology, designed to be used in UWB communication and radar systems have been proposed [hao_09]. The structure included three layers; the periodic pattern has been etched as a 1D slotted structure in the ground plane.

A modification of the ladder microstrip line, performed by inserting loaded grounded strips between the signal strips allowed the construction of third-order Chebyshev filters with claimed pass-band ripple of 0.05 dB and a relative bandwidth of 10% [chang_11].

The research we are presenting in the next sections has been performed by using a commercial full-wave field solver [CST] which relies on the *Finite Integration Technique* [weil_77] for solving the integral forms of Maxwell's equation. A presentation of relevant issues related to such field solvers can be found in [weil_08].

We will present the results obtained in the field of high impedance surfaces (HISs) and metamaterials in a logical sequence rather than in a time order following publication. We present fixed surfaces in the first subsection and switchable ones in the second subsection.

B. Fixed Surfaces

The first presented work (in 2009) and published paper (2011) dealing with HISs reported a parametric study of the shielded Sievenpiper structure [11_08_M].

The structure and the dimensions of the first HIS we have considered are represented in Fig. 1. It consists of a microstrip board with the periodic metallic pattern impressed on one side. The other side of the board plays the role of a ground plane. In order to obtain a parallel plate waveguide, a metallic plane is placed at a distance g above. In fact, an electric condition has been imposed in the simulation and periodic conditions have been imposed on the planes perpendicular to the structure that contain the edges of the unit cell; the origin of the reference system has been taken at the center of the basic pattern. The following parameters have been varied during the simulations: the dimensions x and y of the rectangular patch and the distance g between the upper metallic wall and the patch.

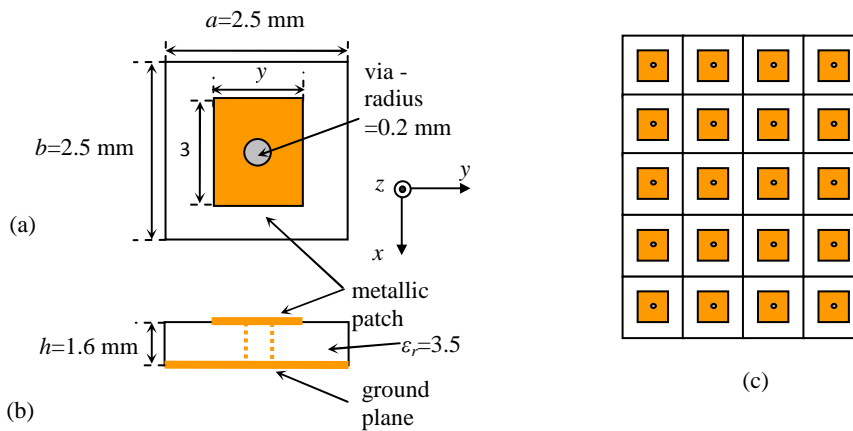


Fig. 1. (a) Basic pattern: top view; (b) basic pattern: side view; (c) high impedance surface obtained by repetition of the basic pattern.

The DD for some specific values of the geometric parameters and the light lines are reported in Fig. 2. Unlike the other simulations that will be presented below, we performed calculation on the entire Brillouin irreducible zone $\Gamma X M \Gamma$. The figure shows some features of the DD consistent with other results that have been reported in the past. The DD for the first mode is tangent to the light lines, and it presents regions of positive and negative group velocities. The group velocities are zero at points X and M. DD's of higher order modes intersect the light lines so that fast and slow waves may be launched. As indicated on the figure, the EBG is comprised between the maximum frequency corresponding to the first mode and the minimum frequency of the next mode. The figure also suggests that, in order to determine the central frequency and the width of the band gap, the DD for the ΓX portion of the Brillouin zone suffices.

The widths and the central frequencies of the EBG for various dimensions of the rectangular patch and a fixed value of g are reported in Fig. 3 and Fig. 4 respectively. The central frequency is calculated by taking the geometric mean of the two frequencies that define the limits of the EBG. The reason why we preferred the geometric mean rather than the arithmetic one is that, in an effective medium model, the surface impedance behaves like a second-order parallel resonant circuit [siv_99] whose central frequency is defined in this way.

The same quantities are represented in Figs. 5 and 6 for another value of g . The decrease of the central frequency with the increase of the patch dimension might be associated with the increase of the capacitive effects due to the fact that adjacent patches become closer together.

In order to gather more information on the EBG, we have performed two other simulations. In the first one, we kept constant the y dimension of the patch and varied the x dimensions, for two different values of g that are also different from the values we have used in the previously reported simulations.

In the second one, we imposed a square shape for the patch, so that we varied simultaneously the dimensions x and y for the same values of g as previously. The frequencies that define the limits of the EBG are represented in Fig. 7 and 8. It can be seen that the height of the waveguide has a greater influence on the upper limit than on the lower one.

Figs. 7 and 8 suggest that the central frequency and the bandwidth diminish when g is increased, which is in accordance to Figs. 3..6.

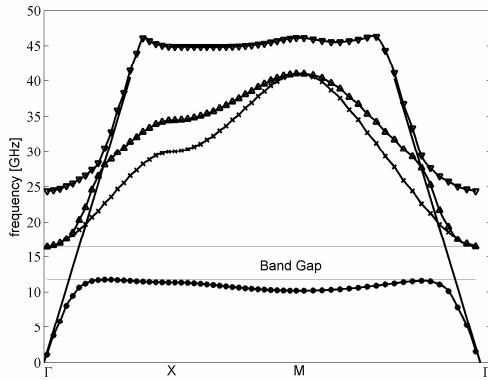


Fig. 2. Dispersion diagram for $g=2h$ and $x=y=2.1$ mm (light lines have no markers).

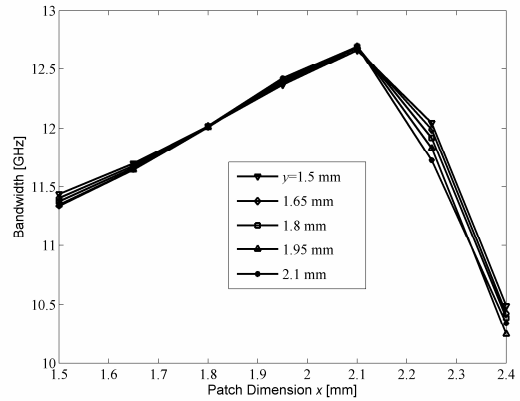


Fig. 3. Widths of the bandgap for various patch dimensions and $g=0.5h$.

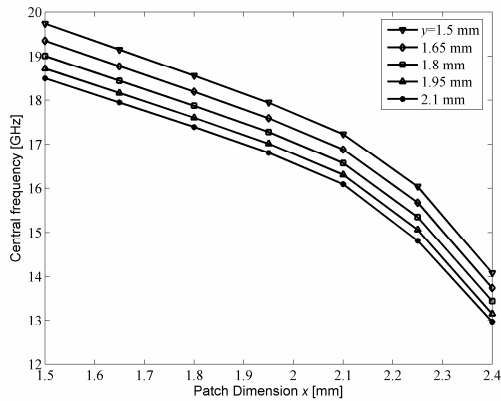


Fig. 4. Central frequencies of the bandgap for various patch dimensions and $g=0.5h$.

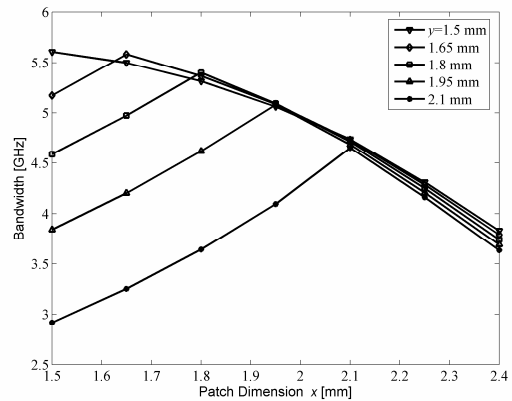


Fig. 5. Width of the bandgap for various patch dimensions and $g=2h$.

We considered a variation of the structure obtained by replacing the rectangular patch with a circular one, of radius r and keeping constant the other geometrical parameters and the dielectric constant of the substrate. The top view of the basic pattern is represented in Fig. 9.

The DD for the new structure is quite similar to the DD of the previous one. An example, for some specific values of the radius r and of the height g is presented in Fig. 10. Only the ΓX portion of the Brillouin zone has been considered and the horizontal axis has been marked in radians, measuring the normalized wave-number. As it can be seen, the EBG is well defined in this case too.

The limits of the EBG for a specific value of g , but different from the previous one are reported in Fig. 11, in function of the patch radius r . Both limits decrease with the decrease of the distance between two adjacent patches, like in the case of rectangular ones (Figs. 7 and 8).

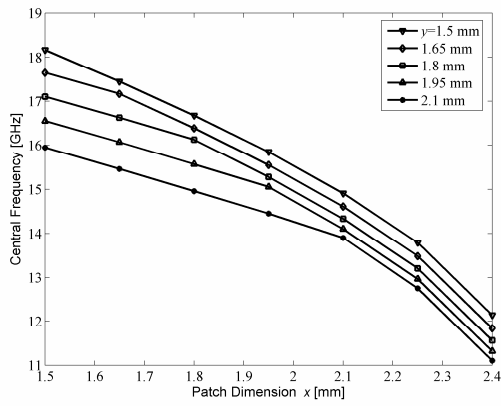


Fig. 6. Central frequency for various patch dimensions and $g=2h$.

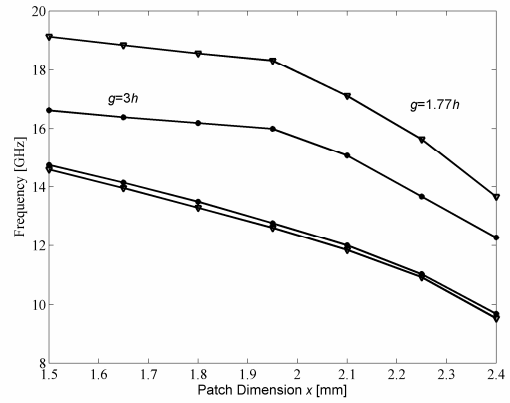


Fig. 7. Minimum and maximum frequencies that define the bandgap in function of x , for two values of g and $y=1.95$ mm.

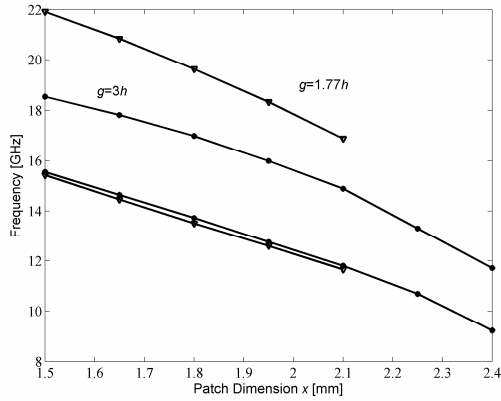


Fig. 8. Minimum and maximum frequencies that define the bandgap in function of the patch dimension ($x=y$).

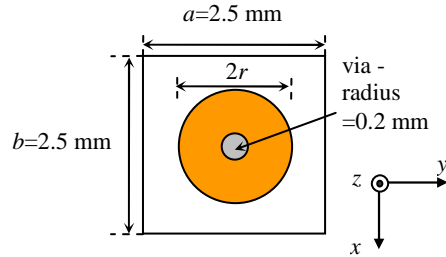


Fig. 9. Circular patch.

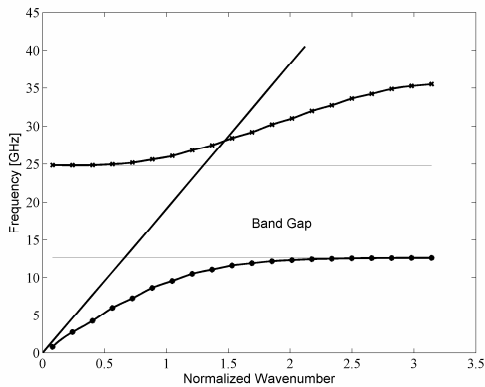


Fig. 10. The first two modes in the GX region of the dispersion diagram for the case of a circular patch: $g=0.5h$, $r=2.1$ mm.

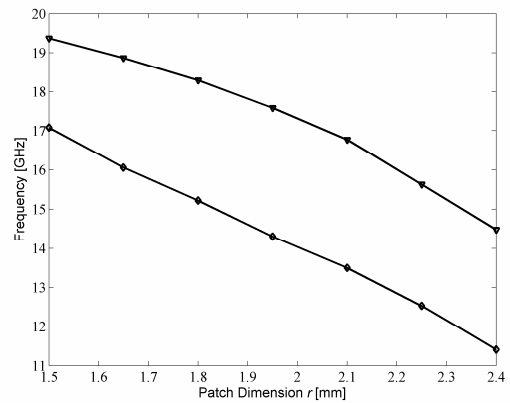


Fig. 11. Minimum and maximum frequencies that define the bandgap in function of the circular patch radius ($g=3h$).

We have calculated the widths of the bandgap and the central frequencies (defined again as geometric means of the limits of the EBG) in function of the radius of the patch, for various values of g and represented the results in Figs. 12 and 13 respectively. The shapes of the curves are similar to those obtained for rectangular patches.

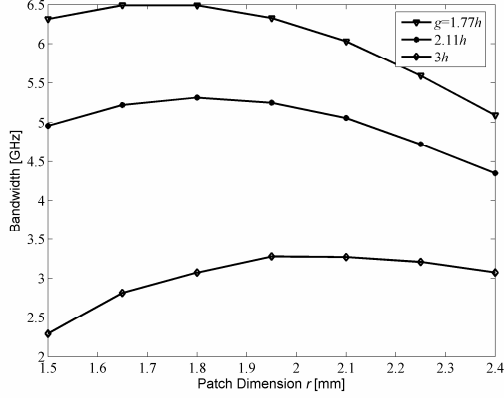


Fig. 12. The widths of the bandgap in the case of circular patches, for various values of g .

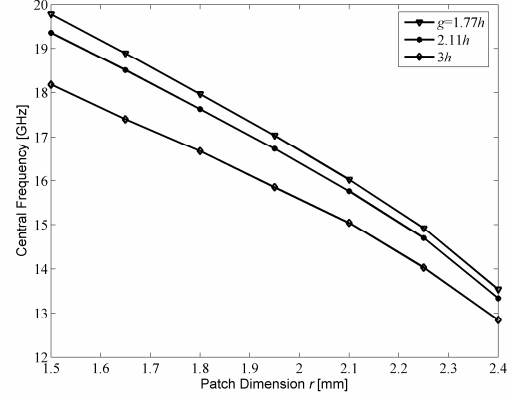


Fig. 13. Central frequencies of the bandgap in function of the radii of the circular patches, for various values of g .

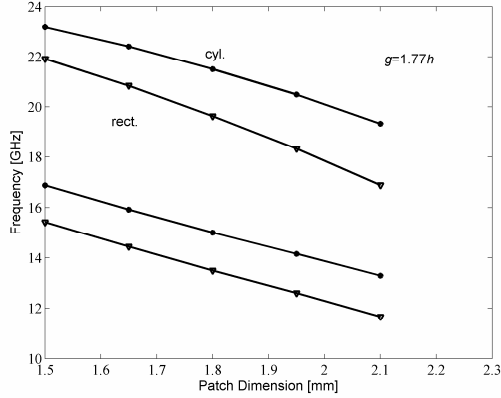


Fig. 14. Positions of the bandgaps for a circular and a rectangular patch, for various dimensions of the patches ($x=y=2r$).

In order to compare a HIS based on square patches to a HIS based on circular ones, we have represented, in Fig. 14, the limits of the EBG in function of the patches dimensions, for a specific value of g , when the side of the square is equal to the diameter of the circle. The limits result lower in the square (rectangular) case than in the circular case and the shape of the curves are similar. However, the ratios of the corresponding frequency limits have a very slight variation with r (being around 0.9).

The parameterized families of curves presented consistent variations and have been intended to be used in the design activity.

After gaining some insight into properties of square and circular patches, we have introduced the elliptical patches for three reasons: i) provision of smooth edges for the current density, like the circular patches; ii) provision of design flexibility in the same way as rectangular patches present versus square metal patches and iii) larger bandwidths that can be obtained (as demonstrated below). We have introduced and studied parametrically the elliptical patches in [09_01_M].

The geometry of the HIS and relevant dimensions and parameters are represented in Fig. 15. The origin of the coordinate system is at the center of the patch. The upper metallic plane (not represented) is situated at a distance $g=0.5h$ from the patches plane. The influence of g on the EBG has been already established and reported (e.g. in the above mentioned paper): a smaller g provides a larger width of the EBG. Therefore, this parameter has been kept constant throughout this work.

The DD corresponding to this structure, with $x=2.4$ mm and $y=1.8$ mm is reported in Fig. 16, where the first four modes have been considered, and the (air) light line has been also represented. The shape of the DD is consistent with other patch geometries and an EBG exists between the first two modes. It is interesting to compare the width of the EBG of this HIS to EBG widths of other structures characterized by similar parameters. We have considered a rectangular patch and an elliptical one with two vias, situated on the x axis at half distances between the origin and the extreme points of the ellipse (Fig. 17). The radii of the vias are the same in all situations and so are the x and y dimensions of the patches. The results are synthesized in Table 1.

The frequencies f_{min} and f_{max} correspond to the lower and upper limits of the band gap defined in Fig. 16, and the bandwidth B is the difference of the two. The central frequency f_0 is the geometric mean of

the limit frequencies: $f_0 = \sqrt{f_{min} f_{max}}$. The reason why we preferred the geometric mean rather than the arithmetic one is the same as in the case of rectangular patches: in an effective medium model [siv_99], the HIS impedance behaves like a parallel resonant circuit. The quality factor is defined as usual by $Q = \frac{f_0}{B}$. We have also added results concerning HIS built with unit cells with elliptical patches having the same x dimension but $y=1.5$ mm (last column of Table 1). Since interpolation has been used, some numerical inaccuracies might be present.

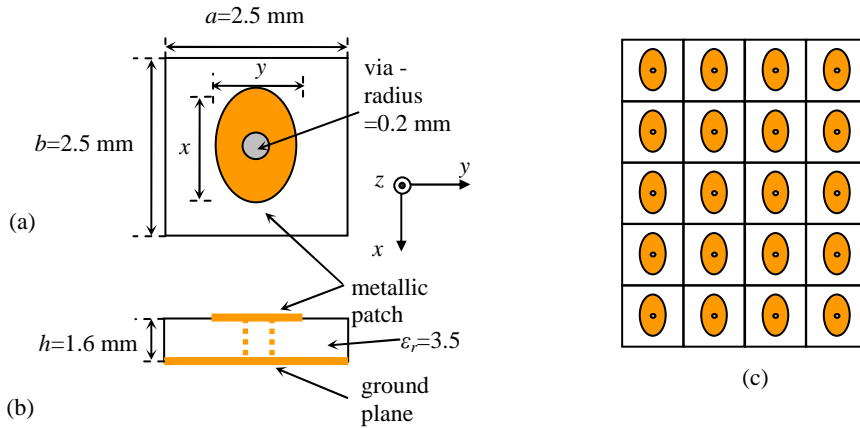


Fig. 15. (a) Unit cell: top view; (b) unit cell: side view; (c) high impedance surface obtained by repetition of the unit cell.

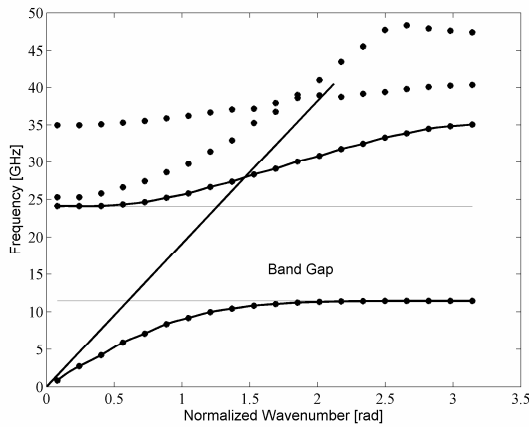


Fig. 16. Dispersion diagram for a HIS with elliptical patches (the light line has no marker).

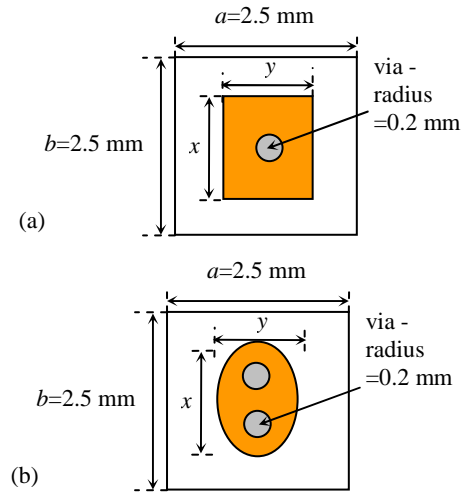


Fig. 17. Patches: (a) rectangular, (b) elliptical with two vias.

The results in Table 1 may be explained in terms of the circuit parameters of the HIS from the effective medium model [siv_99]: the vias have an important inductive effect, while adjacent patches introduce capacitive effects. When two vias are used instead of one, the path for the current induced by electromagnetic surface waves gets shortened, resulting in a reduced inductance and hence a higher central frequency. The surfaces of an elliptical patches are lower than those of rectangular ones, resulting in reduced capacitive effects and again an increased central frequency. For similar reasons, decreasing the y dimension of a HIS based on a unit cell with an elliptical patch results in increased frequency characteristics of the EBG. The DD's of the HIS based on unit cells with elliptical patch and two vias and rectangular patch with dimensions specified above are presented in Figs. 18 and 19 respectively.

Table 1: Frequency characteristics of EBG's

	Elliptical patch, two vias, $x=2.4$ mm, $y=1.8$ mm	Elliptical patch, one via, $x=2.4$ mm, $y=1.8$ mm	Rectangular patch, one via, $x=2.4$ mm, $y=1.8$ mm	Elliptical patch, one via, $x=2.4$ mm, $y=1.5$ mm
f_{min} [GHz]	16.1730	11.4610	9.2169	12.1154
f_{max} [GHz]	26.1362	24.0922	19.5651	24.7499
B [GHz]	9.9632	12.6312	10.3482	12.6345
f_0 [GHz]	20.5597	16.6169	13.4287	17.3163
Q	2.0636	1.3155	1.2977	1.3706

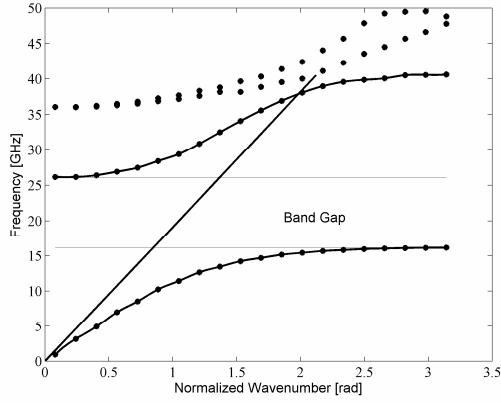


Fig. 18. Dispersion diagram for a HIS with elliptical patches and two vias.

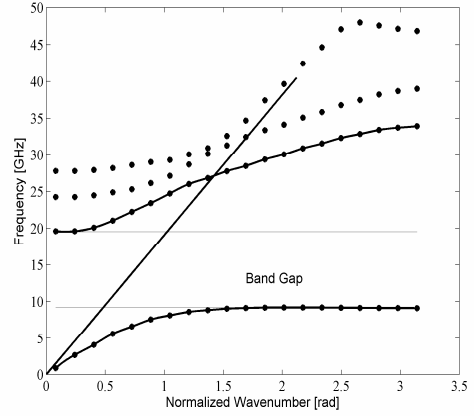


Fig. 19. Dispersion diagram for a HIS with rectangular patch.

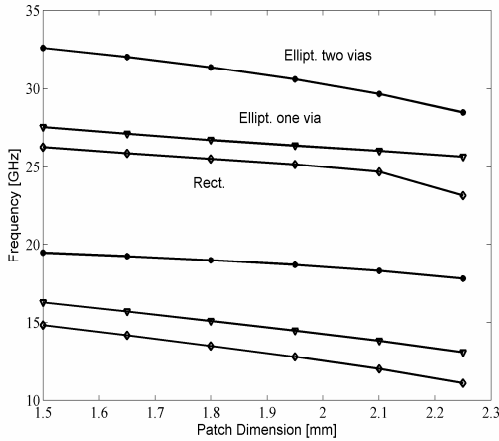


Fig. 20. Minimum and maximum frequencies defining the EBG for elliptical patches with two vias, elliptical patches with one via and rectangular patches. The dimension y is kept constant at 1.5 mm, while the dimension x is varied.

For a quantitative characterisation of the position in frequency of the EBG for various dimensions of the patches, we have determined the DD's for a fixed value of y , namely 1.5 mm but we have varied the x dimension in the range 1.5..2.25 mm, for the three cases we have considered above: elliptical patches with two vias, elliptical patches with one via and rectangular patches. The other geometrical dimensions and the value of the dielectric constant are the same as above. From the DD's we have determined the minimum and maximum frequencies and represented the results in Fig. 20. The monotonicity properties of the curves in Fig. 20 tend to confirm what has been said about the influence of the circuit parameters from the effective medium model of the HIS.

The presented results may be useful in the design of HIS with specified EBG parameters, for various applications.

Parametric studies and numerical explorations of the shielded structure with elliptical patches have been performed by varying geometric and material parameters. The obtained results have been reported in [10_01_M] and [10_02_M].

In the first one of the above mentioned papers, we deal with a unit cell including an elliptically shaped patch on a dielectric layer, connected to the metallic ground plane by a variable number of vias. The geometry can be conveniently realized in microstrip technology. The vias are thought to have diodes or FET switches whose state can be externally controlled by a biasing voltage with the aim to generate a tunable geometry. When the active devices are not biased, they exhibit high impedances, which can be modeled for precise characterization or simply assumed to be infinite. On the other hand, when they are biased, their impedances are negligibly small and they act as short-circuits. This preliminary study does not tackle the presence of the control part, but it aims to verify the degrees of freedom of the structure and the feasibility of a tuneable surface with the considered control parameters.

For non-tuneable applications, HIS geometries that provide the largest values for EBG's are of interest. Therefore we have determined the EBG parameters for this particular configuration with the radius of the via which maximizes the band-width.

The numerical study, carried out by commercial software, allows a full characterization of the infinite surface, by adequate periodic boundary conditions imposed to the unit cell. The parametric study regarding the effect of the number of vias and of the aspect ratio of the ellipse allows for collecting information needed to fulfil design inputs. The EBGs for the various geometries have been obtained from the dispersion DD computed by the Eigenmode Solver of the CST Microwave Studio on the entire $\Gamma X M \Gamma$ border of the first irreducible Brillouin zone associated to the rectangular lattice. The DD is useful for finding other relevant quantities, such as the phase and group velocities as well. The applications of HIS in the field of low profile antennas require a precise control of the limits of the band-gaps. Therefore, studies on the influence of the various geometrical parameters on the frequency position of the EBG have been performed.

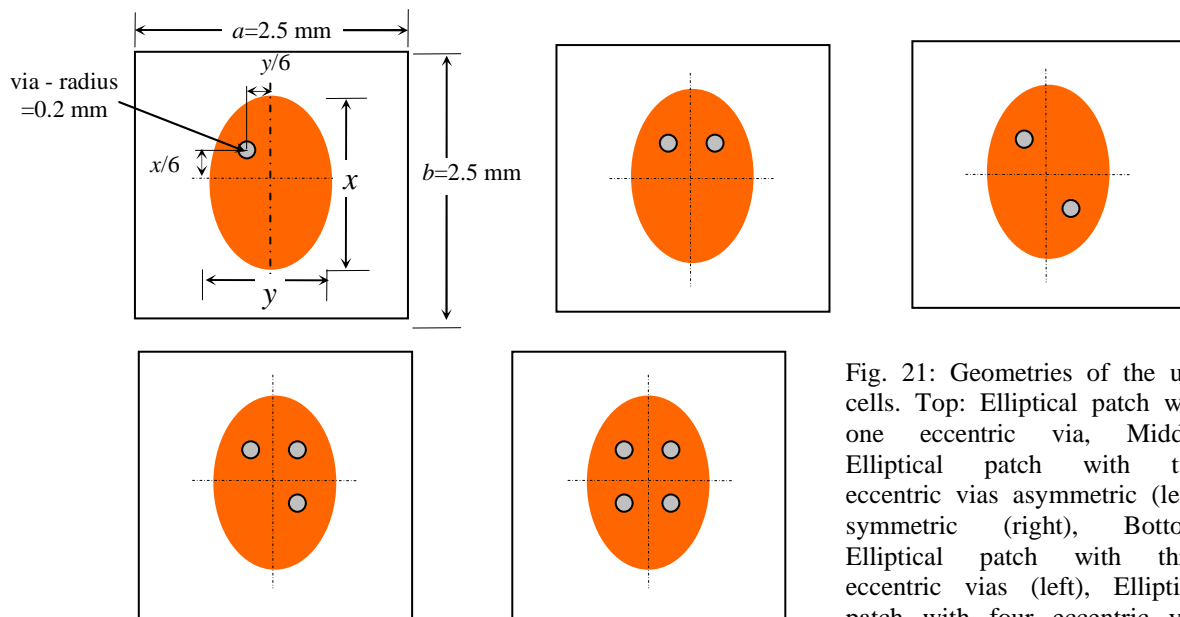


Fig. 21: Geometries of the unit cells. Top: Elliptical patch with one eccentric via, Middle: Elliptical patch with two eccentric vias asymmetric (left), symmetric (right), Bottom: Elliptical patch with three eccentric vias (left), Elliptical patch with four eccentric vias (right).

The unit cells we are considering here, and shown in Fig. 21, have square shape with dimension $a=b=2.5$ mm in the two orthogonal directions. The grounded dielectric of height $h=1.58$ mm is characterized by $\epsilon_r=3.5$. On the top of the dielectric an elliptically shaped patch with the main axes y and x is considered.

In this study, one of the major axis of the ellipse has been maintained constant, while the other one has been varied. The variation has been chosen in such a way to incorporate the degenerate configuration of circular shape. In particular, the y dimension has been fixed to the value of 1.8 mm,

while the dimension along x has varied from $x_{min}=1.5$ mm to $x_{max}=2.25$ mm with steps $\Delta x=0.15$ mm. Different numbers N_V of vias from 1 to 4, all with a radius of 0.2 mm, have been considered. The eccentric vias are shifted with respect to the origin by $S_x = \pm x/6$ and $S_y = \pm y/6$. This means that when x varies, the positions of the vias vary as well: this choice has been considered for scalability reasons. On the top of the entire geometry an air layer has been positioned; the CAD model for $N_V=3$ is shown in Fig. 22.

DDs for all configurations in Fig. 21 have been computed. In Fig. 23 we report those related to the $N_V=4$ vias case. The band-gap and the light-lines are clearly indicated.

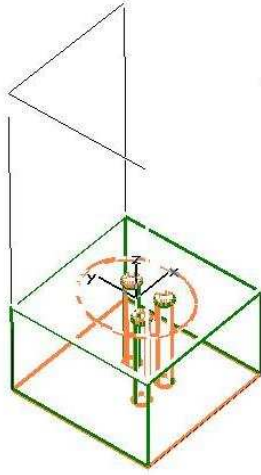


Fig. 22: CAD model of the geometry for $N_V=3$, $x=1.5$ mm, $y=1.8$ mm.

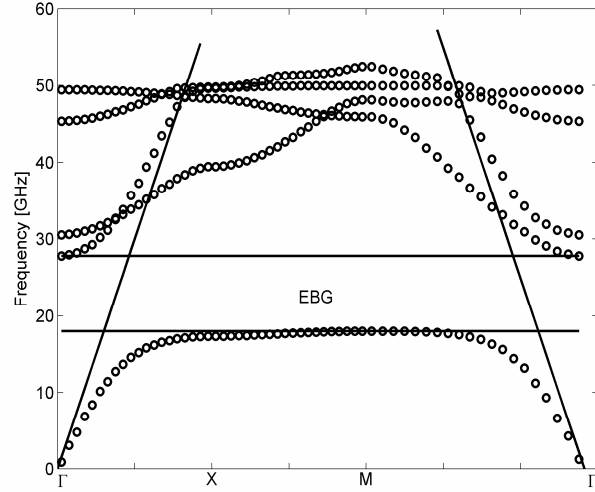


Fig. 23: Dispersion diagram for the elliptic patch with $N_V=4$ vias.

The DDs for the structures with other numbers of vias present similar behaviour, allowing a comparison in terms of band-gap position and width. The results referring to the central frequencies of the band-gaps are reported in the plot in Fig. 24, while band-gap widths are represented in Fig. 25 as a function of the size along the x axis of the ellipses.

The EBG bounds are defined as the maximum of the first, always bounded, mode and the lowest value of first higher order mode. The variation of the band-gap is as high as 10% around 12 GHz. The central frequencies are calculated as the geometric mean of the EBG limits. Moreover we can observe that the maximum width of the band-gap is achieved for a circular configuration, except for the case of $N_V=1$ and $N_V=2$ asymmetric vias. This can be explained by the effect of two opposite behaviours resulting from the variation of the geometry. When the value of x is varied in the indicated interval, the mutual inductance between the various vias decreases, while the capacity between patch and ground plane increases. The effect of the two opposite behaviors gives the results shown in Fig. 25. For the $N_V=1$ case, the variation of the mutual inductance is not present, hence the continuous increase of the width of the band-gap can be observed as a consequence of the increase of the capacitance. Similar observations hold for the $N_V=2$ cases but the responses are affected by the symmetries.

The parameterized results reported here are useful for design issues and for circuit models conception and validation.

Unit cells with the same geometry, but different electromagnetic responses, can be employed in different applications in the field of antenna technology, e.g. controlling of the direction of radiation, sensing etc.

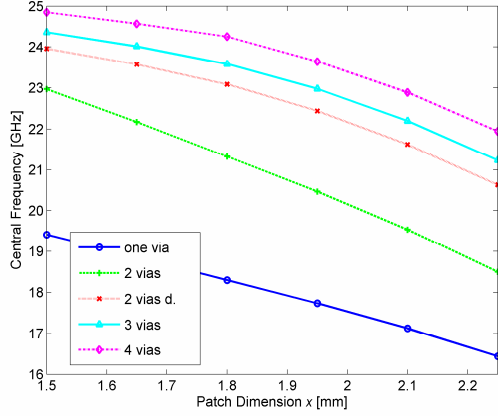


Fig. 24. Central frequencies of the band-gaps for the structures in Fig. 1 with $y=1.8$ mm.

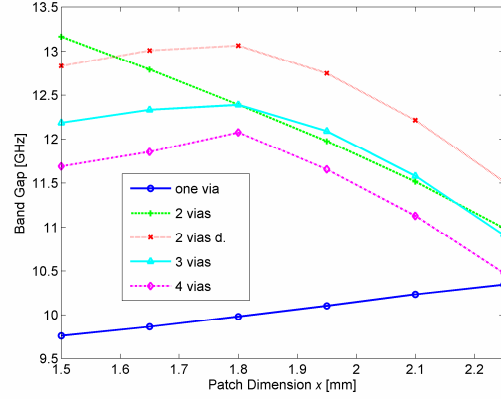


Fig. 25. Extension of the band-gaps for the structures in Fig. 1 with $y=1.8$ mm.

The continuation of the above presented parametric study of EBG planar structures with elliptical patches has been continued in [10_02_M]. We have considered vias with variable radii. The radii of the vias for a single geometry are equal in each simulation; however, three values have been considered, namely $r=r_1=0.2$ mm; $r=r_2=0.15$ mm; and $r=r_3=0.1$ mm. Three vias configurations have been studied: 1° two vias: 1 and 2; 2° three vias: 1, 2 and 3; 3° all four vias. We will refer to a given geometry in the shape (m,n) , where m is the number of vias and n is the index of the radius as denoted above. For reference, the vias are numbered as in Fig. 26, where the position of the xy frame is also represented.

The results of the first simulation, performed on the configuration with three vias of radius 0.2 mm, denoted by $(3,1)$ above, is reported in Fig. 27.

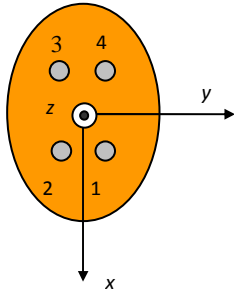


Fig. 26. Via numbering.

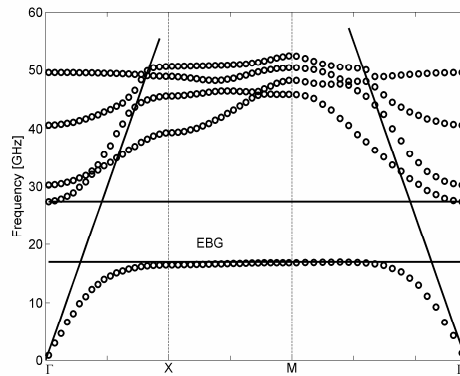


Fig. 27. Dispersion diagram for the structure with three vias of radii $r=0.2$ mm and patch dimensions $p=2.25$ mm, $q=1.8$ mm. Each graph corresponds to a propagation mode. The free space light lines are also represented.

The DD corresponds to the whole $\Gamma X M \Gamma$ border of the Brillouin irreducible zone. The general shape is consistent with other geometries. The EBG is clearly outlined; the comparison with the light lines shows the presence of waves with phase velocities greater and smaller than the speed of light; regions with negative group velocities are also apparent, and the group velocities vanish at X and M. It is interesting to note the points of higher order modes intersections. These points might be used for

applications involving power exchange between modes; however this issue is not considered in this context.

The rest of the simulations have been performed on the ΓX edge of the Brillouin zone, involving surface waves that propagate along the x direction only. The obtained band-gaps and the center frequencies of the EBG's are reported in Fig. 28 and Fig. 29 respectively. The central frequencies have been calculated at midpoints between the frequency limits of the band-gap. A geometric mean would have been an appropriate choice too, since e.g. the impedance of Sievenpiper's HIS admits an effective medium model in the shape of a parallel resonant circuit, as mentioned above. However, the arithmetic mean is easier to interpret in this context.

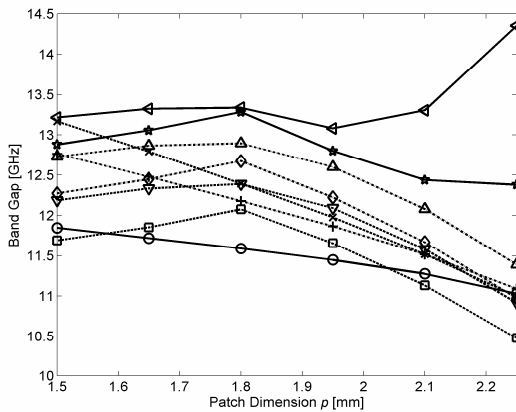


Fig. 28. Band gap as a function of the p patch dimension for $q=1.8$ mm. The graphs are marked as follows. Two vias with $r=0.2$ mm: x mark, $r=0.15$ mm: plus, $r=0.1$ mm: circle. Three vias with $r=0.2$ mm: down triangle, $r=0.15$ mm: up triangle, $r=0.1$ mm: left triangle. Four vias with $r=0.2$ mm: square, $r=0.15$ mm: diamond, $r=0.1$ mm: pentagram. Identical radii are drawn with the same line type.

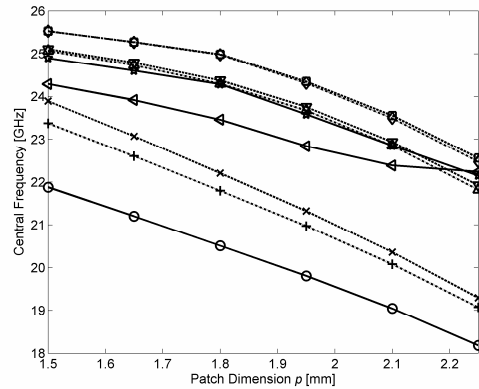


Fig. 29. Arithmetic central frequency as a function of the p patch dimension. The graphs are marked as in Fig. 28.

The following relevant data may be derived from Figs. 28 and 29. The largest band-gap widths, between 13.33 and 14.35 GHz correspond to (3,3), while the smallest one, of 10.47 GHz, occurs for (4,1), at $p=2.25$ mm. The $m=4$ vias geometry is similar to a closed resonator. The role of the vias is to confine the electromagnetic field. Similarly to the shorting pins used to prevent generation of the fundamental parallel plate modes in the strip line configurations, they inhibit the “passing thru” of the electromagnetic field from the inside of the cavity toward its exterior (and vice-versa) when the wavelength is smaller than the distance between them. The volume in-between the vias corresponds to a closed resonator, with high Q . Increasing the patch dimension p the volume of the resonator increases and consequently the resonant frequency decreases in accordance to the data in Fig. 29. When $m=3$, the closed resonator becomes an open resonator where the field intensity in correspondence to the “missing” vias externally to the resonator is different from the 4-vias case. Consequently the Q factor decreases corresponding to an enlargement of the band-width. The distributions of the electromagnetic field in the dielectric for the $m=3$ vias cases in the first two pass-bands and stop band are reported in Fig. 30. The data have been obtained with a phase shift of $(\phi_x, \phi_y)=(40.5,0)$ degrees between the input and output ports.

The band-gap widths for the geometries $(2,n)$, $n=1..3$ have an almost linear variation, which is very convenient for design purposes. For the rest of the geometries, maxima occur when ellipses become circles ($p=q=1.8$ mm), while (3,3) and perhaps (4,3) also admit minima. When two vias are used, a decrease in the vias diameter have the effect of decreasing the bandwidth due to the variation of the self inductance of the vias, while the effect is opposite for geometries with three and four vias, because of the different role of the vias as explained above.

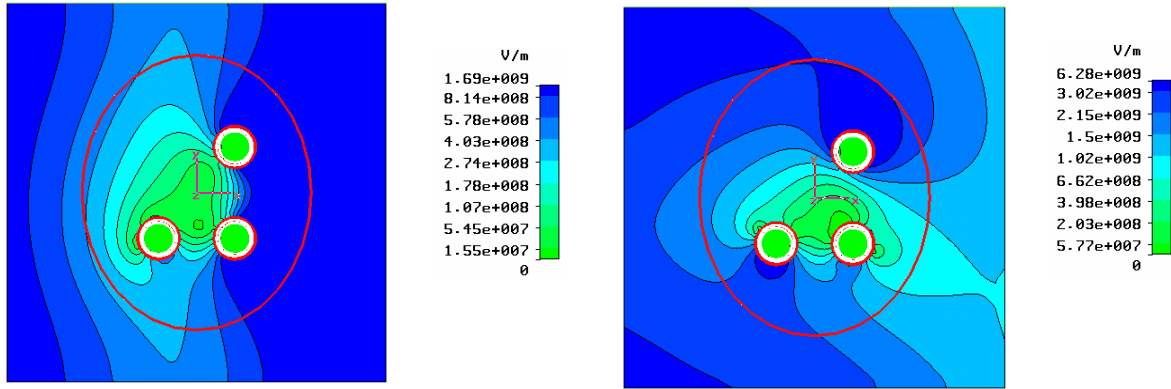


Fig. 30. Distribution of the electromagnetic field a) in the first pass-band (first mode, $f=8.07$ GHz); b) in the second pass-band ($f=31.47$ GHz) of the $m=3$ via case (same case as in Fig. 3). The cuts are parallel to the ground plane in the dielectric at half of its height.

All central frequency curves decrease with the increases of p , which correspond to a larger area of the capacitor formed by the ground plane and patch. Increasing the capacitance, the resonant frequency will decrease. Again, the geometries with two vias provide almost linear variations. The central frequencies for (4,1) and (4,2) are almost coincident, and so are (3,1), (3,2) and (4,3); however the bandgaps are different. Regardless of the number of vias, decreasing diameter leads to a decrease of the central frequency. The largest central frequency, of 25.53 GHz corresponds to (4,1) or (4,2), while the smallest one, of 18.18 GHz, occurs for the (2,3) geometry.

For the two-via geometry, the largest bandgap width, of 13.17 GHz and the largest central frequency, of 23.89 GHz occur for (2,1) at $p=1.5$ mm, while the smallest bandgap width, of 11.03 GHz and the smallest central frequency, of 18.18 GHz occur for (2,3), at $p=2.25$. The frequency span is from 12.67 to 30.47 GHz.

The three-via geometry provides a frequency span from 15.07 to 31.20 GHz. The minimum occurs for (3,3) at $p=2.25$ mm and the maximum occurs for (3,1), at $p=1.5$ mm. The band-gap widths are 14.35 and 12.29 GHz, while the central frequencies are 22.24 and 25.11 GHz respectively.

For the four-via case, a frequency span between 15.96 and 31.38 GHz is obtained. The results that correspond to those presented above are: (4,3) and $p=2.25$ mm for the minimum and (4,2), $p=1.5$ mm for the maximum. The band-gap widths and central frequencies are 12.38 GHz, 22.15 GHz and 12.27 GHz, 25.53 GHz respectively.

The global frequency span is from 12.67 GHz to 31.38 GHz, the limits being in a ratio of 2.48:1.

The presented results are relevant for the design of fixed or tuneable HIS in view of various applications.

A passive, low-cost device built with a textured surface, consisting of a periodic lattice of metal patches, embedded in an inhomogeneous parallel-plate waveguide has been proposed in [11_12_M]. It acts as a band-pass filter in the microwave frequency range and it can be also used in sensor applications. We presented the frequency related properties of the structure by means of the dispersion diagram calculated by full-wave electromagnetic simulation. We performed a parametric study in function of the dielectric constant of one of the materials entering the construction of the device.

The structure of the device we have proposed is reported in Fig. 31 (a). It consists of two parallel metal plates that contain in between two different media of dielectric constants ϵ_{r1} and ϵ_{r2} respectively. At the border of the two media, a textured surface consisting of metal patches arranged in a periodic 2D lattice is impressed. Circular shaped patches have been chosen for each unit cell of the lattice. Metal pins connect the upper metal plate to the patches and vias connect the lower metal plate to the same patches, one of each for every unit cell. We have chosen pins instead of vias for the connection

of the upper plate as ϵ_{r2} may be equal to unity, so that air fills the corresponding space. Therefore, the mechanical structure is more robust in this case. A unit cell of the textured surface is represented in Fig. 31 (b) and the HIS obtained by the repetition of the unit cell is reported in Fig. 31 (c). Fig. 31 (d) shows the CAD model used for the unit cell of the device.

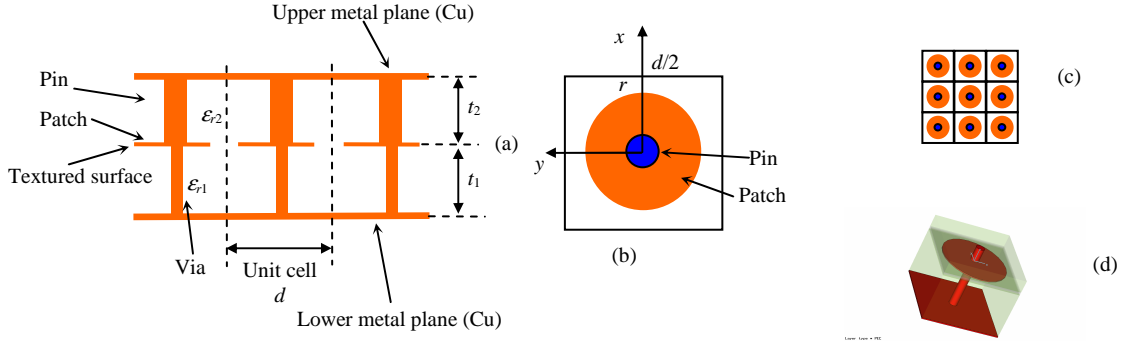


Fig. 31. (a) Proposed structure; (b) unit cell of the textured surface; (c) textured surface; (d) CAD model with upper metal plane removed for visualization.

We have used the following parameters: dimension of the square shaped unit cell $d=2.5$ mm, patch diameter $2r=2.1$ mm, $t_1=1.6$ mm, $t_2=0.3t_1$, radius of vias 0.1 mm, radius of pins 0.15 mm. The dielectric constant of the lower layer has been kept constant $\epsilon_{r1}=3.5$, while that of the upper layer, ϵ_{r2} , has been varied between 1 and 12 during simulations.

The DD of the structure for the case $\epsilon_{r2}=12$ is reported in Fig. 32. The shape of the border of the first irreducible Brillouin zone in the wave-numbers space is drawn in the inset of the figure. Light lines (LL's) are also represented, by assuming an effective dielectric constant of the inhomogeneous medium defined by ϵ_{r1} and ϵ_{r2} [rogers_05]. LL's are used for separation between fast and slow surface waves.

The first EBG spreads from DC up to f_0 , which is the minimum frequency of the first mode.

The second EBG is defined by f_1 , the maximum frequency of the first mode and f_2 the minimum frequency of the second mode. The fact that low frequency waves are cut up to DC is motivated by the DC connection between the two metal plates.

The frequency positions and widths of the EBG's can be adjusted according to requirements of various applications by varying the geometrical and material parameters of the device. We have performed a study on the influence of the dielectric constant of the upper layer on the relevant frequencies f_0 , f_1 and f_2 , Fig. 33. This choice is motivated by availability of a large range of low loss materials for high frequency applications.

The frequency span is sensitive to the material of the upper layer. The width of the pass-band (between f_0 and f_1) diminishes with the increase of the dielectric constant, making the filter more selective.

Several other parametric studies, in function of the geometric parameters will be performed in the future in order to provide further degrees of freedom in design.

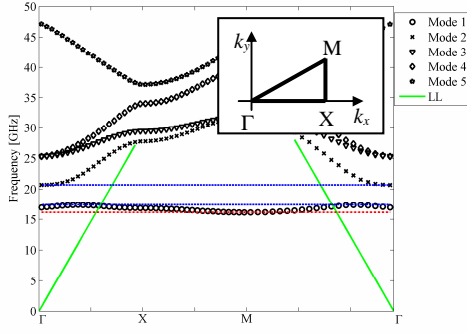


Fig. 32. DD of the proposed structure, featuring the first five modes. Inset: border of the first irreducible Brillouin zone.

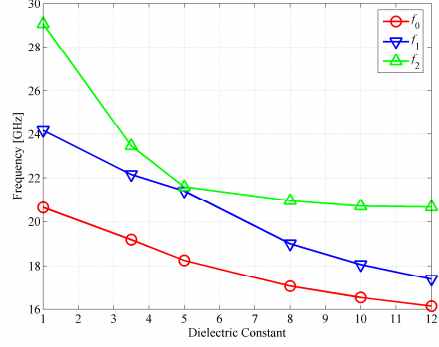


Fig. 33. Frequency limits of the EBGs versus dielectric constant of the upper material layer.

A solution for mitigation of parallel-plate noise in power distribution networks of high speed digital and mixed-signal circuits and of printed circuit boards based on an inhomogeneous parallel-plate waveguide (PPW) has been proposed in [12_01_M]. The PPW consisted of two different dielectric layers and a high impedance surface (HIS) at their interface. The frequency related properties of the structure have been studied through the numerically computed DD.

The general structure of a power distribution network in a multilayered environment is presented in Fig. 34 (a). The patterned surface is embedded within the upper and lower metal plates. Two materials, generally of different dielectric constants, fill the space in between the planes. The structure obtained in this way is an inhomogeneous PPW. Vias of type 1 connect the upper and lower metal plates and are electrically insulated from the patterned surface by a surrounding dielectric slot. The patterned surface consists of a periodic lattice of metal patches that can be connected by metallic pads. The patches may be connected to the lower metal plate by means of hollow vias. Additionally, pins are inserted between patches and the upper metal plane, and they may electrically connect the two in the limit. The idea of using pins has been first introduced in the context of coplanar waveguides, involving 1D periodicity. Here we prefer to test the effect of pins in a 2D setting.

Not all elements in the figure are actually present in a special solution. In fact, three configurations are generally used. First, a "mushroom" like configuration, when the upper metal plate, the vias type 1 and the pins are absent and $\epsilon_{r2}=1$. In this case, vias type of 2 must not be present and metal pads connecting patches must exist in order to provide two conducting plates for power supply. An example of a unit cell of a patterned surface and the surface itself are shown in Fig. 34 (b) and (c) (the pin must be removed in this case). This solution is not compact enough since radiation occurs in the stop-band.

In the other two solutions, both upper and lower metal plates are present. If vias of type 1 connect the two metal plates, the metal pads connecting the patches on the middle plane must be present in order to provide two power supply lines at different DC potentials. However, if vias of type 1 are absent, then it can be shown that the structure with pads does not have a band-gap. Therefore, in the third solution, only vias of type 2 are present. The patches are electrically connected to the lower metal plane and disconnected from the upper plane.

We have considered a structure of the third kind. Therefore, vias of type 1 and pads are absent from the diagram in Fig. 34 (a). The unit cell with elliptically shaped metal patch and the textured surface are represented in Fig. 34 (b) and (c) respectively. This structure is a variation of a solution we have proposed in the past for building passive band-pass filters based on a HIS. A CAD model we have used is reported in Fig. 34 (d). The DD's have been calculated for waves propagating in the x direction.

Let us consider a unit cell with $d=2.5$ mm. In a first example, we take $\tau_1=\tau_2=0$ i.e. the pin extends from the patch plane to the upper plate. The DD in Fig. 35 shows a very wide EBG starting from zero frequency and a narrower one at higher frequencies. The light line (LL) is also represented in Fig. 35, and in subsequent figures. Although this result triggered the idea of introducing pins, it is not a

realistic solution in this context since the metal plates are short-circuited. However, a small gap ($\tau_1 > 0$) corrects for this fact and the corresponding DD is reported in Fig. 36. In can be seen that the EBG is still wide enough in the lower frequency range, although low frequency waves are now propagated.

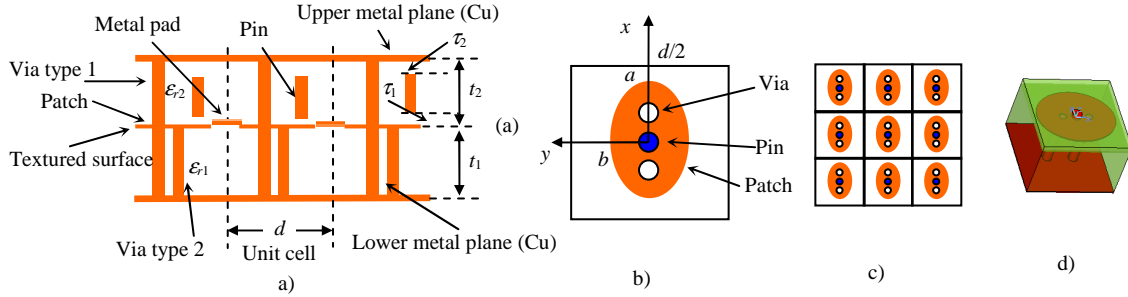


Fig. 34. (a) PPW- transverse section; (b) unit cell; (c) textured surface; (d) CAD model (upper metal plane removed for better visualization).

Next, we have approached the influence of geometrical dimensions on the location and width of the DD. We also took advantage of the availability of a wide range of dielectric materials with negligible losses in order to consider various values for ϵ_{r1} and ϵ_{r2} . This study is motivated by the necessity to find geometrical and material parameters for the structure such that the frequency limits of the first EBG in the DD be relevant for the noise mitigation problem. As known, the parallel-plate noise spectrum has a low-pass pattern with a cutoff frequency of about 6GHz.

The structure we have started from is characterized by the following parameters: $d=2.5$ mm; $t_1=1.6$ mm; $t_2=0.1t_1$; $\tau_1=0.035$ mm; $\tau_2=0$; $r_{via}=r_{pin}=0.1$ mm; $2a=2.25$ mm; $2b=1.8$ mm; pin (0,0); vias ($\pm a/3,0$); $\epsilon_{r1}=3.5$ and the associated DD is similar to that represented in Fig. 36. In order to match the frequency position of the EBG to the necessities of noise suppression, we have the option to vary the geometrical and material parameters. The results we present may be used for design of the device in order to meet specifications of various applications, not necessary related to the noise mitigation problem.

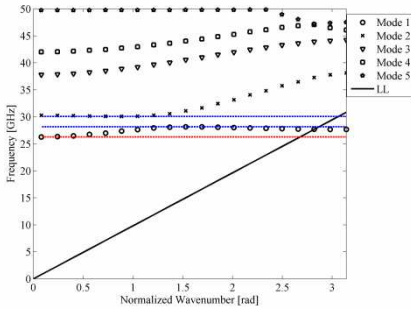


Fig. 35. DD - pins electrically connected to patches.

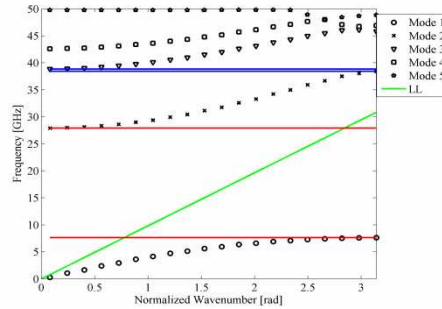


Fig. 36. DD - pins are not electrically connected to patches.

The position of the EBG in function of the dielectric constant of the upper layer (of width t_2) is reported in Table 2. We have denoted by f_{Mi} and f_{mi} the maximum and minimum frequency limits of mode i respectively. Increasing ϵ_{r2} leads to both decrease of frequency limits of the EBG and increase of the gap width. Therefore, a large value of the dielectric constant is recommended for the considered application

Table 2 EBGs in function of the dielectric constant of the upper layer

ϵ_{r2}	f_{M1}	f_{m2}	EBG
5	7.53	27.90	20.38*
10	7.14	27.83	20.69
12	7.05	27.82	20.77
30	6.77	27.78	21.01

* A second EBG appears between $f_{M2}=38.41$ GHz and $f_{m3}=38.59$ GHz.

A larger value for the first dielectric constant $\epsilon_{r1}=12$ and taking $\epsilon_{r2}=30$ leads to two EBGs, namely $f_{M1}=5.73$ GHz and $f_{m2}=15.41$ GHz (BW=9.68 GHz) and $f_{M2}=21.43$ GHz and $f_{m3}=22.87$ GHz (BW=1.44 GHz). A comparison with the corresponding line in Table 2 reveals that, as expected, increasing the dielectric constant leads to a shift of the DD towards lower frequencies.

The effect of increasing geometrical dimensions has been tested by increasing the radius of the pin to $r_{pin}=0.2$ mm. We obtained, for $\epsilon_{r1}=3.5$ and $\epsilon_{r2}=5$ the following EBGs: $f_{M1}=7.26$ GHz to $f_{m2}=27.88$ GHz (BW=20.61 GHz) and $f_{M2}=38.43$ GHz to $f_{m3}=38.83$ GHz (BW=0.40 GHz). A comparison with the corresponding line of Table 2 reveals a shift towards lower frequencies of the first EBG (which is the major concern in this context), while the second EBG is shifted towards higher frequencies, probably motivated by the change in reactive elements following the increase of the pin radius. If the position of the pin is changed to $(0, b/3)$, the first EBG results in between $f_{M1}=7.95$ GHz and $f_{m2}=29.58$ GHz (BW=21.64 GHz) and the second EBG does not occur. The increase in the EBG width motivates keeping this position of the pin. We have tested the effect of changing positions of the vias, to $(\pm 2a/3, 0)$ and obtained two EBGs: $f_{M1}=8.80$ GHz to $f_{m2}=29.08$ GHz (BW=20.28 GHz) and $f_{M4}=47.06$ GHz to $f_{m3}=48.08$ GHz (BW=1.02 GHz).

It is interesting to note that the variation of the dielectric constant and/or geometrical dimensions can lead to important qualitative differences in the behavior of the HIS. For example, we have tested the following situation: $\epsilon_{r1}=3.5$, $\epsilon_{r2}=12$, $2a=2b=2.25$ mm, $t_1=1.1$ mm, $t_2=0.1t_1$, $\tau_1=0.035$ mm; $\tau_2=0$; $r_{via}=r_{pin}=0.1$ mm, pin $(0,0)$; via $(\pm a/3, 0)$. We obtained two EBGs, but the second one resulted much larger than other secondary EBG widths we have reported until now. The results are: $f_{M1}=7.53$ GHz to $f_{m2}=27.65$ GHz (BW=20.12 GHz) and $f_{M4}=38.74$ GHz to $f_{m3}=45.66$ GHz (BW=6.92 GHz). The second EBG does not occur when geometrical parameters that were used for Table 1 are selected.

Turning now to the PPW noise mitigation problem, the position of the EBGs must be moved to much lower frequencies than in the situations considered above, since it is known that this type of noise has a low-pass spectrum, below 6 GHz. An obvious solution for this is to increase all the geometrical dimensions of the structure. We have performed five simulations in order to optimize the design, which are reported below in the increasing order of performance (and also by observing the time order in which we have gradually approached the final solution).

We have begun by doubling the sizes of the unit cell and patch: $d=5$ mm; $t_1=1.6$ mm; $t_2=0.1t_1$; $\tau_1=0.035$ mm; $\tau_2=0$; $r_{via}=r_{pin}=0.2$ mm; $2a=4.5$ mm; $2b=3.6$ mm; pin $(0, b/2)$; vias $(\pm a/2, 0)$; $\epsilon_{r1}=3.5$; $\epsilon_{r2}=5$. Three EBGs resulted, one from 4.43 to 14.61 GHz (BW=10.18 GHz), the second one from 20.57 GHz to 21.91 GHz (BW=1.34 GHz) and the third one from 24.24 to 24.81 GHz (BW=0.57 GHz).

We have then tried two alternative solutions. In the first one, we doubled the height of the structure, $t_1=3.2$ mm; $t_2=0.1t_1$ and obtained two EBG: one from 3.65 to 14.31 GHz (BW=10.65 GHz) and the second one from 21.54 to 21.85 GHz (BW=0.31 GHz).

As a second solution, we have kept the height of the structure $t_1=1.6$ mm; $t_2=0.1t_1$ and increased instead the dielectric constant ϵ_{r2} to 30. We obtained three EBGs: one from 3.54 GHz to 14.42 GHz (BW=10.88 GHz), the second one from 19.53 to 20.92 GHz (BW=1.39 GHz) and the third one from 21.82 to 22.48 GHz (BW=0.66 GHz).

The obtained results for EBG1 are quite similar in the two cases. Therefore, we doubled again the size of the structure in the xy plane: $d=10$ mm; $t_1=1.6$ mm; $t_2=0.1t_1$; $\tau_1=0.035$ mm; $\tau_2=0$; $r_{via}=r_{pin}=0.4$ mm; $2a=9.0$ mm; $2b=7.2$ mm; pin $(0, b/2)$; vias $(\pm a/2, 0)$; $\epsilon_{r1}=3.5$; $\epsilon_{r2}=30$. The three obtained EBGs have been: from 1.83 to 7.13 GHz (BW=5.29 GHz), from 9.76 to 10.77 GHz (BW=1.01 GHz) and from 11.13 to 11.42 GHz (BW=0.29 GHz).

A further decrease of the frequency parameters have been obtained by increasing four times the height of the structure: $t_1=6.4$ mm; $\tau_1=0.035$ mm. The two EBGs that occurred are from 1.24 to 6.76 GHz (BW=5.52 GHz) and from 10.14 to 10.34 GHz (BW=0.20 GHz).

The last two presented HISs clearly satisfy the frequency requirements for PPW noise mitigation. The corresponding DDs are reported in Figs. 37 and 38.

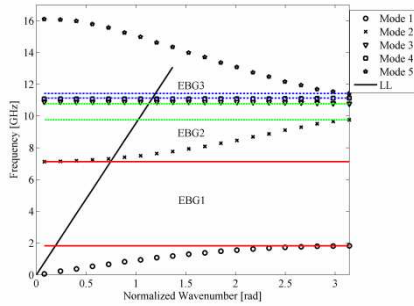


Fig. 37. DD for $d=10$ mm and $t_1=1.6$ mm

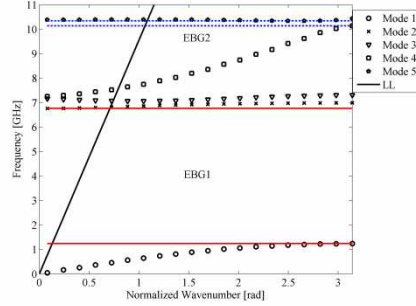


Fig. 38. DD for $d=10$ mm and $t_1=6.4$ mm

The presented study has been performed in view of applications of mitigation of parallel-plate noise in power distribution networks for high-speed digital and mixed-signal multilayer integrated circuits and for printed circuit boards. After a quite large number of simulations, we have derived a configuration suitable for solving the approached problem. Moreover, the influence of parameter variation on positions of EBGs may be used, qualitatively or quantitatively, to the design of similar structures in view of meeting frequency filtering specifications in various situations.

Since we proposed a number of switched periodic structures, to be presented in the next subsection, we preformed and reported a study of the effects of the biasing network on the dispersion characteristics of the network [11_01_M].

The unit cell geometry with elliptical patches we have introduced, as shown above, for easy fabrication in stripline technology, consisting of an elliptical-shaped patch grounded with a variable number of vias has been selected for demonstration. The encouraging results of this passive, fixed geometry offering a 2-D stopband as wide as 13 GHz around a central frequency of 20 GHz, i.e., approximately 65%, have motivated the extension of this research to construct tunable configurations. A novel technique easily implementable in coplanar transmission line technology for biasing a tunable configuration has been introduced.

The main difference between passive and tunable configurations is represented by the presence of the active devices, which could be diodes, field effect transistors (FETs), or microelectromechanical systems (MEMS). Typically, tunable impedance surfaces are biased using a network of biasing tracks, located on the opposite side of the ground plane from the tunable impedance surface, to minimize interaction of the biasing lines with the impedance surface operation. However, this solution is affordable when only a smaller number of switches are to be controlled; it becomes prohibitively expensive for large, 2-D periodic configurations.

To overcome such a limitation, a novel configuration of biasing network has been introduced and investigated. The biasing signal is conducted to the diodes through a coplanar waveguide (CPW) positioned directly in the ground plane itself. As the insertion of such a CPW in the geometry of the unit cell implicitly means that it will be periodically repeated, it is expected that the DD of the present solution is affected by the presence of the biasing network, but on the other hand, it also represents a further degree of freedom, which can be exploited with appropriate design. To the best of our knowledge, similar investigation has not been proposed in the literature.

Because of the aforementioned periodicity of the biasing network, we explicitly concentrate on its effect on the dispersion characteristics of the periodic structure. These effects are studied by monitoring the variation of the full DD for any additional pieces of the biasing network as it is

introduced in the unit cell geometry, allowing a better understanding of its frequency response. The wide band-gap structure in [10_01_M] has been used for the investigation since it allows an easier observation of the spectral rearrangement of the characteristic modes.

In the UC proposed in [10_01_M], the patch is of elliptical shape, with the two symmetry axes parallel to those of the square UC. In each UC, several vias are positioned off-axis, with nodes on a two-dimensional nonuniform Cartesian lattice. The number of vias per UC is a variable and, together with the patch dimensions, represents degrees of freedom for the design. The computer-aided design (CAD) model for the $N_V = 2$ case is presented in Fig. 39, with the leading dimensions of the geometry. With the emphasis on guided-wave applications, a top metal sheet is added to the unit cell, but for better visualization, it has been removed in the CAD model shown in Fig. 39. The circular-shaped hollow vias, centered in $(x_{vi}, y_{vi})_{i=1,2}$, are described in terms of internal and external radii of the metallization, which has a finite thickness. Because of the small dimensions of the hollow cavity, the resulting air-filled circular waveguide is always below cutoff. The characteristics for different values of t_2 and for $q=1.8$ mm, $p=2.25$ mm, and for the symmetric case $(-p/6, -q/6)|_1$ and $(p/6, q/6)|_2$ are summarized in the first three rows of Table 3, where f_{min} and f_{max} denote the minimum propagation frequency of the second mode and maximum propagation frequency of the first (fundamental) mode over the entire DD. $w_{BG} = f_{max} - f_{min}$ and $f_c = 0.5(f_{max} - f_{min})$ denote the width and the central frequency of the band-gap respectively.

Starting from the reference structure above, the modifications incorporated to the CAD model and represented in Fig. 40 are the following.

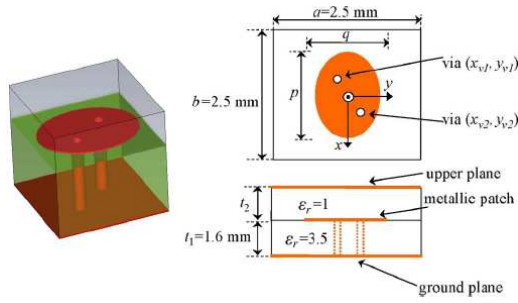


Fig. 39. Geometry with two vias positioned symmetrically with respect to the center. (left) CAD model with top metallic sheet removed. (right) Dimensions.

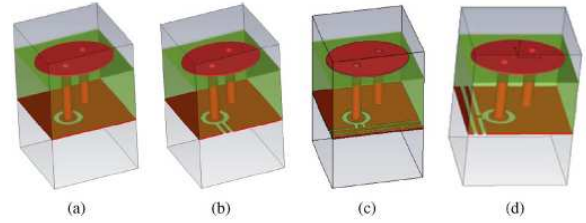


Fig. 40. Evolution of the geometry: (a) slot around the via, (b) slot and access CPW line, (c) final CPW_x configuration, and (d) final CPW_y configuration.

Table 3. Characteristics of the reference configuration (rows 1–3) and modified structure (rows 4–5)

t_2	f_{max} (GHz)	f_{min} (GHz)	w_{BG} (GHz)	f_c (GHz)
$0.1t_1$	12.6139	35.8458	23.2319	24.2298
$0.3t_1$	15.3796	31.2417	15.8621	23.3107
$0.5t_1$	16.0625	27.1765	11.1140	21.6195
$0.5t_1 + \text{slot}$	14.4616	26.8267	12.3651	20.6442
$0.5t_1 + \text{slot + sh. line}$	9.1653	12.6093	3.4439	10.8873
	22.2233	26.7882	4.5649	24.5058

- 1) The vias that need to be commanded are circumscribed by slots (Fig. 40 (a)). The simplest case is a circular slot around the base of the vias. The slot radii R_{in} and R_{out} represent degrees of freedom that can be considered for an optimization of the DD. Rectangular/elliptical shapes can also be considered.
- 2) A short CPW starting from the external rim of the circular slot towards the boundary of the UC in Fig. 40 (b).
- 3) The other end of the previous CPW is connected to a second CPW going through the UC, and orthogonal to the previous one (Fig. 40(c)). This main CPW is connected to the voltage supply.

Contrarily to the drawing in Fig. 40(c), where the main CPW is parallel to (Fig. 39), denoted hereafter by CPW_x, in Fig. 40 (d) the BN has been rotated by 90 degrees and the main line is parallel to (configuration CPW_y). Even if the UC has a square shape, the two configurations are different because of the elliptic shape of the patch. The region below the ground plane is considered to be air.

One of the potential drawbacks of such a solution is the possible radiation from the CPW itself. The problem of radiation of such structures has been studied in the literature [fang_1999]. However, because of the balanced structure, and of the same RF polarity (only dc polarities are different), the radiation is quite reduced. A second issue to be taken into account regards the symmetry breaking of the geometry of the unit cell. Changing the unit cell geometry, without changing the EBG's spatial lattice dimensions, will not result in a different irreducible Brillouin zone since the shape of this latter depends only on the EBG grid. However, breaking the unit cell's symmetry may result in the necessity to investigate wave propagation in the whole irreducible Brillouin zone and not only on the triangle given by the spectral direction vectors Γ , X , and M (for the considered rectangular unit cell) in order to determine the complete band structure. This issue has also been addressed in, e.g., [noj_2008].

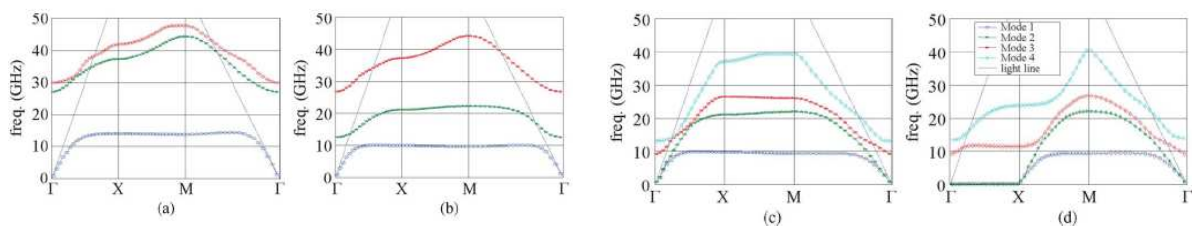


Fig. 41. DDs for different steps of the design. Indexing from (a) to (d) corresponds to the cases in Fig. 40.

DDs of the geometries in Fig. 40 have been computed on the $\Gamma X M \Gamma$ contour by commercial software [CST_2011]. Corresponding results are reported in Fig. 41, and numerical values are given in the last two rows of Table 3. The presence of the slot has no significant effect on the DD, as can be observed when comparing the third and fourth rows in Table 3. The DD of the configuration without the slot (not reported) is quite similar to that in Fig. 41 (a). The selection of the slot dimensions, as $R_{in}=0.25$ mm and $R_{out}=0.4$ mm, has been essentially based on geometrical constraints. Since here we are interested in the global effect, they were not optimized to reach specific target values for the band-gap. The resonant frequency f_r of the slot can be computed by $f_r = c / 4\pi R_{med} \sqrt{\epsilon_{eff}}$, where c is the speed of light in vacuum, R_{med} is the arithmetic mean of the inner and outer radii, and ϵ_{eff} is the effective dielectric constant. For the values considered, it results that $f_r \cong 40$ GHz, i.e., the resonance of the concentrated, high- Q slot is far away from the upper edge of the band-gap. Its presence does not affect the spectral arrangement of the modes in the vicinity of the band-gap. The short CPW has a much higher impact on the DD, as can be observed in Fig. 41 (b). The resonance of the short line occurring inside the band-gap introduces an additional mode, splitting the otherwise wide band-gap into two narrower band-gaps with limits summarized in Table 3. This effect can be avoided by changing the length of the line using, e.g., a tilt (nonparallel to the Cartesian axes) geometry, pushing the resonance below or above the initial band-gap. The through CPW introduces an additional TEM mode with zero cutoff frequency, clearly present in the DD in Fig. 41 (c). Consequently, the band-gap disappears for the considered dimensions. Slowing down the phase velocity on this line, the upper limit of the mode can be decreased to a value below the lower limit of the initial band-gap. This can be obtained by periodic loading of the line itself, by simple stubs, or the fishlike geometry studied for a different application in [matek_2008].

In Fig. 41, another interesting phenomenon can be observed, namely some group velocities do not vanish at the indicated limits X and M for the irreducible Brillouin zone. This clearly indicates that anisotropy has been introduced when the symmetry of the UC has been broken down as mentioned earlier. This phenomenon requires further investigation for the full description of the propagation of the EM waves in any direction inside the 2-D lattice. If study of one-dimensional propagation only (inside the 2-D periodic arrangement) is of interest, e.g., x -direction in our case, anisotropy has no meaning.

The following step of our study extends the investigation to the case when an active switch is inserted across the slots, connecting the base of the via to the central conductor of the CPW, as illustrated in the magnified Fig. 42. The prism models a diode in the “ON” state, while the absence of the prism models the “OFF” state of the diode. The diode has been modeled as a rectangular metal prism, i.e., a short circuit, when it is in the “ON” state, and as an air gap in the “OFF” state. The simple model used for the diodes allows understanding of the effect of the biasing network only. It is expected that a more realistic *RLC* model will slightly change the limits of the band-gaps when they are present.



Fig. 42. Details of the connection between the biasing line and via base: (left) top view and (right) bottom view.

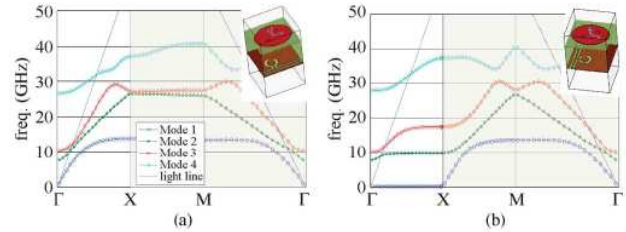


Fig. 43. DDs for CPW_x (a) and CPW_y (b) cases with diode in “ON” state. Clear zone refers to the x -direction propagation.

DDs for both CPW_x and CPW_y configurations have been computed and reported in Fig. 5. Because of the above discussed anisotropy, only one-dimensional propagation (along x -direction) gives useful results (IX path). Anisotropy is clearly present. Comparing these DD’s to the results in Fig. 3, it can be seen, that switch between the ON and OFF states of the diode corresponds to a change from passband to stopband in the 20–28-GHz frequency band for the CPW_y configuration.

The analysis we have just presented gives a close insight on the effects of different parts of the biasing on the DD of a periodic structure. The link between each component and its effect allows breaking down the overall geometry when optimization for a specific application is required. Because of the balanced configuration of the CPW, the solution exhibits low radiation leakage. For a specific design, the issue has to be carefully considered, and full 2-D DD must be computed that takes into account the introduced anisotropy. While the proposed solution allows individual control of the UCs for 1-D structure, for 2-D extension, row-by-row control can be achieved.

The use of materials with various constitutive parameters in the construction of waveguides based on metamaterials is also an important issue for miniaturization, scaling and field confinement [park_01]. This problem has been tackled in [11_10_M]. Materials with a wide range of dielectric constants have been realized, either from ceramics or by arrangements of layers of different substances [siev_05, lim_05]. However, the construction of low-loss materials with various permeabilities, this latter being an important factor for equalization of electric and magnetic stored energy, is a much more difficult task [ark_01]. The solution also relies on metamaterials, by incorporating electrically small inductors, split-ring resonators or wires in dielectric materials. If randomly arranged, the effective permeability has a scalar characteristic, otherwise anisotropy occurs. The problem has also been approached in view of photonic applications, and with the fast developing technology, 3D optical magnetic materials are expected to be feasible in the near future [matek_09].

The use of magnetic materials in advanced magnetic switches, or controlled drug delivery are examples from other fields, where such materials find their applications. Applications to sensors has also been investigated in [zhang_09]. However, the use of such materials at high frequency, e.g. X band, is still a challenging operation. Some encouraging results have been recently published on this issue.

We have realized a study of the dispersion characteristics relative to a PPW unit cell with one of the conductor plates being substituted by a metamaterial. The structure presents no symmetry planes, resulting in a strong anisotropic medium for the propagation. The frequency response of the structure when the space between the two walls is filled by lossless magnetic materials has been found by simulation.

Nevertheless the aforementioned anisotropic behaviour, the frequency responses are described by the DDs on the $\Gamma X M \Gamma$ border of the first irreducible Brillouin zone by means of the CST. The values of electromagnetic band-gap (EBG) positions and widths obtained in this way are conservative, as we are interested mainly on waves propagating along the positive x direction (Fig. 44). However, the DDs for the whole first zone provide a better insight into the structure properties, even if the geometry does not present the required symmetries such that these DDs completely characterize the device for the whole zone, but only for the ΓX portion. As the best of our knowledge, similar studies are only sporadically present in the literature.

The CAD model of the unit cell of the metamaterial based PPW is presented in Fig. 44. The unit cell is square shaped with a side of 2.5 mm. The lower metal ground plane is separated from the patch plane, situated $t_{sub}=1.8$ mm above, by a dielectric, non-magnetic material with a dielectric constant of $\epsilon_{r,sub}=3.5$. The elliptically shaped patch with axes of 2.25 and 1.8 mm, is connected to the ground plane by two hollow, metalized vias of radii 0.1 mm. The positions of the vias are symmetric with respect to the center of the unit cell and are at $1/6$ of the lengths of the patch in the considered directions.

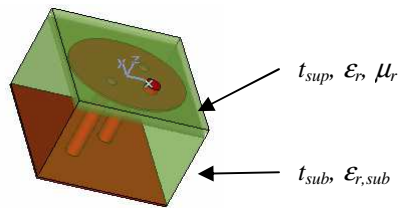


Fig. 44. CAD model of the unit cell.

The use of elliptical shape patch has been considered; insofar it represents an additional degree of freedom with respect to the circular one, maybe more diffused in applications. Moreover, the rounded shape without corners reduces the presence of discontinuities of the current on the radiator. As for the choice of the position of the vias, in some previous investigations [10_01_M, 10_02_M] it results that such values can give reasonable results.

A dielectric layer, of thickness $t_{sup}=0.18$ mm, characterized by a dielectric constant ϵ_r and relative permeability μ_r , is inserted in between the patch plane and the upper metal plane, which has been removed in Fig. 44 in order to improve visibility. In our study, we have considered different values for these two material parameters. The patch is connected to the upper planes by a metal pin of radius 0.1 mm.

The DD of the presented structure have been computed in two different situations: firstly when the top layer has a permittivity $\epsilon_r=1$ and permeability equal to $\mu_r=1$ and to $\mu_r=2$ respectively. Results are reported in Fig. 45 (a) and (b). In the second investigation the top layer has had a permittivity $\epsilon_r=3.5$ (similar to the bottom layer) and a permeability $\mu_r=3$ (Fig. 46). The first situation allows for demonstrating the impact of the variation of the permeability. As it may be noticed by examination of Fig. 35, two EBGs are present. EBG1, which starts from zero frequency, is explained by the DC path between the ground plane and the patch plane, while EBG2 is characteristic for such structures [siev_99, tav_07]. The first mode of propagation is confined by the patch surface. The pins concentrate the magnetic field (and the surface current), as shown in Fig. 47.

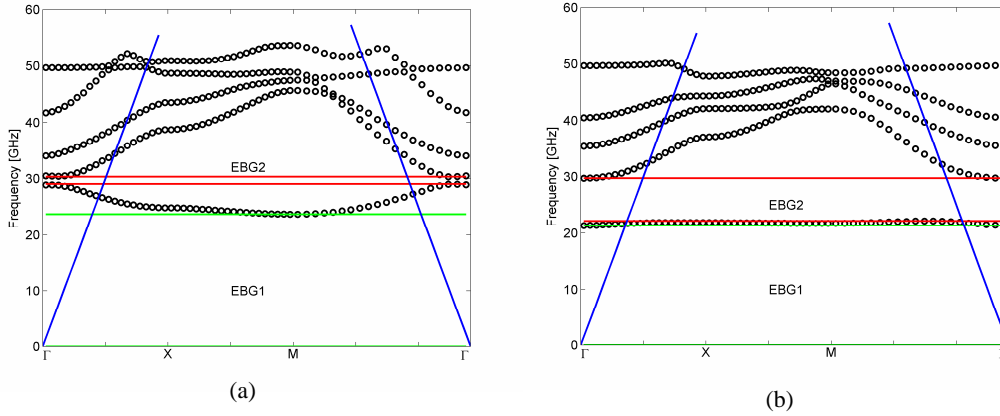


Fig. 45. DD for the structure in Fig. 1: (a) $\epsilon_r=1$, $\mu_r=1$; (b) $\epsilon_r=1$, $\mu_r=2$.

Furthermore, the group velocity of waves carried by the first mode is almost constant and has a small value. The second situation ($\epsilon_r=3.5$, $\mu_r=3$) is a better choice for a more compact mechanical structure. By examining the DD in Fig. 46, one sees that two EBGs are present again.

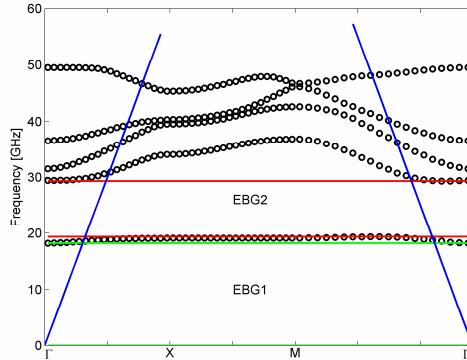


Fig. 46. DD for the structure in Fig. 1: $\epsilon_r=3.5$, $\mu_r=3$.

In the next phase of the analysis, the relative permeability of the upper dielectric material has been varied from 1 to 6 with a step of 1, considering constant value for the dielectric constants of the material equal to $\epsilon_r=3.5$. The corresponding positions and width of the EBGs have been determined and reported in Fig. 48.

In Fig. 45, EBG1 is defined by the minimum frequency of the first mode, while the limits of EBG2 are defined by the maximum frequency of mode 1 and minimum frequency of mode 2. Since all aforementioned values are in the ΓX segment, the limits of the EBGs are those relative to the propagation along x direction. The lower EBG is large (more than 20 GHz) for low values of permeability, while the upper EBG is more than 7 GHz. The pass-band in between the two EBGs is minimum between $1 < \mu_r < 2$, when the frequency limits are the highest. After that point, the frequency limits decrease monotonically with μ_r . However, the highest frequency limit decreases slower than the lower and intermediate ones, so that EBG1 is smaller and EBG2 is larger for high values of permeability.

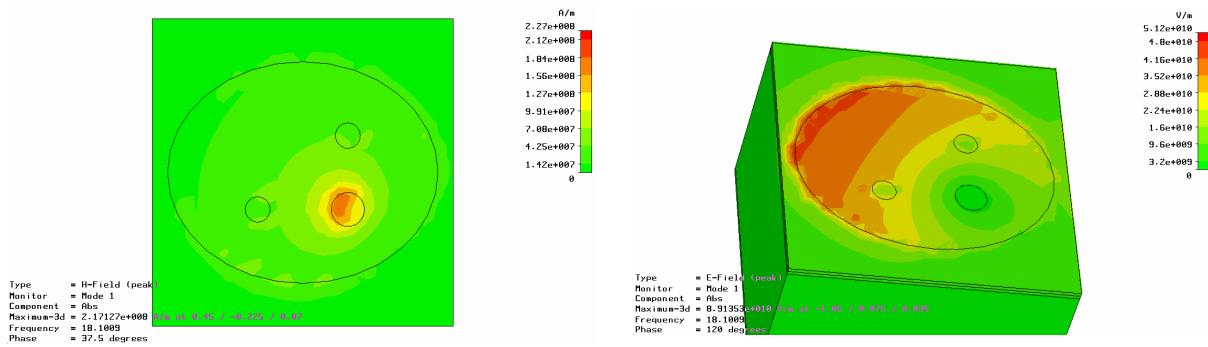


Fig. 47. Magnitude of intensity of magnetic field (top) and electric field (bottom) at the patch plane (mode 1).

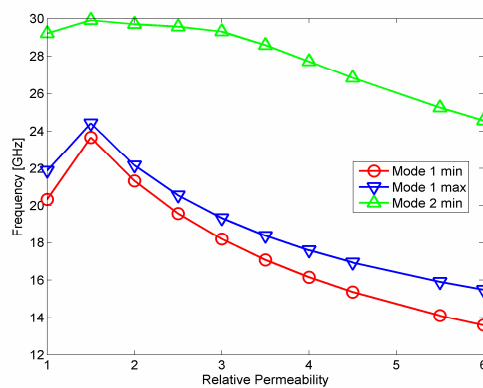


Fig. 48. EBG limits versus relative permeability of the upper dielectric material with $\epsilon_r=3.5$.

The results of this study concerned the modification of the frequency response of a PPW built in metamaterial technology when one of the dielectric substrates' entering its composition is replaced by a lossless magnetic material. The EBG structure has been discussed and it has been demonstrated that it is sensitive to changes in the relative permeability of the material. The preliminary results of our investigation show that this is another structure that may be efficiently used in sensor and measurement applications.

We proposed a multiband passive filter in the microwave frequency range based on a strip-line technology metamaterial with rectangular, hollow patches and two vias [11_04_M]. The pattern impressed inside the unit cell has a novel structure introducing three electromagnetic band gaps ranging across of the first six modes of operation. The relatively large band-gaps, allowing to be controlled by the geometrical and material parameters of the unit cell, recommend the structure for applications as band-pass, band-stop or multi-band filter or in sensor related applications. The structure is also fit for construction of switchable devices.

Our goal has been devising a patterned surface on grounded dielectric board having several EBG's in between the first modes of operation. A solution for the unit cell that satisfies these constraints is reported in Fig. 49 (a) – top view and Fig. 49. (b) – side view. The unit cell is square and it contains, like the "mushroom" structure, a square shaped central patch, connected to the ground plane through a grounding via. The via is in an eccentric position, allowing for an additional degree of freedom in the design. The central patch is surrounded by a metallization, with sides parallel to those of the unit cell and having a via in a position that can also be varied in order to gain further design flexibility. The patterned surface is obtained by 2D periodic repetition of the unit cell, Fig. 49 (c).

The frequency related properties of the structure in Fig. 49 have been tested by constructing the DD on the boundary of the first irreducible Brillouin zone in the wave-number space. We have concentrated on propagation along the x axis only, Fig. 49. The geometric dimensions we have chosen for the first experiment have been: $D_x=D_y=2.5$ mm, $a=0.35$ mm, $b=0.6$ mm, $c=1.1$ mm, $t_1=1.6$ mm and $t_2=0.1t_1$. The vias, having equal radii $r=0.1$ mm, have been positioned at $(-0.15$ mm,0) and $(0.85$ mm,0) respectively. The relative dielectric constant of the substrate has been chosen as $\epsilon_{r1}=3.5$.

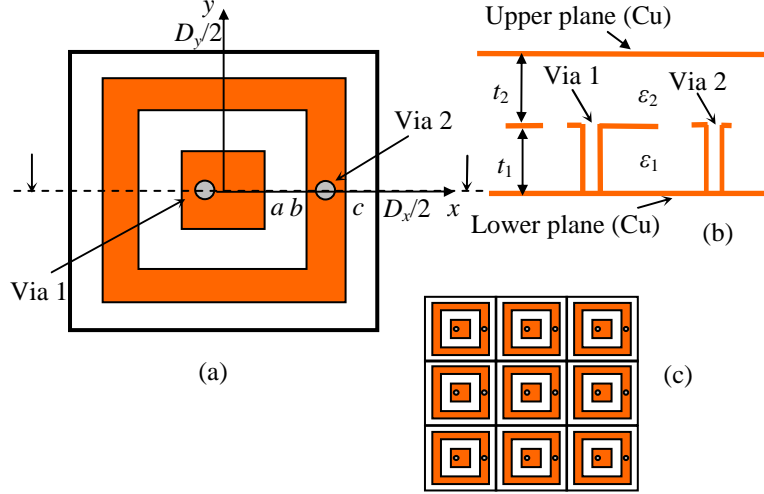


Fig. 49. (a) Basic cell: top view. (b) Side view. (c) HIS.

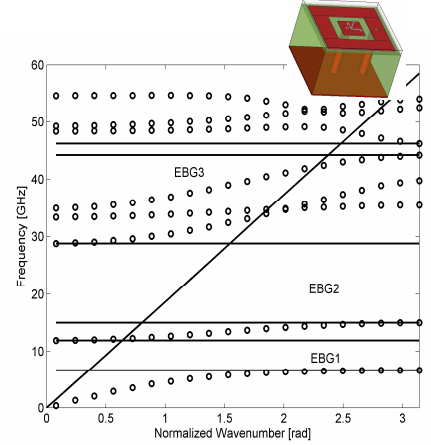


Fig. 50. DD for the case $a=0.35$ mm and $t_2=0.1t_1$. Inset: CAD model

We have tested the closed structure, which is obtained by placing a metallic plane at a distance $t_2=0.1t_1$ above the open structure and clearly indicates the band-stop properties of the surface. Closed structures, which may be assimilated to inhomogeneous parallel plate wave guides, find applications in various fields. For the beginning, we assume that the space in between the patch plane and the upper metallic plane is filled with air, $\epsilon_2=\epsilon_0$, i.e. $\epsilon_{r2}=1$, Fig. 49 (b).

The DD obtained by simulation, featuring the first eight propagation modes, is reported in Fig. 50.

Normalized wave-number $k_x D_x = \frac{2\pi}{\lambda_x} D_x$, ranging between 0 and π , corresponding to the ΓX edge of

the first Brillouin zone, is displayed on the horizontal axis. The light line and the CAD model are also shown on Fig. 50. The patterned structure features three EBG's, in between the first and the second mode, the second and the third and in between the fifth and the sixth. The frequency ranges of the aforementioned band-gaps in GHz are [6.67; 11.88], [15; 28.79] and [44.17; 46.18] respectively. The EBG widths are 5.22, 13.79 and 2.01 GHz respectively. We also mention that all of the three band-gaps present partially bounded wave operational regime, useful for filter application. The above observation is more relevant for open structure where radiation is possible, but it allows better understanding of the physics of the propagation of the electromagnetic field. Furthermore, we note the flatness of the second mode. It is an effect of a lumped resonator internal to the unit cell, which does not feel, or feel in a weak manner the external periodic boundary condition. Similar behavior has been observed in other comparable situations. Here, the mode feels the external boundary conditions in a weak manner, due to presence of the vias which increase the mutual coupling between adjacent cells.

In this way, the initial goal of finding a multi-band patterned surface with a simple pattern etched on the unit cell has been achieved. Next we follow the influence of some geometrical parameters on the positions and widths of the EBG's.

We have considered some variations of the structure. The first parameter we have varied has been the dimension a of the central patch, Fig. 49 (a), by considering five equidistant points between 0.3 and 0.5 mm. The variations of the limit frequencies versus the design parameter a are presented in Fig. 51. An EBG is comprised in between two curves indicated by the same type of markers. While the lower limit of the first EBG, the upper limit of the second EBG and both limits of the third EBG

remain approximately constant, the upper limit of the first EBG and the lower limit of the second vary almost linearly, allowing for a convenient design. The second EBG becomes particularly large for $a=0.5$ mm: 15.73 GHz, between 11.94 and 27.67 GHz (79%, or 86.5% if the central frequency is considered as the geometric mean of the limits).

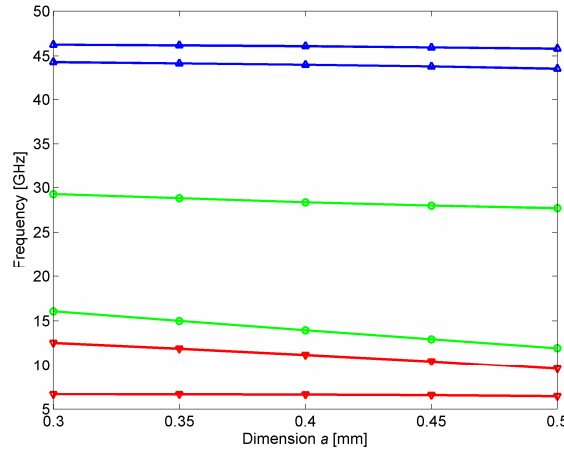


Fig. 51. Variation of EBG's versus the dimension a of the central patches. The limits of an EBG are indicated with similar markers.

The simulation results on the influence of the parameter t_2 are listed in Table 4. The widths w of the EBG's diminish when t_2 increases. This is an expected behavior, similar to that exhibited by the "mushroom" structure. However, a larger value of t_2 is necessary when additional electronic lumped components have to be mounted on the patch plane in order to accomplish various functions, such as additional filtering or control.

Table 4. Limits and widths of the EBG's for various positions of the upper metallic plane.

	f_{m1} [GHz]	f_{M1} [GHz]	w_{EBG1} [GHz]	f_{m2} [GHz]	f_{M2} [GHz]	w_{EBG2} [GHz]	f_{m3} [GHz]	f_{M3} [GHz]	w_{EBG3} [GHz]
$t_2=0.5t_1$	8.17	11.97	3.80	17.99	21.15	3.16	44.50	45.54	1.04
$t_2=0.3t_1$	7.84	12.22	4.39	17.47	24.59	7.13	44.34	46.89	2.55
$t_2=0.1t_1$	6.67	11.88	5.22	15.00	28.79	13.79	44.17	46.18	2.01

Results obtained by considering the original dimensions listed in above but various positions of vias are presented in Table 5. The first row in Table 5 corresponds to the DD in Fig. 50 and has been added for comparison. The limits and widths of the EBG's can be modified by 1..2 GHz. This is not very much, however it is significant and can be used as some kind of "fine tuning".

The PBG surface we have proposed may find applications in multiband, wideband, microstrip filters and in sensor applications.

Table 5. Limits and widths of the EBG's for various positions of the vias.

via 1 [mm]	via 2 [mm]	f_{m1} [GHz]	f_{M1} [GHz]	w_{EBG1} [GHz]	f_{m2} [GHz]	f_{M2} [GHz]	w_{EBG2} [GHz]	f_{m3} [GHz]	f_{M3} [GHz]	w_{EBG3} [GHz]
(-0.15,0)	(0.85,0)	6.67	11.88	5.22	15.00	28.79	13.79	44.17	46.18	2.01
(0,0.15)	(0.85,0)	6.71	12.17	5.45	15.17	28.17	12.99	44.49	46.27	1.78
(0.15,0)	(0.85,0)	6.77	12.77	6.00	15.62	27.29	11.67	44.19	46.05	1.86
(-0.15,0)	(0.85,0.5)	6.60	11.60	5.00	14.97	29.20	14.21	45.53	46.34	0.81

The structure introduced in [11_04_M] has been further investigated due to its properties with potential applications in fixed and switchable filtering [11_05_M]. The investigation detailed in the following regards the effect of the variation of the dielectric constant of the upper, thinner layer. It is expected that a small change in the material parameters reflects in a highly sensible manner, allowing the construction of selective filters or sensors with advanced performances.

In a practical realization, dielectrics present in the device can be chosen from a wide range of materials with various dielectric constants. In order to simplify the analysis, here the dielectric constant of the bottom layer has been maintained constant, and only that of the top layer has been varied. In particular, the dielectric constant of the lower layer has been fixed to $\epsilon_{r1}=3.5$, while that of the upper layer has been scanned in the interval from 1 to 13. This quite large variation allows for individuating frequency ranges where the behavior of the structure excited with electromagnetic signals exhibits abrupt changes, if any. Furthermore, knowledge of the behavior on large frequency ranges is useful in the design of wideband surface wave launchers.

DD's for integer values of ϵ_{r2} between 1 and 13 and also for $\epsilon_{r2}=\epsilon_{r1}=3.5$ have been calculated as shown above, for positive wave-numbers corresponding to propagation along the x direction. The DD's for the bounds of the interval are reported in Figs. 52 and 53.

The light lines (LL's), also represented on Figs. 52 and 53, mark the difference between slow and fast waves. Fast waves are evanescent in the case of open structures and may be used for the construction of leaky wave antennas [rogers_05]. The situation is however different in closed structures. The slopes of the LL's have been calculated relying on the effective dielectric constant

$$\epsilon_{r,eff} = \frac{t_1 + t_2}{\frac{t_1}{\epsilon_{r1}} + \frac{t_2}{\epsilon_{r2}}} \quad (1)$$

which corresponds to a PPW with the two layers of dielectric, but without patches and subject to magnetic rather than periodic conditions on the lateral walls. Therefore, this choice is appropriate for the quasi TEM fundamental mode.

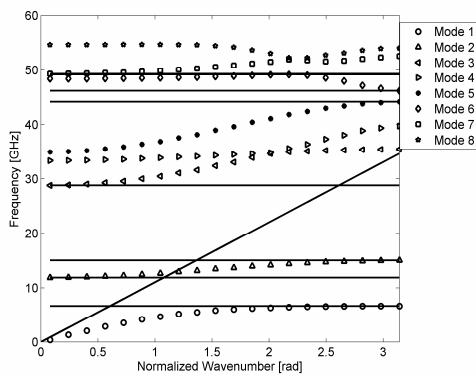


Fig. 52. DD for $\epsilon_{r2}=1$, featuring 4 EBG's. The LL is also represented.

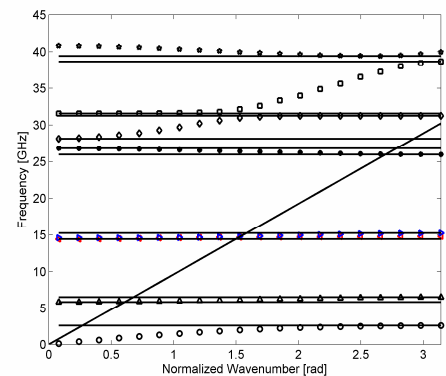


Fig. 53. DD for $\epsilon_{r2}=13$, featuring 6 EBG's. Modes are marked as in Fig. 2. Modes 3 and 4 are (almost) degenerate.

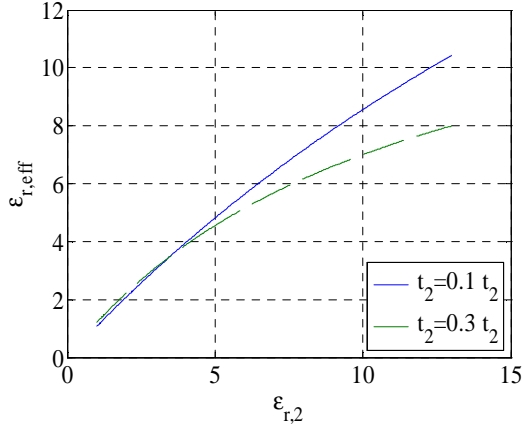


Fig. 54. Variation of the effective dielectric constant versus the dielectric constant of the upper layer for different ratios t_2/t_1

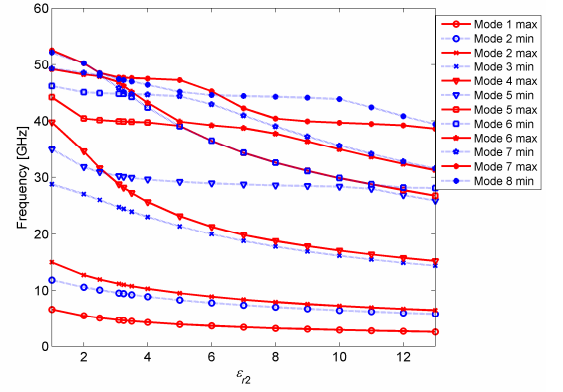


Fig. 55. Maximum (solid line) and minimum (dotted line) frequencies of modes versus dielectric constant of the upper layer.

The corresponding values of the effective dielectric constant for two different ratios between the thicknesses of the layers, 0.1 and 0.3 respectively, are reported in Fig. 54. A further observation that can be made based on the reported data regards the dynamic of the effective value of the resulting dielectric constant, i.e. the lower the ratio, the higher is the excursion of the effective value of the dielectric constant. The higher variation enriches the possible application range, and demonstrates the statement in the previous section on the performances of the EBG characteristics.

Since the dielectric constants of the upper and lower layer are different in general, the structure cannot support a TEM fundamental mode, but it does support a quasi TEM one. An exception is the case $\epsilon_{r1} = \epsilon_{r2}$, also considered in simulations, when the middle (patch) layer is surrounded by a homogeneous dielectric and when a TEM fundamental mode may be supported. Investigation around this point has been deepened.

The structure we have introduced present DD's rich in EBG's: 4 for $\epsilon_{r2} = 1$ and 6 for $\epsilon_{r2} = 13$ respectively. The number of EBG's for the rest of the cases is in between these two values. The EBG limits have been calculated by the difference between the minimum frequency of the upper mode $f_{min,n+1}$ and the maximum frequency of the lower one $f_{max,n}$. The variations of these quantities versus ϵ_{r2} for the relevant modes are represented in Fig. 55, regardless of the fact that an EBG exists or not for the particular value of ϵ_{r2} . An EBG exists if $f_{min,n+1} > f_{max,n}$.

The EBG's present in all situations and situated in regions of slow waves are in between modes 1 and 2 and modes 2 and 3 respectively. All curves have similar shapes. Central frequency and band width decreases when the dielectric constant of the top layer increases.

As shown above, the obtained results have potential applications in multi-band planar filter design and in sensor devising.

In [11_09_M] we have proposed a filter built with a lattice entering the construction of a PPW and having three or four EBGs. We have considered several variations for the unit cell geometry and have chosen the one that provides the largest EBGs. We have determined the positions in frequency of the EBGs and studied the variations of these positions when the dielectric filling the wave guide was changed.

The design of the unit cell and the CAD models of the structures we have considered are reported in Fig. 56. In the CAD models, the upper metal plane entering the structure of the PPW has been removed for a better visualization. The unit cell is square shaped, with dimensions $D_x = D_y = 2.5$ mm and it is composed, from bottom to top, of a metal (ground) plane, a material with dielectric constant $\epsilon_{r1} = 3.5$ and height $h_1 = 1.8$ mm, a patch plane (the patches are etched in the upper copper plane of a microstrip board), another material of dielectric constant ϵ_{r2} and height $h_2 = 0.1h_1$, and the removed upper metal plane.

The patch pattern of the unit cell comprises three rectangular, concentric shapes, with parallel sides. The inner shape is connected to the ground plane through a metalized via V_2 . The two other patches are hollow. The outer one is connected to the ground plane through two metalized vias V_2 and V_3 . All vias have radii of 0.1 mm.

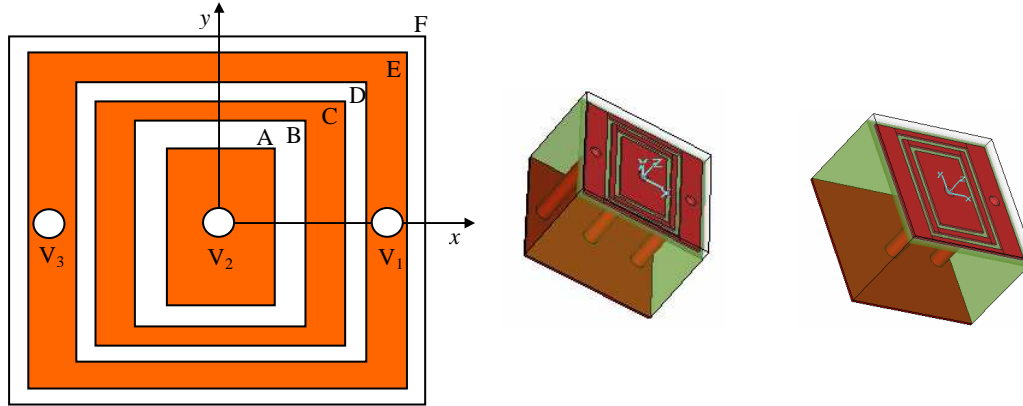


Fig. 56. Design of the unit cell and CAD models (three and two vias).

The dimensions of the patches result from the following coordinates of the points represented in Fig. 1 with respect to the reference system $Oxyz$ (all values are in mm): A(0.35;0.75), B(0.55;0.85), C(0.65;0.95), D(0.75;1.05), E(1.15;1.15) and obviously F(1.125;1.125). The positions of the vias are given by $V_1(0.95;0)$, $V_2(0;0)$ and $V_3(-0.95;0)$.

The DD of this structure, with the above presented geometric parameters, is reported in Fig. 57 (a). The frequencies of the first seven modes are represented versus the normalized wavenumber corresponding to propagation in the x direction, $k_x D_x$, which ranges between 0 and π . The straight, oblique line is the light line (LL) corresponding to (1). The LL separates slow waves from fast waves. In the case of open structures (upper metal plane absent), fast waves are leaky.

The DD in Fig. 57 (a) shows the existence of three EBGs, between modes 1 – 2, 2 – 3 and 3 – 4 respectively, of which the middle one is quite large, approx. 10 GHz. Nevertheless the lower one is narrower than we would like, the possibility of obtaining three EBGs has been demonstrated.

The result of an attempt to obtain a better result, by lowering the space between the inner patch and the middle one, by moving A to (0.45;0.75) and keeping the symmetries is reported in Fig. 57 (b). The situation has not improved: the main influence of the modification being at the higher order modes.

Another alteration of the original idea has been to remove one of the vias. The DD corresponding to the unit cell of Fig. 56 with via V_3 removed is presented in Fig. 57 (c) and this time the lower EBG has resulted large enough. Consequently, we have chosen this solution as final.

One parameter that may be considered being modified in the presented design is the dielectric constant ϵ_{r2} of the upper material. As shown above, unlike magnetic ones, low-loss materials with a wide range of dielectric constants are readily available. The interest in using higher dielectric constants stems from possibilities of scaling, electric energy concentration and miniaturization, as higher dielectric constants reduce wavelength. As an example, the DD for the presented structure but with an upper dielectric layer with $\epsilon_{r2}=5$ is reported in Fig. 57 (d). As expected, the three EBGs occupy now lower positions in the frequency domain, and the second and third EBGs are wider. Furthermore, a fourth, narrow EBG has appeared between modes 4 and 5.

The variations of the frequency limits that define the EBG versus the dielectric constant of the upper layer are represented in Fig. 58. We have denoted by f_{mini} and f_{maxj} the minimum and maximum frequencies of mode i and j respectively.

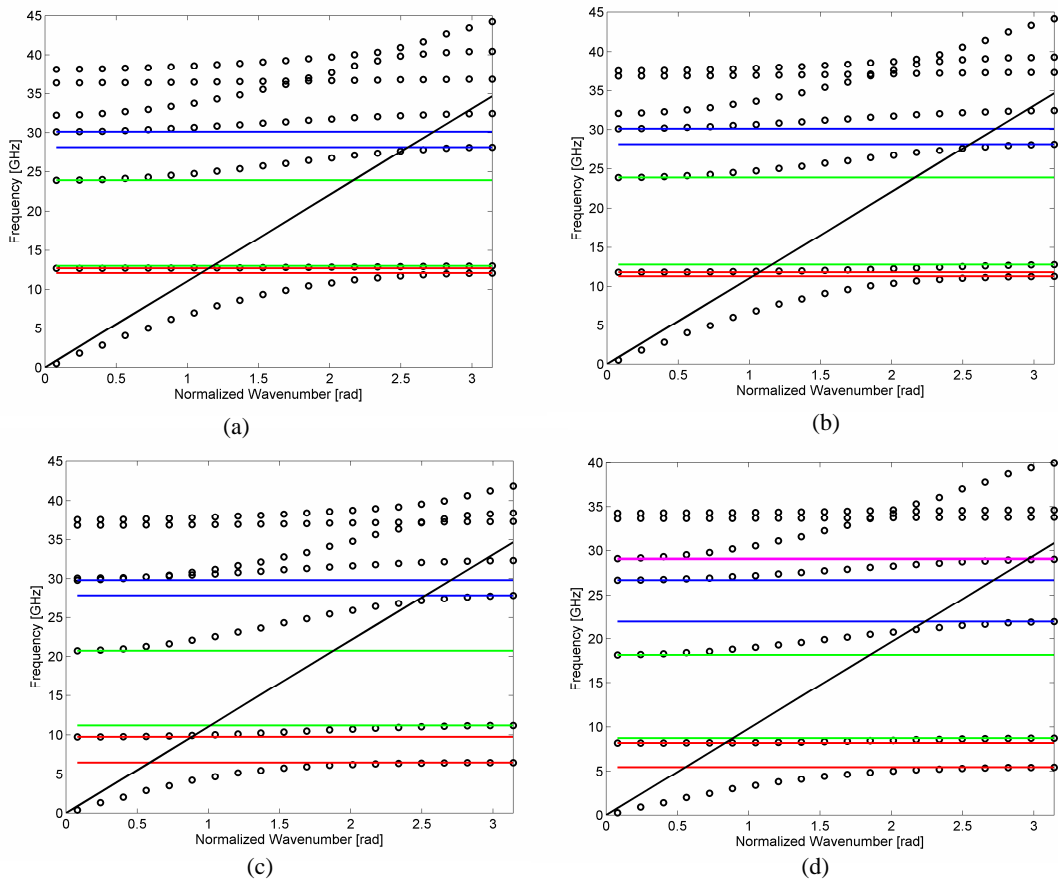


Fig. 57. DDs (a) First unit cell with three vias; (b) Second unit cell with three vias; (c) Unit cell with two vias, $\epsilon_{r2}=1$; (d) Unit cell with two vias $\epsilon_{r2}=5$.

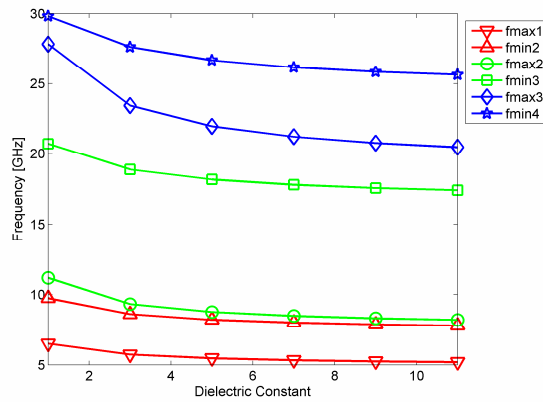


Fig. 58. Limit frequencies of EBGs versus the dielectric constant of the upper layer.

A novel geometry of unit cells relying on printed technology and featuring full DD exhibiting an unusual large number of electromagnetic band-gaps (EBGs) has been proposed in [12_02_M]. The printed patch consisted of a filter like geometry, meandered around the symmetry center of the unit cell and has been connected to the ground plane by three collinear vias, locally increasing the loading inductances; the multiple resonances the structure exhibits determined the limits of the band-gaps. In particular, as many as seven EBGs have been proven to exist in between every two consecutive modes from the first eight ones in the case of one directional propagation. The same phenomenon has been attested for 2D propagation, where four EBGs have been proven to exist between the first five modes in the case of arbitrary directed propagation in the main plane of the structure. The 2D scanning required for building up the full DDs has been realized by computer simulation with dedicated software - CST. The small differences in band limits between the 1- and 2-D cases reflect small amount of anisotropy, since in the present study the symmetry of geometry has been approximately maintained. The wide range of mono-modal behavior recommends the structure for applications requiring selective filtering, e.g. direct incorporation into antenna feeders. As of the best of the authors' knowledge, geometries with similar electromagnetic properties have not been reported in the scientific literature up to the time of the publication of the [12_02_M].

A novel structure that consists of a patterned, periodic surface impressed on one side of a single-layer, grounded dielectric board and connected to the ground plane by three vias has been considered. The patterned surface is covered with a second layer of dielectric material, metallized on the opposite side to the interface where the periodic pattern is positioned.

The geometry with corresponding dimensions of the considered unit cell is presented in Fig. 59, where the upper metal plane has been removed for a clearer rendering. The grounded dielectric layer, of height $h_1=1.6$ mm, has a dielectric constant $\epsilon_r=3.5$. The shape of the unit cell is square in the horizontal plane, $d_x=d_y=2.5$ mm. (These dimensions have been considered for illustration purpose only, without targeting any particular application at this point.) Extending the square shape of the unit cell to a rectangular one corresponds to introducing an additional degree of freedom that can be efficiently exploited if properly considered. The patch is of spiral shape, facilitating multiple resonances; it is composed of several rectangular sub-patches, whose dimensions are listed in Table 6, according to the numbering in Fig. 59.

Table 6. Sub-patch dimensions

Sub-patch	x limits [mm]	y limits [mm]
1	-0.35; 0.35	-0.75; 0.75
2	0.25; 0.35	-0.85; -0.75
3	-0.55; 0.35	-0.95; -0.85
4	-0.65; -0.55	-0.95; 0.95
5	-0.55; 0.55	0.85; 0.95
6	0.55; 0.65	-1.05; 0.95
7	-0.75; 0.65	-1.15; -1.05
8	-1.15; -0.75	-1.15; 1.15
9	-0.75; 0.75	1.05; 1.15
10	0.75; 1.15	-1.15; 1.15

Looking at the geometry from a different point of view, the metallization, previously called patch, can be seen as a meandered sequence of a finite number of transmission lines with different lengths and widths: such an approach better accounts for the presence of multiple resonances. One notes that the meandering and 2D periodicity change the coupling between the various parts of the resonators with respect to the linear arrangement and, consequently, the resonance frequencies.

Because of the presence of the two closing continuous, metallic plates, the patch prevalently acts as a parallel-plate capacitance. In the periodic arrangement, the coupling between the various cells is mainly capacitive [siev_99, rogers_05]; hence a resonant behavior is quite difficult to be reached because of the very low inductance present in the configuration. On the other hand, it has been shown that an inductive behavior can be augmented by using vias [rogers_05]. Therefore, three collinearly positioned vias, each of radius $r=0.1$ mm, have been added to the initial planar patch. The vias are

located parallel to the x axis along the mid-line and at the centers of the sub-patches as shown in Fig. 59 and connect the patch to the ground plane. The simple collinear, equi-space disposition of the vias has been chosen mainly to reduce the complexity: the spatial arrangement of such reactive loads represents a further degree of freedom for application driven design. Results reported below demonstrate that the inductive loading remains quite similar if vias are moved along the y axis, but this placement alters the symmetry of the unit cell.

The increased number of vias with respect to a usual "mushroom" configuration will result to be responsible for achieving a large number of EBGs. In fact, simulations (not shown) we have performed with only two vias present have resulted in a lower number of EBGs.

We note, that a similar kind of configuration has also been considered in [kam_08] - explicitly a spiral-based, inductance-enhanced structure, with a patch featuring varying metallization bandwidth, connected to the ground plane through a central via - for a different application, namely multichip module packages. Consequently, the authors of the cited reference have been interested in the lower frequency band behavior of the device. Although the unit cell considered in [kam_08] is not symmetric, the existence of two EBGs between the first three modes on the $\Gamma X M \Gamma$ border of the first irreducible Brillouin zone has been demonstrated. In our case, we have increased the number of vias, in order to enhance the inductive character of the structure at higher frequencies and used a different pattern for the metallization. Furthermore, we considered both 1D DDs for waves propagating along the x direction and 2D DDs for waves propagating in an arbitrary direction, this latter extension being motivated by the lack of symmetry of the unit cell.

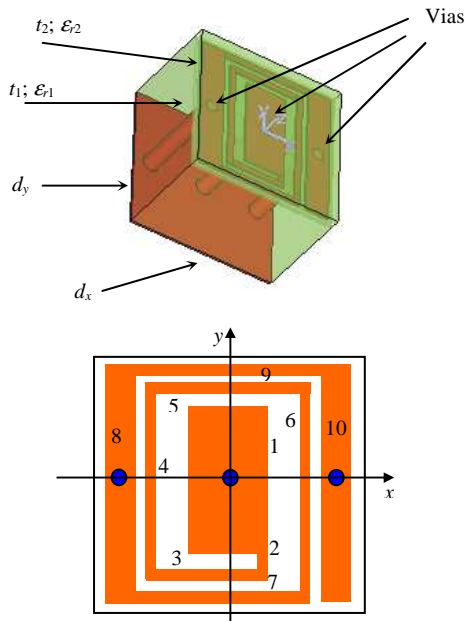


Fig. 59. Unit cell: CAD model (top), patch with numbered sub-patch decomposition (bottom)

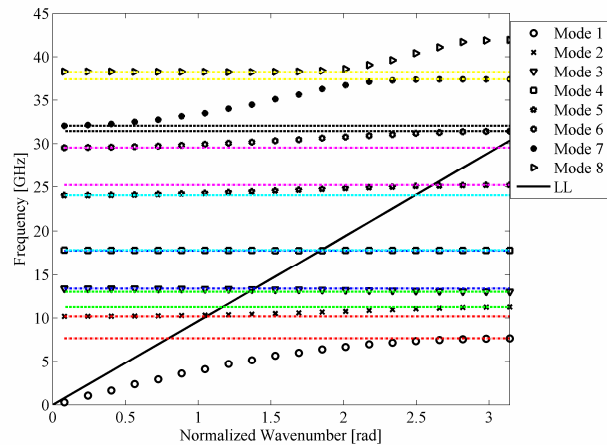


Fig. 60. 1D dispersion diagram, the first eight modes and light line.

In the numerical analysis, the characteristics of the upper layer (indicated by subscript 2 in Fig. 59), i.e. height and ϵ_r , have been taken as parameters. In particular, a height $t_2=0.1t_1$ has been considered since it has been previously demonstrated that it guarantees a broad-band performance [rogers_05]. The relative dielectric constant ϵ_{r2} has been varied, and results for two different values of this parameter are presented below.

The DD corresponding to the first eight proper modes of the periodic structure with the unit cell of Fig. 59, for a value $\epsilon_{r2}=10$ of the dielectric constant of the upper dielectric layer is reported in Fig. 60.

The diagram has been computed along 21 equi-spaced points between 4.5° and 175.5° and the

result has been spline interpolated.

Only waves propagating along the x direction (according to the reference frame shown in Fig. 59) have been considered. The horizontal axis represents the normalized wavenumbers $k_k d_x$ and the vertical axis represents the corresponding modes frequencies. The light line (LL), separating slow and fast modes, and corresponding to propagation of plane waves through an effective medium characterized by (1) is also represented on Fig. 60. EBGs are considered to spread between the maximum frequency of mode i , denoted $f_{M,i}$, and the minimum frequency of mode $i+1$, denoted $f_{m,i+1}$.

By inspection of Fig. 60, existence of EBGs between every two consecutive modes can be observed. The flat, quasi phase independent dispersion curves correspond to high Q resonators, which can be represented by pairs of capacitances and inductances that are internal to the unit cell. The limits and widths of the EBGs are reported in Table 7, together with similar results corresponding to the case when the leftmost via in Fig. 59 is shifted along the negative y axis by 0.55 mm. Such a shift is an example of parameterization of the structure.

Table 7. Limits and widths of EBGs: propagation along x axis

i	$f_{M,i}$ [GHz]	$f_{m,i+1}$ [GHz]	EBG Width [GHz]
1	7.68 (7.69)*	10.20 (10.12)	2.52 (2.43)
2	11.28 (10.34)	13.03 (13.17)	1.75 (2.83)
3	13.39 (13.45)	17.76 (17.53)	4.37 (4.08)
4	17.80 (17.86)	24.04 (23.60)	6.24 (5.74)
5	25.23 (25.01)	29.53 (29.47)	4.30 (4.46)
6	31.44 (31.39)	32.05 (34.57)	0.61 (3.18)
7	37.41 (37.75)	38.26 (38.12)	0.85 (0.37)

*) Values in parentheses correspond to the shifted position of the first via

One can further note that every single pass-band is defined by a single mode, i.e. a very large frequency band of mono-modal characteristics of the structure can be efficiently exploited for dispersion engineering applications, e.g. self-collimation [matt_07], super lens, super prisms [enoch_03] and propagation control [notomi_00].

The next considered problem has been finding whether this property, namely the existence of a large number of EBGs, extends to waves propagating along other directions. The patch in Fig. 59 is not symmetrical with respect to either x or y axis, although the lack of symmetry is quite reduced.

Nevertheless, we considered that a simple evaluation of the DD along a spectral triangle, such as $\Gamma X M \Gamma$, is not sufficient and proceeded to a full 2D propagation analysis. Since the procedure of calculating the DD is computationally extremely time-consuming, the analysis is restricted to the determination of the first five modes. This choice guarantees a shorter computational time, since the mesh required for the lower frequency characterization is less dense with respect to the previous case. For this second set of investigations, a value of $\epsilon_r=30$ has been considered, which in turn increases the discretization details, i.e. number of mesh cells. The DD has been calculated on a 24×24 points grid, between -172.5° and 172.5° on both the x and y directions. The result is reported in Fig. 61. The lowest, highlighted triangular contour is the spectral one referred above. Its projections on the frequency surfaces are also represented.

Again EBGs may be observed between every two consecutive modes; the limits and widths of these EBGs are listed in Table 8, while the corresponding limits on the ΓX line are reported in Table 9 allowing a quantitative comparison of the band limits between the 1- and 2-D characterizations. As it can be observed, the difference between the minimum and maximum values of the boundaries are quite similar, at least for the first three modes, a clear indicator of the low anisotropy. Secondly, by comparing the data in Tables 7 and 9, one can note that the increase of the relative dielectric constant from 10 to 30 reflects in narrower band-gaps.

We also note that the fundamental mode of the considered structure is TEM, i.e. with zero cut-off, with a relatively large band-width, not allowing the mitigation of low frequency noise. Modification of the geometrical and material parameters, similarly to the solution presented in [12_01_M], allows finding appropriate structures for this application. Moreover, we note that the presented passive

structure allows for insertion of active devices in a similar manner as recently discussed in [11_01_M].

Table 8. Limits and widths of EBGs: arbitrary propagation.

i	$f_{M,i}$ [GHz]	$f_{m,i+1}$ [GHz]	EBG Width [GHz]
1	7.44	9.68	2.24
2	10.92	12.65	1.73
3	13.09	17.17	4.08
4	17.84	23.31	5.47

Table 9. Limits and widths of EBGs: second experiment, propagation along x axis.

i	$f_{M,i}$ [GHz]	$f_{m,i+1}$ [GHz]	EBG Width [GHz]
1	7.29	9.85	2.56
2	10.92	12.65	1.73
3	13.07	17.17	4.10
4	17.30	23.31	6.01

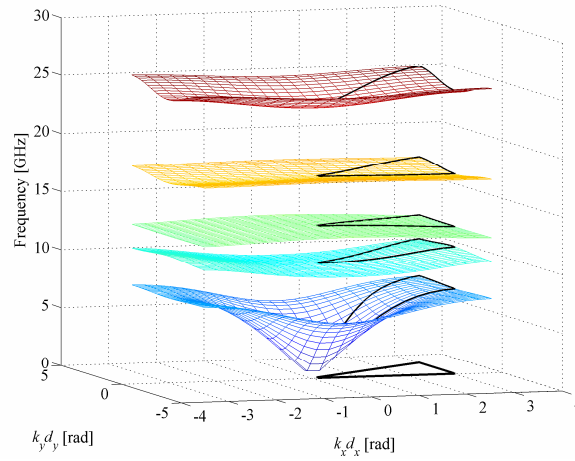


Fig. 61. 2D dispersion diagram, the first five modes.

If different values of geometrical or material parameters are chosen, the DDs are expected to look different from the reported ones. This fact will be exploited in the future, after carrying out parametric studies (and by taking into consideration other degrees of freedom), for multi-band filter design that fits requirements of various applications. Another direction for applications is in the field of dispersion engineering, by taking advantage of the shape of the 2D DD.

C. Switched Surfaces

In order to obtain switched patterned surfaces, electronic control elements have to be introduced for altering the geometry. We have tested various geometries of the patches in order to devise EBG structures with convenient switched frequency properties.

A parametric study of a high impedance surface built in microstrip technology is reported and the feasibility of an electronically switched parallel-plate waveguide is demonstrated in [10_03_M]. Full wave electromagnetic simulation is used for obtaining relevant parameters and for operation demonstration.

The geometry of the unit cell is presented in Figs. 62 (a) and (b). The dimensions we used have been: $D_x=D_y=2.5$ mm, $p=2.25$ mm, $t_1=1.6$ mm, $t_2=0.5t_1$. The internal radii of the two vias have been set to $r=0.1$ mm. In order to electrically separate the patch plane and the ground plane, slots have been inserted around the vias in the ground plane with interior radii of 0.25 mm and exterior radii of 0.4 mm. The dielectric constant of the microstrip substrate has been set to $\epsilon_1 = 3.5$, while the space in between the board and the upper plane is filled with air facilitating the insertion of the diodes. The HIS, obtained by the periodic repetition of the unit cell, is presented in Fig. 62 (c), where the diodes have not been drawn.

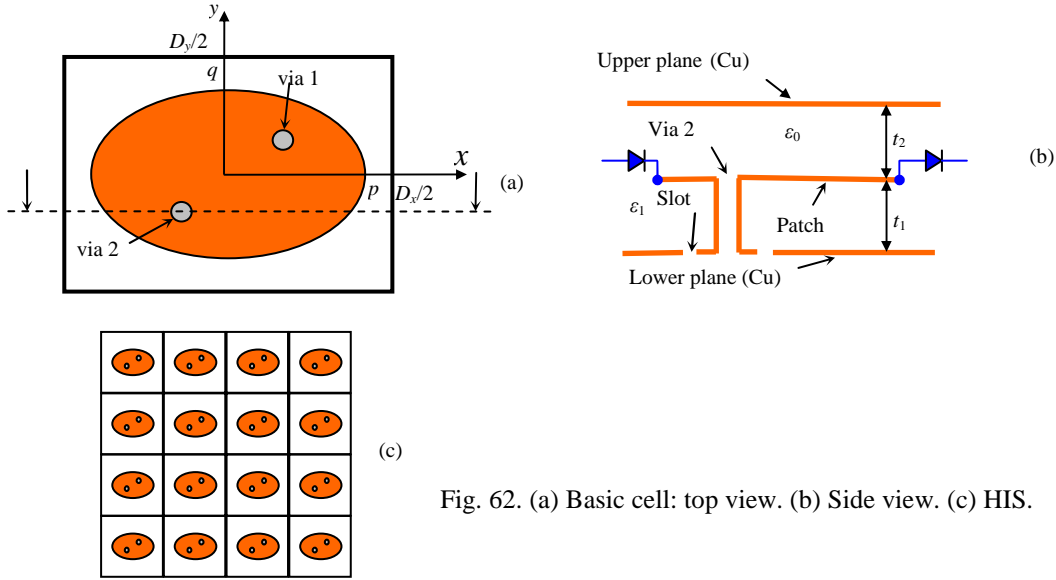


Fig. 62. (a) Basic cell: top view. (b) Side view. (c) HIS.

In order to gain some insight on the properties of the underlying HIS, the DD has been found by electromagnetic simulation (as shown above) and the result is reported in Fig. 63. The diodes and slots were not present in this experiment and the first five modes have been considered. The light lines are also represented in Fig. 63 and the EBG is indicated, between modes 1 and 2. The obtained limits of the EBG have been [16.09; 27.18] GHz, resulting a width of 11.11 GHz. If only modes having frequencies below the frequency corresponding to the light line for the same wave-numbers are considered, then the upper limit of the EBG extends to about 30 GHz. However, we have chosen to consider a global EBG, regardless of the slow or fast character of the waves.

A second simulation involved the influence of the patch dimension on the characteristics of the EBG. The q dimension of the patch has been kept constant at $q = 1.8$ mm, while the p dimension has been varied by considering six equidistant points between 1.5 and 2.25 mm. The positions of the vias vary with respect to the cell, but their relative positions with respect to the patch do not. The results are reported in Figs. 64 and 65, parameterized by three values for the radius of the vias.

The simulations have been performed only for the ΓX edge of the Brillouin zone, so that results apply for waves propagating along the x direction. As Fig. 64 shows, the maximum value of the EBG

width is obtained for the circular configuration $a = b = 1.8$ mm, while the central frequency decreases with the increase of a .

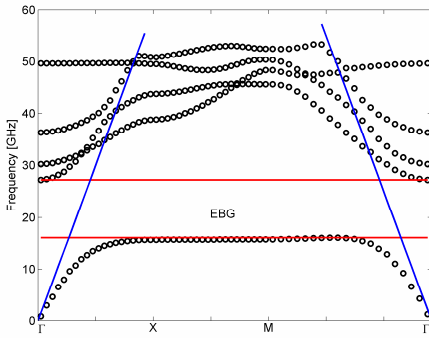


Fig. 63. DD for the HIS without slots and diodes. The radii of the vias: $r=0.2$ mm.

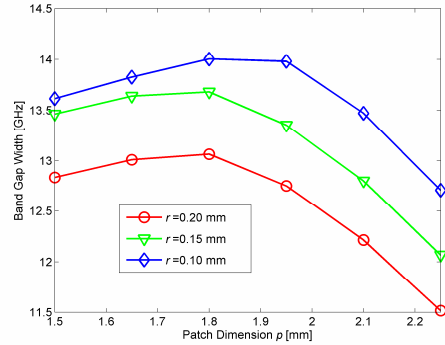


Fig. 64. EBG width in versus the p patch dimension.

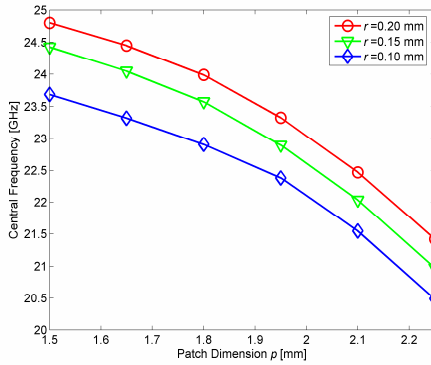


Fig. 65. Central frequency versus the p patch dimension.

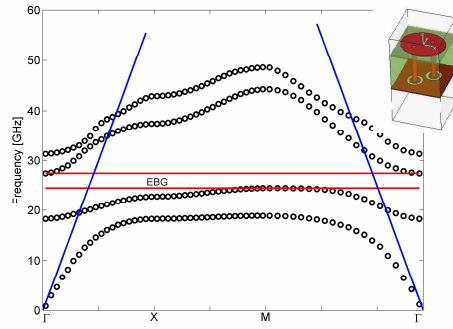


Fig. 66. DD for the HIS modified by inserting slots in the ground plane. Inset: CAD model.

Such a behavior may be explained in terms of a circuit model [rogers_05]. Circuit models are useful for predicting the EBG characteristics with a certain degree of approximation, but with a low calculation complexity. Although finding such a model is beyond our scope, some remarks may be appropriate.

The model devised in [rogers_05] for PPW built with HIS with rectangular patches and central vias is composed of two sections of transmission line and a shunt LC branch circuit. The inductance L depends on the vias dimensions, while the capacitance C is determined by the overlapping surfaces of the patch and upper metallic wall. Both parameters depend mainly on surface: L varies according to $\alpha - \ln(\alpha)$, $\alpha = \pi r^2 / D_x^2$ and does not depend on p , while C decreases with r^2 and increases with p . In our case, the mutual inductance M of the vias must also be taken into account. M decreases when p increases, as the distance between vias increases, but its dependence on r may be neglected [grov_73]. These variations explain the behavior of the EBG parameters reported in Figs. 64 and 65.

The decrease in central frequency with the increase of p is determined mainly by the increase of the capacitance. Additionally, the presence of a maximum value for the EBG width may be foreseen if we mentally extrapolate the graphs in Fig. 64. For $p=0$ (no patch) the structure becomes a PPW with two parallel layers of dielectric between two metallic planes, which clearly does not present an EBG. The same situation occurs for $p=2.25$ mm, when adjacent patches are in contact and the rows of patches become metallic strips between two metallic planes. Therefore, the shapes of the curves in Fig. 64 are explained once we know that EBGs exist for some patch dimension and so does the maximum.

As we have already mentioned, some switching elements must be inserted in order to obtain a tunable device. It is advisable to use the same structure that has been relied upon for obtaining the EBG in order to bias the devices; therefore, a possible solution relies on the interruption of the DC path between patches and ground. We have tested the influence of slots around the vias in the ground plane. The CAD model of the considered structure is reported in the inset of Fig. 66, where the upper metallic plane has been removed for illustration purposes. On the corresponding DD represented in Fig. 66, the presence of the EBG may be remarked between modes 2 and 3, covering the interval [24.47; 27.41] GHz and having a total width of 2.94 GHz (a larger width by more than 100% is obtained if only the region below the light lines in the DD is considered). Then we have performed a simulation of the case when diodes connect adjacent patches, as can be seen in the CAD model reported in the inset of Fig. 67. The forward biased diodes are modeled as small metallic parallelepipeds; when the diodes are not biased, they are supposed to be absent in the CAD model. A possible influence might be a slight increase in the fringe capacitance between patches in this case, with the consequence of some modifications of the EBG properties.

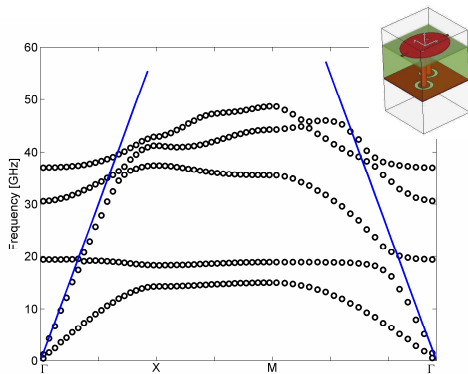


Fig. 67. DD for HIS with slots and diodes. Inset: CAD model.

When the diodes are biased, a direct metallic connection between patches exists, so that a new propagation mode is introduced. As this is indeed the case can be seen from Fig. 67, where the DD is reported. By comparing the DDs of the two states of the diodes (Figs. 66 and 67), the new TEM propagation mode can be observed. One can note that the phase velocity of the additional mode is equal to the speed of light, indicating that it propagates in the air-filled region. Therefore, depending of the bias, the surface is in one of two states: with or without EBG.

Some criticism may be addressed to the proposed scheme. The diodes bias is accomplished through the plane containing the patches, so that diodes are in a series connection, a solution with well known drawbacks such as weak reliability and current limited by one of the diodes if the current-voltage characteristics are not matched. Nevertheless, the absence of a biasing network makes the structure of easy fabrication.

In this work, we have demonstrated the feasibility of a new tuneable surface in a PPW, and the proposed solution of easy manufacturing geometry fulfils this requirement. Other solutions, involving separate bias for each diode are presented below.

The HIS we have introduced in [10_05_M] presents several EBG's, so it may be used as a multi-band filter. If intended for use as a single filter, the HIS may play the role of a band-pass or band-stop filter. We have determined the position of the EBG's by means of full-wave simulation in view of finding the DD. We have been interested in the propagation properties of electromagnetic surface waves along one of the directions parallel with the sides of the patches, so that we have calculated the DD only for the ΓX edge of the first irreducible Brillouin zone in the 2D wave-number space. This corresponds to propagation along the x direction defined in Fig. 68. We have adapted the introduced structure to a switched application.

The initial configuration of the HIS we have introduced and tested is also presented in Fig. 68. The following dimensions have been chosen: $D_x=D_y=2.5$ mm, $a=0.35$ mm, $b=0.6$ mm, $c=1.1$ mm and

$t_1=1.6$ mm. The vias have equal radii, of 0.1 mm and are centered at points $(-0.15$ mm, 0) and $(0.85$ mm, 0) respectively. This dimensions are kept throughout all the rest of the simulations, unless specified differently. The structure is scalable so that the results obtained here can be extrapolated to other dimensions and frequency bands. The dielectric constant of the substrate of the microstrip circuit board has been $\epsilon_1=3.5$.

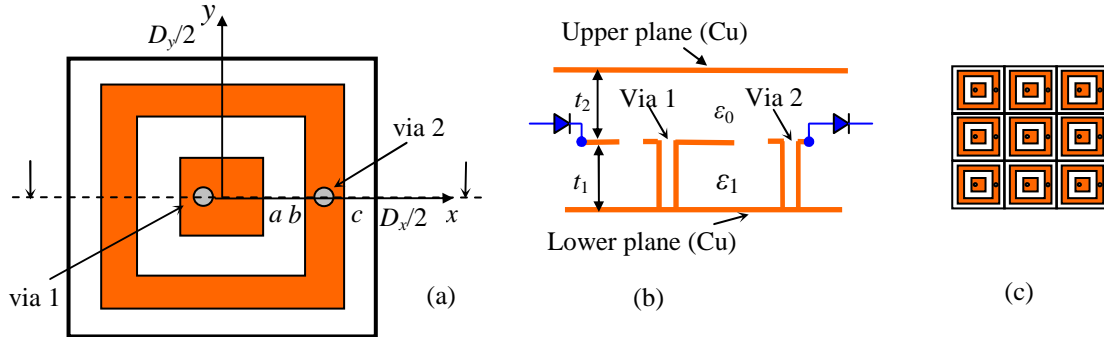


Fig. 68. (a) Basic cell: top view. (b) Side view. (c) HIS.

The most interesting feature of the DD is the presence of three EBG's, Fig. 69. The DD in Fig. 69, featuring the first eight propagation modes, has been obtained for an air space $t_2=0.1t_1$. Normalized wave-numbers $k_x D_x = \frac{2\pi}{\lambda_x} D_x$ [rad] are represented on the horizontal axis. The CAD model of the main period is reported in the inset of the figure, without the upper metallic plane. The light line (LL) is also represented on Fig. 69.

We have repeated the experiment for two other distances between the patches and the upper metallic plane: $t_2=0.3t_1$ and $t_2=0.5t_1$. The positions in frequency of the EBG's and their widths are reported in Table 10. While the widths of EBG1 and EBG2 diminish with the increase of the air layer thickness, the width of EBG3 first increases, then decreases. The behavior of EBG1 is consistent with the prediction of circuit models devised for the EBG of the "mushroom" structure [siev_99]. The behavior of higher frequencies EBG's need more sophisticated models in order to be predicted. This may be subject of future work.

Table 10. Position and widths of the EBG's

	$t_2=0.1 t_1$	$t_2=0.3 t_1$	$t_2=0.5 t_1$
f_{m1} [GHz]	6.67	7.84	8.17
f_{M1} [GHz]	11.88	12.22	11.97
BW1 [GHz]	5.22	4.39	3.80
f_{m2} [GHz]	15.00	17.47	17.99
f_{M2} [GHz]	28.79	24.59	21.15
BW2 [GHz]	13.79	7.13	3.16
f_{m3} [GHz]	44.17	44.34	44.50
f_{M3} [GHz]	46.18	46.89	45.54
BW3 [GHz]	2.01	2.55	1.04

The graph of Fig. 69 indicates that the HIS behaves like a multi-band band-stop filter. It may also be used as a band-pass filter e.g. in the range of frequencies in between the upper frequency of EBG1 and the lower frequency of EBG2.

Table 10 shows that favorable values for the EBG parameters are obtained for $t_2=0.1t_1$, so that this value should be used for simple filtering applications. However, we intend to test the structure for the case when electronic components, such as diodes, are mounted on the side of the board containing the patches. Therefore, in the next simulations, the larger value $t_2=0.5t_1$ has been chosen.

The CAD model of the first variation we have considered is reported in the inset of Fig. 70: we have removed one of the sides of the shape that surrounds the patch. The DD is presented in Fig. 70.

Only two EBG's are present. The first one is in the range [8.30 11.58] GHz, having a width of 3.28 GHz and the second one occupies the frequency range [18.31 21.07] GHz having a width of 2.76 GHz. By comparing these values with the last column of Table 10, we see that the parameters of the EBG's have been modified. This result should have been expected, as both the fringe capacitance between patches and the capacitances between the patch plane and the metallic planes have been modified.

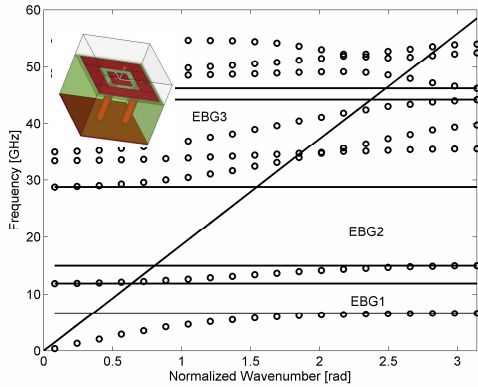


Fig. 69. DD for the basic structure.

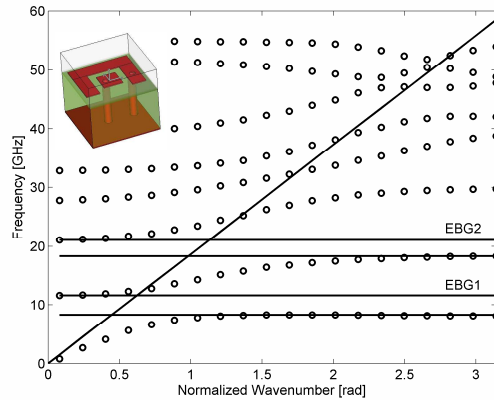


Fig. 70. DD – lower metallic patch removed.

The next two experiments involve the influence of the second via on the DD. The CAD model in the inset of Fig. 71 shows the absence of the second via combined with an extension of the hollow patch up to the sides of the unit cell, i.e. $c=D_x/2$. The consequence on the DD, presented in the same figure, is the disappearance of the EBGs, caused by the existence of a direct metallic path along the middle layer of the structure, which give rise to a TEM mode. If however the old value of c is used (the patch surrounding the central on not extended), two EBGs are obtained (Fig. 72): [17.84, 21.02] GHz (3.17 GHz width) and [44.82, 45.50] GHz (0.68 GHz width). This result will be used for devising a switched surface.

Finally some modifications less extended in the space of the unit cell have been tested: two small patches placed as shown in the insets of Figs. 73 and 74. The patches are 0.1 mm wide along the y axis and have a length of 0.3 mm parallel to the x axis. They are placed along the symmetry axis of the initial patches in the first case, while the second small patched is displaced by -0.5 mm in the y direction in the second case. Another distinction stems from the fact that the second via has not been considered in the first situation and it is present in the second one. The EBG in the DD of Fig. 73 is between [33.10, 36.63] GHz, having a width of 5.53 GHz. The EBGs in Fig. 74 are [7.95, 11.84] GHz (3.89 GHz width); [17.93, 21.15] GHz (3.22 GHz width) and [44.57, 45.52] GHz (0.95 GHz width, not represented explicitly in the figure).

The simulation results presented above show that, a wide range of HISs with various parameters of the EBGs may be constructed with minor modifications of the original structure. A special attention worth the structures in Figs. 72 and 73. The small patches in Fig. 72 may be thought to model biased diodes, while these small patches are absent in Fig. 73, which can be thought as a situation modeling unbiased diodes. Therefore, by means of biasing diodes, the structures in the two figures can be switched. In a practical situation, the HISs are of finite extent. The bias voltage may be applied between the input hollow patch and the output one, so that the series connection of diodes is connected to the supply voltage. This is the reason why we considered the situation when the second via in a basic cell is absent: otherwise the supply voltage source would have been short-circuited.

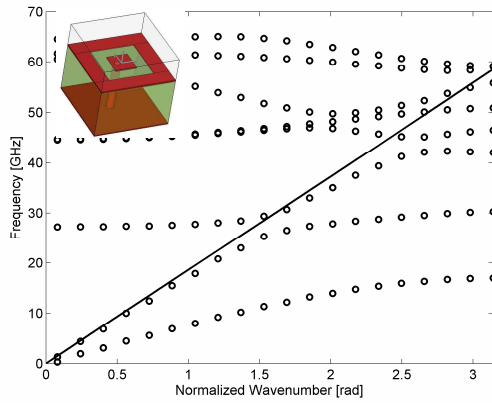


Fig. 71. DD – via 2 removed and external patch extended to the size of the unit cell.

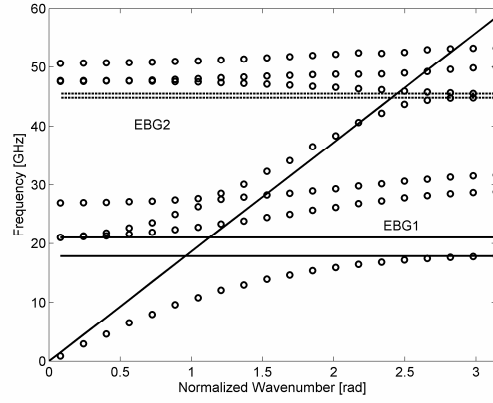


Fig. 72. DD – structure from Fig. 2 with via 2 removed.

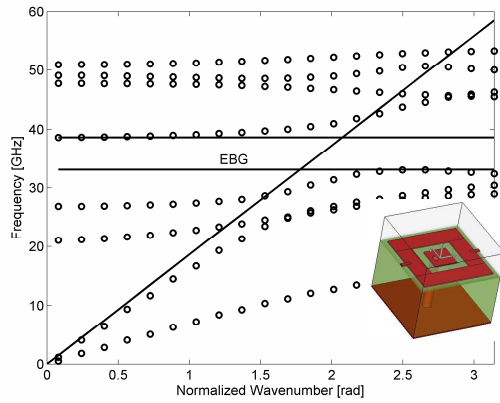


Fig. 73. DD – basic structure completed with biased diodes.

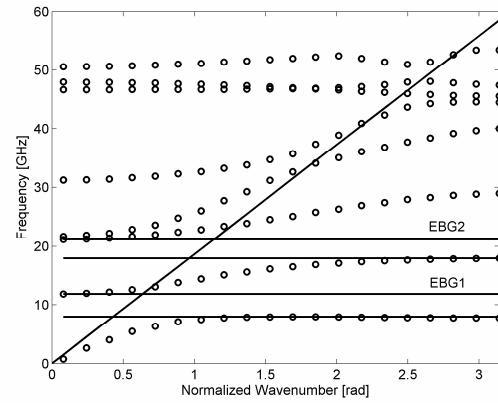


Fig. 74. DD – basic structure completed with two small patches.

The HIS we have introduced above has been demonstrated to feature three EBGs and therefore may be used as a multi-band band-stop filter or as a band-pass filter. We have shown that the parameters of the EBGs can be modified by means of small geometric alterations of the original structure so that an electronically switched surface with interesting frequency related properties can be obtained from the original structure.

A novel HIS built in microstrip technology that is used as one face of a PPW in view of switched filtering applications has been reported in [11_06_M]. The structure presents several EBGs. Diodes are used as switching elements and the structure itself may be used for applying the bias voltage to the switching elements, i.e. no additional circuit elements are inserted. When diodes are switched on, we have shown that a low-frequency EBG is introduced, changing the low-frequency properties from band-stop to band-pass. As expected, EBGs situated at higher frequencies are also affected. The introduced new structure is inspired by the well-known "mushroom" one, but presents several differences, as a large number of off-center vias, or two patches of circular symmetry. We describe the development process step-by-step and provide appropriate CAD models and DD for the intermediate and the passive configurations for a better understanding.

A unit cell of a HIS, having a square shape with sides $D_x=D_y=2.5$ mm, is presented in Fig. 75. It is realized on a microstrip board with a thickness $t_1=1.6$ mm and a substrate with dielectric constant $\epsilon_{r1}=3.5$. The circular patch on the upper face of the board has a radius $c=1.05$ mm. The surface is obtained by a 2D periodic repetition of the unit cell. A metal plate is supposed to be placed above the HIS at a distance $t_2=0.5t_1$ in order to create a PPW. Four vias, each with radii $r=0.1$ mm connect the

patches to the ground plane. Results for similar structures with more general elliptical patches and a variable number of grounding vias have been reported in the preceding section. The corresponding DD, having a typical shape [siev_99], and the CAD model are reported in Fig. 76.

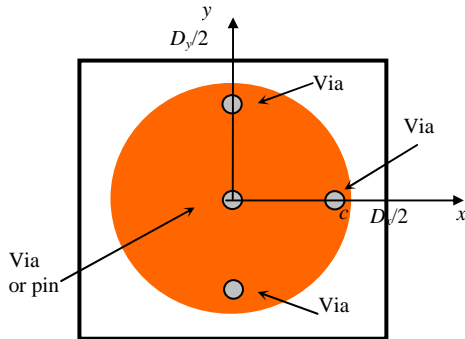


Fig. 75. Unit cell of a "mushroom" HIS with circular patch and four vias.

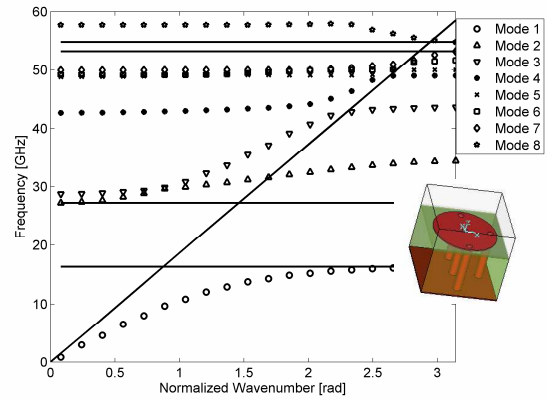


Fig. 76. DD for "mushroom" HIS with circular patch and four vias. Inset: CAD model (with removed cover metallic sheet for better visualization).

In the present analysis only propagation along the positive x direction (Fig. 75) has been considered, avoiding in this way to be trapped by any symmetry breaking effect on the 2D dispersion characteristics, when this latter is not fully computed. The normalized wave-number on the horizontal axis of Fig. 76 is $k_x D_x$. Two EBGs are present, one between 16.29 GHz and 27.19 GHz, and a narrower one between 53.21 and 54.81 GHz.

In order to stop propagation of surface waves starting with zero frequency, a direct metal path between the upper and lower metallic planes must be present reducing the number of independent metalisation from two to one. A solution is to replace the central grounding via with a metallic pin that connects the patch to the upper metal plate. This design also improves the mechanical stability of the structure, whose DD is presented in Fig. 77. It can be seen that a multi-band frequency behavior is obtained. The lower EBG ranges from DC to 22.94 GHz. The other three EBGs are in the ranges 26.70-28.83 GHz, 34.47-37.44 GHz and 57.16-57.76 GHz respectively.

As a next step we have split the patch in two: a circular one with smaller radius surrounded by a second annular patch with the aim of obtaining a switch, i.e. introducing some space where the switches can be accommodated. In the above operation the inner radius of this latter is larger than the radius of the inner circular patch. The resulting geometry is shown in Fig. 78. Fig. 78 (b) shows the side view of the structure with the original central via, while Fig. 78 (c) shows the central via replaced by the pin. The switching device is a diode connected as shown in Fig. 78 (c). When the diode is switched on, a DC path between the metal plates is present, so that waves are prevented to propagate starting from zero frequency. When the diode is switched off, the connection between the two external plates is interrupted, and low frequency to zero cut-off wave does propagate.

The proposed solution further allows for the bias voltage to be applied by means of the upper and lower metal plates entering the structure of the PPW, so that there is no need of additional biasing circuitry that might alter the high frequency behavior of the device.

The electromagnetic characteristics and behavior of the HIS is presented next. The study is enriched with the preliminary analysis of one of the many parameters on the control of the position and width of the band-gap.

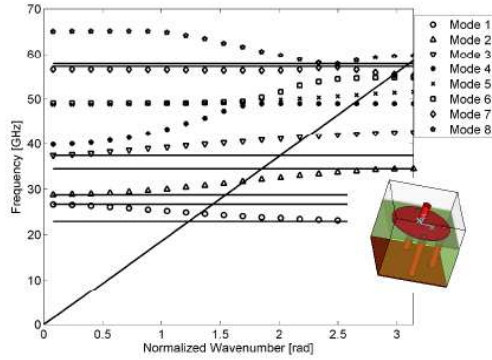


Fig. 77. DD for HIS with circular patch, three vias and pin. Inset: CAD model (with removed cover metallic sheet for better visualization).

For full-wave analysis, the presence of the biased diode has been simulated by a small metal prism, which is absent when the diode is not biased [matek_09], as reported in the insets of Figs. 79 and 80. All geometrical and material parameters are those from the previous section allowing direct comparison between results. The radii a and b from Fig. 78 (a) have been chosen for demonstration as 0.35 mm and 0.65 mm respectively.

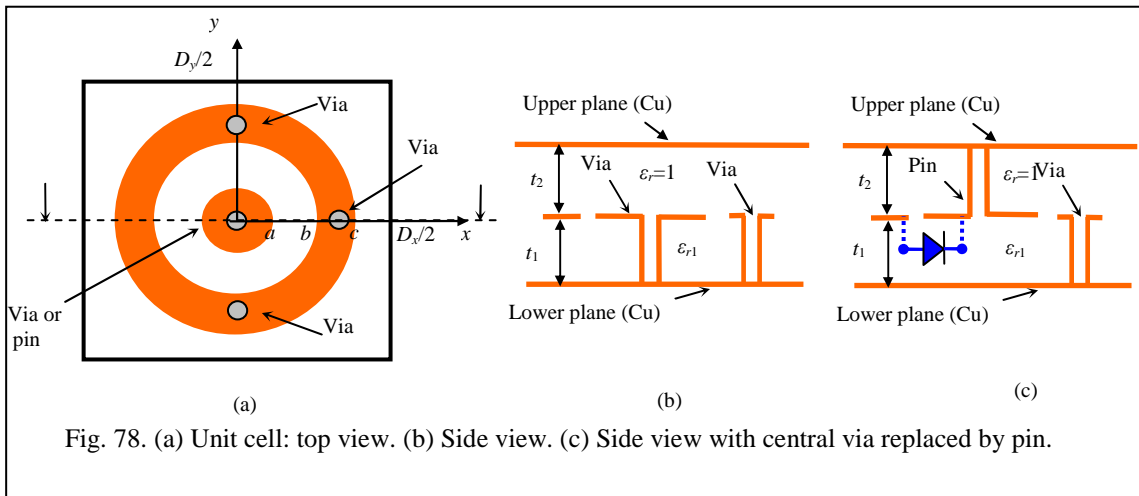


Fig. 78. (a) Unit cell: top view. (b) Side view. (c) Side view with central via replaced by pin.

In Fig. 79, the DD corresponding to the absence of the diode is reported. Three EBGs may be identified: from 13.73 to 25.79 GHz (12.06 GHz wide), from 33.29 to 39.41 GHz and from 42.45 to 45.79 GHz. In Fig. 80, the DD corresponding to the presence of the diode is displayed. The following five EBGs are obtained: from DC to 20.79 GHz, from 21.48 to 27.99 GHz, from 36.64 to 39.63 GHz, from 44.10 to 45.81 GHz and from 54.55 to 54.82 GHz.

A special attention worth the lowest frequency EBGs in the two situations considered above. When diodes are switched on, a narrow pass-band exists between 20.79 and 21.48 GHz, while when diodes are switched off, the first EBG listed above is present and covers this pass-band. Therefore, the surface is switched from a pass-band to a stop-band behavior around 21 GHz with a guard of more than 7 GHz in the lower frequencies range and more than 4 GHz in the high frequencies range.

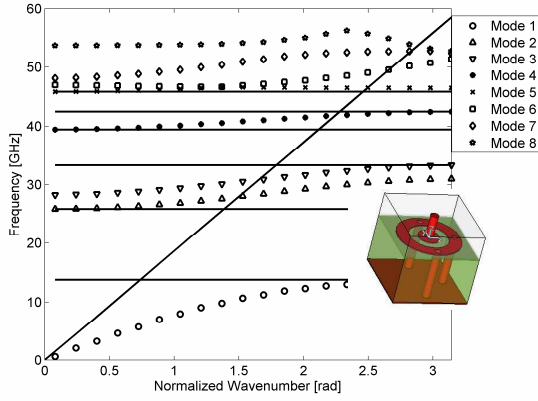


Fig. 79. DD for HIS with two circular patches, three vias and pin. Inset: CAD model (with removed cover metallic sheet for better visualization).

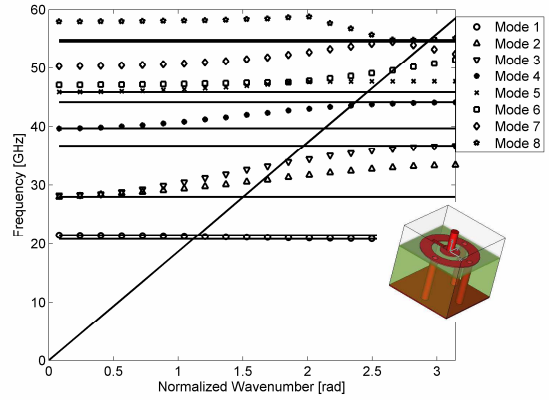


Fig. 80. DD for HIS with two circular patches, three vias pin and diode. Inset: CAD model (with removed cover metallic sheet for better visualization).

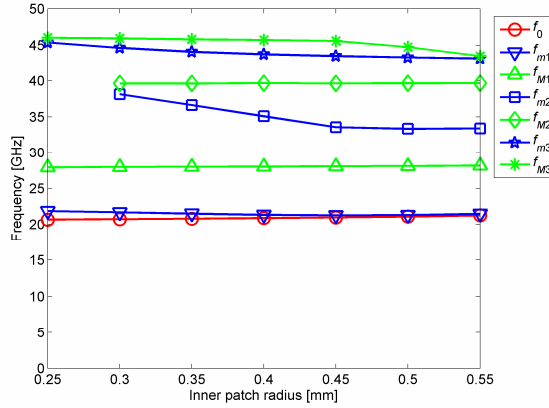


Fig. 81. EBG limits versus inner patch radius – diode connected.

In order to change the limits of the EBGs for design issues, several geometrical parameters and the number of vias may be varied. This investigation will be subject to future work. However some insight is provided here in Fig. 81 which reports the limits of the EBGs when only the value of radius of the inner patch a is varied between 0.25 and 0.55 mm and the diode is supposed to be present: f_0 denotes the upper limit of the first EBG, while f_{mi} and f_{Mi} , $i=1..3$ denote the limits of the other EBGs (the second EBG is not present for $a=0.25$ mm and the fifth EBG is not considered as being very narrow). The upper limit of the first EBG varies between 20.66 and 21.25 GHz. Although the variation is conveniently linear, the range is quite small, so the other solutions, such as varying the number of vias, might be considered in this case. However the third and fourth EBG's vary significantly, so that the radius a may be considered as a design parameter for multi-band applications.

We have just demonstrated that a narrow-band pass-band filter could be switched on and off by controlling the biasing voltage of the diodes.

A novel, multi-element unit cell in parallel plate PPW has been proposed and analyzed both in its passive and active configurations for 1D propagation [11_11_M]. The passive configuration consisted of up to three concentric rings, some of them being connected to the closing metallic planes by a variable number of vias. The large number of stop-bands the structure has been proven to exhibit is due to the different resonances of the various constituent elements. The active counterpart obtained by insertion of diodes between different rings allows for real-time modifying of the electromagnetic

response of the unit cell, consisting of change in the number and characteristics of the stop-bands and in the in-band behavior. The biasing through the vias represents an elegant and efficient solution avoiding the need of the presence of any biasing network. Sensibility of the structure to the geometrical dimensions, to the material properties and to the number of vias have been in depth investigated by dedicated numerical software based on finite integration technique of the Maxwell's equations. The DDs have been obtained by standard approach, considering the eigen-solution of the homogeneous problem with appropriate periodic boundary conditions in 2D. Filters for cognitive radio systems, or multi-objective sensors are just some of the possible applications for this unit cell, with versatile electromagnetic properties.

Like all the PPWs we have considered, a metamaterial surface plays the role of one wall and a metal plane plays the role of the other wall, Fig. 82 (a) [11_11_M]. The metamaterial relies on a microstrip board with a textured pattern on one side, which faces the interior of the PPW. The other side of the board, a continuous metal plane acting as ground for the patterned surface, ensures the electromagnetic insulation of the device. The unit cell of the textured face contains two or three circularly shaped, concentric metal patches, Fig. 82 (b). External patches are connected to the lower ground plane through one, two or three metalized vias. A unique feature is provided by the fact that the upper metal plane is connected to the central patch plane by a metal pin. This fact provides a direct DC path between the metal planes when the two patches are electrically connected, ensuring rejection of low frequencies, while the structures considered in the cited literature are high pass.

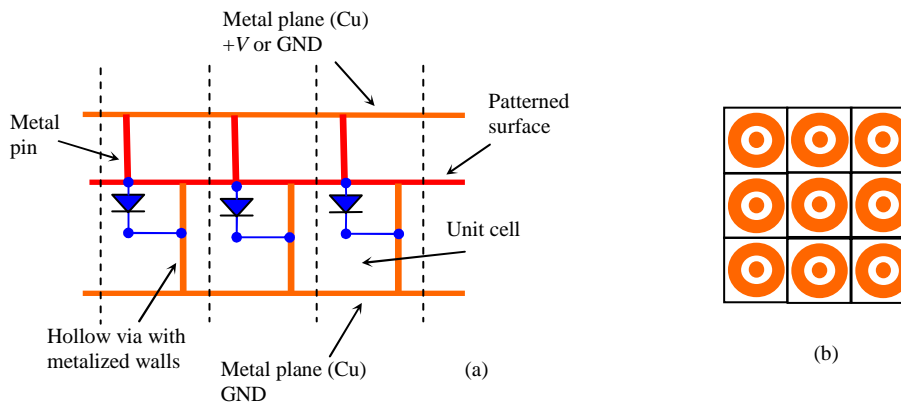


Fig. 82. Inhomogeneous PPW (a) and patterned surface (b).

The electric connection between the two patches may be switched ON or OFF by diodes, changing in this way the frequency response from low-pass to high-pass. The bias of the diodes is applied through the metal walls, thus avoiding the presence of an additional biasing network that might perturb the electromagnetic behavior of the device. Furthermore, as discussed below, the frequency response for both states of the diode has a multi-band structure. This characteristic allows increasing the selectivity of a sensor, or device sensors with multiple observables.

The importance of knowledge of the change in the behavior of the structure versus various geometrical and material parameters is of fundamental importance in the design activity [rajo_07]. We present such a study by varying the number of vias connecting the external annular patch to the ground plane and the radius of the inner circular patch. Creation of new materials [she_05] allows for increased flexibility in design. The variation of their dielectric properties to different external solicitations can be used for monitoring or sensing applications. Therefore, we have also tested our structure by filling the space in between the patch plane and the upper metal plane with materials of various dielectric constants.

In the last two decades, the advent of CAD systems dramatically decreased experiment costs in microwave industry and education [gupta_02]. In this context, we have simulated again the proposed structure by means of a commercial software [CST] that relies on the finite integration technique for solving the Maxwell equations [weil_77, weil_08]. As shown above, the incorporated eigenmode

solver allows for the determination of the DD. Therefore, the frequency behavior of the proposed device is reported in terms of DDs.

Since computation of the DD is a numerically onerous task, we have mentioned that many published papers [siev_99, tav_07, abhari_03, rogers_05, zhang_08] are dedicated to finding circuit models for electromagnetic structures similar to that we have proposed here. Such models are intended for easy prediction (i.e. without the needs of dedicated computation resources and reduced time required to obtain the electromagnetic responses) of EBGs positions in frequency and their bandwidths. Although acceptably accurate, the cited models are generally employed for predicting a smaller number of EBGs than up to five, like in our case. A circuit model able to predict four EBGs could be quite complicated in terms of number of reactive elements and circuit topology. Furthermore, circuit models are reliable when the involved wavelengths are large in comparison with the unit cell dimensions. The advantages in computation time motivate research for circuit models, which will be also a future goal for our investigation. However, it is worth to note that the drawback represented by the changing circuit characteristics with the geometry limits the flexibility of such approach. When accurate band structure is needed, full-wave simulation has to be chosen [rajo_07, rajo_09]. For the moment, results obtained by full-wave electromagnetic simulation that we present here in tabular and graphic forms may be considered accurate enough for current design activity and for validation of circuit model to be looked for in the future.

The CAD model of a unit cell of the PPW with three patches is presented in Fig. 83 (a). The unit cell dimensions, defined in Fig. 83 (b), where the two-patch unit cell is reported are $D_x=D_y=2.5$ mm. The microstrip board, of height $t_1=1.6$ mm, is built with a dielectric material of dielectric constant $\epsilon_{r1}=3.5$. Three concentric patches, one circular of radius 0.35 mm, the second one annular of internal radius 0.5 mm and external radius 0.65 mm and the third one equally annular, of internal radius 0.75 mm and external radius 1.15 mm generate the texture of the HIS. Three vias, of radii 0.1 mm, connect the outer patches to the ground. A pin, of radius of 0.1 mm, connects the inner patch to the upper metal plane, situated at a distance $t_2=0.8$ mm above (the upper metal plane is not represented in order to increase visibility). The space in between the patch plane and the upper plane is filled with a material of dielectric constant ϵ_{r2} . The whole structure is mechanically compact, due to the pins.

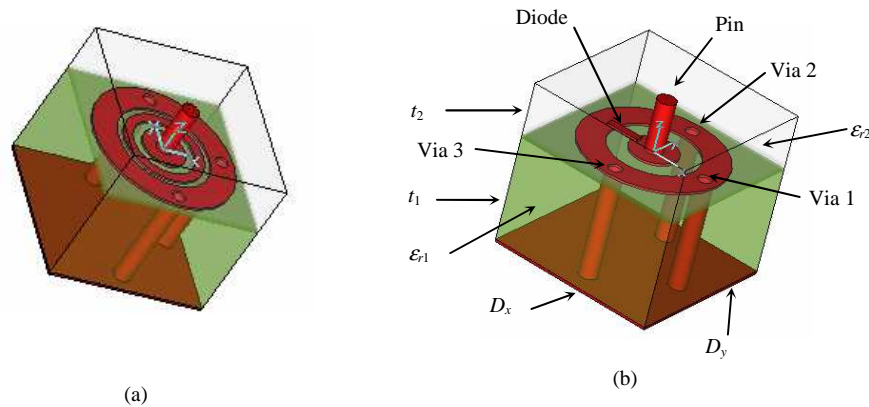


Fig. 83. (a) Cad model of the unit cell with three vias and three patches and upper metal plane removed for better rendering. (b) CAD model for unit cell with two patches and up to three vias, upper metal plane removed and definition of geometric dimensions.

In the context of filtering applications, we are interested in propagation along the x direction. The DD corresponding to $\epsilon_{r2}=1$ (simply air) and $\epsilon_{r2}=5$ are represented in Figs. 84 and 85 respectively. The DDs illustrate the frequencies of the first seven proper modes versus normalized wave-numbers $k_x D_x$. The EBGs are emphasized and light lines (LLs) are also represented. LLs separating fast waves from slow waves have been drawn corresponding to plane waves propagating through a medium with an effective dielectric constant defined and motivated in [rogers_05] (see (1)).

Since the positions and widths of the EBGs are quite different in the two considered situations, the dielectric constant of the upper material layer may be used for varying the frequency characteristics of the structure. From a dispersion engineering point of view, it is interesting to note that mode 4 in Fig. 85 features negative group velocity.

The frequency limits of the EBGs versus the dielectric constant of the upper material layer are reported in Fig. 86. The EBGs are defined between the maximum frequency of mode i and minimum frequency of mode $i+1$, which are marked similarly.

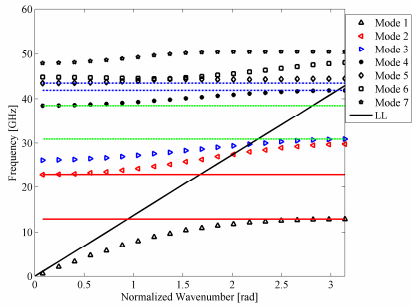


Fig. 84. DD for the three-patch structure, $\epsilon_{r2}=1$. The CAD model is reported in Fig. 2 (a) .

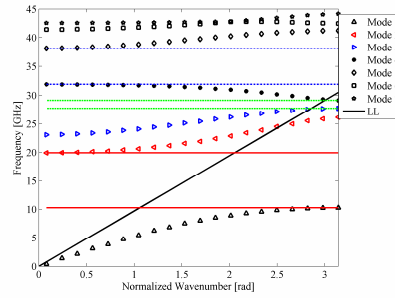


Fig. 85. DD for the three-patch structure, $\epsilon_{r2}=5$. The CAD model is reported in Fig. 2 (a).

It may be concluded that, while the lowest frequency EBG has a rather constant width, but various positions in frequency, the parameters of the higher frequency ones have important variation, providing flexibility in filter and sensor design. The highest frequency EBG occurs only for a limited range of the considered dielectric constant.

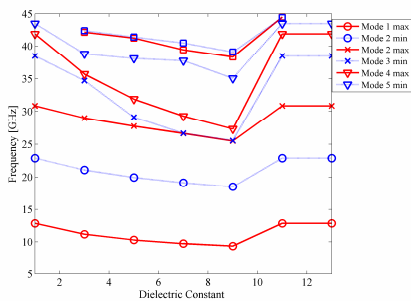


Fig. 86. Frequency limits of the EBGs versus the dielectric constant of the upper material layer.

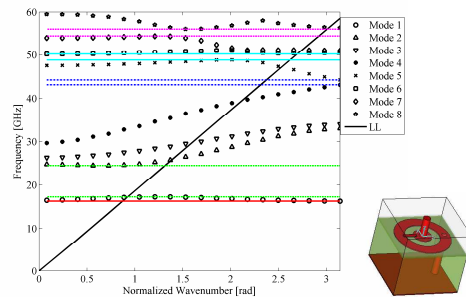


Fig. 87. DD and CAD model for the structure with one via and diode on $\epsilon_{r2}=1$.

An active version of the structure considered above can be obtained by a diode, inserted in between the patches which may be switched ON or OFF, by applying appropriate DC potentials to the metal plates. Like we did before, the ON state of the diode is simulated by the small metal prism in Fig. 83 (a), while the "OFF" state corresponds to the absence of the prism. This simplified model has been considered mainly to check the possibility of changing the resonant response of the structure.

The DD of the device having only one via (via 82 in Fig. 2 (b)), an air upper layer $\epsilon_{r2}=1$ and diodes switched on is reported in Fig. 87. The first 8 proper modes have been considered. Normalized wavenumbers $k_x D_x$ are represented on the horizontal axis. Five EBGs are present, the lower frequency one starting from zero frequency due to the direct DC path between the upper metal plate and the ground plane. When the diode is switched OFF, the DD in Fig. 88 is obtained (see the inset for the CAD model). Four EBGs are now present, the structure allowing modes with low frequencies to pass. The filtering properties are switched in the lower frequency range from band-pass to band-stop following

switching OFF the diode. The positions of the upper frequency EBGs are different in the two figures, i.e. after switching the diode. LLs corresponding to propagation of TEM waves in free space are also represented in Figs 87 and 88, in order to mark the difference between slow and fast waves.

The positions and dimensions of the EBGs for various numbers of vias is a question of interest for design. Simulations similar to those leading to Figs. 87 and 88 have been performed with two vias present (via 1 and via 2) and all three vias present, for both states of the diode. The results are reported in Table 11, showing that frequency limits for different modes can increase or decrease with the number of vias.

Another set of simulations have investigated the influence of the radius of the inner patch. Results for two other values than the initial one are also reported in Table 11 [11_03_M].

As shown above, the possibility of choosing in a wide range of materials makes an important opportunity by increasing flexibility in filter design. The DD associated to the structure having an upper layer of dielectric material with $\epsilon_{r2}=10$ is presented in Fig. 89 (the diode is switched ON, as in following simulations regarding the effect of the dielectric constant). By comparing Figs. 87 and 88, one can see that, as expected, the DD is shifted towards lower frequencies. Surface waves do not propagate any more through air. Accordingly, the LL in Fig. 85 has been drawn corresponding to waves propagating through a medium with an effective dielectric constant, as shown above.

Table 11. Limits of the EBGs [GHz]

Modes	0-1	1-2	2-3	3-4	4-5	5-6	7-8
1 via, diode on	16.23	17.24-24.47			43.08-44.21	48.81-50.17	54.39-56.01
1 via, diode off		9.40-17.55			39.49-44.11	47.52-47.90	51.53-54.28
2 vias, diode on	19.28	20.30-25.22			43.74-46.63		
2 vias, diode off		12.39-22.32		33.49-34.98	41.74-46.43		
3 vias, diode on	20.79	21.48-27.99		36.64-39.63	44.10-45.85		54.55-54.82
3 vias, diode off		13.73-25.79		33.29-39.41	42.46-45.79		
3 vias, diode on, $a=0.45$ mm	20.97	21.27-28.06		33.57-39.65	43.51-45.58		
3 vias, diode off, $a=0.45$ mm		12.82-25.82	28.14-28.24	33.29-39.41	42.37-44.96		52.567-52.568
3 vias, diode on, $a=0.50$ mm	21.09	21.30-28.09		33.34-39.66	43.33-44.74		54.57-54.74
3 vias, diode off, $a=0.50$ mm		12.20-25.86	26.98-28.26	33.30-39.40	42.34-43.67		

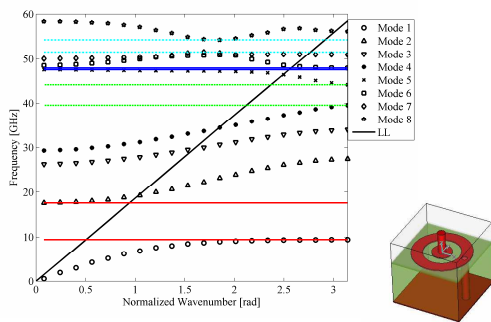


Fig. 88. DD and CAD model for the structure with one via and diode off, $\epsilon_{r2}=1$.

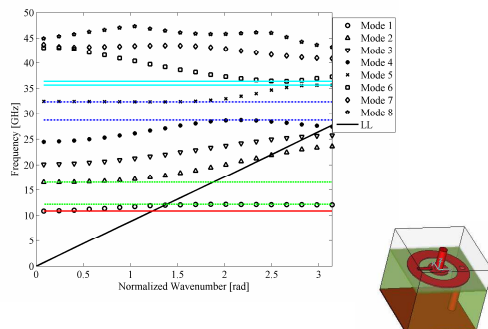


Fig. 89. DD and CAD model for the structure with one via, diode on and $\epsilon_{r2}=10$.

The variations of the frequency limits of relevant modes versus the dielectric constant of the upper layer are represented in Figs. 90 and 91. Again shift towards lower frequencies with the increase of the dielectric constant has been observed. However, the presented graphs also give quantitative results that can be used for tuning the structure to practical requirements.

The presented results are intended for design of high frequency filters to be employed in advanced systems or high sensibility sensor applications.

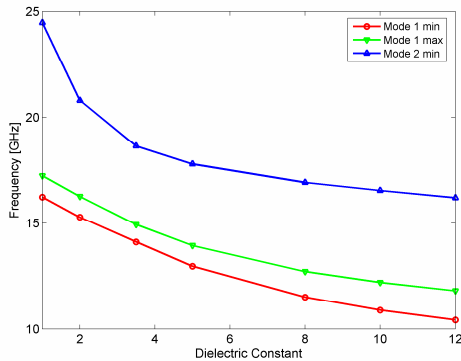


Fig. 90. Frequency limits of the modes that define the first two EBGs. The lowest frequency of the first EBG is zero.

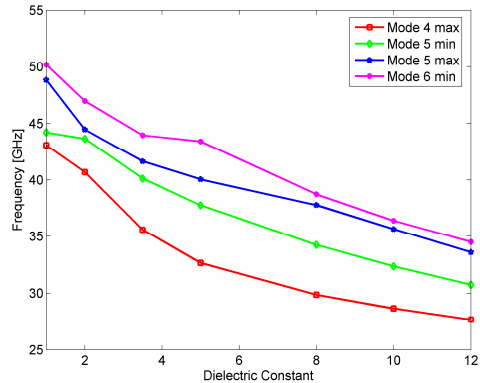


Fig. 91. Frequency limits of the modes that define the upper two EBGs (in between modes 4 and 5 and modes 5 and 6).

We have introduced two versions of switched surfaces that rely on the same basic configuration of the PBG [11_02_M]. The control elements are diodes that are placed either on the upper plane or on the ground plane of a microstrip board. Additionally, the structure is covered with a metallic plane at a certain distance above, so that an inhomogeneous PPW is obtained. The frequency parameters of the EBGs are determined in the two states of the diodes by full wave simulation, using the commercial field solver [CST]. The behavior of the surface is tested by means of the DD on the first irreducible Brillouin zone.

The basic structure consisted of a 2D periodic pattern impressed on one side of a microstrip board, having a square shaped unit cell, Fig. 92. The unit cell contained a square inner patch, connected to the ground plane through a metallic via, and an outer patch around the first one. The via has been placed in an eccentric position in order to increase the design flexibility by changing position if needed [gao_06]. However, the situation of the via has not been changed during the simulations reported in this paper.

The geometrical dimensions with respect to the reference system in Fig. 92 are: $D_x=D_y=2.5$ mm, $a=3.5$ mm, $b=0.6$ mm, $c=1.1$ mm and the via has been placed at point $(-0.15$ mm,0). The lower metallic plane has been situated at a distance $t_1=1.6$ mm, the space in between the patch plane and the ground plane being filled with a material having a dielectric constant $\epsilon_r=3.5$. The upper plane has been placed at a distance $t_2=0.5t_1$ from the patch plane, the space in between being filled with air.

We have been interested in propagation of surface waves along the x direction, so that the DD has been calculated on the ΓX edge of the first Brillouin irreducible zone, Fig. 93, where the light line is also represented. The PBG surface we have introduced presents two EBG's: EBG1=[17.84; 21.02] GHz, having a width of 3.17 GHz and a narrow one, EBG2=[44.82; 45.50] GHz, having a width of 0.68 GHz. These EBGs have been considered between adjacent modes, regardless of their propagating or evanescent character.

The diodes have then been connected as shown on Fig. 92. In a practical setting, the surface is of finite dimensions, so that diodes are connected in series and the bias voltage is applied at the two ends of the structure. The outer patches provide a dc path between diodes.

In order to find the DD in this case, the diodes have to be modeled for the electromagnetic solver. Following the same idea from [matek_09], diodes have been considered as small metallic prisms, as shown on the CAD model in the inset of Fig. 94, where the DD of the structure is reported. Only one

EBG appears when the diodes are biased. However, its width is larger than in the case when the diodes are unbiased, $EBG=[33.10; 36.63]$ GHz, having a width of 5.53 GHz.

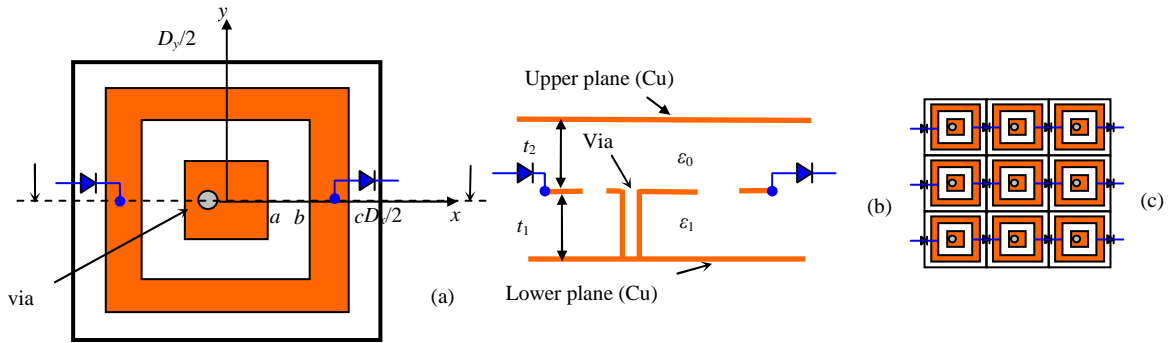


Fig. 92. (a) Unit cell: top view. (b) Side view. (c) HIS.

EBG1 is comprised between the first two modes of propagation, while EBG2 and EBG are comprised between modes 4 and 5. Therefore, it may be concluded that, following switching of diodes, EBG1 vanishes, while EBG2 is switched to EBG, which is wider and translated towards lower frequencies.

While the proposed structure accomplishes the function of switching EBG's, the diodes are connected in series. A malfunction of one element affects all elements connected behind it. A solution that circumvents this drawback is presented next.

Another solution for the unit cell geometry is presented in Fig. 95. The control elements have been moved to the ground plane and another via has been added between the outer patch and the ground plane. The center of the via has been situated at point (0.85 mm,0). The additional via presents a reactance that changes the EBGs with respect to the previous solution. However, its main role has been to provide a dc path between the outer patch and the ground plane when the control elements are biased. In order to break this dc path for the case when the diodes are not biased, a slot has been placed around the end of the via in the ground plane, having a width of 0.1 mm.

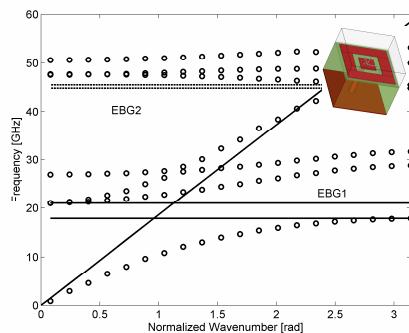


Fig. 93. DD, diodes unbiased. Inset: CAD model.

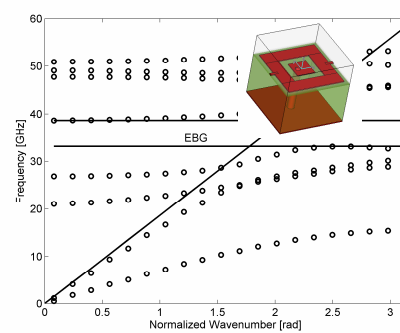


Fig. 94. DD, diodes biased. Inset: CAD model.

The supply voltage has been applied to the outer patches by means of the small rectangular patches represented in Fig. 95 (a). The direction of the supply path is orthogonal to the direction of propagation. This solution allows for a selective switch of the diodes, which provides flexibility for applications. However, simulations have been performed only for the case when all diodes are biased at once.

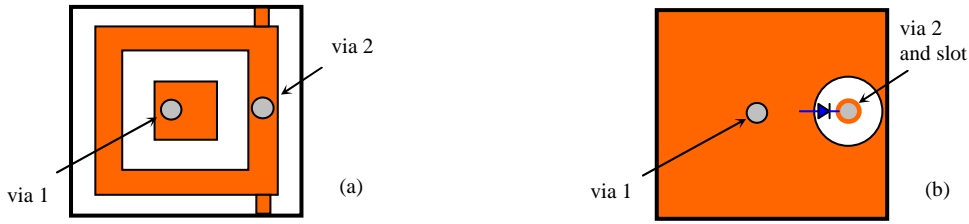


Fig. 95. (a) Unit cell with two vias and slot: top view. (b) Back view.

The DD corresponding to the HIS with unbiased diodes is reported in Fig. 96. As it can be seen from the CAD model represented in the inset of the figure, the ground plane is not connected to the outer patches in this case. The DD shows the existence of three EBGs: the first one, between modes 1 and 2, is very narrow, [17.61; 17.68] GHz, having a width of 0.073 GHz. The second EBG is between modes 2 and 3, [20.65; 24.35] GHz, having a width of 3.71 GHz, while the third one is between [46.08; 47.64] GHz, with a width of 1.56 GHz.

When the diodes are biased, the slots are shorted by metallic prisms in the CAD model, as represented in the inset of Fig. 97. Two EBGs are present. The first one, between modes 1 and 2, [7.96; 11.57] GHz, having a width of 3.61 GHz may be considered to be switched on from the corresponding small EBG of the previous case. The second one, between modes 2 and 3 [17.71; 21.82] GHz, having a width of 4.10 GHz corresponds to the second EBG from the case when diodes are unbiased, but it is wider and translated towards lower frequencies. The third EBG of the previous case is switched off. This behavior is consistent with the results presented above.

The second solution allows for a selective choice of the rows of unit cells that are switched. This might provide flexibility in controlling the positions of the EBGs.

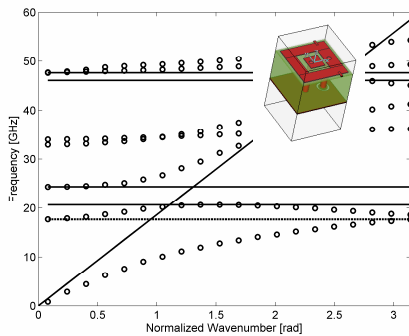


Fig. 96. DD for HIS with slots, diodes unbiased. Inset: CAD model.

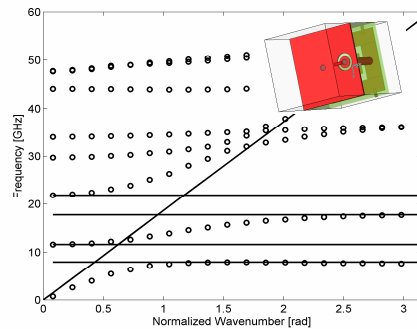


Fig. 97. DD for HIS with slots, diodes biased. Inset: CAD model, back view.

The solutions for switched patterned surfaces we have proposed have potential applications in construction of filters with switched or tunable characteristics and in devising sensors with modifiable sensitivity.

2.3. Magnetic Fluid Bearings

In the period 2001-2003, the calculation of the restoring force in magnetic bearings has been a research interest. The problem arise following development of magnetic fluids applications at UPT: [ant_1990], [ant_1987], [des_1992], [popa_1999], [popa_1997].

The magnetic bearing with poles placed on the stator has been conceived by R. E. Rosensweig [ros_1978]. The restoring force has been investigated analytically, in a plane-parallel approximation of the magnetic field, in [ber_1971], [des_1989]. A numerical approach can be found in [bla_1988].

When the poles are placed on the shaft, the levitation force has been determined analytically, by using again a plane-parallel approximation for the magnetic field, in [01_01_M], [01_05_M], and numerically in [gre_2003].

In [02_01_M], the problem of evaluating the restoring force in a magnetic bearing with poles placed on the stator has been revisited, using a plane-meridian model for the magnetic field. The same approach, i.e. the plane-meridian model, has been used in [03_01_M] for the case when the poles are placed on the shaft.

The reason for calculating the restoring force by two different models has been the necessity of validating the predictions. The results of our studies have shown that the predictions provided by the two models were sufficiently close on the range of parameters where the approximations for both model were holding.

We present here only the part of the work were we have contributed. Therefore, the calculation of the restoring force with a plane-parallel model for the case of poles placed on the stator will be skipped.

A. Rotor with Alternating poles, Plane-Parallel Approximation

We start with the calculation of the force acting on a rotor with alternating poles in a plane-parallel approximation [01_01_M]. The expression of the force can be used for the optimal geometrical design of the bearing, and for gathering information about the influence of various magnetic quantities on the force.

The sketch of the bearing with alternating poles on the rotor is presented in Fig. 1. The displacement between the rotor axis and the stator axis is denoted by Δ . The magnetic liquid is considered as a linear medium of permeability μ_l and it fills the space between the rotor and the stator. In order to obtain information on the dependency of the force that acts on the rotor and the geometrical dimensions of the bearing, we have adopted the model of Fig. 2. The magnetic field is considered to be plane-parallel.

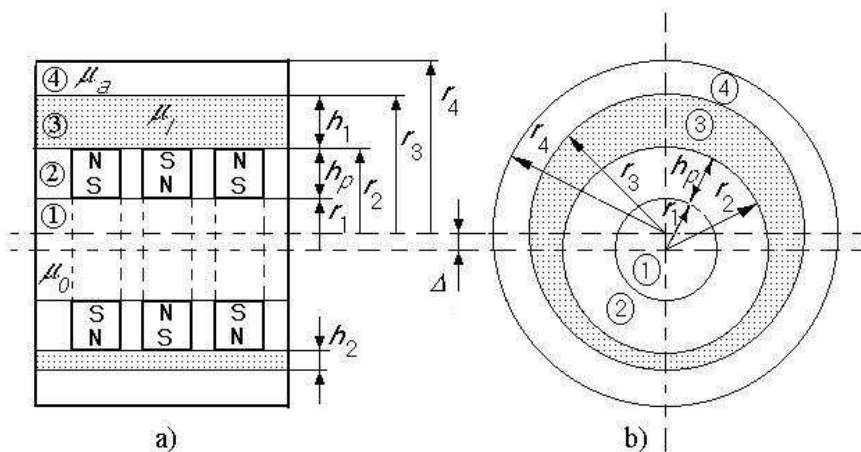


Fig.1 – Bearing with alternating poles on the rotor. a) Cross sectional view; b) top view; 1: rotor; 2: magnetic poles; 3: magnetic fluid; 4: stator.

The permanent magnet is supposed to have a radial permanent magnetization M_p of zero divergence, and of rectangular shape on the surfaces $r = r_2$ and $r = r_1$ (Fig.3b).

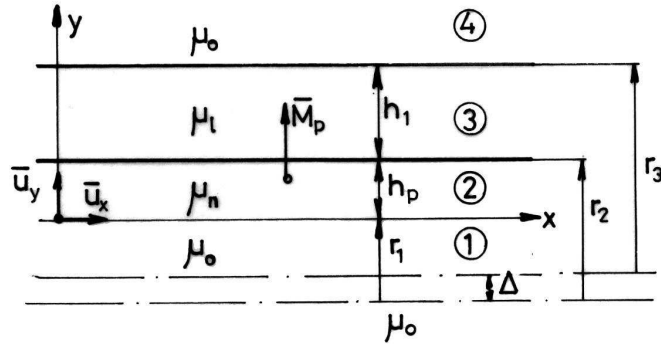


Fig.2 – Mathematical model for the calculation of the magnetic field.

With the notations of Fig.3.a, by taking into account the cylindrical symmetry of the field \mathbf{M}_p and the fact that $\text{div}\mathbf{M}_p = 0$, there results $M_{p2} 2\pi r_2 l_p = M_{p1} 2\pi r_1 l_p$, and

$$M_{p2} = M_{p1} \frac{r_1}{r_2} = M_{p1} \frac{r_1}{r_1 + h_p}, \quad (1)$$

where M_{p2} and M_{p1} are the permanent magnetizations at $r = r_2$ and $r = r_1$.

The amplitude of the fundamental harmonic of M_{p2} is

$$M_{02} = \frac{4}{\lambda} \int_0^{\frac{\lambda}{2}} M_{p2} \sin kx \, dx,$$

where $\lambda = 2l_p + 2l_0$ is the wavelength, and $k = 2\pi/\lambda$ is the wavenumber.

We obtain

$$M_{02} = \frac{4}{\pi} M_{p2} \sin k \frac{l_p}{2}, \quad (2)$$

so that

$$M_2(x) = M_{02} \sin kx. \quad (3)$$

Similarly, on the surface $r = r_1$, the amplitude of the first harmonic of the magnetization is

$$M_{01} = \frac{4}{\pi} M_{p1} \sin k \frac{l_p}{2} = \frac{4}{\pi} \frac{r_1 + h_p}{r_1} M_{p2} \sin k \frac{l_p}{2},$$

and

$$M_1(x) = M_{01} \sin kx. \quad (3')$$

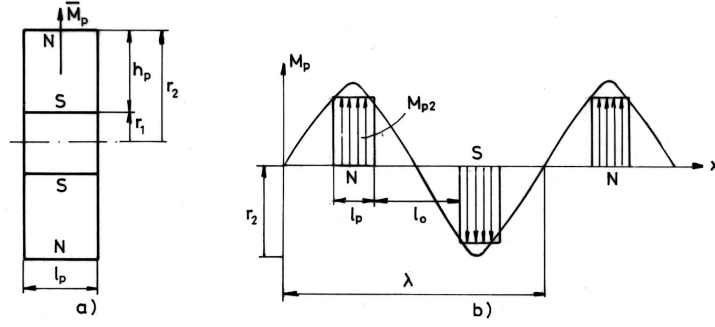


Fig.3 – a) Magnetized permanent magnet in radial direction; b) rectangular shape of the magnetization.

In the four domains of the bearing represented in Fig. 2, the scalar magnetic potential V_H satisfies a Laplace equation: $\nabla^2 V_{Hi} = 0$, $i = \overline{1,4}$ since $\text{div}\mathbf{B} = 0$, $\text{curl}\mathbf{H} = 0$, $\text{div}\mathbf{M}_p = 0$ and $\mathbf{B} = \mu\mathbf{H} + \mu_0\mathbf{M}_p$ in medium 2, $\mathbf{B} = \mu_1\mathbf{H}$ in the magnetic liquid 3, $\mathbf{B} = \mu_0\mathbf{H}$ in media 1 and 4.

The variables separate, and the solution of the Laplace equation takes the form

$$V_{H_i} = (A_1 e^{ky} + A_2 e^{-ky}) (C_1' \sin kx + C_2' \cos kx). \quad (4)$$

In media 1 and 4 the field is attenuated and, by tacking into account the expressions (3) and (3') for \mathbf{M}_p , we shall use solutions of the shape

$$\begin{aligned} V_{H1} &= C_1 e^{ky} \sin kx, & V_{H2} &= (C_2 e^{ky} + C_3 e^{-ky}) \sin kx, \\ V_{H3} &= (C_4 e^{ky} + C_5 e^{-ky}) \sin kx, & V_{H4} &= C_6 e^{-ky} \sin kx. \end{aligned} \quad (5)$$

The integration constants will be determined from interface conditions on the surfaces S_{12} ($y = 0$), S_{23} ($y_1 = h_p$), S_{34} ($y_2 = h_p + h_1$): continuity of potentials and normal components of the magnetic induction. We have

$$\begin{aligned} \text{on } S_{12} : & \begin{cases} (V_{H1})_{y=0} = (V_{H2})_{y=0}, \\ \left(\frac{\partial V_{H1}}{\partial y} \right)_{y=0} - \mu_{r_m} \left(\frac{\partial V_{H2}}{\partial y} \right)_{y=0} = -M_1; \end{cases} \\ \text{on } S_{23} : & \begin{cases} (V_{H2})_{y=y_1} = (V_{H3})_{y=y_1}, \\ \mu_{r_m} \left(\frac{\partial V_{H2}}{\partial y} \right)_{y=y_1} - \mu_{r_l} \left(\frac{\partial V_{H3}}{\partial y} \right)_{y=y_1} = M_2; \end{cases} \\ \text{on } S_{34} : & \begin{cases} (V_{H3})_{y=y_2} = (V_{H4})_{y=y_2}, \\ \mu_{r_l} \left(\frac{\partial V_{H3}}{\partial y} \right)_{y=y_2} = \left(\frac{\partial V_{H4}}{\partial y} \right)_{y=y_2}. \end{cases} \end{aligned}$$

With (5) we obtain

$$\begin{aligned} C_1 &= C_2 + C_3, & C_1 - \mu_{r_m} (C_2 - C_3) &= -m_1, \\ C_2 \varepsilon_1^2 + C_3 &= C_4 \varepsilon_1^2 + C_5, \\ \mu_{r_m} (C_2 \varepsilon_1^2 - C_3) - \mu_{r_l} (C_4 \varepsilon_1^2 - C_5) &= m_2 \varepsilon_1, \\ C_4 \varepsilon_2^2 + C_5 &= C_6, & \mu_{r_l} (C_4 \varepsilon_2^2 - C_5) &= -C_6, \end{aligned} \quad (6)$$

where we have denoted $\varepsilon_1 = e^{kh_p}$, $\varepsilon_2 = \varepsilon_1 e^{kh_1}$, $m_1 = \frac{M_{01}}{k}$ and $m_2 = \frac{M_{02}}{k}$.

For magnets that do not polarize temporarily ($\mu_{r_m} = 1$), the constants are

$$C_2 = \frac{(\varepsilon_2^2 - \varepsilon_1^2) \left[m_1 (1 - \mu_{r_i}^2) - 2m_2 \varepsilon_1 \right] - 2m_2 \varepsilon_1 \mu_{r_i} (\varepsilon_2^2 + \varepsilon_1^2)}{2\varepsilon_1^4 (\mu_{r_i} - 1)^2 - 2\varepsilon_1^2 \varepsilon_2^2 (\mu_{r_i} + 1)^2}, \quad (7)$$

$$C_3 = -\frac{m_1}{2}, \quad C_1 = C_2 + C_3,$$

$$C_4 = \frac{(\mu_{r_i} - 1)(m_1 - m_2 \varepsilon_1)}{\varepsilon_1^2 (\mu_{r_i} - 1)^2 - \varepsilon_2^2 (\mu_{r_i} + 1)^2}, \quad C_5 = \frac{\varepsilon_2^2 (\mu_{r_i} + 1)}{\mu_{r_i} - 1} C_4.$$

We can calculate now the field intensities

$$\begin{aligned} \bar{\mathbf{H}}_1 &= -\nabla V_{H1} = -k C_1 e^{ky} (\cos kx \bar{\mathbf{u}}_x + \sin kx \bar{\mathbf{u}}_y), \\ \bar{\mathbf{H}}_2 &= -\nabla V_{H2} = -k (C_2 e^{ky} + C_3 e^{-ky}) \cos kx \bar{\mathbf{u}}_x - \\ &\quad -k (C_2 e^{ky} - C_3 e^{-ky}) \sin kx \bar{\mathbf{u}}_y, \\ \bar{\mathbf{H}}_3 &= -\nabla V_{H3} = -k (C_4 e^{ky} + C_5 e^{-ky}) \cos kx \bar{\mathbf{u}}_x - \\ &\quad -k (C_4 e^{ky} - C_5 e^{-ky}) \sin kx \bar{\mathbf{u}}_y, \\ \bar{\mathbf{H}}_4 &= -\nabla V_{H4} = -k C_6 e^{-ky} (\cos kx \bar{\mathbf{u}}_x - \sin kx \bar{\mathbf{u}}_y). \end{aligned} \quad (8)$$

At equilibrium, the force that acts on the rotor is opposed to the force that acts on the stator, and has the expression [ros_1978]

$$\bar{\mathbf{F}} = -\mu_0 \oint_{\Sigma_0} \left[\frac{M_n^2}{2} + \int_0^H M dH \right] \bar{d}\mathbf{S}, \quad (9)$$

where Σ_0 is the interface surface between the magnetic fluid and the rotor, and $\bar{d}\mathbf{S} = dS \bar{\mathbf{n}}_{34}$ is the surface unit vector oriented outwards the magnetic fluid, Fig.4.

If the magnetic fluid is linear, of susceptibility χ_{ml} , we have

$$\int_0^H M dH = \chi_{m_i} \frac{H^2}{2} = (\mu_{r_i} - 1) \frac{H^2}{2}, \quad M_n^2 = (\mu_{r_i} - 1)^2 H_n^2,$$

and the integrand in (9) becomes

$$\frac{M_n^2}{2} + \int_0^H M dH = \frac{(\mu_{r_i} - 1)^2}{2} H_n^2 + \frac{(\mu_{r_i} - 1)}{2} (H_n^2 + H_t^2) = \frac{(\mu_{r_i} - 1)}{2} (\mu_{r_i} H_n^2 + H_t^2).$$

As a consequence, the force (9) that acts on the rotor can be written

$$\bar{\mathbf{F}} = -\mu_0 \frac{(\mu_{r_i} - 1)}{2} \oint_{\Sigma_0} (\mu_{r_i} H_n^2 + H_t^2) \bar{d}\mathbf{S} = \oint_{\Sigma_0} \bar{t}_{n_{34}} \bar{d}\mathbf{S},$$

wherefrom the normal strain results:

$$\bar{t}_{n_{34}} = -\mu_0 \frac{(\mu_{r_i} - 1)}{2} (\mu_{r_i} H_n^2 + H_t^2) \bar{\mathbf{u}}_y. \quad (10)$$

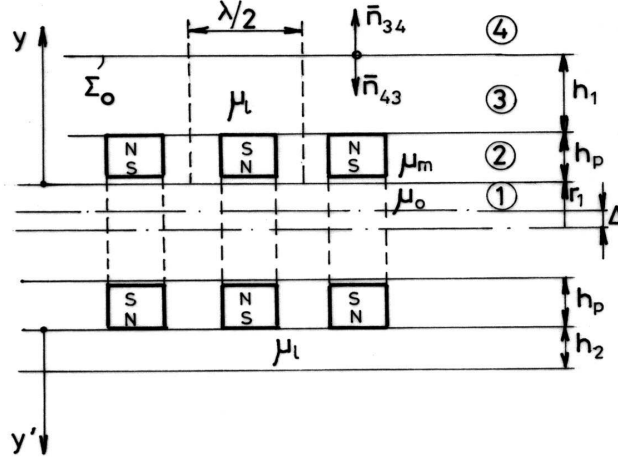


Fig. 4 – Definition of integration surface and normal, unit vectors.

We shall calculate the force that acts on a length of $\lambda/2$, Fig.4. As $\bar{\mathbf{t}}_{n_{34}}(y_2) = t_n(y_2)\bar{\mathbf{u}}_y$, and on the symmetric face $\bar{\mathbf{t}}_{n_{34}}(y'_2) = t_n(y'_2)(-\bar{\mathbf{u}}_y)$, we obtain the resulting tension

$$\bar{\mathbf{t}}_n = \bar{\mathbf{t}}_{n_{34}}(y_2) + \bar{\mathbf{t}}_{n_{34}}(y'_2) = [t_n(y_2) - t_n(y'_2)]\bar{\mathbf{u}}_y, \quad (11)$$

where $y_2 = h_p + h_1$ and $y'_2 = h_p + h_2$, Fig.4. By using (10), there results

$$\bar{\mathbf{t}}_n = -\mu_0 \frac{\mu_{r_i} - 1}{2} [\mu_{r_i} (H_{3y}^2 - H_{3y'}^2) + (H_{3x}^2 - H_{3x'}^2)] \bar{\mathbf{u}}_y, \quad (12)$$

where the unprimed components refer to the surface y_2 , the primed components refer to the surface y'_2 , and all the components are associated to points from the fluid (medium 3).

With (8) we have

$$\begin{aligned} H_{3y} &= -k(C_4 e^{ky_2} - C_5 e^{-ky_2}) \sin kx, & H_{3y'} &= -k(C'_4 e^{ky'_2} - C'_5 e^{-ky'_2}) \sin kx, \\ H_{3x} &= -k(C_4 e^{ky_2} + C_5 e^{-ky_2}) \cos kx, & H_{3x'} &= -k(C'_4 e^{ky'_2} + C'_5 e^{-ky'_2}) \cos kx, \end{aligned}$$

where C'_4 and C'_5 have the values (4) with ε_1 and ε_2 substituted with $\varepsilon'_1 = \varepsilon_1$ and $\varepsilon'_2 = e^{k(h_p+h_2)} = \varepsilon_1 e^{kh_2}$ respectively.

There results

$$\begin{aligned} H_{3y}^2 - H_{3y'}^2 &= k^2 \left[C_4^2 e^{2ky_2} - C_4'^2 e^{2ky'_2} + C_5^2 e^{-2ky_2} - \right. \\ &\quad \left. - C_5'^2 e^{-2ky'_2} - 2(C_4 C_5 - C_4' C_5') \right] \sin^2 kx, \\ H_{3x}^2 - H_{3x'}^2 &= k^2 \left[C_4^2 e^{2ky_2} - C_4'^2 e^{2ky'_2} + C_5^2 e^{-2ky_2} - \right. \\ &\quad \left. - C_5'^2 e^{-2ky'_2} + 2(C_4 C_5 - C_4' C_5') \right] \cos^2 kx. \end{aligned}$$

After integration, the force on a length of $\lambda/2$ becomes

$$\begin{aligned} \bar{\mathbf{F}}_{\lambda/2} &= -\mu_0 \frac{\mu_{r_i} - 1}{2} k^2 \frac{\lambda}{4} \left\{ (\mu_{r_i} + 1) (C_4^2 e^{2ky_2} - C_4'^2 e^{2ky'_2} + C_5^2 e^{-2ky_2} - \right. \\ &\quad \left. - C_5'^2 e^{-2ky'_2}) - 2(\mu_{r_i} - 1) (C_4 C_5 - C_4' C_5') \right\} \bar{\mathbf{u}}_y, \end{aligned} \quad (13)$$

where we have used $\int_0^{\lambda/2} \sin^2 x \, dx = \int_0^{\lambda/2} \cos^2 x \, dx = \frac{\lambda}{4}$.

The following first order geometrical approximations hold, Fig.5:

$h_1 = \delta + \Delta \sin \theta$, $h_2 = \delta - \Delta \sin \theta$, where Δ is the displacement, and $\delta = r_3 - r_2$; there results $h_1 - h_2 = 2\Delta \sin \theta = 2\Delta'$, with $\Delta' = \Delta \sin \theta$, and, since $h_1 = h_2 - 2\Delta'$, we have $y'_2 = h_p + h_2 = h_p + h_1 - 2\Delta' = y_2 - 2\Delta'$.

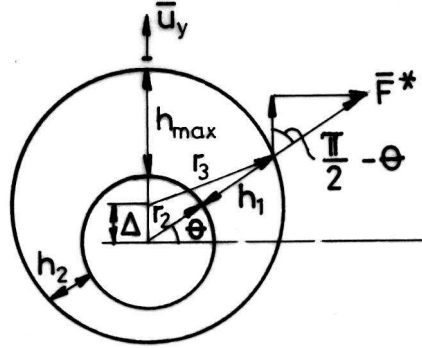


Fig.5 – Geometrical parameters definition.

By substituting y'_2 in (13) we obtain

$$\begin{aligned} \bar{\mathbf{F}}_{\lambda/2} = & -\mu_0 \frac{\mu_{rl} - 1}{2} k^2 \frac{\lambda}{4} \left\{ (\mu_{rl} + 1) \left[e^{2ky_2} (C_4^2 - C_4'^2 e^{-4k\Delta'}) + \right. \right. \\ & \left. \left. + e^{-2ky_2} (C_5^2 - C_5'^2 e^{4k\Delta'}) \right] - 2(\mu_{rl} - 1)(C_4 C_5 - C_4' C_5') \right\} \bar{\mathbf{u}}_y. \end{aligned} \quad (14)$$

For the constant C_4 in (7) we shall use the approximation

$$C_4 = \frac{(\mu_{rl} - 1)(m_1 - m_2 \varepsilon_1)}{\varepsilon_1^2 (\mu_{rl} - 1)^2 - \varepsilon_2^2 (\mu_{rl} + 1)^2} \cong -\frac{(\mu_{rl} - 1)(m_1 - m_2 \varepsilon_1)}{\varepsilon_2^2 (\mu_{rl} + 1)^2}. \quad (15)$$

There follows

$$C_4' \cong C_4 e^{4k\Delta'}, C_5 \cong C_5' \cong -\frac{m_1 - m_2 \varepsilon_1}{\mu_{rl} + 1}. \quad (16)$$

After the substitution of these values into (14) we have

$$\bar{\mathbf{F}}_{\lambda/2} \cong \frac{2\mu_0 \mu_{rl} (\mu_{rl} - 1)}{(\mu_{rl} + 1)^3} (m_1 - m_2 \varepsilon_1)^2 e^{-2k(h_p + \delta)} k^2 \frac{\lambda}{2} \sinh(2k\Delta') \bar{\mathbf{u}}_y. \quad (17)$$

We shall calculate now the force $\bar{\mathbf{F}}^*$ that acts on the unit length of the rotor in order to reduce the displacement, by integrating (17) in the direction of h_{max} , whose orientation is defined by $\bar{\mathbf{u}}$, Fig.5

$$\begin{aligned} \bar{\mathbf{F}}^* = & \frac{2}{\lambda} \bar{\mathbf{u}} \int_0^\pi F_{\lambda/2} \sin \theta r_3 d\theta = \\ = & 2\mu_0 \frac{\mu_{rl} (\mu_{rl} - 1) k^2 (m_1 - m_2 e^{kh_p})^2 r_3}{(\mu_{rl} + 1)^3} e^{-2k(h_p + \delta)} \bar{\mathbf{u}} \cdot \int_0^\pi \sinh(2k\Delta \sin \theta) \sin \theta d\theta. \end{aligned} \quad (18)$$

The series expansion of the integrand yields

$$\begin{aligned} \bar{\mathbf{F}}^* = & 2\mu_0 \frac{\mu_{rl} (\mu_{rl} - 1) k^2 (m_1 - m_2 e^{kh_p})^2 r_3}{(\mu_{rl} + 1)^3} e^{-2k(h_p + \delta)} \cdot \\ & \left[\sum_{i=1}^{\infty} (2k\Delta)^{2i-1} \int_0^\pi \frac{\sin^{2i} \theta}{(2i-1)!} d\theta \right] \bar{\mathbf{u}} \end{aligned} \quad (19)$$

If we denote by I_{2i} the integral under the summation, and integrate by parts, we get $I_{2i} = \frac{2i-1}{2i} I_{2i-2}$ and as $I_0 = \pi$, we obtain $I_{2i} = \pi \frac{(2i-1)!}{2^i i!}$. After substitution and rearrangement of terms (19) becomes

$$\bar{\mathbf{F}}^* = 2\pi\mu_0 \frac{\mu_{rl}(\mu_{rl}-1)k^2(m_1 - m_2 e^{kh_p})^2 r_3}{(\mu_{rl}+1)^3} e^{-2k(h_p+\delta)} \sum_{i=1}^{\infty} \frac{(k\Delta)^{2i-1}}{i!(i-1)!} \bar{\mathbf{u}}. \quad (20)$$

We shall restrict ourselves to the first two terms of the series, consider the maximal displacement $\Delta = \delta$, and substitute m_1 and m_2 . We get, for the resulting force, the expression

$$\bar{F}^* = M_{01}^2 2\pi\mu_0 \frac{\mu_{rl}(\mu_{rl}-1)k^2 r_3}{(\mu_{rl}+1)^3} \left(1 - \frac{r_1}{r_2} e^{kh_p}\right)^2 \cdot e^{-2k(h_p+\delta)} \left[k\delta + \frac{(k\delta)^3}{2} \right] \bar{\mathbf{u}}. \quad (21)$$

By denoting $h_p = \alpha\delta$, we have $r_2 = r_1 + \alpha\delta$. The substitution of M_{01} from (3') yields

$$\bar{\mathbf{F}}^* = \frac{32\mu_0 M_{p1}^2}{\pi} \frac{\mu_{rl}(\mu_{rl}-1)k^2}{(\mu_{rl}+1)^3} U(k, \alpha) \bar{\mathbf{u}}, \quad (22)$$

where

$$U(k, \alpha) = \left(e^{-k\alpha\delta} - \frac{r_1}{r_1 + \alpha\delta} \right)^2 [r_1 + (\alpha+1)\delta] \left[k\delta + \frac{(k\delta)^3}{2} \right] e^{-2k\delta} \sin^2 \frac{kl_p}{2}. \quad (23)$$

It follows from (22) and (23) that the force on the unit length of the rotor, at maximum displacement, depends on the geometrical dimensions of the system, on the square of the permanent magnetization, and on the permeability of the fluid.

For $l_0 = l_p/2$, we have $l_p = \lambda/3$ and $\sin \frac{kl_p}{2} = \frac{\sqrt{3}}{2}$, and (23) becomes

$$U(k, \alpha) = \frac{3}{4} \left(e^{-k\alpha\delta} - \frac{r_1}{r_1 + \alpha\delta} \right)^2 [r_1 + (\alpha+1)\delta] \left[k\delta + \frac{(k\delta)^3}{2} \right] e^{-2k\delta}. \quad (24)$$

As an example, in order to find optimal dimensions for the permanent magnet in Fig. 1, we have represented U from (24) as a function of k and α , for $r_1 = 1$ cm, and $\delta = 0.1$ cm. As shown in Fig. 6, the maximum is $U = 0.1115$ cm, and it occurs for $k = 9.74$ rad/cm and $\alpha = 3.57$. If $r_1 = 5$ cm, $\delta = 0.1$ cm, the maximum occurs at $k = 7.929$ rad/cm, $\alpha = 5.754$ and its value is $U = 0.7137$ cm.

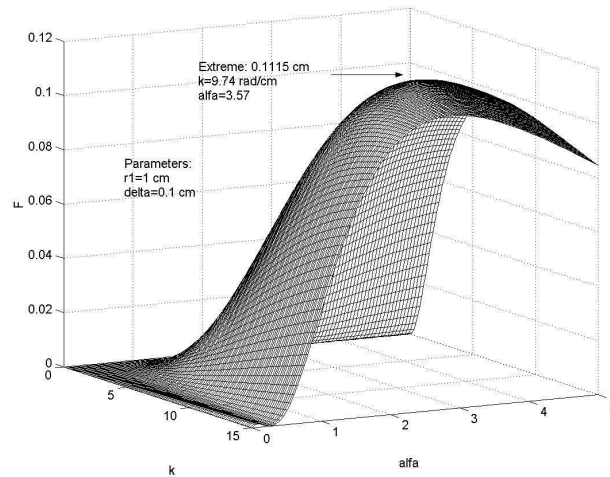


Fig.6 – The function U .

B. Poles on the Stator, Plane-Meridian Model

The purpose of this work has been to obtain values of the restoring force when a plane-meridian model is used for approximating the magnetic field [02_01_M]. The results have been compared to those obtained with the plane-parallel model.

The plane-meridian approximation is physically better than the plane-parallel one. However, numerical evaluation of integrals must be done in the final expression of the restoring force. Consequently, our results are presented in a graphical form.

The geometrical configuration of the bearing is represented in Fig. 7. Region 1 corresponds to the shaft, built of a non-magnetic material, the magnetic fluid, of relative permeability μ_l , is situated in Region 2, and the permanent, ring shaped magnets are situated in Region 3. We admit the simplifying assumptions that the bearing is very long, and the exterior poles of the permanent magnets have no influence on the field within the magnetic liquid. Furthermore, the permanent magnets do not magnetize temporarily, their relative permeability is $\mu_m = 1$, so that the restoring force is strongest, and the permanent magnetization is in a radial direction $\mathbf{M}_p = M_p \mathbf{u}_\rho$, with a square shaped spatial variation, of spatial period λ . We shall consider only the first harmonic of the magnetization in the form

$$\mathbf{M}_p = \frac{M_m}{\rho} \sin(kz) \mathbf{u}_\rho, \quad k = \frac{2\pi}{\lambda} \quad (25)$$

We have selected the above form for \mathbf{M}_p in order to have a solenoidal field $\nabla \cdot \mathbf{M}_p = 0$.

First, we calculate the magnetic field intensity in region 2. Due to the cylindrical symmetry, the field has a radial symmetry in every plane perpendicular to the axis of the shaft. Next, we calculate the restoring force that acts on the unit length of the shaft when it is displaced (Fig. 8). For this purpose we apply the plane-meridian approximation, by admitting that, at every point from the surface of the shaft, the magnetic field corresponds to a non-displaced shaft, having a radius larger (or smaller) than the true one with the value of the displacement in the direction of the point with respect to the shaft axis.

Finally, we present in a graphical form the variation of the restoring force as a function of various parameters.

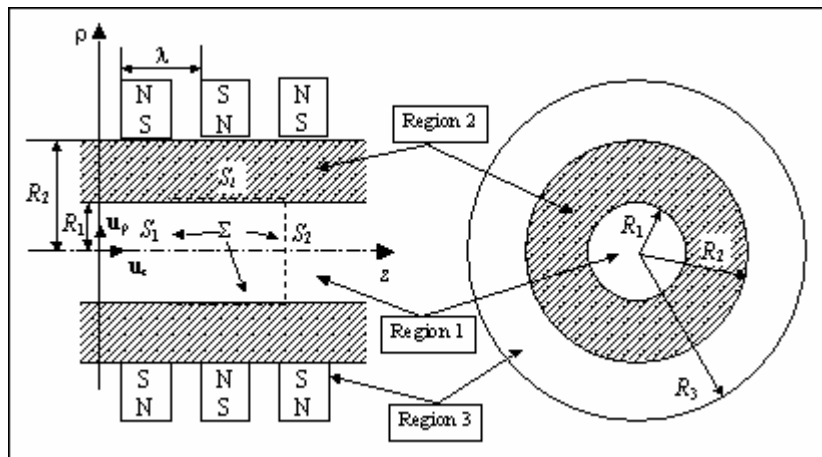


Fig. 7. Geometry of the bearing. Region 1: shaft; region 2: magnetic liquid; region 3: cylindrical magnets.

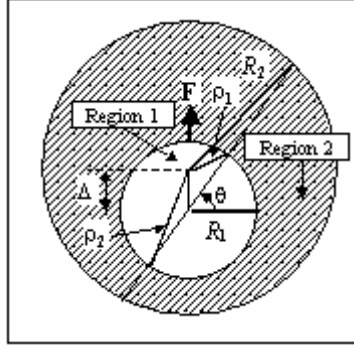


Fig. 8. Displacement Δ of the shaft and the restoring force.

The equations that govern the magnetic fields in the three regions of Fig. 1 are $\mathbf{B}_1 = \mu_0 \mathbf{H}_1$, $\mathbf{B}_2 = \mu_0 \mu_l \mathbf{H}_2$, $\mathbf{B}_3 = \mu_0 (\mathbf{H}_3 + \mathbf{M}_p)$, $\nabla \times \mathbf{H}_i = 0, \nabla \cdot \mathbf{B}_i = 0, i = 1..3$. There follows that the \mathbf{H}_i are potential fields $\mathbf{H}_i = -\nabla V_{Hi}$, and the field potentials satisfy the Laplace equations $\nabla^2 V_{Hi} = 0, i = 1..3$. The interface conditions on the separation surfaces $[S_{ij}]$ between Regions i and j , which result from $\nabla_S \times \mathbf{H} = 0, \nabla_S \cdot \mathbf{B} = 0$, are

$$[S_{12}]: (V_{H1})_{R_1} = (V_{H2})_{R_1}; \quad \left(\frac{\partial V_{H1}}{\partial \rho} \right)_{R_1} = \mu_l \left(\frac{\partial V_{H2}}{\partial \rho} \right)_{R_1}; \quad (26)$$

$$[S_{23}]: (V_{H1})_{R_2} = (V_{H3})_{R_2}; \quad -\mu_l \left(\frac{\partial V_{H2}}{\partial \rho} \right)_{R_2} + \left(\frac{\partial V_{H3}}{\partial \rho} \right)_{R_2} = M \sin(kz),$$

$$M = \frac{M_m}{R_2}.$$

In the cylindrical coordinates (ρ, θ, z) , the Laplace equation independent of θ reads $\nabla^2 V_H = \frac{1}{\rho} \frac{\partial V_H}{\partial \rho} + \frac{\partial^2 V_H}{\partial \rho^2} + \frac{\partial^2 V_H}{\partial z^2} = 0$. After substitution, division with RZ , and separation, one obtains the equations $\frac{1}{\rho} \frac{dR}{d\rho} + \frac{d^2 R}{d\rho^2} = \pm n^2 R$ and $\frac{d^2 Z}{dz^2} = \mp n^2 Z$, where n is a constant to be determined later. The change of variable $x = n\rho$ in the first equation turns it in a modified Bessel equation: $\frac{d^2 R}{dx^2} + \frac{1}{x} \frac{dR}{dx} - R = 0$, with the general solution $R(x) = A_1 I_0(x) + A_2 K_0(x)$, where I_n and K_n are the modified Bessel functions of the first and second kind respectively, and of order n . The second equation has the general solution $Z = C_1 \cos(nz) + C_2 \sin(nz)$. The separation of variables can be applied by putting $V_H = R(\rho)Z(z)$.

By taking into account the interface conditions (26) and the fact that $K_0(x)$ decreases exponentially with x , and it has an infinite value at $x=0$, we shall try solutions of the form:

$$\begin{aligned} V_{H1} &= A I_0(x) \sin(nz), \\ V_{H2} &= [C_1 I_0(x) + C_2 K_0(x)] \sin(nz), \\ V_{H3} &= D K_0(x) \sin(nz). \end{aligned} \quad (27)$$

After imposing the interface conditions (26) and by taking into account that $I_0'(x) = I_1(x)$ and $K_0'(x) = -K_1'(x)$ [abr_1964] we obtain:

$$[S_{12}]: \begin{cases} AI_0(nR_1) = C_1 I_0(nR_1) + C_2 K_0(nR_1) \\ AnI_1(nR_1) = \mu_l [C_1 nI_1(nR_1) - C_2 nK_1(nR_1)], \end{cases}$$

$$[S_{23}]: \begin{cases} C_1 I_0(nR_2) + C_2 K_0(nR_2) = DK_0(nR_2) \\ -\{\mu_l [C_1 nI_1(nR_2) - C_2 nK_1(nR_2)] - DnK_1(nR_2)\} \sin(nz) = M \sin(kz) \end{cases}$$

The last equation implies $n = k$. For the determination of the constants, the following linear system of equations results:

$$\begin{cases} AI_{01} = C_1 I_{01} + C_2 K_{01} \\ AI_{11} = \mu_l [C_1 I_{11} - C_2 K_{11}] \\ DK_{02} = C_1 I_{02} + C_2 K_{02} \\ \mu_l [-C_1 I_{12} + C_2 K_{12}] - DK_{12} = \frac{M}{k} \end{cases} \quad (28)$$

where we have used the notations

$$I_{mn} = I_m(kR_n), \quad K_{mn} = K_m(kR_n) \quad (29)$$

The solutions of (4) are

$$\begin{aligned} C_1 &= \frac{M(\mu_l I_{01} K_{11} + I_{11} K_{01}) K_{02}}{kN} \\ C_2 &= \frac{M(\mu_l - 1) I_{01} I_{11} K_{02}}{kN} \\ A &= \frac{M \mu_l K_{02} (I_{01} K_{11} + I_{11} K_{01})}{kN} \\ D &= \frac{M [I_{02} (\mu_l I_{01} K_{11} + I_{11} K_{01}) + (\mu_l - 1) I_{01} I_{11} K_{02}]}{kN} \\ N &= (\mu_l - 1)^2 I_{01} I_{11} K_{02} K_{12} - (\mu_l I_{01} K_{11} + I_{11} K_{01}) \cdot \\ &\quad \cdot (\mu_l I_{12} K_{02} + I_{02} K_{12}). \end{aligned} \quad (30)$$

Next, we are interested in the magnetic field intensity in Region 2. From (27) and the above consequences there results

$$\begin{aligned} \mathbf{H}_2 &= -\nabla V_{H2} = -\frac{\partial V_{H2}}{\partial \rho} \mathbf{u}_\rho - \frac{\partial V_{H2}}{\partial z} \mathbf{u}_z = \\ &= -[C_1 k I_0'(k\rho) + C_2 k K_0'(k\rho)] \sin(kz) \mathbf{u}_\rho - \\ &\quad - [k C_1 I_0(k\rho) + k C_2 K_0(k\rho)] \cos(kz) \mathbf{u}_z = \\ &= -k [C_1 I_1(k\rho) - C_2 K_1(k\rho)] \sin(kz) \mathbf{u}_\rho - \\ &\quad - k [C_1 I_0(k\rho) + C_2 K_0(k\rho)] \cos(kz) \mathbf{u}_z. \end{aligned} \quad (31)$$

The force that acts on a cylindrical region of side surface $\Sigma = S_l \cup S_1 \cup S_2$ (Fig. 7) is

$$\mathbf{F} = \mu_0 \left[\oint_{\Sigma} \left(\frac{M_n^2}{2} + \int_0^H M dH \right) \mathbf{n} ds \right] \quad (32)$$

where M_n is the normal component of the magnetization, and \mathbf{n} is the normal unit vector directed towards the interior of the surface Σ . Since the liquid is linear, for reasons of symmetry, the integrals over the side faces S_1 and S_2 cancel each other. The expression of the restoring force becomes

$$\mathbf{F} = \mu_0 \frac{\mu_l - 1}{2} \int_{S_l} (\mu_l H_\rho^2 + H_z^2) \mathbf{n} ds, \quad \mathbf{H} = \mathbf{H}_2$$

It follows that the magnetic liquid acts on the shaft with a pressure:

$$p = \mu_0 \frac{\mu_l - 1}{2} (\mu_l H_\rho^2 + H_z^2), \quad \rho \in S_l, \quad \mathbf{H} = \mathbf{H}_2. \quad (33)$$

The substitution of the calculated intensities yields

$$\begin{aligned} p &= \frac{\mu_0 \mu_l (\mu_l - 1)}{2} k^2 [C_1 I_1(k\rho) - C_2 K_1(k\rho)]^2 \sin^2(kz) + \\ &+ \frac{\mu_0 (\mu_l - 1)}{2} k^2 [C_1 I_0(k\rho) + C_2 K_0(k\rho)]^2 \cos^2(kz), \\ \rho &\in S_l. \end{aligned} \quad (34)$$

We are interested in the average pressure \tilde{p} on a spatial period. By taking into account that

$$\frac{1}{\lambda} \int_0^\lambda \sin^2(kz) dz = \frac{1}{\lambda} \int_0^\lambda \cos^2(kz) dz = \frac{1}{2}, \text{ there results}$$

$$\begin{aligned} \tilde{p} &= \frac{1}{\lambda} \int_0^\lambda p dz = \frac{\mu_0 \mu_l (\mu_l - 1)}{4} k^2 [C_1 I_1(k\rho) - C_2 K_1(k\rho)]^2 + \\ &+ \frac{\mu_0 (\mu_l - 1)}{2} k^2 [C_1 I_0(k\rho) + C_2 K_0(k\rho)]^2. \end{aligned} \quad (35)$$

Consider two points on the shaft, situated in a plane perpendicular on its axis, and opposed on a certain diameter, as in Fig. 8. In order to apply the plane-meridian approximation in the way we have defined it above, we consider that the average pressure \tilde{p}_{12} , in a direction given by an angle θ , can be obtained by taking the difference between the values that result by substituting in (35) first $\rho = \rho_2$, and then $\rho = \rho_1$. For a given displacement Δ , the average pressure is function only of the angle θ , since, from simple geometrical arguments, we have:

$$\begin{aligned} \rho_1^2 &= \Delta^2 + R_1^2 - 2\Delta R_1 \sin \theta, \\ \rho_2^2 &= \Delta^2 + R_1^2 + 2\Delta R_1 \sin \theta. \end{aligned} \quad (36)$$

If the shaft displacement Δ is small, $\Delta \ll R_1$, then the following first order geometrical approximations can be used:

$$\begin{aligned} \rho_1 &\cong R_1 - \Delta \sin \theta, \\ \rho_2 &\cong R_1 + \Delta \sin \theta. \end{aligned} \quad (37)$$

We obtain the following expression for the average pressure:

$$\begin{aligned} \tilde{p}_{12}(\theta) &= \\ &= P \left\{ [C_1 I_1(k\rho_2) - C_2 K_1(k\rho_2)]^2 - [C_1 I_1(k\rho_1) - C_2 K_1(k\rho_1)]^2 \right\} + \\ &+ \left\{ Q [C_1 I_0(k\rho_2) + C_2 K_0(k\rho_2)]^2 - [C_1 I_0(k\rho_1) + C_2 K_0(k\rho_1)]^2 \right\}, \\ P &= \frac{\mu_0 \mu_l (\mu_l - 1)}{4} k^2, \quad Q = \frac{P}{\mu_l}. \end{aligned} \quad (38)$$

By considering the geometrical symmetry, the average restoring force on the unit length of the shaft that acts in the opposite direction of the displacement can be calculated from

$$F = 2R_1 \int_0^{\pi/2} \tilde{p}_{12}(\theta) \sin \theta d\theta \quad (39)$$

The analytical evaluation of (39) requires integration of squares and products of modified Bessel functions. We present next the results of a numerical evaluation of (39). The numeric approach is facilitated by the fact that modified Bessel functions are smooth.

We have represented in Fig. 9 the restoring force as a function of the displacement Δ of the shaft with respect to the axis of the bearing. The parameter is the permeability of the magnetic liquid, and the chosen geometrical dimensions and magnetization are relevant in a practical situation. Note that the plane-meridian model predicts an increase of the force with the displacement.

The restoring force as a function of the maximum displacement $\delta = R_2 - R_1$ and the spatial period of the permanents magnets λ is represented in Fig. 10. The other parameters are those of Fig. 9. It can be seen that the surface is smooth and flat in the considered range of geometrical dimensions. These features are favorable for the stability of the optimal design (in view of a maximum restoring force). In the considered case, the maximum force $F \cong 2 \text{ N/cm}$ occurs for $\delta \cong 0.06 \text{ cm}$ and $\lambda \cong 0.5 \text{ cm}$.

In Fig. 11, the optimal spatial wavelength that ensures a maximum force, for a previously chosen value of the maximum displacement, is represented. The other constructive parameters are listed again for convenience.

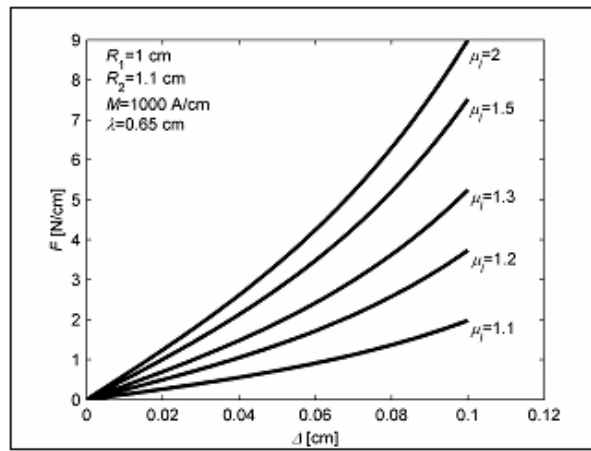


Fig. 9. Restoring force as function of the displacement.

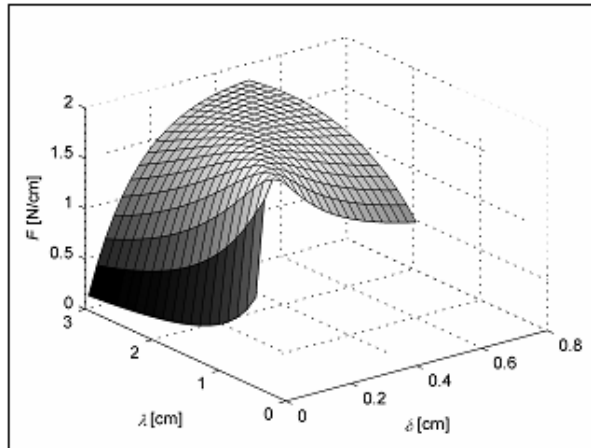


Fig. 10. Restoring force as function of the maximum displacement and the wavelength for $R_1=1 \text{ cm}$, $M=1000 \text{ A/cm}$, $\mu_l=1.1$.

Figs. 12 and 13 correspond to Figs. 9 and 10, but are derived from the plane-parallel model of the magnetic field [des_1989]. The expression of the restoring force in the cited reference is

$$F = \frac{\mu_0 (\mu_l^2 - 1) M^2 R_1 \pi}{2(\mu_l + \mu_m)} \exp(-2k\Delta) I_1(2k\Delta) \quad (40)$$

where μ_m is the relative permeability of the permanent magnet, a value that we shall take equal to 1 (in fact, the modified Bessel function I_1 appears in its series representation in the cited reference). Since

the first order geometric approximations (37) have been used in deriving (40), we had to restrict ourselves to a smaller range for δ in the calculations. The rest of the parameters are identical, in order to facilitate the comparison, although M has a different meaning in the two models.

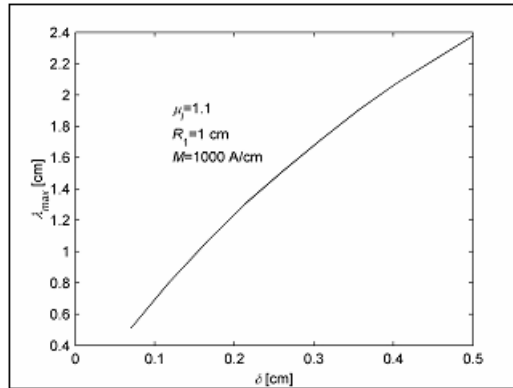


Fig. 11. Optimum value of the wavelength as function of the maximum displacement.

The magnitude of the force in Fig. 12 is remarkably close to the one in Fig. 9. The shape of the curve is different: the plane-parallel model predicts a maximum of the force for a value slightly smaller than δ since, at $\delta = \Delta$, when at the contact line between the shaft and the bearing there exists no magnetic liquid, the plane-parallel model cannot be applied.

Fig. 13 cannot be directly compared to Fig. 10, since the ranges of δ are different in the two situations. One can notice however that the optimum design is also stable in the case of the plane-parallel model.

In Fig. 14, the optimum wavelength as a function of the maximum displacement δ , predicted by the two models, for the same range of δ is represented. The coincidence of the shapes of the two curves, as well as of the order of magnitude (within 10..12%) can be observed. The almost linear dependence between λ_{max} and δ simplifies the design of the bearing.

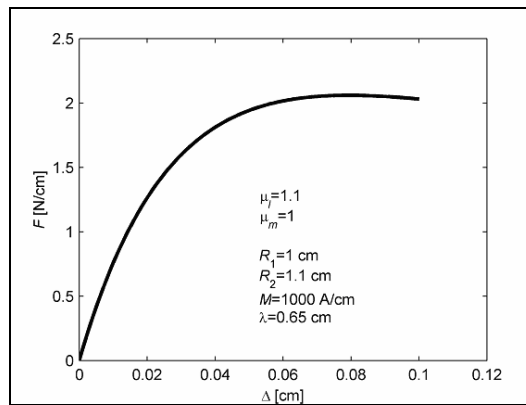


Fig. 12. Force as a function of the displacement in the plane-parallel model.

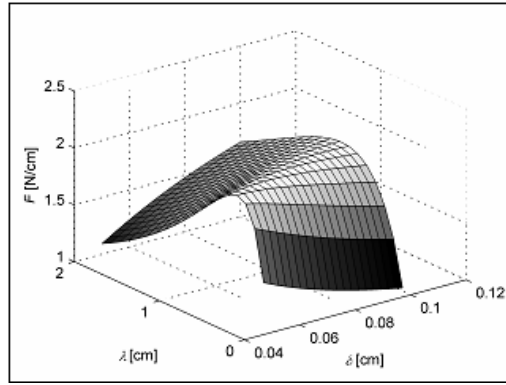


Fig. 13. Force as a function of the displacement and wavelength, in the plane-parallel model, for $R_1=1$ cm, $M=1000$ A/cm, $\mu_l=1.1$, $\mu_m=1$.

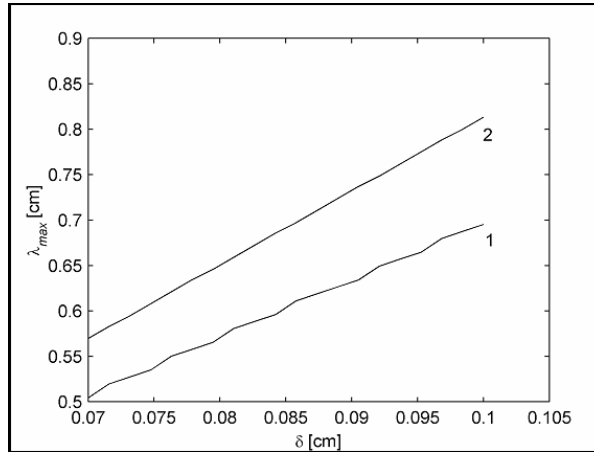


Fig. 14. Optimum wavelength as function of the maximum displacement. 1 – plane-meridian model; 2 – plane-parallel model. $R_1=1$ cm, $M=1000$ A/cm, $\mu_l=1.1$, $\mu_m=1$.

The purpose of the calculations we have reported above has been finding the optimum design of the bearing with magnetic fluid and alternating poles. In order to evaluate the restoring force, we have used a plane-parallel model and a plane-meridian model. A numerical computation of the magnetic field has been used in the cited references. The results obtained with these methods have been concordant.

The restoring force depends on the square of the magnetization. Consequently, an efficient construction must use permanent magnets with high magnetization. The force increases with the permeability of the magnetic liquid. Use of magnets with high temporary magnetization is not recommended, since it decreases the field in the magnetic liquid, and the levitation force.

For a given geometry of the cylinders, and given parameters of the magnetic liquid, there exists an optimum spatial wavelength of the permanent magnets, that determines a maximum restoring force, and that can be determined with the results presented here or in [des_1989]. The value of the wavelength is not critical, since the shape of the surface representing the restoring force in function of the maximum displacement and spatial wavelength of the permanent magnets is smooth and flat around its maximum.

C. Poles on the Shaft, Plane-Meridian Model

The purpose of the next calculation is to report the results obtained with a plane-meridian approximation of the magnetic field in the bearing with magnetic poles placed on the shaft, and to compare them to the results provided by the plane-parallel model. Of the two, the plane-meridian model is more realistic, and some first order geometric approximations that have been used in the other case are not necessary. However, the plane-parallel model provides a simple and closed-form formula for the calculation of the force.

After the calculation of the magnetic field, the second order levitation force on unit length is determined by means of a perturbation method. The field is determined analytically, and the integrals that appear in the expression of the force are calculated by quadratures. The results are presented in a graphical form, and can be used for the design of the bearing.

The geometry of the bearing is similar to the one in Fig. 1 and it is repeated in Fig. 15 in order to reveal the coordinates. Region 1 corresponds to the shaft, which is built of a non-magnetic material.

The permanent magnets, of relative permeability μ_m , placed on the shaft, are contained in Region 2, and are supposed not to magnetize temporarily. The magnetic liquid, of relative permeability μ_l , is situated in Region 3, and the stator, built of a non-magnetic material, is situated in Region 4.

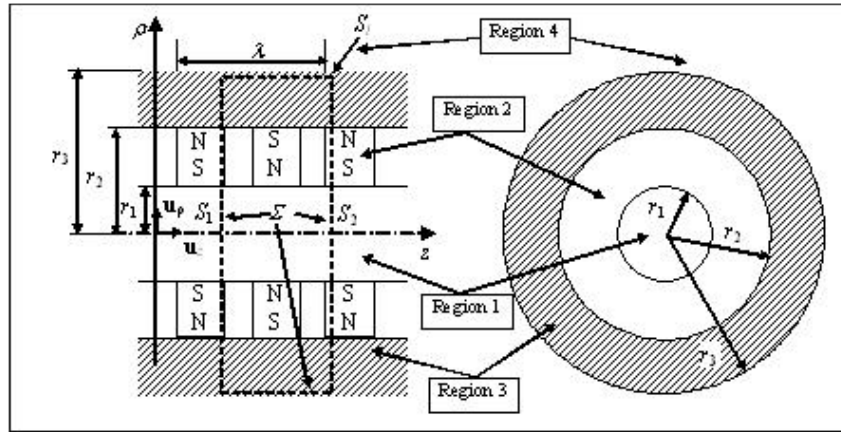


Fig. 15. Geometry of the magnetic bearing.

For keeping the derivation simple, the bearing is supposed very long, and the displacement of the magnetic poles are supposed not to influence the field in the magnetic liquid. As shown above, the permanent magnetization is a solenoidal field, of radial direction $\mathbf{M}_p = M_p \mathbf{u}_\rho$, and it has a rectangular shape of spatial period λ . By denoting with M_{pi} the magnetization of the poles at $\rho = r_i, i = 1..2$, it can be shown that $M_{p1}r_1 = M_{p2}r_2$, and, by denoting the length of the poles with l_p ,

the amplitude of the first harmonic of the magnetization is $M_{0i} = \frac{4}{\pi} M_{pi} \sin\left(\frac{kl_p}{2}\right), i = 1..2, k = \frac{2\pi}{\lambda}$. We

will denote $M_{01}r_1 = M_{02}r_2 = A_m$, which is obviously also the product between the magnetization and the radius at every point of the poles. From the waveform of the permanent magnetization, only the first harmonic will be considered, of the shape (25), which is repeated here for convenience:

$$\mathbf{M}_p = \frac{A_m}{\rho} \sin(kz) \mathbf{u}_\rho. \quad (41)$$

The magnetic field intensity will be calculated for the case when the stator and the shaft are coaxial, so that the problem has a cylindrical symmetry. The mathematical model for the calculation of the field is represented in Fig. 16. For determining the restoring force on the unit length of the shaft when displaced, a perturbation method will be applied, Fig. 17. For this purpose, in the plane-meridian approximation, it is supposed again that, at every point from the surface of the stator, the magnetic field corresponds to a non-displaced shaft, but for a radius of the stator larger or smaller than the real one with an amount equal to the displacement of the shaft in the direction of the given point.

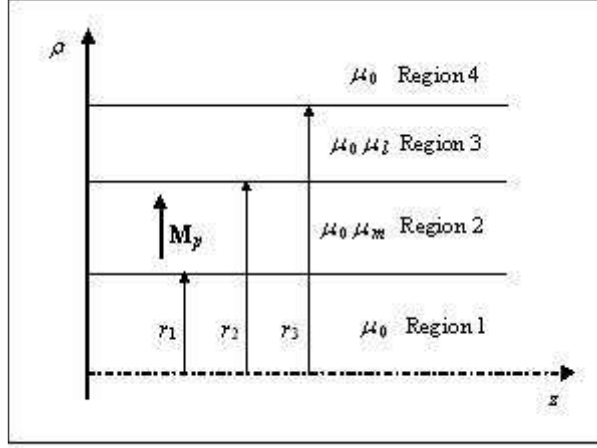


Fig. 16. Mathematical model for the bearing.

The equations that determine the magnetic field in the four regions (Fig. 15) are $\mathbf{B}_1 = \mu_0 \mathbf{H}_1$, $\mathbf{B}_2 = \mu_0 (\mu_m \mathbf{H}_2 + \mathbf{M}_p)$, $\mathbf{B}_3 = \mu_0 \mu_l \mathbf{H}_3$, $\mathbf{B}_4 = \mu_0 \mathbf{H}_4$, $\nabla \times \mathbf{H}_i = 0$, $\nabla \cdot \mathbf{B}_i = 0$, $i = 1..4$. There results $\mathbf{H}_i = -\nabla V_{Hi}$, and the potentials V_{Hi} satisfy the Laplace equations $\nabla^2 V_{Hi} = 0$, $i = 1..3$. The interface conditions on the surfaces $[S_{ij}]$, between regions i and j , that result from $\nabla_S \times \mathbf{H} = 0$, $\nabla_S \cdot \mathbf{B} = 0$, are:

$$\begin{aligned}
 [S_{12}]: (\rho = r_1) \quad V_{H1} = V_{H2}, \quad \frac{\partial V_{H1}}{\partial \rho} - \mu_m \frac{\partial V_{H2}}{\partial \rho} &= -\frac{A_m}{r_1} \sin(kz). \\
 [S_{23}]: (\rho = r_2) \quad V_{H2} = V_{H3}, \quad \mu_m \frac{\partial V_{H2}}{\partial \rho} - \mu_l \frac{\partial V_{H3}}{\partial \rho} &= \frac{A_m}{r_2} \sin(kz). \\
 [S_{34}]: (\rho = r_3) \quad V_{H3} = V_{H4}, \quad \mu_l \frac{\partial V_{H3}}{\partial \rho} = \frac{\partial V_{H4}}{\partial \rho}, \quad \lim_{\rho \rightarrow \infty} V_{H4} &= 0.
 \end{aligned} \tag{42}$$

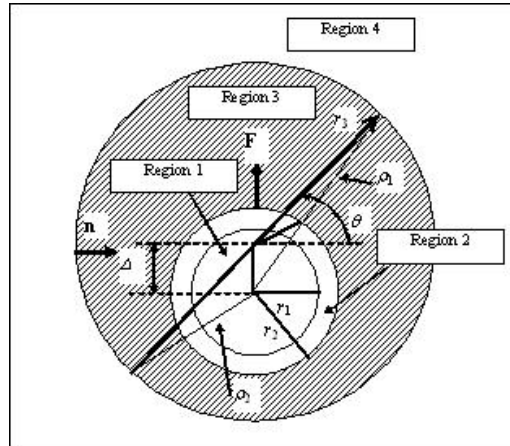


Fig. 17. Geometry of the bearing when the shaft is displaced. \mathbf{F} is the restoring force.

In the cylindrical coordinates (ρ, θ, z) , the Laplace equation independent of θ reads $\nabla^2 V_H = \frac{1}{\rho} \frac{\partial V_H}{\partial \rho} + \frac{\partial^2 V_H}{\partial \rho^2} + \frac{\partial^2 V_H}{\partial z^2} = 0$. Following a method analog to the one used in the case of poles placed on the stator, the variables can be separated $V_H = R(\rho)Z(z)$. After substitution, division of the obtained equation with RZ , and separation, the following two equations result: $\frac{1}{\rho} \frac{dR}{d\rho} + \frac{d^2 R}{d\rho^2} = \pm n^2 R$, and $\frac{d^2 Z}{dz^2} = \mp n^2 Z$, n being a constant to be determined. After substituting $x = n\rho$ in the first equation,

a modified Bessel equation is obtained: $\frac{d^2 R}{dx^2} + \frac{1}{x} \frac{dR}{dx} - R = 0$, with the general solution

$R(x) = A_1 I_0(x) + A_2 K_0(x)$, where I_n and K_n are the modified Bessel functions of the first and second kind respectively, and order n . The second equation has the general solution $Z = C_1 \cos(nz) + C_2 \sin(nz)$.

As explained in the preceding case, the solutions must be of the form

$$\begin{cases} V_{H1} = A I_0(x) \sin(nz) \\ V_{H2} = [C_1 I_0(x) + C_2 K_0(x)] \sin(nz) \\ V_{H3} = [D_1 I_0(x) + D_2 K_0(x)] \sin(nz) \\ V_{H4} = E K_0(x) \sin(nz). \end{cases} \quad (43)$$

Now the interface conditions (42) must be imposed. By taking into account that $I_0'(x) = I_1(x)$ and $K_0'(x) = -K_1'(x)$, we obtain $n = k$ and

$$\begin{cases} A I_{01} - C_1 I_{01} - C_2 K_{01} = 0 \\ A I_{11} - \mu_m C_1 I_{11} + \mu_m C_2 K_{11} = -\frac{A_m}{k r_1} \\ C_1 I_{02} + C_2 K_{02} - D_1 I_{02} - D_2 K_{02} = 0 \\ \mu_m C_1 I_{12} - \mu_m C_2 K_{12} - \mu_l D_1 I_{12} + \mu_l D_2 K_{12} = \frac{A_m}{k r_2} \\ D_1 I_{03} + D_2 K_{03} - E K_{03} = 0 \\ \mu_l D_1 I_{13} - \mu_l D_2 K_{13} + E K_{13} = 0, \end{cases} \quad (44)$$

where we have denoted

$$I_{mn} = I_m(kr_n), \quad K_{mn} = K_m(kr_n). \quad (45)$$

The solutions of interest, for Region 3, of (44) are

$$D_1 = \frac{A_1}{A_2}, \quad (46)$$

$$D_2 = \frac{1}{\mu_l - 1} \left(\frac{I_{03}}{K_{03}} + \mu_l \frac{I_{13}}{K_{13}} \right) D_1,$$

with

$$\begin{aligned} A_1 &= \frac{\mu_m}{\mu_m - 1} \left(\frac{K_{02}}{I_{02}} + \frac{K_{12}}{I_{12}} \right) \frac{M_1}{k I_{11}} - \left[\frac{K_{02}}{I_{02}} + \frac{1}{\mu_m - 1} \left(\frac{K_{01}}{I_{01}} + \mu_m \frac{K_{11}}{I_{11}} \right) \right] \frac{M_2}{k I_{12}}, \\ A_2 &= \mu_l \frac{K_{02}}{I_{02}} + \mu_m \frac{K_{12}}{I_{12}} + \frac{\mu_l - \mu_m}{\mu_m - 1} \left(\frac{K_{01}}{I_{01}} + \mu_m \frac{K_{11}}{I_{11}} \right) \\ &\quad - \frac{\mu_l - \mu_m}{\mu_l - 1} \left(\frac{I_{03}}{K_{03}} + \mu_l \frac{I_{13}}{K_{13}} \right) \frac{K_{02} K_{12}}{I_{02} I_{12}} - \\ &\quad - \frac{1}{(\mu_m - 1)(\mu_l - 1)} \left(\frac{K_{01}}{I_{01}} + \mu_m \frac{K_{11}}{I_{11}} \right) \left(\frac{I_{03}}{K_{03}} + \mu_l \frac{I_{13}}{K_{13}} \right) \left(\mu_l \frac{K_{12}}{I_{12}} + \mu_m \frac{K_{02}}{I_{02}} \right). \end{aligned} \quad (46')$$

Now the magnetic field intensity in Region 3 can be determined:

$$\begin{aligned} \mathbf{H}_3 &= -\nabla V_{H3} = -\frac{\partial V_{H3}}{\partial \rho} \mathbf{u}_\rho - \frac{\partial V_{H3}}{\partial z} \mathbf{u}_z \\ &= -[D_1 k I_0'(k\rho) + D_2 k K_0'(k\rho)] \sin(kz) \mathbf{u}_\rho - [k D_1 I_0(k\rho) + k D_2 K_0(k\rho)] \cos(kz) \mathbf{u}_z \\ &= -k [D_1 I_1(k\rho) - D_2 K_1(k\rho)] \sin(kz) \mathbf{u}_\rho - k [D_1 I_0(k\rho) + D_2 K_0(k\rho)] \cos(kz) \mathbf{u}_z. \end{aligned} \quad (47)$$

The force that acts on a cylindrical region of the shaft can be obtained by integration on the surface $\Sigma = S_l \cup S_1 \cup S_2$ (Fig. 15), and it is given by (32) which is repeated here

$$\mathbf{F} = \mu_0 \left[\oint_{\Sigma} \left(\frac{M_n^2}{2} + \int_0^H M dH \right) \mathbf{n} ds \right], \quad (48)$$

where M_n is the normal component of the magnetization, and \mathbf{n} is the unit normal vector directed inwards the volume bounded by Σ . For reasons of linearity and symmetry, (48) reduces again to

$$\mathbf{F} = \mu_0 \frac{\mu_l - 1}{2} \int_{S_l} (\mu_l H_\rho^2 + H_z^2) \mathbf{n} ds, \quad \mathbf{H} = \mathbf{H}_3, \quad (49)$$

and the integrand is in fact the pressure p that acts on S_l , and it is numerically equal with the pressure that acts on the shaft. The average pressure on a spatial period $\tilde{p} = \frac{1}{\lambda} \int_0^\lambda p d\lambda$ can be determined after the substitution of (47) and some calculations:

$$\begin{aligned} \tilde{p} = & \frac{\mu_0 \mu_l (\mu_l - 1)}{4} k^2 [D_1 I_1(k\rho) - D_2 K_1(k\rho)]^2 + \\ & \frac{\mu_0 (\mu_l - 1)}{4} k^2 [D_1 I_0(k\rho) + D_2 K_0(k\rho)]^2. \end{aligned} \quad (50)$$

In order to apply the perturbation method, two points opposed on the same diameter of the stator must be considered, Fig. 17. In the plane-meridian approximation, the resulting mean pressure \tilde{p}_{12} , in a direction given by the angle θ , can be obtained by taking the difference between the values given by (50) after the substitutions $\rho = \rho_2$, and $\rho = \rho_1$. The mean pressure is a function of the displacement Δ and the angle θ as

$$\begin{aligned} \rho_1^2 &= \Delta^2 + r_3^2 + 2\Delta r_3 \sin \theta, \\ \rho_2^2 &= \Delta^2 + r_3^2 - 2\Delta r_3 \sin \theta. \end{aligned} \quad (51)$$

In the plane-parallel model, it has been considered that $\Delta \ll r_3$, so that some first order geometrical approximations could be used:

$$\begin{aligned} \rho_1 &\cong r_3 + \Delta \sin \theta, \\ \rho_2 &\cong r_3 - \Delta \sin \theta. \end{aligned} \quad (52)$$

Finally

$$\begin{aligned} \tilde{p}_{12}(\theta) = & P \left\{ [D_1 I_1(k\rho_2) - D_2 K_1(k\rho_2)]^2 - [D_1 I_1(k\rho_1) - D_2 K_1(k\rho_1)]^2 \right\} + \\ & + Q \left\{ [D_1 I_0(k\rho_2) + D_2 K_0(k\rho_2)]^2 - [D_1 I_0(k\rho_1) + D_2 K_0(k\rho_1)]^2 \right\}, \\ P = & \frac{\mu_0 \mu_l (\mu_l - 1)}{4} k^2, \quad Q = \frac{P}{\mu_l}. \end{aligned} \quad (53)$$

The restoring force on unit length can be obtained from (53) by integration:

$$F = 2r_3 \int_0^{\pi/2} \tilde{p}_{12}(\theta) \sin \theta d\theta. \quad (54)$$

We present the results obtained when the force is evaluated according to this expression compared to the results from the plane-parallel model.

The expression of the restoring force derived from the plane-parallel model, for a unity value of the magnet permeability, which determines a maximum value for the force in function of this parameter) is (20). This expression may be simplified by noticing that the infinite summation can be expressed in terms of I_1 :

$$\begin{aligned} F = & \frac{A_m^2}{r_1^2} 2\pi\mu_0 \frac{\mu_l (\mu_l - 1)}{(\mu_l + 1)^3} r_3 \left[1 - \frac{r_1}{r_2} \exp(k(r_2 - r_1)) \right]^2 \times \\ & \times \exp[-2k(r_2 - r_1)] I_1(2k\Delta) \end{aligned} \quad (55)$$

In order to highlight the differences and the coincidences between the results predicted by the two models, we represented in Fig. 18 the variation of the unit length restoring force versus the maximum displacement of the shaft $\delta = r_3 - r_1$, for some values of the other parameters we have used previously. The curve derived with the plane-meridian model is drawn with solid line, while the one derived with the plane-parallel model is dotted, a convention we respect in the following figures too. The differences are larger for extreme values of the displacement, and around the maximum of the force. However, these differences have moderate values: the maximum value of the force is 6.48 N/cm, for a displacement of 0.05 cm in the plane-meridian model, while for the plane-parallel model the values are 5.82 N/cm, and 0.07 cm respectively.

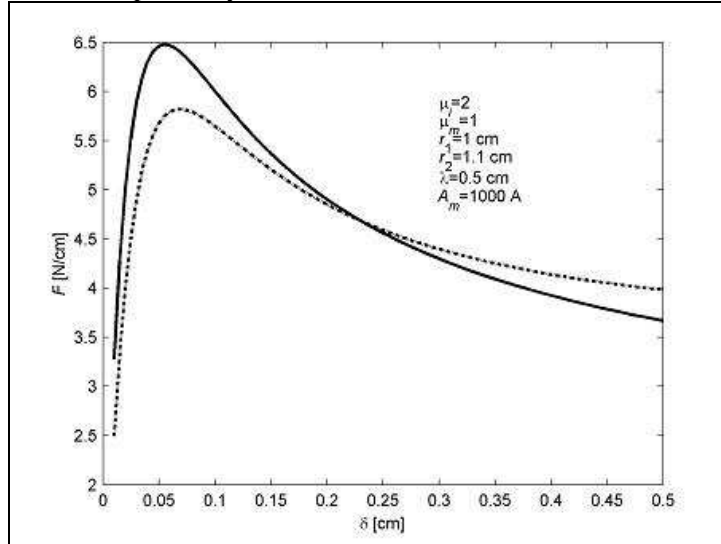


Fig. 18. Restoring force in function of the maximum displacement.

For a given bearing, the values of the restoring force for various displacements of the shaft, are represented in Fig. 19. Differences between the predictions of the two models increase with the increase of the displacement, when the magnetic field becomes more intense. Other calculations show that the differences increase with the spatial period of the magnetic poles too.

The graphs in Fig. 20 are used for finding the optimal value of the spatial period in the case of a bearing with given geometrical dimensions. The plane-meridian model gives a value of 1.08 cm, and a maximum force of 12.35 N/cm. The corresponding values for the plane-parallel model are 0.89 cm and 11.80 N/cm. Differences are moderate in this case too.

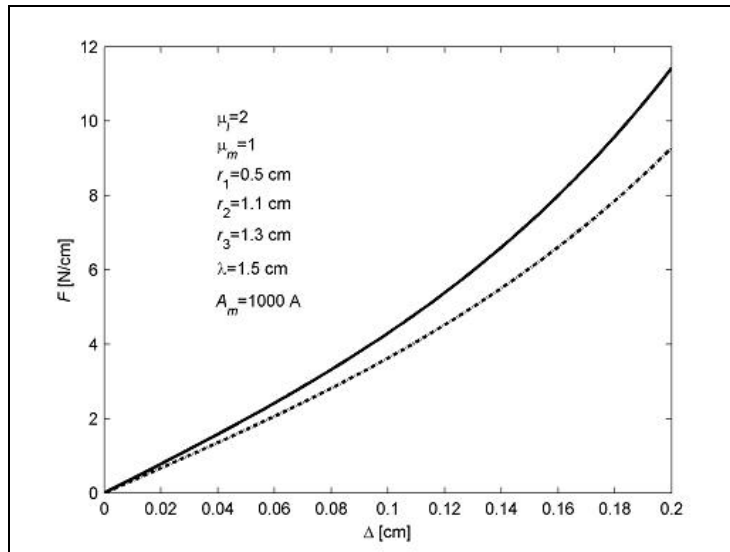


Fig. 19. Restoring force in function of the displacement, for a given bearing.

In order to get some insight about the variation of the restoring force around its maximum, in the plane-meridian model, we have represented it in Fig. 21 as a function of the spatial period and the

maximum displacement. The radius of the shaft, the height of the poles, the relative permeabilities, and A_m are as in the last two figures. It can be seen that the saddle shape of the function around the maximum is quite flat, a fact that is advantageous for the design, as the parameters can be approximated roughly around their optimum values. This is also a feature of the plane-parallel model.

The results of the calculations we have reported can be used for finding the optimal set of parameters that provide a maximum restoring force. We have compared the predictions of the two models: plane-parallel and plane-meridian. The plane-meridian model is more realistic, but its application requires a computer program for integrals quadrature. The plane-parallel model is less rigorous, but the closed form formula for the force it provides is simple.

From a qualitative point of view, both models predict the same shapes of the dependencies of the restoring force on various geometrical parameters. There exists an optimal point when the force is maximum, and the variation of the force around it is quite small, providing the possibility of rough approximations for the parameters.

From a quantitative point of view, there exist some differences between the two predictions, which can be neglected when the design must not be highly precise. When the approximations used for the plane-parallel model do not hold true (for example, the maximum displacement of the shaft much smaller than the interior radius of the stator), the plane-meridian model must be selected.

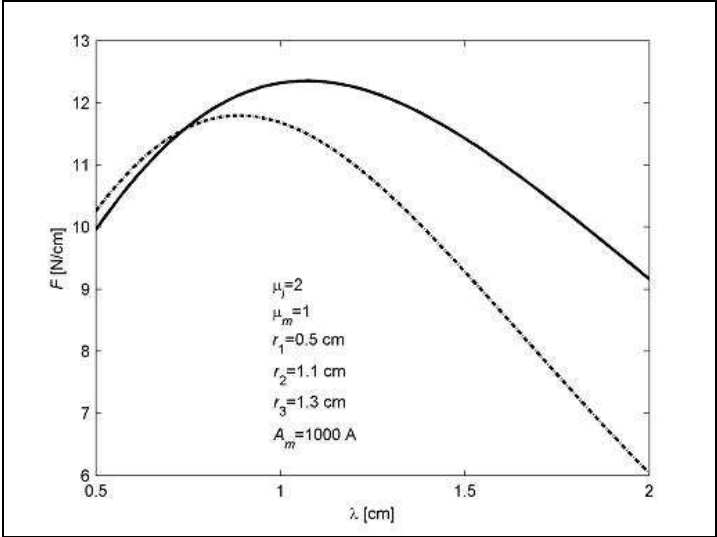


Fig. 20. Restoring force versus spatial period of the poles.

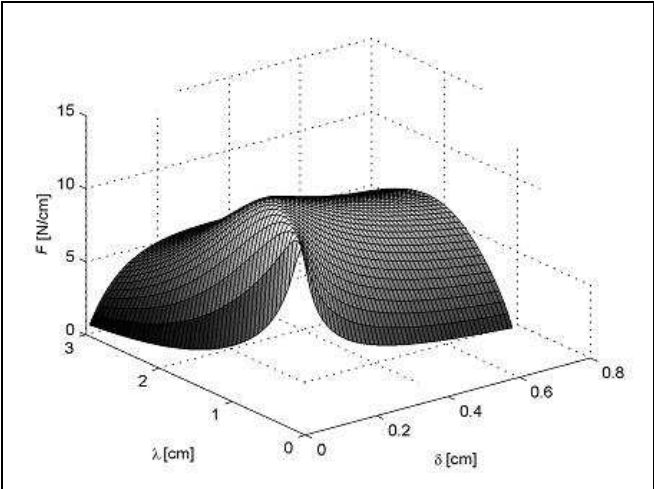


Fig. 21. Restoring force in function of the maximum displacement and the spatial period of the poles.

The presented results are useful for the optimal design of magnetic fluid bearings.

2.4. Spectral Analysis

A. Closed Form Expression of the Small Sample Variance of a Frequency Estimator

In many situations, a signal consisting of a single tone corrupted by additive white noise is available, and the frequency of the tone must be estimated. This problem has applications in communications, radar, sonar, measurements, adaptive control, speech processing etc [stoica_97], and it belongs to the wider class of spectrum estimation problems [kay_81]. Both complex and real signals have been considered in the literature. As maximum likelihood (ML) estimators perform very well but are not computationally efficient [rife_74, ken_87], various estimation algorithms have been proposed (see [tret_85, kay_89, fitz_94, luisse_95, kim_96, ros_06, fu_07] for the complex case and [ken_87, sakai_84, chan_03, sav_03, so_04] for the real case). It is known that efficient methods designed for real-time estimation of the frequency of complex signals cannot be applied to the real case [lui_08], which is considered here.

We have also introduced some frequency estimations techniques that will be reviewed below and we have proposed closed-form expressions for estimators based on a small number of samples.

In a first contribution [06_04_S], we have considered a frequency estimation method, called reformed Pisarenko harmonic decomposer (RPHD) [so_02_1, so_02_2, so_04]. In the cited references, a closed form, asymptotically unbiased frequency estimator has been proposed and analyzed, based on the linear prediction (LP) property of sinusoidal signals, and on a modified least-squares (LS) cost function. The same frequency estimator has been derived in [sav_03] from a constrained notch-filter point of view.

In our contribution we have derived a closed-form expression of the RPHD variance, based on the same variance analysis technique used in [So_04, Chan_03]. We obtained a much more convenient formula as compared to [So_04].

In single frequency estimation, the following signal model is used [So_04]:

$$x(n) = s(n) + q(n) = \alpha \cos(\omega_0 n + \varphi) + q(n), \quad n = 1, 2, \dots, N \quad (1)$$

where $\alpha, \omega_0 \in (0, \pi)$, and φ are the unknown amplitude, frequency and phase of the sinusoid, and $q(n)$ is a zero-mean white noise, which is supposed Gaussian. The sinusoid is linearly predictable from the past samples:

$$s(n) = 2 \cos(\omega_0) s(n-1) - s(n-2), \quad (2)$$

a fact that allows to define an error function

$$e(n) = x(n) - 2 \cos(\lambda) x(n-1) + x(n-2), \quad (3)$$

where λ is the parameter to be determined.

In order to obtain an asymptotically unbiased frequency estimator a modified error function is defined in [so_04] as follows:

$$\varepsilon(n) = \frac{e(n)}{\sqrt{2(2 + \cos(2\lambda))}}. \quad (4)$$

The corresponding LS cost function is

$$J_N(\lambda) = \sum_{n=3}^N \frac{e^2(n)}{2(2 + \cos(2\lambda))}. \quad (5)$$

Solving $\frac{dJ_N(\lambda)}{d\lambda} = 0$ yields [so_02_1, so_02_2, so_04]:

$$2A_N \cos^2(\lambda) - B_N \cos(\lambda) - A_N = 0, \quad (6)$$

where

$$A_N = \sum_{n=3}^N (x(n) + x(n-2))x(n-1), \quad (7)$$

and

$$B_N = \sum_{n=3}^N \left((x(n) + x(n-2))^2 - 2x^2(n-1) \right). \quad (8)$$

The root of (6) that provides the estimate is

$$\rho_k^* = \frac{B_{kN} + \sqrt{B_{kN}^2 + 8A_{kN}^2}}{4A_{kN}}. \quad (9)$$

The frequency estimate, which is denoted by $\hat{\omega}_0$, is computed as

$$\hat{\omega}_0 = \cos^{-1}(\rho^*). \quad (10)$$

The variance analysis technique [so_04] is based on defining a second order polynomial

$$f(\rho) = 2A_N \rho^2 - B_N \rho - A_N \quad (11)$$

and utilize the following formulas

$$\text{var}\{\rho^*\} \approx \frac{E\{f^2(\rho)\}}{(E\{f'(\rho)\})^2} \Bigg|_{\rho=\cos(\omega_0)} \quad (12)$$

$$\text{var}(\hat{\omega}_0) \approx \frac{\text{var}(\rho^*)}{\sin^2(\omega_0)}. \quad (13)$$

By using

$$\rho = \cos(\omega_0) \quad (14)$$

and (11) there results

$$f^2(\rho) = \cos^2(2\omega_0) A_N^2 - 2\cos(\omega_0)\cos(2\omega_0) A_N B_N + \cos^2(\omega_0) B_N^2 \quad (15)$$

$$f'(\rho) = 4\cos(\omega_0) A_N - B_N. \quad (16)$$

In order to compute the variance of ω_0 using (12) and (13), the values of $E\{A_N\}$, $E\{B_N\}$, $E\{A_N^2\}$, $E\{A_N B_N\}$, and $E\{B_N^2\}$ are required. The computation is presented below. The result is

$$E\{A_N\} = \alpha^2 (N - 2 + \beta(2, N - 1)) \cos(\omega_0), \quad (17)$$

$$E\{B_N\} = \alpha^2 (N - 2 + \beta(2, N - 1)) \cos(2\omega_0), \quad (18)$$

$$\begin{aligned}
E\{A_N^2\} &= \alpha^4 (N-2 + \beta(2, N-1))^2 \cos^2(\omega_0) \\
&+ \alpha^2 \sigma_q^2 [4N-10 + (4N-12)\cos(2\omega_0) + \beta(2, N-1)(2 + \cos(2\omega_0)) \\
&\quad + 2\beta(2, N-2) + 2\beta(3, N-1) + \beta(3, N-2)] \\
&\quad + \sigma_q^4 (4N-10), \tag{19}
\end{aligned}$$

$$\begin{aligned}
E\{A_N B_N\} &= \alpha^4 (N-2 + \beta(2, N-1))^2 \cos(\omega_0) \cos(2\omega_0) \\
&\quad + \alpha^2 \sigma_q^2 [(4N-14)(\cos(\omega_0) + \cos(3\omega_0)) \\
&\quad + 2(\beta(2, N-2) + \beta(3, N-1)) \frac{\cos(2\omega_0)}{\cos(\omega_0)} + 4\beta(3, N-2)\cos(\omega_0)], \tag{20}
\end{aligned}$$

$$\begin{aligned}
E\{B_N^2\} &= \alpha^4 (N-2 + \beta(2, N-1))^2 \cos^2(2\omega_0) \\
&+ \alpha^2 \sigma_q^2 [4N + 4(N-4)\cos(4\omega_0) + 8\beta(2, N-1)(2 + \cos(2\omega_0)) \\
&\quad - 16\beta(2, N-2) - 16\beta(3, N-1) + 8\beta(3, N-2)(1 + \cos(2\omega_0))] \\
&\quad + \sigma_q^4 (4N-8), \tag{21}
\end{aligned}$$

where

$$\beta(k_1, k_2) = \sum_{n=k_1}^{k_2} \cos(2(\omega_0 n + \varphi)) = \frac{\sin(\omega_0(k_2 - k_1 + 1)) \cos(\omega_0(k_2 + k_1) + 2\varphi)}{\sin(\omega_0)}. \tag{22}$$

By using (12)...(21) and after denoting the signal-to-noise ratio

$$SNR = \frac{\alpha^2}{2\sigma_q^2}, \tag{23}$$

we obtained the closed-form variance formula of the RPHD single-tone frequency estimator as

$$\begin{aligned}
\text{var}\{\hat{\omega}_0\} &\cong \frac{2 + (2 + \cos(2\omega_0))\beta(2, N-1) - 2(\beta(2, N-2) + \beta(3, N-1)) + \beta(3, N-2)}{2SNR(N-2 + \beta(2, N-1))^2 \sin^2(\omega_0)} \\
&\quad + \frac{(2N-5)\cos^2(2\omega_0) + (2N-4)\cos^2(\omega_0)}{2SNR^2(N-2 + \beta(2, N-1))^2 (2 + \cos(2\omega_0))^2 \sin^2(\omega_0)}. \tag{24}
\end{aligned}$$

The shape of the variance in (24) is more convenient and it has a simpler structure when compared to the original results presented in [So_04]. In that paper, an asymptotic form of the variance is also considered. That form can be approached by making $\beta=0$ in (24):

$$\begin{aligned}
\text{var}_{\text{asympt}}\{\hat{\omega}_0\} &\cong \frac{1}{SNR(N-2)^2 \sin^2(\omega_0)} \\
&\quad + \frac{(2N-5)\cos^2(2\omega_0) + (2N-4)\cos^2(\omega_0)}{2SNR^2(N-2)^2 (2 + \cos(2\omega_0))^2 \sin^2(\omega_0)} \tag{25}
\end{aligned}$$

Minor differences are probably caused by small calculation errors in the original work.

We present now the derivation. We outline the main steps that we used in computing the values of $E\{A_N\}$, $E\{B_N\}$, $E\{A_N^2\}$, $E\{A_N B_N\}$, and $E\{B_N^2\}$.

We use (1), (2), (7), and (22) in order to get

$$A_N = T_{A1} + T_{A2} + T_{A3}, \tag{26}$$

where

$$\begin{aligned} T_{A1} &= \sum_{n=3}^N 2\alpha^2 \cos(\omega_0) \cos^2(\omega_0(n-1) + \varphi) \\ &= \alpha^2 (N-2 + \beta(2, N-1)) \cos(\omega_0), \end{aligned} \quad (27)$$

$$T_{A2} = \sum_{n=3}^N \alpha \cos(\omega_0(n-1) + \varphi) (2 \cos(\omega_0) q(n-1) + q(n) + q(n-2)), \quad (28)$$

and

$$T_{A3} = \sum_{n=3}^N q(n-1) (q(n) + q(n-2)). \quad (29)$$

As $q(n)$ is white, with zero mean, we have

$$E\{q(n)\} = 0; \quad E\{q(n)q(m)\} = \delta_m^n \sigma_q^2. \quad (30)$$

There results $E\{T_{A2}\} = E\{T_{A3}\} = 0$, $E\{A_N\} = E\{T_{A1}\} = T_{A1}$ and (17).

In order to calculate $E\{A_N^2\}$, we note that, due to (30), we have $E\{T_{A_i}T_{A_j}\} = 0$ for $i \neq j$. Therefore

$$E\{A_N^2\} = T_{A1}^2 + E\{T_{A2}^2\} + E\{T_{A3}^2\}. \quad (31)$$

We evaluate now the second and the third term in the RHS of (31).

$$\begin{aligned} E\{T_{A2}^2\} &= \sum_{n=3}^N \alpha^2 \cos^2(\omega_0(n-1) + \varphi) \\ &\quad \times [4 \cos^2(\omega_0) E\{(q(n-1))^2\} + E\{(q(n))^2\} + E\{(q(n-2))^2\}] \\ &\quad + 2 \sum_{n=3}^N \sum_{m=n+1}^N \alpha^2 \cos(\omega_0(n-1) + \varphi) \cos(\omega_0(m-1) + \varphi) \\ &\quad \times E\{(2 \cos(\omega_0) q(n-1) + q(n) + q(n-2)) \\ &\quad \times (2 \cos(\omega_0) q(m-1) + q(m) + q(m-2))\}. \end{aligned}$$

By performing the multiplications and by using (30) there results

$$\begin{aligned} E\{T_{A2}^2\} &= \sum_{n=3}^N \alpha^2 \frac{1 + \cos(2\omega_0(n-1) + 2\varphi)}{2} (4 \cos^2(\omega_0) \sigma_q^2 + 2\sigma_q^2) + \\ &\quad + \sum_{n=2k+1}^N \sum_{m=n+1}^N \alpha^2 [\cos(\omega_0(n+m-2) + 2\varphi) + \cos(\omega_0(m-n))] \\ &\quad \times [2 \cos(\omega_0) E\{q(n-1)q(m-2)\} + \\ &\quad + 2 \cos(\omega_0) E\{q(n)q(m-1)\} + E\{q(n)q(m-2)\}]. \end{aligned}$$

Using again (30) we get

$$\begin{aligned}
E\{T_{A2}^2\} &= \alpha^2 \sigma_q^2 (N-2 + \beta(2, N-1))(\cos(2\omega_0) + 2) \\
&\quad + \alpha^2 \sigma_q^2 \sum_{n=3}^{N-1} 4 \cos(\omega_0) (\cos((2n-1)\omega_0 + 2\varphi) + \cos(\omega_0)) \\
&\quad + \alpha^2 \sigma_q^2 \sum_{n=3}^{N-2} (\cos(2\omega_0 n + 2\varphi) + \cos(2\omega_0)) \\
&= \alpha^2 \sigma_q^2 [4N - 10 + (4N - 12)\cos(2\omega_0) \\
&\quad + \beta(2, N-1)(2 + \cos(2\omega_0)) + 2\beta(2, N-2) \\
&\quad + 2\beta(3, N-1) + \beta(3, N-2)].
\end{aligned} \tag{32}$$

Then

$$\begin{aligned}
E\{T_{A3}^2\} &= E\left\{ \sum_{n=3}^N [(q(n-1)q(n))^2 + 2q^2(n-1)q(n)q(n-2) \right. \\
&\quad \left. + (q(n-1)q(n-2))^2] \right\} + 2E\left\{ \sum_{n=3}^N \sum_{m=n+1}^N q(n-1)q(m-1) \right. \\
&\quad \left. \times (q(m) + q(m-2))(q(n) + q(n-2)) \right\} \\
&= 2(N-2)\sigma_q^4 + 2 \sum_{n=3}^{N-1} E\{q^2(n)q^2(n-1)\} \\
&= (4N-10)\sigma_q^4.
\end{aligned} \tag{33}$$

With the use of (27), (31), (32), and (33) we obtain (19).

We now consider (1), (2), (8), and (22) in order to get

$$B_N = T_{B1} + T_{B2} + T_{B3}, \tag{34}$$

where

$$T_{B1} = \alpha^2 (N-2 + \beta(2, N-1)) \cos(2\omega_0), \tag{35}$$

$$\begin{aligned}
T_{B2} &= 4\alpha \sum_{n=3}^N \cos(\omega_0(n-1) + \varphi) \\
&\quad \times (\cos(\omega_0)(q(n) + q(n-2)) - q(n-1)),
\end{aligned} \tag{36}$$

and

$$T_{B3} = \sum_{n=3}^N (q^2(n) + q^2(n-2) + 2q(n)q(n-2) - 2q^2(n-1)). \tag{37}$$

Using (30) yields as before $E\{B_N\} = T_{B1}$, (17) and

$$E\{B_N^2\} = T_{B1}^2 + E\{T_{B2}^2\} + E\{T_{B3}^2\}. \tag{38}$$

We have

$$\begin{aligned}
E\{T_{B2}^2\} &= 16\alpha^2 \sum_{n=3}^N \cos^2(\omega_0(n-1) + \varphi) (2\sigma_q^2 \cos^2(\omega_0) + \sigma_q^2) \\
&\quad + 32\alpha^2 \sum_{n=3}^N \sum_{m=n+1}^N \cos(\omega_0(n-1) + \varphi) \cos(\omega_0(m-1) + \varphi) \\
&\quad \times E\{(\cos(\omega_0)(q(n) + q(n-2)) - q(n-1)) \\
&\quad \times (\cos(\omega_0)(q(m) + q(m-2)) - q(m-1))\}.
\end{aligned}$$

By performing the multiplications and by using again (30) we get

$$\begin{aligned}
E\{T_{B2}^2\} &= 16\alpha^2 \sigma_q^2 (2\cos^2(\omega_0) + 1) \sum_{n=3}^N \frac{1 + \cos(2\omega_0(n-1) + 2\varphi)}{2} \\
&\quad + 16\alpha^2 \sum_{n=3}^N \sum_{m=n+1}^N (\cos(\omega_0(m+n-2) + 2\varphi) + \cos(\omega_0(m-n))) \\
&\quad \times [\cos^2(\omega_0) E\{q(n)q(m-2)\} \\
&\quad - \cos(\omega_0) (E\{q(n)q(m-1)\} + E\{q(n-1)q(m-2)\})] \\
&= 8\alpha^2 \sigma_q^2 (N-2 + \beta(2, N-1)) (\cos(2\omega_0) + 2) \\
&\quad + 16\alpha^2 \sigma_q^2 \sum_{n=3}^{N-2} (\cos(2\omega_0 n + 2\varphi) + \cos(2\omega_0)) \cos^2(\omega_0) \\
&\quad - 32\alpha^2 \sigma_q^2 \sum_{n=3}^{N-1} (\cos(\omega_0(2n-1) + 2\varphi) + \cos(\omega_0)) \cos(\omega_0).
\end{aligned}$$

After some manipulations there results

$$\begin{aligned}
E\{T_{B2}^2\} &= \alpha^2 \sigma_q^2 [4N + 4(N-4)\cos(4\omega_0) + 8\beta(2, N-1)(2 + \cos(2\omega_0)) \\
&\quad - 16\beta(2, N-2) - 16\beta(3, N-1) + 8\beta(3, N-2)(1 + \cos(2\omega_0))].
\end{aligned} \tag{39}$$

For the last term in (34) we have

$$\begin{aligned}
E\{T_{B3}^2\} &= 4(N-2)\sigma_q^4 \\
&\quad + 2 \sum_{n=3}^N \sum_{m=n+1}^N E\{(q^2(n) + q^2(n-2) + 2q(n)q(n-2) - 2q^2(n-1)) \\
&\quad \times (q^2(m) + q^2(m-2) + 2q(m)q(m-2) - 2q^2(m-1))\} \\
&= 4(N-2)\sigma_q^4.
\end{aligned} \tag{40}$$

With the use of (35), (38), (39), and (40) we obtain (21).

We now consider (26)...(29) and (34)...(37) in order to obtain

$$E\{A_N B_N\} = T_{C1} + T_{C2} + T_{C3}, \quad (41)$$

where

$$T_{C1} = \alpha^4 \cos(\omega_0) \cos(2\omega_0) (N - 2 + \beta(2, N - 1))^2, \quad (42)$$

$$\begin{aligned} T_{C2} &= \alpha^2 \sum_{n=3}^N \sum_{m=3}^N 4 \cos(\omega_0(n-1) + \varphi) \cos(\omega_0(m-1) + \varphi) \\ &\quad \times E\{(2 \cos(\omega_0) q(n-1) + q(n) + q(n-2)) \\ &\quad \times (\cos(\omega_0)(q(m) + q(m-2) - q(m-1)))\}, \end{aligned} \quad (43)$$

and

$$\begin{aligned} T_{C3} &= E\left\{ \sum_{n=3}^N \sum_{m=3}^N q(n-1)(q(n) + q(n-2)) \right. \\ &\quad \left. \times (q^2(m) + q^2(m-2) + 2q(m)q(m-2) - 2q^2(n-1)) \right\} \\ &= 0 \end{aligned} \quad (44)$$

The last equality in (44) follows from (30).

The quantity defined in (43) can be calculated as follows

$$\begin{aligned} T_{C2} &= 2\alpha^2 \sum_{n=3}^N \sum_{m=3}^N (\cos(\omega_0(m+n-2) + 2\varphi) + \cos(\omega_0(m-n))) \\ &\quad \times \left((4 \cos^2(\omega_0) - 2) q(n-1) q(m) + 2 \cos(\omega_0) q(n-1) q(m) \right) \\ &= 4\alpha^2 \sigma_q^2 \sum_{m=3}^{N-1} \cos(2\omega_0) (\cos(\omega_0(2m-1) + 2\varphi) + \cos(\omega_0)) \\ &\quad + 4\alpha^2 \sigma_q^2 \sum_{m=3}^{N-2} \cos(\omega_0) (\cos(2\omega_0 m + 2\varphi) + \cos(2\omega_0)). \end{aligned}$$

After some straightforward transformations we get

$$\begin{aligned} T_{C2} &= \alpha^2 \sigma_q^2 [(4N - 14) (\cos(\omega_0) + \cos(3\omega_0)) \\ &\quad + 2(\beta(2, N - 2) + \beta(3, N - 1)) \frac{\cos(2\omega_0)}{\cos(\omega_0)} + 4\beta(3, N - 2) \cos(\omega_0)]. \end{aligned} \quad (45)$$

With the use of (41), (42), (44), and (45) we obtain (20).

In order to confirm the expression (24) for the variance, and to compare it with its asymptotic form (25), we have performed some computer experiments. RPHD variances have been measured for data sequences we have generated using (1), with $\alpha = \sqrt{2}$, and several values for σ_q^2 . In every experiment we computed the frequency estimate using (9) and (10) for 500 independent runs, and we evaluated the measured frequency variance of the RPHD method in terms of the mean square frequency errors.

We used for evaluation purposes the Cramer-Rao bound (CRB) for the frequency estimator of a single sinusoid [Kay_93]

$$CRB[\text{dB rad}^2] = \frac{24\sigma_q^2}{N(N^2 - 1)\alpha^2}. \quad (46)$$

The measured frequency variances, the theoretical frequency variances calculated with (24), the asymptotic forms calculated with (25), and the Cramer-Rao bounds are shown in the figures that illustrate the experimental results.

In Fig. 1 and Fig. 2, the frequency variances of the RPHD estimator versus ω_0 are represented, for $N = 20$, $SNR = 20$ dB, $\varphi=0$, and $\varphi=\pi/4$ respectively. The measured variances are very close to the calculated variances and fluctuate in function of frequency and phase around the curve representing the asymptotic variance (they are not always symmetric around $\omega_0 = \pi/2$; $\beta(k_1, k_2)$ is symmetric around $\omega_0 = \pi/2$ for $\varphi = 0$, but it is not for $\varphi = \pi/4$).

In Fig.3 and Fig. 4, the frequency variances versus SNR are represented, at $\omega_0 = 0.2\pi$, $N = 20$, $\varphi=0$, and $\varphi=\pi/4$ respectively. It can be noticed that, like for all methods, errors increase at low values of the SNR . By comparing the two figures, there results that the relation between the variance and its asymptotic expression depends on φ .

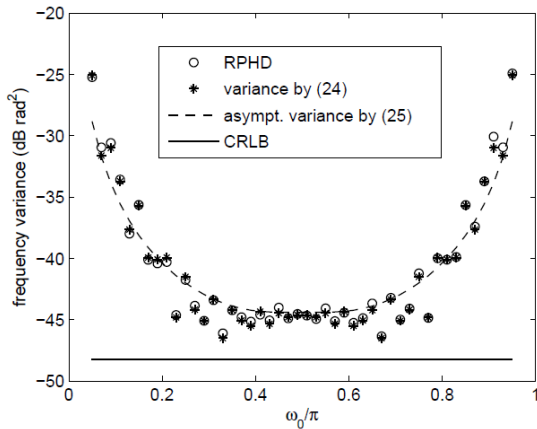


Fig. 1. Frequency variances versus ω_0 at $SNR=20$ dB, $N=20$ and $\varphi=0$.

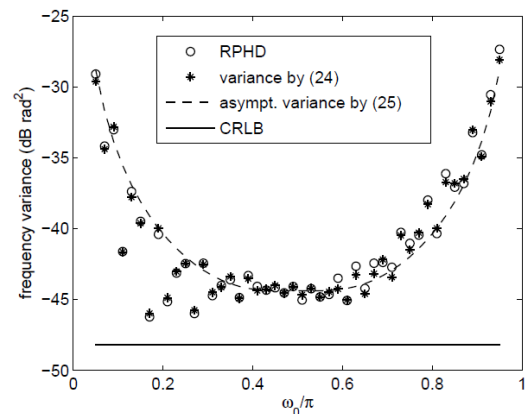


Fig. 2. Frequency variances versus ω_0 at $SNR=20$ dB, $N=20$ and $\varphi=\pi/4$.

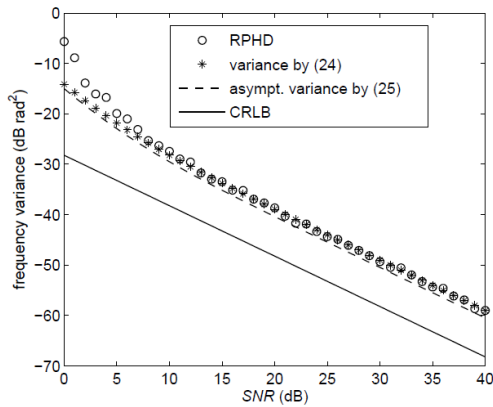


Fig. 3. Frequency variances versus SNR at $\omega_0=0.2\pi$, $N=20$ and $\varphi=0$.

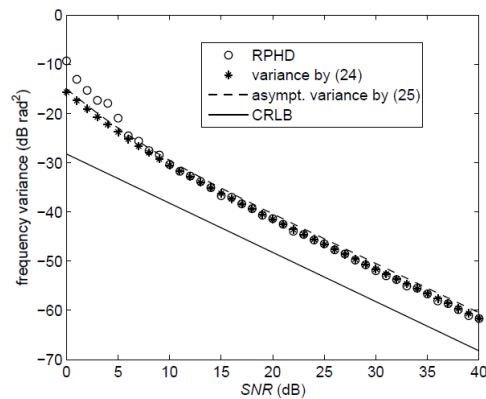


Fig. 4. Frequency variances versus SNR at $\omega_0=0.2\pi$, $N=20$ and $\varphi=\pi/4$.

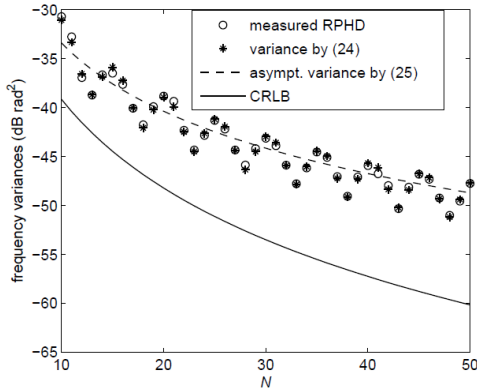


Fig. 5. Frequency variances versus N at $\omega_0=0.2\pi$, $SNR=20$ dB and $\phi=0$.

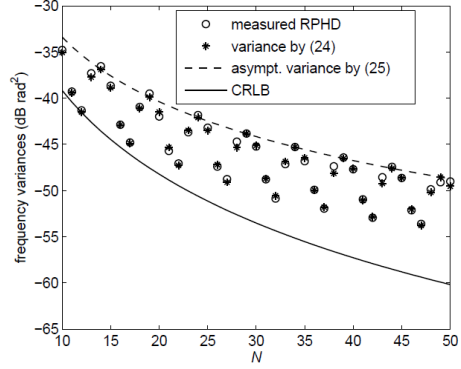


Fig. 6. Frequency variances versus N at $\omega_0=0.2\pi$, $SNR=20$ dB and $\phi=\pi/4$.

Fig. 5 and Fig. 6 show the frequency variances in function of N for $\omega_0 = 0.2\pi$, $SNR = 20\text{dB}$, $\phi=0$, and $\phi=\pi/4$ respectively. The coincidence between the measured and the calculated variances is remarkable again. As in the preceding experiment, it can be noticed the dependence on ϕ of the relation between the variance and its asymptotic evaluation, as well as the fact that the differences between them can become quite large for small N .

In conclusion, in the contribution [06_04_S] we provided a very convenient closed form expression for the variance of the frequency estimator in the RPHD method of single tone frequency estimation from a finite set of data samples. We also derived an asymptotic form of the variance, which agreed with previously published results.

We validated our results by means of several computer experiments. Coincidence between experimental and calculated variances was remarkable in all cases, except for very low signal to noise ratios. From our experimental results, it could be seen that the relation between the variance and its asymptotic evaluation depended very much on the phase of the sampled sinusoid, so that quite large errors are possible in the case of a small number of samples. This is an argument for the usefulness of our closed form formula as, in common applications, a number as small as possible of signal samples is desired.

B. Two-Step Procedure for Reducing Variance in Single Tone Frequency Estimation

A general method for decreasing the variance of a frequency estimator has been proposed in [07_02_S]. The procedure consists of estimating an integer multiple of the frequency and in resolving the induced aliasing by a two-step procedure. The general idea will be outlined below. The procedure is illustrated using the RPHD method for the first step, and a new generalized RPHD (GRPHD) method that we have introduced for the second step. We also present explicit relations needed for implementation and statistical analysis of the GRPHD. Results of computer experiments are reported in order to confirm the theory.

In many single sinusoid frequency estimation techniques, the estimate $\hat{\omega}_{01}$ of the unknown frequency ω_0 is calculated from an estimator $\rho_1^* = \cos(\hat{\omega}_{01})$ using $\hat{\omega}_{01} = \cos^{-1}(\rho_1^*)$ [so_04]. If the estimator is unbiased, the relation between the variances of $\hat{\omega}_{01}$ and ρ_1^* is $\text{var}(\hat{\omega}_{01}) \approx \frac{\text{var}(\rho_1^*)}{\sin^2(\omega_0)}$. We propose to generalize this procedure by finding an estimator $\rho_k^* = \cos(\hat{\omega}_{0k})$ of an integer multiple $k\omega_0$ of the frequency ω_0 . Solving this equation yields the following roots

$$\hat{\omega}_{0j} = \frac{1}{k} \left((-1)^{j-1} \cos^{-1}(\rho_k^*) + \left[\frac{j}{2} \right] 2\pi \right), \quad j=1, 2, \dots, k \quad (47)$$

where we have denoted by $[x]$ the largest integer smaller than x . If we dispose of a first, rough frequency estimate $\hat{\omega}_{01}$, then the second frequency estimate corresponds to $j=1 + \left[\frac{k\hat{\omega}_{01}}{\pi} \right]$.

As we will show below by statistical analysis and computer experiments for the GRPHD, the variance of the second estimate is smaller than the variance of the first one. An a priori argument might be as follows.

If the estimator ρ_k^* is unbiased, its variance can be evaluated from:

$$\begin{aligned} \text{var}(\rho_k^*) &= E \left\{ \left(\cos(k\omega_0) - \cos(\hat{\omega}_{0k}) \right)^2 \right\} = E \left\{ \left(\cos(k\omega_0) - \cos(k\hat{\omega}_0) \right)^2 \right\} \\ &= E \left\{ 4 \sin^2 \left(\frac{k(\hat{\omega}_0 + \omega_0)}{2} \right) \sin^2 \left(\frac{k(\hat{\omega}_0 - \omega_0)}{2} \right) \right\}. \end{aligned} \quad (48)$$

For small k and for a good estimation (small $|\hat{\omega}_0 - \omega_0|$), we have

$$\text{var}(\hat{\omega}_0) \approx \frac{\text{var}(\rho_k^*)}{k^2 \sin(k\omega_0)}. \quad (49)$$

In frequency estimation methods such as PHD and RPHD, the variances of the frequency estimates are evaluated in terms of some quantities proportional to the autocorrelation function of the signal, calculated at lags 0, 1, and 2. As we will show later, the variance (49) can also be evaluated in terms of quantities proportional to the signal's autocorrelation function, calculated at lags 0, k , and $2k$. Thus, for a sufficiently large number of data points N , and comparatively small k , $\text{var}(\rho_k^*)$ increases much less with respect to $\text{var}(\rho_1^*)$ than the increase of the denominator in (49) with k .

The variance in (49) is unbounded at frequencies $\omega_{Mi} = i \frac{\pi}{k}$, $i=0, 1, \dots, k$, and minimum at

$$\omega_{mi} = \left(i + \frac{1}{2}\right) \frac{\pi}{k}, \quad i = 0, 1, \dots, k-1. \quad (50)$$

In the two-step procedure, we use N data points and a method such as MC, PHD or RPHD in order to obtain a first estimate $\hat{\omega}_{01}$, and to choose a value of $k \ll N$ such that the first estimate be as close as possible of an ω_{mi} . We then refine the search by using the same N data points in order to estimate the $\rho_k^* = \cos(\hat{\omega}_{0k})$.

We analyzed and tested the two-step procedure by using the RPHD method for the first step, and the GRPHD, to be introduced below, for the second step. In single frequency estimation, the considered signal model is (1), repeated here for convenience:

$$x(n) = s(n) + q(n) = \alpha \cos(\omega_0 + \varphi) + q(n), \quad n = 1, 2, \dots, N \quad (51)$$

where $\alpha > 0$, $\omega_0 \in (0, \pi)$, and φ are the unknown amplitude, frequency and phase of the sinusoid, and $q(n)$ is assumed to be a Gaussian white noise with zero mean and variance σ_q^2 . We denote the signal-to-noise ratio $SNR = \alpha^2 / (2\sigma_q^2)$. The sinusoid is linearly predictable from the past samples according to:

$$s(n) = 2 \cos(k\omega_0) s(n-k) - s(n-2k), \quad k = 1, 2, \dots \quad (52)$$

a fact that suggests the definition of an error function $e_k(n) = x(n) - 2 \cos(k\lambda) x(n-k) + x(n-2k)$, where λ is the parameter to be determined.

However, by generalizing the RPHD method introduced in [so_04], in order to obtain an asymptotically unbiased frequency estimator we must define a modified error function

$$\varepsilon_k(n) = \frac{e_k(n)}{\sqrt{2(2 + \cos(2k\lambda))}}, \quad \text{and the corresponding LS cost function } J_{kN}(\lambda) = \sum_{n=2k+1}^N \varepsilon_k^2(n). \quad \text{Solving}$$

$$\frac{dJ_{kN}(\lambda)}{d\lambda} = 0 \quad \text{yields}$$

$$2A_{kN} \cos^2(k\lambda) - B_{kN} \cos(k\lambda) - A_{kN} = 0 \quad (53)$$

where

$$A_{kN} = \sum_{n=2k+1}^N (x(n) + x(n-2k))x(n-k) \quad (54)$$

$$B_{kN} = \sum_{n=2k+1}^N \left((x(n) + x(n-2k))^2 - 2x^2(n-k) \right). \quad (55)$$

The root of (53) that provides the estimate is

$$\rho_k^* = \frac{B_{kN} + \sqrt{B_{kN}^2 + 8A_{kN}^2}}{4A_{kN}}. \quad (56)$$

The above equations generalize the corresponding results from [so_04], which can be obtained by setting $k=1$.

For a theoretical evaluation of the proposed two-step procedure, we calculated the variance of the new estimate by generalizing the analysis followed in [so_04]. The variance analysis technique is based on the definition of a second order polynomial motivated by (53)

$$f(\rho) = 2A_{kN}\rho^2 - B_{kN}\rho - A_{kN} \quad (57)$$

on (3), and on the following formula [so_04]

$$\text{var}\{\rho_k^*\} \approx \frac{E\{f^2(\rho)\}}{(E\{f'(\rho)\})^2} \Big|_{\rho=\cos(k\omega_0)} \quad (58)$$

By using $\rho = \cos(k\omega_0)$ and (57) we obtain

$$f^2(\rho) \Big|_{\rho=\cos(k\omega_0)} = \cos^2(2k\omega_0)A_{kN}^2 - 2\cos(k\omega_0)\cos(2k\omega_0)A_{kN}B_{kN} + \cos^2(k\omega_0)B_{kN}^2 \quad (59)$$

$$f'(\rho) \Big|_{\rho=\cos(k\omega_0)} = 4\cos(k\omega_0)A_{kN} - B_{kN} \quad (60)$$

In order to compute the variance of $\hat{\omega}_0$ using (49) and (58), the values of $E\{A_{kN}\}$, $E\{B_{kN}\}$, $E\{A_{kN}^2\}$, $E\{B_{kN}^2\}$, and $E\{A_{kN}B_{kN}\}$ are required. The main steps we followed in computing these terms are outlined at the end of this subsection, together with an argument for the unbiasedness of the estimator. We obtained:

$$\begin{aligned} \text{var}\{\hat{\omega}_0\} &\approx \frac{2k + (2 + \cos(2k\omega_0))\beta(k+1, N-k) - 2\beta(k+1, N-2k)}{2k^2 \text{SNR} (N - 2k + \beta(k+1, N-k))^2 \sin^2(k\omega_0)} \\ &\quad - \frac{2\beta(2k+1, N-k) - \beta(2k+1, N-2k)}{2k^2 \text{SNR} (N - 2k + \beta(k+1, N-k))^2 \sin^2(k\omega_0)} \\ &\quad + \frac{(2N-5k)\cos^2(2k\omega_0) + (2N-4k)\cos^2(k\omega_0)}{2k^2 \text{SNR}^2 (N - 2k + \beta(k+1, N-k))^2 (2 + \cos(2k\omega_0))^2 \sin^2(k\omega_0)} \end{aligned} \quad (61)$$

where

$$\begin{aligned} \beta(k_1, k_2) &= \sum_{n=k_1}^{k_2} \cos(2(\omega_0 n + \varphi)) \\ &= \frac{\sin(\omega_0(k_2 - k_1 + 1))\cos(\omega_0(k_2 + k_1) + 2\varphi)}{\sin(\omega_0)} \end{aligned} \quad (62)$$

An asymptotic form of this variance results by formally making $\beta=0$ in (61). Due to the closed-form, simple structure of (61), the asymptotic form brings no major simplifications. Moreover, the dependence of the variance on φ is lost. For $k=1$, this asymptotic variance essentially reduces to the corresponding one calculated in [so_04].

The decrease in the calculated variances for the two-step method as compared to the one-step method is illustrated in Fig.7, where we have plotted the variance (61) versus frequency, for $k=2$, and 3, at $N=20$, $\text{SNR}=10$ dB, and $\varphi=0$. We have also shown (61) for $k=1$ (one-step method). It is clear that,

for every frequency, there exist values of $k > 1$ such that the variance provided by the two-step method is lower than the variance provided by the one-step method. The smallest errors correspond indeed to frequencies around those defined in (50). Similar results are obtained with the asymptotic form of (61).

Computer experiments have been carried out in order to evaluate the proposed two-step method by comparing it with the RPHD method [so_04].

The data sequences for single real, noisy sinusoids were generated using (51), with $\alpha = \sqrt{2}$ and $\varphi = 0$. Different noise variances σ_q^2 were chosen in order to obtain the desired SNRs.

The first step in our method was identical with the RPHD method and gave an initial frequency estimate $\hat{\omega}_{01}$ that corresponded to $k=1$ (although any other estimation method could be used in this first step). The purpose of computer experiments was to prove that one can choose some $k > 1$ for the second step, in order to obtain a better frequency estimate.

We made use of (54)-(56), and (47) with the appropriate value for j , with $k=2$ and 3, for finding the second-step GRPHD estimates. In order to evaluate the frequency estimator performances, the mean square frequency errors (MSFEs) were computed by averaging 500 independent runs. These measured MSFEs for $k=1, 2$ and 3 are represented in the figures that illustrate the experimental results, together with the corresponding variances (61).

In Fig. 7, the MSFEs are plotted versus ω_0 , for $N=20$, $SNR=10$ dB, and $\varphi=0$. Note that, for every frequency, one can choose $k=2$ or $k=3$ in order to get a better frequency estimate than in the case $k=1$. Similar results were obtained for other values of φ .

In Fig. 8, the MSFEs versus SNR are represented, at $\omega_0=0.1\pi$, $N=20$, and $\varphi=0$. The errors are smaller with the two-step method as compared with the one-step method for all values of the SNR . Note the excellent agreement between the calculated and experimental variances, except for very low values of the SNR .

Fig. 9 shows the MSFEs in function of N for $\omega_0=0.1\pi$, $SNR=10$ dB, and $\varphi=0$. It can be noticed the decrease of the variance and of the MSFE for all values of N . Experiments have been performed for various values of φ , with similar results.

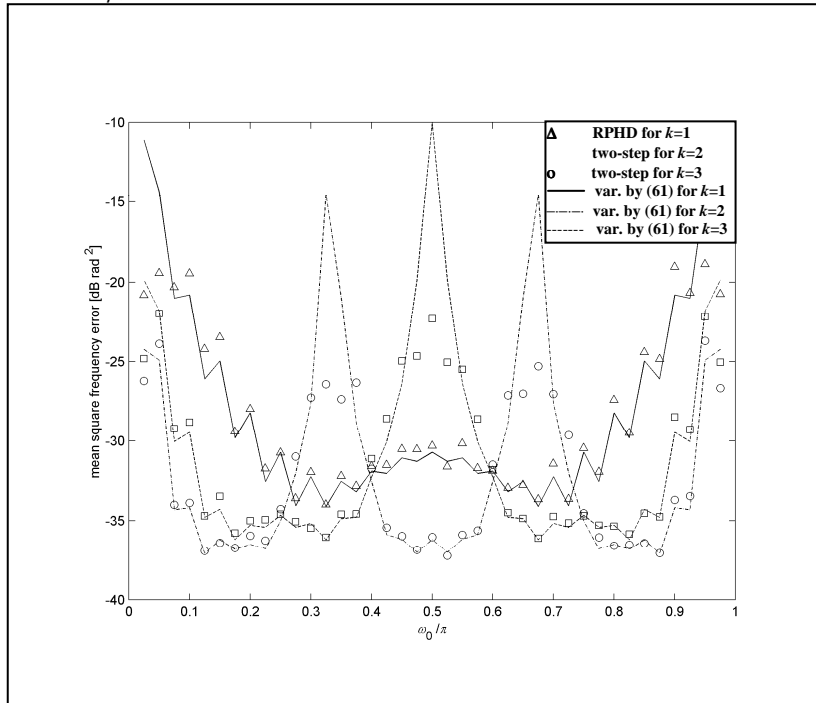


Fig. 7. Mean square frequency errors and variances versus ω_0 at $SNR=10$ dB, $N=20$, and $\varphi=0$.

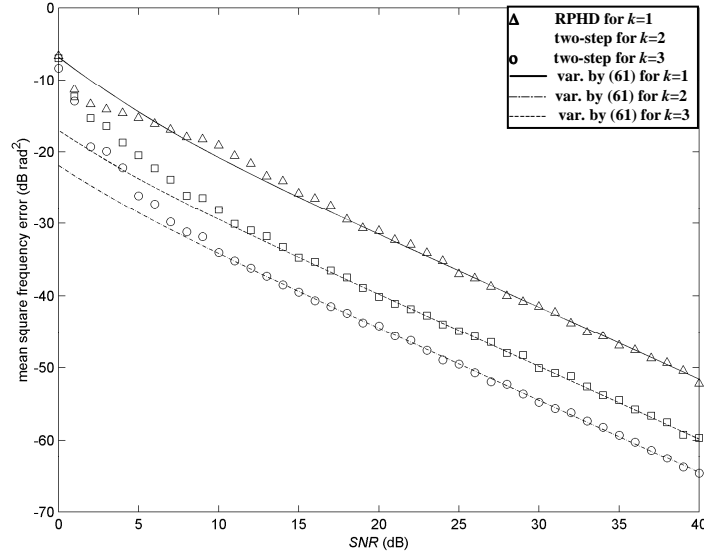


Fig. 8. Mean square frequency errors and variances versus SNR at $\omega_0=0.1\pi$, $N=20$, and $\varphi=0$.

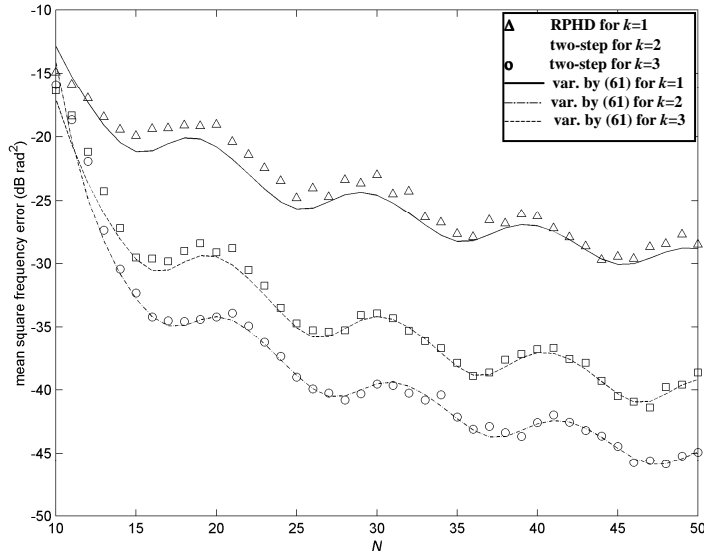


Fig. 9. Mean square frequency errors and variances versus N at $\omega_0=0.1\pi$, $SNR=10$ dB, and $\varphi=0$.

We present now the derivation of the mathematical expressions used above. The quantities A_{kN} and B_{kN} can be written as sums of three uncorrelated terms. For example, we can use (51), (52), (53) and (62) in order to get $A_{kN}=T_{A1}+T_{A2}+T_{A3}$, with

$$\begin{aligned}
 T_{A1} &= \sum_{n=2k+1}^N 2\alpha^2 \cos(k\omega_0) \cos^2(\omega_0(n-k) + \varphi) \\
 &= \alpha^2 (N - 2k + \beta(k+1, N-k)) \cos(k\omega_0)
 \end{aligned} \tag{63}$$

$$T_{A_2} = \sum_{n=2k+1}^N \alpha \cos(\omega_0(n-k) + \varphi) \times (2 \cos(k\omega_0)q(n-k) + q(n) + q(n-2k)). \quad (64)$$

$$T_{A_3} = \sum_{n=2k+1}^N q(n-k)(q(n) + q(n-2k)). \quad (65)$$

We have $E\{T_{A_2}\} = E\{T_{A_3}\} = 0$, and $E\{A_{kN}\} = E\{T_{A_1}\} = T_{A_1}$.

In order to calculate $E\{A_{kN}^2\}$, we note that $E\{T_{A_i}T_{A_j}\} = 0$ for $i \neq j$. Therefore

$$E\{A_{kN}^2\} = T_{A_1}^2 + E\{T_{A_2}^2\} + E\{T_{A_3}^2\}. \quad (66)$$

The second term in the RHS of (66) can be evaluated as follows

$$\begin{aligned} E\{T_{A_2}^2\} &= \sum_{n=2k+1}^N \alpha^2 \cos^2(\omega_0(n-k) + \varphi) \times \left[4 \cos^2(k\omega_0) E\{(q(n-k))^2\} \right. \\ &\quad \left. + E\{(q(n))^2\} + E\{(q(n-2k))^2\} \right] \\ &\quad + 2 \sum_{n=2k+1}^N \sum_{m=n+1}^N \alpha^2 \cos(\omega_0(n-k) + \varphi) \cos(\omega_0(m-k) + \varphi) \\ &\quad \times E\{(2 \cos(\omega_0 k)q(n-k) + q(n) + q(n-2k)) \\ &\quad \times (2 \cos(\omega_0 k)q(m-k) + q(m) + q(m-2k))\} \\ &= \sum_{n=2k+1}^N \alpha^2 \frac{1 + \cos(2\omega_0(n-k) + 2\varphi)}{2} (4 \cos^2(k\omega_0)\sigma_q^2 + 2\sigma_q^2) + \\ &\quad + \sum_{n=2k+1}^N \sum_{m=n+1}^N \alpha^2 [\cos(\omega_0(n+m-2k) + 2\varphi) + \cos(\omega_0(m-n))] \\ &\quad \times [2 \cos(\omega_0 k) E\{q(n-k)q(m-2k)\} + 2 \cos(\omega_0 k) E\{q(n)q(m-k)\} \\ &\quad + E\{q(n)q(m-2k)\}]. \end{aligned}$$

Hence:

$$\begin{aligned} E\{T_{A_2}^2\} &= \alpha^2 \sigma_q^2 [4N - 10k + (4N - 12k) \cos(2k\omega_0) \\ &\quad + \beta(k+1, N-k)(2 + \cos(2k\omega_0)) + 2\beta(k+1, N-2k) \\ &\quad + 2\beta(2k+1, N-k) + \beta(2k+1, N-2k)]. \end{aligned} \quad (67)$$

With similar calculations, the expression of the last term in the RHS of (66) can be shown to be $E\{T_{A_3}^2\} = (4N - 10k)\sigma_q^4$, so that

$$\begin{aligned}
E\{A_{kN}^2\} &= \alpha^4 (N - 2k + \beta(k + 1, N - k))^2 \cos^2(k\omega_0) \\
&+ \alpha^2 \sigma_q^2 [4N - 10k + (4N - 12k) \cos(2k\omega_0)] \\
&+ \beta(k + 1, N - k) (2 + \cos(2k\omega_0)) + 2\beta(k + 1, N - 2k) + 2\beta(2k + 1, N - k) \\
&+ \beta(2k + 1, N - 2k)] + \sigma_q^4 (4N - 10k).
\end{aligned} \tag{68}$$

The steps we followed in order to calculate $E\{B_{kN}\}$ and $E\{B_{kN}^2\}$ are similar to those presented above, and will be skipped for brevity. The results are

$$E\{B_{kN}\} = \alpha^2 (N - 2k + \beta(k + 1, N - k)) \cos(2k\omega_0) \tag{69}$$

$$\begin{aligned}
E\{B_{kN}^2\} &= \alpha^4 (N - 2k + \beta(k + 1, N - k))^2 \cos^2(2k\omega_0) \\
&+ \alpha^2 \sigma_q^2 [4N + 4(N - 4k) \cos(4k\omega_0) + 8\beta(k + 1, N - k) (2 + \cos(2k\omega_0)) \\
&- 16\beta(k + 1, N - 2k) - 16\beta(2k + 1, N - k) \\
&+ 8\beta(2k + 1, N - 2k) (1 + \cos(2k\omega_0))] + \sigma_q^4 (4N - 8k).
\end{aligned} \tag{70}$$

Based on the decomposition of A_{kN} and B_{kN} in sums of three uncorrelated terms, it can be shown that $E\{A_{kN} B_{kN}\} = T_{C1} + T_{C2} + T_{C3}$, with

$$T_{C1} = \alpha^4 \cos(k\omega_0) \cos(2k\omega_0) (N - 2k + \beta(k + 1, N - k))^2 \tag{71}$$

$$\begin{aligned}
T_{C2} &= \alpha^2 \sum_{n=2k+1}^N \sum_{m=2k+1}^N 4 \cos(\omega_0(n-k) + \varphi) \cos(\omega_0(m-k) + \varphi) \\
&\times E\{(2 \cos(k\omega_0) q(n-k) + q(n) + q(n-2k)) \\
&\times (\cos(k\omega_0) (q(m) + q(m-2k) - q(m-k)))\}
\end{aligned} \tag{72}$$

$$\begin{aligned}
T_{C3} &= E\left\{ \sum_{n=2k+1}^N \sum_{m=2k+1}^N q(n-k) (q(n) + q(n-2k)) \right. \\
&\left. \times (q^2(m) + q^2(m-2k) + 2q(m)q(m-2k) - 2q^2(n-k)) \right\} = 0.
\end{aligned} \tag{73}$$

After performing the calculations we obtained

$$\begin{aligned}
E\{A_{kN} B_{kN}\} &= \alpha^4 (N - 2k + \beta(k + 1, N - k))^2 \cos(k\omega_0) \cos(2k\omega_0) \\
&+ \alpha^2 \sigma_q^2 \left[(4N - 14k) (\cos(k\omega_0) + \cos(3k\omega_0)) + 2(\beta(k + 1, N - 2k) \right. \\
&\left. + \beta(2k + 1, N - k)) \frac{\cos(2k\omega_0)}{\cos(k\omega_0)} + 4\beta(2k + 1, N - 2k) \cos(k\omega_0) \right].
\end{aligned} \tag{74}$$

The proof that $\rho_k^* = \cos(\hat{\omega}_{0k})$ is asymptotically unbiased is a generalized version of the proof introduced in [so_04] for the case $k=1$. Namely, a first order Taylor series evaluation of f at ρ_k^* starting from f at $\rho_k = \cos(k\omega_0)$ gives

$$f(\rho_k^*) = 0 = f(\cos(k\omega_0)) + (\rho_k^* - \cos(k\omega_0))f'(\cos(k\omega_0)),$$

wherefrom: $\cos(\hat{\omega}_{0k}) = \cos(k\omega_0) - \frac{f(\rho)}{f'(\rho)} \Big|_{\rho=\cos(k\omega_0)}$. Therefore it must be proved that

$\lim_{N \rightarrow \infty} \frac{f(\rho)}{f'(\rho)} \Big|_{\rho=\cos(k\omega_0)} = 0$. The proof is based on the ergodic and statistical properties of the signal and noise, and the main steps can be outlined as follows:

$$\begin{aligned} \lim_{N \rightarrow \infty} \frac{f(\rho)}{f'(\rho)} \Big|_{\rho=\cos(k\omega_0)} &= \lim_{N \rightarrow \infty} \frac{A_{kN} \cos(2k\omega_0) - B_{kN} \cos(k\omega_0)}{4A_{kN} \cos(k\omega_0) - B_{kN}} \\ &= \frac{0}{\alpha^2 (4\cos^2(k\omega_0) - \cos(2k\omega_0)) + 0} = 0. \end{aligned}$$

The proposed solution for decreasing the errors in the estimation of the frequency of a sinusoid embedded in additive, gaussian white noise by means of a two-step procedure works equally well for other estimators than RPHD.

A similar study has been carried out starting from the Pisarenko Harmonic Decomposition [07_04_S]. A rough PHD estimation has been performed in the first step, and a multiple of the unknown frequency has been estimated in the second step. The variance of the PHD estimator has been significantly reduced in this way.

C. Frequency Estimation by an Iterative Procedure

We have proposed an iterative algorithm for estimating the frequency of a real sinusoid embedded in additive noise. The Pisarenko harmonic decomposer (PHD) [sakai_84, chan_03, pis_73, eri_93], and the reformed Pisarenko harmonic decomposer (RPHD) [so_04, so_02_a, so_02_b] are among the algorithms that perform well and are computationally efficient in this case.

The theory for both the above mentioned algorithms assumes a white noise. We have introduced an iterative method designed to improve the performance of the RPHD such that frequency error variances close to the Cramer-Rao lower bound (CRLB) are obtained for signal-to-noise ratios (SNR) as low as 3 dB in a few iterations [09_03_S]. An iteration consists of filtering the initial data sequence with a frequency selective filter whose maximum of the frequency response is at the frequency estimate obtained in the previous iteration and in computing a better frequency estimate based on the data sequence at the filter output by means of the RPHD. Although the noise in the filtered sequence is no more white, experiments show that the considered estimators perform well in this case too.

We consider again the signal model of a sinusoid embedded in white noise:

$$x(n) = s(n) + q(n) = \alpha \cos(\omega_0 n + \varphi) + q(n), \quad n = 1, 2, \dots, N \quad (75)$$

where $\alpha > 0$, $\omega_0 \in (0, \pi)$ and φ are the deterministic but unknown amplitude, (angular) frequency and phase of the sinusoid respectively, and $q(n)$ is a zero-mean Gaussian white noise of variance σ^2 .

The signal-to-noise ratio is

$$SNR_0 = \frac{\alpha^2}{2\sigma^2}. \quad (76)$$

In order to estimate the frequency we propose the following procedure: we initialize the algorithm by using the RPHD for the calculation of an initial estimate $\hat{\omega}_0$ for ω_0 ; then we start iterations such that, at iteration $k \geq 1$, we filter the initial data sequence with a selective filter centered at the frequency estimated at iteration $k-1$, $\hat{\omega}_{k-1}$, and we apply to the signal from the filter output the RPHD in order to calculate a new frequency estimate $\hat{\omega}_k$.

The purpose of filtering the data sequence is to increase the SNR. The filtered signal contains a colored noise component that does not fit into the theory of the frequency estimation algorithm we have mentioned, so that its performance has to be tested for this case.

We have considered the second-order noise rejection filter with the following transfer function:

$$H(z) = \frac{z^2}{z^2 - 2\rho \cos(\omega_r)z + \rho^2} \quad (77)$$

where ρ is a parameter close to unity in order to provide selectivity (but smaller, for stability) and, at each iteration k of the algorithm we have made $\omega_r = \hat{\omega}_{k-1}$.

The performance of the noise-rejection filter can be illustrated by evaluating the enhancement η of the SNR

$$\eta = \frac{SNR_1}{SNR_0} \quad (78)$$

where $SNR_1 = \frac{P_{1s}}{P_{1q}}$ is defined at the filter output and SNR_0 has been defined in (7) (we have denoted

by P_{1s} and P_{1q} the signal power and noise power at the filter output respectively). For evaluation purposes, we consider $\omega_r = \omega_0$.

Denoting further by $P_s(\omega) = \frac{\pi A^2}{2} [\delta(\omega - \omega_0) + \delta(\omega + \omega_0)]$ and $P_q(\omega) = \sigma^2$ the power spectral densities of the signal and noise defined in (1) respectively, and by taking into account their statistical independence, we have

$$P_{1s} = \frac{1}{2\pi} \int_{-\pi}^{\pi} |H(e^{j\omega})|^2 P_s(\omega) d\omega = \frac{\alpha^2}{2(1-\rho)^2 \left((1+\rho)^2 - 4\rho \cos^2 \omega_0 \right)} \quad (79)$$

$$P_{1q} = \frac{1}{2\pi} \int_{-\pi}^{\pi} |H(e^{j\omega})|^2 P_q(\omega) d\omega = \frac{\sigma^2(1+\rho^2)}{(1-\rho^2)(\rho^4 - 2\rho^2 \cos(2\omega_0) + 1)}. \quad (80)$$

The integral in (79) is a simple application of the properties of the Dirac pulse, while the integral in (80) can be calculated by means of the residuum theory as follows.

Let

$$H(z) = \frac{1}{1 - 2\rho \cos \omega_0 z^{-1} + \rho^2 z^{-2}} = \frac{z^2}{z^2 - 2\rho \cos \omega_0 z + \rho^2}$$

and

$$\begin{aligned} I_n &= 2\pi J_n = \int_{-\pi}^{\pi} |H(e^{j\omega})|^2 e^{j\omega n} d\omega \\ &= \int_{-\pi}^{\pi} H(e^{j\omega}) H^*(e^{j\omega}) d\omega = \int_{-\pi}^{\pi} H(e^{j\omega}) H(e^{-j\omega}) e^{j\omega n} d\omega \end{aligned}$$

With the substitution $e^{j\omega} = z$ one gets

$$\begin{aligned} I_n &= \int_{|z|=1} H(z) H\left(\frac{1}{z}\right) \frac{z^{n-1}}{j} dz = \int_{|z|=1} \frac{\frac{z^{n+1}}{j\rho^2}}{(z - \rho e^{j\omega_0})(z - \rho e^{-j\omega_0}) \left(z - \frac{e^{j\omega_0}}{\rho}\right) \left(z - \frac{e^{-j\omega_0}}{\rho}\right)} dz = \\ &= 2\pi j \sum_{|z_i| < 1} \text{rez}(z_i). \end{aligned}$$

The integrand has two poles inside the unit circle, namely $z_{1,2} = \rho e^{\pm j\omega_0}$, as $|\rho| < 1$. The residuum in z_1 is

$$\begin{aligned} R_1 &= \frac{\rho^{n+1} e^{j(n+1)\omega_0}}{j\rho^2 (\rho e^{j\omega_0} - \rho e^{-j\omega_0}) \left(\rho e^{j\omega_0} - \frac{e^{j\omega_0}}{\rho}\right) \left(\rho e^{j\omega_0} - \frac{e^{-j\omega_0}}{\rho}\right)} = \\ &= \frac{\rho^n \left[\rho^2 \cos((n-1)\omega_0) - \cos((n+1)\omega_0) \right] + j\rho^n \left[\rho^2 \sin((n-1)\omega_0) - \sin((n+1)\omega_0) \right]}{2 \sin \omega_0 (1 - \rho^2) (\rho^4 - 2\rho^2 \cos(2\omega_0) + 1)}. \end{aligned}$$

The residuum in $z_2 = \rho e^{-j\omega_0}$ turns out to be $R_2 = -R_1^*$. Therefore

$I_n = 2\pi J_n = 2\pi j (R_1 + R_2) = -4\pi \text{Im}(R_1)$. After substitution, one gets

$$J_n = \rho^n \frac{\sin((n+1)\omega_0) - \rho^2 \sin((n-1)\omega_0)}{\sin \omega_0 (1 - \rho^2) (\rho^4 - 2\rho^2 \cos(2\omega_0) + 1)}.$$

Simpler approximate expression for (79) and (80) are obtained by taking into account that $\rho < 1, \rho \cong 1$. The above results become:

$$P_{1s} \cong \frac{\alpha^2}{8(1 - \rho)^2 \sin^2 \omega_0} \quad (81)$$

$$P_{1q} \cong \frac{\sigma^2}{4(1 - \rho) \sin^2 \omega_0}. \quad (82)$$

Finally, using (78), (81) and (82) we get

$$\eta = \frac{1}{1 - \rho}. \quad (83)$$

Equation (83) reveals an important increase of the signal-to-noise ratio if we take into account the range of ρ ($\rho < 1, \rho \cong 1$). These noise rejection properties of the filter and the fact that, due to the good estimation provided by the RPHD, the estimated frequency does not differ significantly from the true frequency are in support of an iterative procedure that consists of computing $\hat{\omega}_k, k = 1, 2, \dots$ by using the signal at the filter output, with the previous estimate $\hat{\omega}_{k-1}$ substituted for the parameter ω_r in the expression of the frequency response. The variance of the estimator decreases at each iteration as the estimated frequency approaches gradually the true frequency. These a priori arguments are confirmed by experimental results presented next.

Computer experiments have been performed in order to evaluate the proposed iterative procedure. For frequency estimation, at each step of the algorithm we used the RPHD method [so_04]. The data sequence for single real, noisy sinusoids was generated using (85) with $\alpha = \sqrt{2}$ and $\varphi = 0$. Relatively low signal-to-noise ratios were chosen in order to prove the efficiency of the noise rejection filter. We compared the estimates resulted from the iterative procedure after one iteration ($k = 1$) and $k = 5$ iterations, to the RPHD method (corresponding to the initialization step of the algorithm) and to the CRLB [kay_93]. The parameter ρ was chosen experimentally. The simulation results presented below are averages of 1000 independent runs.

The results illustrated in Figs. 10 and 11 indicate the decrease of the mean square frequency errors with the number of iterations. After five iterations, the estimator performance approaches the CRLB. The larger SNR for the situation in Fig. 10 with respect to the one in Fig. 11 allowed for a smaller number of signal samples. Generally, a larger value of the SNR allows for a smaller number of signal samples and a value of ρ closer to 1 for achieving good estimates in a low number of iterations. However, at large SNR's, use of iterative algorithms has no justification, as the RPHD performs equally well.

Note that the frequency dependency of the mean square error, which occurs in real sinusoid frequency estimation, tends to decrease with the number of iterations.

The simulation results indicate that the desired performance of the algorithm is achieved in a few iterations. Consequently, the additional computation complexity introduced by iterations does not change the order of magnitude of the complexity of the original estimation method. In our examples, the RPHD (used at the initialization of the algorithm and then at each iteration) takes $3N-4$ real multiplications, $4N-8$ real additions and 5 other operation that are usually implemented by ROM accesses. Additionally, each iteration involves $2N-2$ real multiplications and $2N-3$ real additions for filtering and an RPHD. Therefore, for k iterations, the algorithm takes $(5k+3)N-6k-4$ real multiplications, $(6k+4)N-11k-8$ real additions and $5k+5$ other operations. As shown above, a value of $k=5$ is sufficient for achieving a good performance.

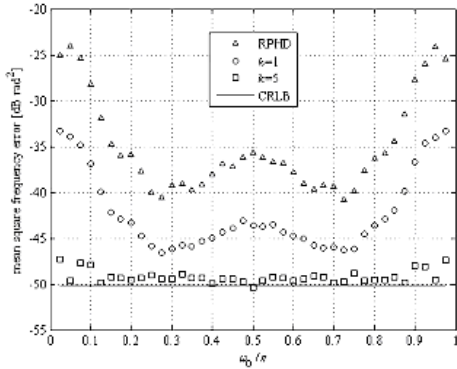


Fig. 10: Mean square frequency errors versus frequency for $N=50$, $\text{SNR}=10$ dB, $\rho=0.98$.

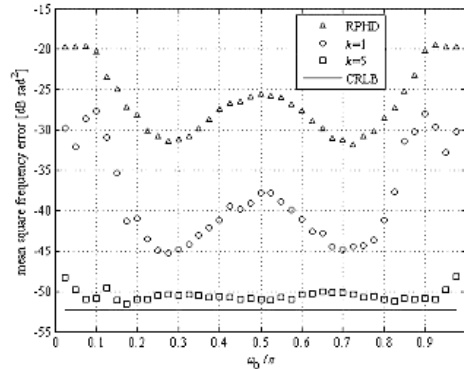


Fig. 11: Mean square frequency errors versus frequency for $N=100$, $\text{SNR}=3$ dB, $\rho=0.95$.

In conclusion, the algorithm we have proposed started from a known, single-step method (RPHD). We have used that method as a first step of the algorithm, then filtered the initial data sequence with a frequency selective filter centered on that estimate and used again that method on the filtered data in order to obtain the next estimate. This process has then been iterated.

Filtering has been introduced in order to significantly improve the signal-to-noise ratio. Although after filtering the noise is colored, experimental results show that the RPHD still provides good frequency estimates.

Experiments indicate that this iterated procedure leads to an estimated frequency with a mean square error close to the CRLB, significantly improving the initial, first-step estimate in just a few iterations (below ten, typically five). As the number of iterations is low, the asymptotic complexity of the algorithm is the same as in the initial method.

D. Analysis of the Iterative Frequency Estimation Algorithm

We have shown that the algorithm we have introduced in [09_03_S] and reviewed in the preceding section has connections with the constrained notch filter approach [sav_03, qui_91]. We have derived an asymptotic cost function and we have evaluated the bias. We have devised a procedure for computing the variance and compared the result to experimentally obtained data [09_04_S]. These results will be outlined below.

We consider again the signal model (75) and the definition of the SNR (76).

The RPHD is an asymptotically unbiased estimator, and a certain bias exists in the small sample case [so_04]. In the following, we will analyze the asymptotic behavior of the estimator consisting of the application of the RPHD to a filtered version of (75), the filter having the transfer function (77). We will refer to this estimator as Filtered RPHD (FRPHD).

The signal at the filter output is

$$y(n) = r(n) + v(n) = \alpha H_0 \cos(\omega_0 n + \varphi + \psi_0) + v(n), \quad (84)$$

where $H_0 e^{j\psi_0} = H(e^{j\omega_0})$, and $v(n)$ is a colored, Gaussian noise. The FRPHD consists of the application of the RPHD to $y(n)$, which is equivalent to the minimization of the following cost function

$$J(\lambda) = \sum_{n=1}^N \frac{\varepsilon^2(n)}{2(2 + \cos(2\lambda))} \quad (85)$$

with respect to λ [sav_03, so_04]. The error signal $\varepsilon(n)$ is related to $y(n)$ through

$$\varepsilon(n) = y(n) - 2\cos(\lambda)y(n-1) + y(n-2), \quad (86)$$

which is a filtering operation with a filter having the transfer function $G(z) = 1 - 2\cos(\lambda)z^{-1} + z^{-2}$. Therefore, $\varepsilon(n)$ is obtained from the initial signal $x(n)$ in (75) by filtering with the cascade of $G(z)$ and $H(z)$, giving an equivalent transfer function

$$F(z) = G(z)H(z) = \frac{z^2 - 2\cos(\lambda)z + 1}{z^2 - 2\rho\cos(\omega_r)z + \rho^2}. \quad (87)$$

It is relevant to compare (87) to the transfer function of a *constrained notch filter* [sav_03]:

$$F_1(z) = \frac{z^2 - 2\cos(\lambda)z + 1}{z^2 - 2\rho\cos(\lambda)z + \rho^2}, \quad 0 < \rho < 1. \quad (88)$$

Clearly, $F(z)$ is obtained from $F_1(z)$ by substituting the variable λ at the denominator with an estimate of ω_0 , namely ω_r . It is known that the infinite impulse response (IIR) structure of the notch filter does not allow for obtaining a closed form expression of the estimator. Our approach relaxes one constraint, allowing for the application of the closed form RPHD estimator, at the cost of the necessity of a first coarse estimation for initializing the ω_r .

We will derive now the asymptotic form of the cost function (85). By the Wiener-Khinchin theorem, the asymptotic counterpart of (85) is related to the power spectral density of $\varepsilon(n)$, denoted $P_\varepsilon(\omega)$, through [sav_03]

$$\begin{aligned} J_a(\lambda) &= \lim_{N \rightarrow \infty} \frac{1}{N} \sum_{n=1}^N \frac{\varepsilon^2(n)}{2(2 + \cos(2\lambda))} \\ &= \frac{1}{2(2 + \cos(2\lambda))} \times \frac{1}{2\pi} \int_{-\pi}^{\pi} P_\varepsilon(\omega) d\omega. \end{aligned} \quad (89)$$

Due to the above mentioned filtering operation, we have

$$P_{\varepsilon}(\omega) = P_x(\omega) \left| F(e^{j\omega}) \right|^2. \quad (90)$$

The input signal power spectral density has the two statistically independent components from (75): $P_x(\omega) = P_s(\omega) + P_q(\omega)$. The asymptotic cost function can be split in two parts accordingly:

$$J_a(\lambda) = J_s(\lambda) + J_q(\lambda). \quad (91)$$

The calculation of the first component involves applications of simple properties of the Dirac pulse:

$$\begin{aligned} J_s(\lambda) &= \frac{1}{2(2 + \cos(2\lambda))} \\ &\times \frac{1}{2\pi} \int_{-\pi}^{\pi} \frac{\pi\alpha^2}{2} [\delta(\omega - \omega_0) + \delta(\omega + \omega_0)] \left| F(e^{j\omega}) \right|^2 d\omega \\ &= \frac{\alpha^2}{8(2 + \cos(2\lambda))} \left[\left| F(e^{j\omega_0}) \right|^2 + \left| F(e^{-j\omega_0}) \right|^2 \right]. \end{aligned}$$

By plugging the expression of F taken from (87) we get, after some calculations:

$$\begin{aligned} J_s(\lambda) &= \frac{\alpha^2}{(2 + \cos(2\lambda))} \\ &\times \frac{(\cos \lambda - \cos \omega_0)^2}{(1 + \rho^2 - 2\rho \cos(\omega_0 - \omega_r))(1 + \rho^2 - 2\rho \cos(\omega_0 + \omega_r))}. \end{aligned} \quad (92)$$

Note that $J_s \geq 0$, so that its minimum is reached at $\lambda = \omega_0$.

The second component of the asymptotic cost function is

$$J_q(\lambda) = \frac{1}{2(2 + \cos(2\lambda))} \times \frac{1}{2\pi} \int_{-\pi}^{\pi} \sigma^2 \left| F(e^{j\omega}) \right|^2 d\omega \quad (93)$$

The calculation of this integral involves complex functions, integration over the unit circle and residues theory [con_78]. The result is

$$\begin{aligned} J_q(\lambda) &= \frac{\sigma^2}{2(2 + \cos(2\lambda))\rho^2} \\ &\times \left\{ 1 - \frac{[1 + \rho^6 - 2\rho^2(1 + \rho^2)(2 + \cos(2\lambda))]\sin \omega_r + 8\rho^3 \cos \lambda \sin(2\omega_r) - \rho^2(1 + \rho^2)\sin(3\omega_r)}{(1 - \rho^2)(\rho^4 - 2\rho^2 \cos(2\omega_r) + 1)\sin \omega_r} \right\} \end{aligned} \quad (94)$$

The shape of the asymptotic cost function for some specific values of the parameters is reported in Fig. 12. Its most important feature is the presence of a well defined minimum; the value of λ at which the minimum occurs is the estimate of the frequency. The displacement of the estimate with respect to the true frequency is the bias, caused by the presence of the term J_q in the cost function (91).

As already mentioned, the RPHD is an asymptotic unbiased estimator, but it has some bias in the small sample case. As experiments show that the mean square error decreases when the FRPHD is applied after the RPHD such that the CRLB is almost reached after a few iterations, it might be expected that the bias greatly decreases too. In order to test this hypothesis we performed the following experiment. We applied 500 times the RPHD to the data with the values of the parameters shown in Fig. 13 (finite sample case, $N=200$). We calculated the means of the estimated frequencies and used these values for evaluating their bias with respect to the true frequencies and for setting the

parameter ω_r of the filter. Finally, we found the minima of the asymptotic cost function ($N \rightarrow \infty$) in order to estimate again the frequencies (with higher precision), and used the results for calculating the bias with respect to the true frequencies. The results reported in Fig. 13 indicate indeed an important decrease of the bias and explain why it becomes insignificant after a few iterations. Note the small value of the SNR (-3dB) allowed by the use of the asymptotic form of the cost function.

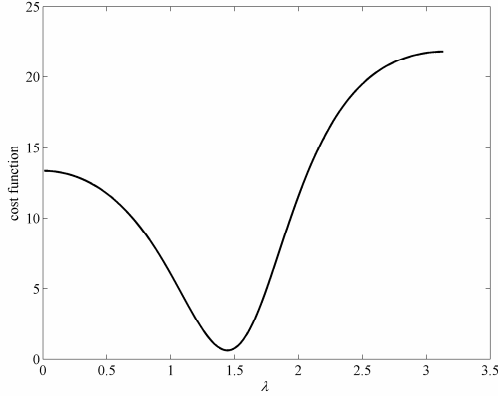


Fig.12. Asymptotic cost function of the FRPHD (one iteration); $SNR=-3$ dB, $\omega_0=4\pi/9$, $\omega_r=\omega_0+0.1$, $\varphi=\pi/8$.

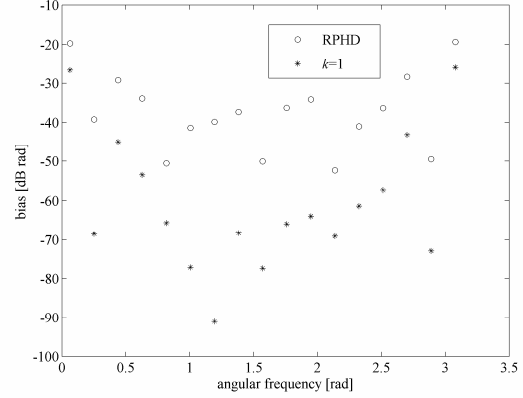


Fig. 13. Small sample bias for the RPHD and asymptotic bias for the filtered RPHD (one iteration); $SNR=-3$ dB, $N=200$; $\xi=0.98$, $\varphi=\pi/8$.

The variance of the RPHD estimator at the filter output when its center frequency ω_r is known can be calculated from [so_04]

$$\text{var}(\hat{\omega}_0) = \frac{E\{A_N^2\} \cos^2(2\omega_0) + E\{B_N^2\} \cos^2(\omega_0) - 2E\{A_N B_N\} \cos(2\omega_0) \cos(\omega_0)}{(4E\{A_N\} \cos(\omega_0) - E\{B_N\})^2 \sin^2(\omega_0)}, \quad (95)$$

where $E\{\cdot\}$ denotes mathematical expectation and

$$\begin{aligned} A_N &= \sum_{n=3}^N (y(n) + y(n-2)) y(n-1), \\ B_N &= \sum_{n=3}^N ((y(n) + y(n-2))^2 - 2y^2(n-1)). \end{aligned} \quad (96)$$

In order to evaluate the expectations, we introduce the following functions

$$\begin{aligned} P(n_1, n_2) &= E\left\{ \sum_{n=3}^N y(n-n_1) y(n-n_2) \right\}, \\ Q(n_1, n_2, m_1, m_2) &= E\left\{ \sum_{n=3}^N \sum_{m=3}^N y(n-n_1) y(n-n_2) y(m-m_1) y(m-m_2) \right\}. \end{aligned} \quad (97)$$

For P we have

$$\begin{aligned}
P(n_1, n_2) &= A^2 \sum_{n=2k+1}^N \cos(\omega_0(n-n_1)+\psi)\cos(\omega_0(n-n_2)+\psi) \\
&\quad + (N-2k)R(n_1-n_2),
\end{aligned} \tag{98}$$

where $A = \alpha H_0$, $\psi = \varphi + \psi_0$ and $R(n)$ is the correlation function of the noise at the filter output, whose expression can be calculated by taking the inverse Fourier transform of the power spectral density. We obtained

$$R(n) = \sigma^2 \frac{\rho^{|n|} \left\{ \sin[\omega_r(|n|+1)] - \rho^2 \sin[\omega_r(|n|-1)] \right\}}{\sin(\omega_r)(1-\rho^2) [\rho^4 - 2\rho^2 \cos(2\omega_r) + 1]}. \tag{99}$$

The expectations of A_N and B_N are

$$\begin{aligned}
E\{A_N\} &= P(0,1) + P(2,1), \\
E\{B_N\} &= P(0,0) + P(2,2) + 2P(0,2) - 2P(1,1).
\end{aligned} \tag{100}$$

(A closed form can be easily derived for the summation in (18).)

Similar expressions can be obtained for Q , by taking into account that higher order moments of a jointly Gaussian process can be expressed in terms of R . We skip these expressions for brevity. Then, we have

$$E\{A_N^2\} = Q(0,1,0,1) + Q(0,1,2,1) + Q(2,1,0,1) + Q(2,1,2,1) \tag{101}$$

In the same way, $E\{A_N B_N\}$ and $E\{B_N^2\}$ can be expressed in terms of Q .

We applied this procedure for evaluating the variance for both the RPHD (when y must be substituted by x and the power spectral density is σ^2) and the FRPHD for the situation in Fig. 14 (note the low value of the SNR). First the variance of the RPHD has been calculated theoretically and then the experimental mean square error has been computed by using 500 independent computer runs (the small sample bias can be neglected). The results in Fig. 14 are expectable, and in agreement with [sO_04]. The averages of the estimated frequencies have been used for setting the ω_r of the filters and the frequencies have been estimated again in 500 independent runs. The MSE 's have been calculated and represented on Fig. 14, together with the variance evaluated theoretically with the procedure presented in this paragraph and the CRLB [kay_93]. The two results are again in good agreement and show how the variances of the estimations decrease when filtering is applied.

The experiments we have performed and the theory we have developed show that the algorithm we have introduced provides estimates with MSE 's close to the CRLB after a few iterations in the case of signals with low values of the SNR . Furthermore, its low complexity allows for real-time applications. Experiments have shown that the algorithm does not improve significantly the results obtained with the existing, lower complexity ones at high values of the SNR .

We showed that our algorithm may be viewed as an extension of the constrained notch filter method, the difference being a larger number of degrees of freedom in choosing the filter coefficients. This approach also provided closed-form frequency estimators, the lack of which is a drawback of the constrained notch filter method.

We calculated the asymptotic cost function and showed that the bias decreased after the filtering operation. We have also shown, both theoretically and experimentally, that the variances of the frequency estimates obtained after the filtering operation are much lower than the variances of the estimates obtained in the first step of the algorithm. This result confirms the experimental evidence showing that the variances of the estimates approach the CRLB after a few iterations of the algorithm.

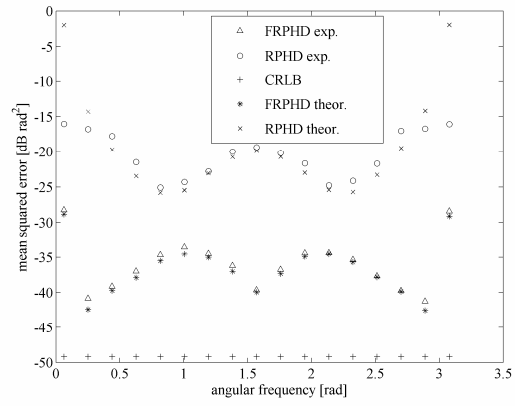


Fig. 14. Mean squared errors for $N=100$, $\zeta=0.8$, $\alpha^2=2$, $\varphi=\pi/8$, $SNR=0$ dB.

We have tested the iterative algorithm and performed an analysis in the case transfer function of the filter other than (77) and obtained similar results as those presented in the last two sections [09_05_S].

2.5. Sampling Theory for Multidimensional Signals

A research topic we have approached is the sampling theory of 2D signals. We have tackled both band-limited finite energy and periodic models. Some results are presented in this and the next subsections.

A. Sampling Theorem for 2D Periodic Signals

We have approached a multi-channel sampling scheme for 2D, band-limited, not necessarily orthogonally periodic signals in order to obtain a generalized sampling expansion [94_02_S].

The well-known Shannon sampling theorem, which applies to band-limited, finite energy signals, has been extended by Papoulis to the m^{th} -order generalized sampling expansion (GSE [cheung_93, p. 86]). The initial work of Papoulis (see e.g. [pap_81]) has been further extended to multidimensional signals [brown_89, brown_91]. A thorough discussion of the subject can be found in [cheung_93].

If the signal to be sampled is periodic, with period T , then the L^2 theory does not apply. However, if it is band-limited, then its spectrum is discrete, with finite support and the signal can be expressed as a trigonometric polynomial

$$x(t) = \sum_{k=-N}^N c_k e^{jk \frac{2\pi}{T} t}.$$

The following sampling expansion holds [spat_87]:

$$x(t) = \sum_{n=0}^{2N} x(nT_E) \frac{\sin[\pi(t/T_E - n)]}{(2N+1) \sin\left[\frac{\pi(t/T_E - n)}{2N+1}\right]}, \quad T_E = \frac{T}{2N+1}.$$

The same result holds if $x(t)$ is of finite duration and it can be expressed on the support interval as a trigonometric polynomial.

We have provided a GSE for 2D, band-limited, doubly periodic signals by generalizing the above sampling expansion. The idea of dealing with such signals forces one to use as a signal model a trigonometric polynomial as in (1) below.

Let us consider a 2D, band-limited, complex valued signal, defined on R^2 , which is doubly periodic (in two independent directions)

$$x(\mathbf{t}) = \sum_{\mathbf{n} \in R_N} a(\mathbf{n}) e^{j2\pi \mathbf{n}' \mathbf{V}^{-1} \mathbf{t}} \quad (1)$$

where

$$R_N = [-N_1 \dots N_1] \times [-N_2 \dots N_2] \quad (2)$$

and $\mathbf{V} = [\mathbf{v}_1 | \mathbf{v}_2]'$ is the periodicity matrix ($\det(\mathbf{V}) \neq 0$). Such a signal satisfies

$$x(\mathbf{t}) = x(\mathbf{t} + \mathbf{V}\mathbf{n}), \quad \forall \mathbf{t}, \forall \mathbf{n} \quad (3)$$

with $\mathbf{t} = [t_1 \ t_2]'$, $\mathbf{n} = [n_1 \ n_2]'$, $\mathbf{v}_1 = [v_{11} \ v_{21}]'$, $\mathbf{v}_2 = [v_{12} \ v_{22}]'$. The terms from the right-hand side of (1) will be referred to as the signal's harmonic components. We shall suppose

$$2N_i + 1 = P_i Q_i, \quad i = 1..2 \quad (4)$$

and we shall denote

$$P_1 P_2 = P. \quad (5)$$

According to Papoulis' multi-channel sampling scheme (MSS) [pap_81], the signal $x(\mathbf{t})$ is, on one hand, the input of linear, shift-invariant filter, $H(\boldsymbol{\omega})$, and, on the other hand, it is input of P linear, shift-invariant filters $H_k(\boldsymbol{\omega})$, $k=1..P$. We shall express the output $y(\mathbf{t})$ of the first system in terms of the sampled outputs $y_k(\mathbf{t})$ of the P systems. We denote

$$\mathbf{Q} = [Q_{ik}] = [Q_i \delta_k^i], \quad i, k = 1..2, \quad (6)$$

$$\boldsymbol{\Omega} = 2\pi(\mathbf{V}^{-1})'. \quad (7)$$

Let \mathbf{m} be some vectors with integer components $\mathbf{m} = [m_1 \ m_2]'$, $m_i = 0..P_i - 1$ lexicographically ordered. We say that the discrete-time functions $g_k(\mathbf{m})$, $k=1..P$, are independent if

$$\det(g_k(\mathbf{n} + \mathbf{Q}\mathbf{m})) \neq 0, \quad n_i = -N_i..-N_i + Q_i - 1, \quad i = 1..2. \quad (8)$$

In the matrix defined in (8), \mathbf{m} indexes the rows and k indexes the columns. We now state the following:

Lemma: Any discrete-time functions $g(\mathbf{n})$ can be expressed on R_N as a linear combination of P given independent functions $g_k(\mathbf{n})$ with coefficients $\phi_k(\mathbf{n})$ that are determined by $g(\mathbf{n})$ and which are periodic with periodicity matrix \mathbf{Q} :

$$g(\mathbf{n}) = \sum_{k=1}^P g_k(\mathbf{n}) \phi_k(\mathbf{n}). \quad (9)$$

Proof: Equation (9) can be written

$$g(\mathbf{n} + \mathbf{Q}\mathbf{n}) = \sum_{k=1}^P g_k(\mathbf{n} + \mathbf{Q}\mathbf{n}) \phi_k(\mathbf{n}), \quad n_i = -N_i..-N_i + Q_i - 1, \quad (10)$$

$$m_i = 0..P_i - 1, \quad i = 1..2$$

Since the g_k are independent, the system (10) has a unique solution for every \mathbf{n} , which defines the functions ϕ_k over one period. These functions can be extended over R_N through periodicity.

Referring to the MSS we can now establish the main theorem.

Theorem: If the functions $H_k(\boldsymbol{\Omega}\mathbf{n})$ are independent, then there exist the interpolation functions $f_k(\mathbf{t})$, $k=1..P$, such that the following GSE holds:

$$y(\mathbf{t}) = \sum_{k=1}^P \sum_{\mathbf{l} \in R_Q} y_k(\mathbf{V}\mathbf{Q}^{-1}\mathbf{l}) f_k(\mathbf{t} - \mathbf{V}\mathbf{Q}^{-1}\mathbf{l}) \quad (11)$$

$$R_Q = [0..Q_1 - 1] \times [0..Q_2 - 1] \quad (12)$$

(y_k are the sampled signals and $\mathbf{V}\mathbf{Q}^{-1}\mathbf{l}$ are the sample points). The construction of the functions f_k will be obtained in the course of the proof.

Proof: The transfer function $H(\boldsymbol{\omega})$ for input signals of the shape of (1) becomes $H(\boldsymbol{\Omega}\mathbf{n})$. The output of the single filter is

$$y(\mathbf{t}) = \sum_{\mathbf{n} \in R_N} a(\mathbf{n}) H(\boldsymbol{\Omega}\mathbf{n}) e^{j2\pi\mathbf{n}'\mathbf{V}^{-1}\mathbf{t}}. \quad (13)$$

Applying the expansion (9) to $H(\boldsymbol{\Omega}\mathbf{n}) e^{j2\pi\mathbf{n}'\mathbf{V}^{-1}\mathbf{t}}$ yields, for every \mathbf{t}

$$H(\mathbf{\Omega}\mathbf{n})e^{j2\pi\mathbf{n}'\mathbf{V}^{-1}\mathbf{t}} = \sum_{k=1}^P H_k(\mathbf{\Omega}\mathbf{n})\phi_k(\mathbf{n}, \mathbf{t}) \quad (14)$$

By expanding $\phi_k(\mathbf{n}, \mathbf{t})$ in a discrete-time Fourier series, we obtain

$$H(\mathbf{\Omega}\mathbf{n})e^{j2\pi\mathbf{n}'\mathbf{V}^{-1}\mathbf{t}} = \sum_{k=1}^P H_k(\mathbf{\Omega}\mathbf{n}) \sum_{\mathbf{l} \in R_Q} b_k(\mathbf{l}, \mathbf{t}) e^{j2\pi\mathbf{n}'\mathbf{Q}^{-1}\mathbf{l}}. \quad (15)$$

By substituting (15) into (13) and by reversing the order of summation there results

$$y(\mathbf{t}) = \sum_{k=1}^P \sum_{\mathbf{l} \in R_Q} b_k(\mathbf{l}, \mathbf{t}) \sum_{\mathbf{n} \in R_N} a(\mathbf{n}) H_k(\mathbf{\Omega}\mathbf{n}) e^{j2\pi\mathbf{n}'\mathbf{V}^{-1}\mathbf{V}\mathbf{Q}^{-1}\mathbf{l}}$$

which gives

$$y(\mathbf{t}) = \sum_{k=1}^P \sum_{\mathbf{l} \in R_Q} b_k(\mathbf{l}, \mathbf{t}) y_k(\mathbf{V}\mathbf{Q}^{-1}\mathbf{l}). \quad (16)$$

We shall now prove that

$$b_k(\mathbf{l}, \mathbf{t}) = b_k(0, \mathbf{t} - \mathbf{V}\mathbf{Q}^{-1}\mathbf{l}). \quad (17)$$

Substituting \mathbf{t} by $\mathbf{t} - \mathbf{V}\mathbf{Q}^{-1}\mathbf{m}$ in (15) and multiplying both sides by $\exp(j2\pi\mathbf{m}'\mathbf{V}^{-1}\mathbf{m})$ yields

$$H(\mathbf{\Omega}\mathbf{n})e^{j2\pi\mathbf{n}'\mathbf{V}^{-1}\mathbf{t}} = \sum_{k=1}^P H_k(\mathbf{\Omega}\mathbf{n}) \sum_{\mathbf{l} \in R_Q} b_k(\mathbf{l}, \mathbf{t} - \mathbf{V}\mathbf{Q}^{-1}\mathbf{m}) e^{j2\pi\mathbf{n}'\mathbf{Q}^{-1}(\mathbf{l} + \mathbf{m})}. \quad (18)$$

Suppose $\mathbf{m} \in R_Q$. The identification of the Fourier coefficients corresponding to $\exp(j2\pi\mathbf{m}'\mathbf{Q}^{-1}\mathbf{m})$ in (15) and (18) (namely $\mathbf{l}=0$ in (18) and $\mathbf{l}=\mathbf{m}$ in (15)) gives (17) with \mathbf{l} replaced by \mathbf{m} .

By defining now the interpolation functions through

$$f_k(\mathbf{t}) = b_k(0, \mathbf{t}) \quad (19)$$

the proof is complete. The output of the single system is expressed in terms of the sampled outputs of the P systems that compose the MSS.

We consider now some special cases.

For a one-channel sampling scheme for the signal $x(\mathbf{t})$ itself: $H(\mathbf{\omega})=1$, $H_1(\mathbf{\omega})=1$, $P_1=P_2=1$. We shall denote, for this case $R_Q=R_N'$ (see (12)), $Q=N$ (see (6)), where, obviously

$$\mathbf{N} = \left[(2N_i + 1) \delta_k^i \right], \quad k, i = 1..2, R_N' = [0..2N_1] \times [0..2N_2]. \quad (20)$$

There results

$$\phi_1(\mathbf{n}, \mathbf{t}) = e^{j2\pi\mathbf{n}'\mathbf{V}^{-1}\mathbf{t}} = \sum_{\mathbf{l} \in R_N'} b(\mathbf{l}, \mathbf{t}) e^{j2\pi\mathbf{n}'\mathbf{N}^{-1}\mathbf{l}} \quad (21)$$

with

$$b(\mathbf{l}, \mathbf{t}) = \frac{1}{\det(\mathbf{N})} \sum_{\mathbf{n} \in R_N} e^{j2\pi \mathbf{n}(\mathbf{V}^{-1}\mathbf{t} - \mathbf{N}^{-1}\mathbf{l})} = S(\mathbf{V}^{-1}\mathbf{t} - \mathbf{N}^{-1}\mathbf{l}). \quad (22)$$

Combining (22) and (6) yields

$$x(\mathbf{t}) = \sum_{\mathbf{l} \in R_N} x(\mathbf{V}\mathbf{N}^{-1}\mathbf{l}) S(\mathbf{V}^{-1}\mathbf{t} - \mathbf{N}^{-1}\mathbf{l}). \quad (23)$$

One can notice that the sampling density is decreased P times (P_i times in each periodicity direction) in the case of the MSS (11) with respect to the one-channel sampling scheme (23). The number of samples is equal to the number of the signal's harmonic components $(2N_1 + 1)(2N_2 + 1)$ in both cases.

A closed form for the function S can be derived in terms of the vector components using the formula

$$\sum_{n=-N}^N e^{jnx} = \frac{\sin[(N+1/2)x]}{\sin(x/2)}. \quad (24)$$

There results

$$S(\mathbf{V}^{-1}\mathbf{t} - \mathbf{N}^{-1}\mathbf{l}) = \prod_{i=1}^2 \frac{\sin[(2N_i + 1)(\Omega_{i1}t_1 + \Omega_{i2}t_2)/2 - \pi l_i]}{(2N_i + 1) \sin[(\Omega_{i1}t_1 + \Omega_{i2}t_2)/2 - \pi l_i / (2N_i + 1)]}. \quad (25)$$

If the periodicity directions of the signal $x(\mathbf{t})$ are the t_1 and t_2 axes, then

$$\mathbf{V} = [T_i \delta_k^i], \quad i, k = 1..2 \quad (26)$$

and by denoting

$$T_{Ei} = \frac{T_i}{2N_i + 1}, \quad i = 1..2 \quad (27)$$

there results

$$x(t_1, t_2) = \sum_{n_1=0}^{2N_1} \sum_{n_2=0}^{2N_2} x(n_1 T_{E1}, n_2 T_{E2}) \prod_{i=1}^2 \frac{\sin[\pi(t_i / T_{Ei} - n_i)]}{(2N_i + 1) \sin[\pi(t_i / T_{Ei} - n_i) / (2N_i + 1)]}. \quad (28)$$

If $x(t_1, t_2) = x(t_1)$, then T_{E2} can have an arbitrary value and, by taking into account that

$$\sum_{k=0}^{2N_2} \frac{\sin[\pi(t_2 / T_{E2} - k)]}{(2N_2 + 1) \sin[\pi(t_2 / T_{E2} - k) / (2N_2 + 1)]} = 1, \quad (29)$$

the 1D finite sampling expansion given at the beginning results.

The presented theorem can be easily specialized for the 1D case.

B. Sampling Expansion for 2D Band-Limited, Finite Energy Signals with Gaps in the Spectrum.

Sampling expansions for 2D signals whose spectrum supports result from integer translations of a parallelogram have been derived [98_03_S]. Nevertheless the spectrum of the signal could contain gaps, reconstruction from samples taken at the Shannon-Landau density has been achieved. The framework has been again the Papoulis multi-channel sampling scheme. Potential applications include MRI imaging or other fields when only some portions of the images are of interest and the acquired signal and the original one are in a Fourier Transform relationship.

The general idea of this sampling procedure was not new [cheung_93] at the time of publication of [98_03_S]. However, we have chosen a model such that the 2D sampling vectors were not necessarily orthogonal and we have provided an example with interpolation functions expressed in closed-form.

We suppose that the image is the Fourier Transform of a finite energy, 2D, complex valued signal, defined on R^2 , and that it is concentrated on a set of parallelograms which result from some integer translations of a basic parallelogram P , along its sides. An example of the support of the signal spectrum is represented in Fig. 1 (the parallelograms are rectangles there; a closed form of a sampling expansion for such a signal is derived below).

If \mathbf{w}_1 and \mathbf{w}_2 are the (vector) sides of P , then the support of the image is:

$$S = \{P + k_1\mathbf{w}_1 + k_2\mathbf{w}_2 \mid k_1 \in S_1, k_2 \in S_2\}, \quad (30)$$

where S_1 and S_2 are some finite sets of integers.

We denote:

$$\text{card}(S_1) = K_1; \text{card}(S_2) = K_2; K_1K_2 = N. \quad (31)$$

We shall consider the 2D quantities as column vectors.

If $x(\mathbf{t})$ is a signal from the considered class, we shall show that there exist N interpolation functions $f_k(\mathbf{t})$ such that:

$$y(\mathbf{t}) = \sum_{k=1}^N \sum_{\bar{\mathbf{n}}} y_k(\mathbf{V}_E \bar{\mathbf{n}}) f_k(\mathbf{t} - \mathbf{V}_E \bar{\mathbf{n}}), \quad (32)$$

where y and the y_k are linearly dependent on x . \mathbf{V}_E is the sampling matrix, whose expression is to be derived below. A prime will denote vector and matrix transposition.

An important result of the Information Theory states that the minimum sampling density which uniquely determines a finite support, finite energy signal is 2π divided by the area of the support of the spectrum (Shannon-Landau). We shall provide now a constructive way of achieving this sampling density by means of the Papoulis' Multi-channel Sampling Scheme (MSS) [pap_81], [cheung_93]. As shown in the previous subsection, in the original arrangement of the MSS [pap_81], the signal $x(\mathbf{t})$ is, on one hand, the input of a filter $H(\boldsymbol{\omega})$, whose output is denoted $y(\mathbf{t})$, and, on the other hand, it is the input of N filters $H_k(\boldsymbol{\omega})$, whose outputs are denoted $y_k(\mathbf{t}), k=0\dots N-1$. The output y can be expressed in terms of the samples of the y_k and some interpolation functions as follows.

From the linear systems theory it is known that:

$$y(\mathbf{t}) = \frac{1}{4\pi^2} \iint_S X(\boldsymbol{\omega}) H(\boldsymbol{\omega}) e^{j\boldsymbol{\omega}'\mathbf{t}} d\bar{\boldsymbol{\omega}} \quad (33)$$

(capital letters denote Fourier Transforms, e. g. $X(\boldsymbol{\omega})$ is the Fourier Transform of $x(\mathbf{t})$).

Consider the 2×2 matrix:

$$\mathbf{W} = [\mathbf{w}_1 \mid \mathbf{w}_2], \quad (34)$$

and let $\Phi_l, l=0\dots N-1$ be some \mathbf{W} -periodic functions in $\boldsymbol{\omega}$ such that:

$$H(\boldsymbol{\omega})e^{j\boldsymbol{\omega}'\mathbf{t}} = \sum_{l=0}^{N-1} H_l(\boldsymbol{\omega})\Phi_l(\boldsymbol{\omega}, \mathbf{t}). \quad (35)$$

The existence and the construction of the Φ_l result from:

$$H(\boldsymbol{\omega} + \mathbf{W}\mathbf{k})e^{j\boldsymbol{\omega}'\mathbf{t}} = \sum_{l=0}^{N-1} H_l(\boldsymbol{\omega} + \mathbf{W}\mathbf{k})\Phi_l(\boldsymbol{\omega}, \mathbf{t}), \quad (36)$$

$$\boldsymbol{\omega} \in P, \mathbf{k} \in S_1 \times S_2$$

where the periodicity of the Φ_l has been taken into account. (36) is an $N \times N$ linear system of equations which admits a unique solution if its determinant is nonzero a. e. on P :

$$\Delta = \det[H_k(\boldsymbol{\omega} + \mathbf{W}\mathbf{k})] \neq 0 \quad \text{a.e. on } P. \quad (37)$$

In the context of the MSS (37) is known as the independence condition (see also the preceding subsection).

From (36) the Φ_l can be calculated on P and extended to S through \mathbf{W} -periodicity. Furthermore, they can be expanded in their Fourier series, with coefficients b_l , for every \mathbf{t} :

$$\Phi_l(\boldsymbol{\omega}, \mathbf{t}) = \sum_{\bar{n}} b_l(\boldsymbol{\omega}, \mathbf{t}) e^{j2\pi\bar{n}'\mathbf{W}^{-1}\boldsymbol{\omega}}. \quad (38)$$

The substitution of (35) and (38) into (33) yields, after interchanging the order of summation and integration:

$$y(\mathbf{t}) = \sum_{l=0}^{N-1} \sum_{\bar{n}} b_l(\mathbf{n}, \mathbf{t}) \times \frac{1}{4\pi^2} \iint_S X(\boldsymbol{\omega}) H_l(\boldsymbol{\omega}) e^{j\boldsymbol{\omega}2\pi(\mathbf{W}^{-1})'\mathbf{n}} d\boldsymbol{\omega}. \quad (39)$$

We can introduce now the sampling matrix:

$$\mathbf{V}_E = [\mathbf{v}_{E1} | \mathbf{v}_{E2}] = 2\pi(\mathbf{W}^{-1})', \quad (40)$$

and, by using again the expression of the output of a linear system, we get:

$$y(\mathbf{t}) = \sum_{l=0}^{N-1} \sum_{\bar{n}} y_l(\mathbf{V}_E \mathbf{n}) b_l(\mathbf{n}, \mathbf{t}). \quad (41)$$

The b_l satisfy:

$$b_l(\mathbf{n}, \mathbf{t}) = b_l(0, \mathbf{t} - \mathbf{V}_E \mathbf{n}) \stackrel{\Delta}{=} f_l(\mathbf{t} - \mathbf{V}_E \mathbf{n}), \quad l=0\dots N-1. \quad (42)$$

Indeed, the substitution of \mathbf{t} with $\mathbf{t} - \mathbf{V}_E \mathbf{m}$ in (35) yields, after some manipulation, and by using (38):

$$H(\boldsymbol{\omega})e^{j\boldsymbol{\omega}'\mathbf{t}} = \sum_{l=0}^{N-1} H_l(\boldsymbol{\omega}) \sum_{\bar{n}} b_l(\mathbf{n}, \mathbf{t} - \mathbf{V}_E \mathbf{m}) \times e^{j2\pi(\mathbf{n}'+\mathbf{m}')\mathbf{W}^{-1}\boldsymbol{\omega}}. \quad (43)$$

There results:

$$b_l(\mathbf{n}, \mathbf{t} - \mathbf{V}_E \mathbf{m}) = b_l(\mathbf{n} + \mathbf{m}, \mathbf{t}), \quad (44)$$

wherefrom (42) can be obtained by making $\mathbf{n} = 0$.

The result in (32) covers more types of gaps in the spectrum than other procedures such as band-pass sampling [vau_91], the multi-band sampling [brown_85], and the gap sampling [hig_87].

An important issue in connection to the MSS is the Cheung-Marks stability, discussed e. g. in [brown_91]. The results presented there can be easily transposed to our case. For example, the scheme presented here is stable if the determinant (37) is bounded away from 0.

We shall give now an example of a 2D signal with spectrum containing gaps and the corresponding sampling expansion at a minimum sampling density. Consider a 2D, finite energy, complex valued signal whose spectrum support is represented in Fig. 1. Due to the particular, rectangular shape of this region, the interpolation kernels f_k from (32) separate. We shall take the H and H_k as pure delays in the first variable, in order to express a shifted version of x in terms of its samples:

$$\begin{aligned} H(\boldsymbol{\omega}) &= e^{j\omega_1 \tau}, \\ H_k(\boldsymbol{\omega}) &= e^{j\omega_1 \tau_k}, \quad k = 0 \dots 3. \end{aligned} \quad (45)$$

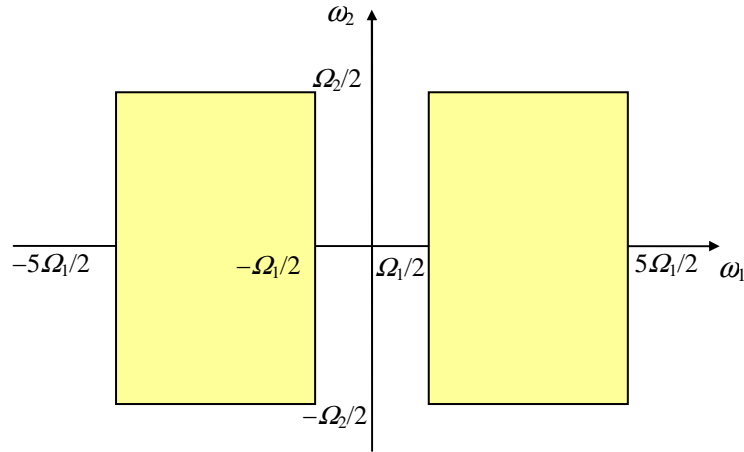


Fig. 1. The support of the spectrum of the signal from the example presented in Section III.

If we choose:

$$P = \left[-\frac{5\Omega_1}{2}, -\frac{3\Omega_1}{2}\right] \times \left[-\frac{\Omega_2}{2}, \frac{\Omega_2}{2}\right] \quad (46)$$

then:

$$S_1 = \{0, 1, 3, 4\}, S_2 = \{0\}. \quad (47)$$

We need the following simple algebraic identity:

$$D(a,b,c,d) = \begin{pmatrix} 1 & 1 & 1 & 1 \\ a & b & c & d \\ a^3 & b^3 & c^3 & d^3 \\ a^4 & b^4 & c^4 & d^4 \end{pmatrix} = V_4(a,b,c,d)(ab+ac+ad+bc+bd+cd), \quad (48)$$

where V_4 is the fourth order Vandermonde determinant. Direct application of the MSS and of (48) leads to:

$$x(t_1 - \tau, t_2) = \sum_{k=0}^3 \sum_{(n_1, n_2)} x(n_1 \frac{2\pi}{\Omega_1} - \tau_1, n_2 \frac{2\pi}{\Omega_2}) \times f_k(t_1 - n_1 \frac{2\pi}{\Omega_1}) f(t_2 - n_2 \frac{2\pi}{\Omega_2}), \quad (49)$$

where:

$$f(t) = \frac{\sin(\frac{\Omega_2}{2} t)}{\frac{\Omega_2}{2} t}, \quad (50)$$

and the f_k can be obtained through the circular shift of the set $\{0,1,2,3\}$ from the $f_0(t)$ listed below (51).

$$f_0(t) = \frac{\sin[\frac{\Omega_1}{2}(t - \tau - \tau_0)]}{\frac{\Omega_1}{2}(t - \tau - \tau_0)} \times \frac{\sin[\frac{\Omega_1}{2}(t - \tau + \tau_1)] \sin[\frac{\Omega_1}{2}(t - \tau + \tau_2)] \sin[\frac{\Omega_1}{2}(t - \tau + \tau_3)]}{\sin[\frac{\Omega_1}{2}(\tau_1 - \tau_0)] \sin[\frac{\Omega_1}{2}(\tau_2 - \tau_0)] \sin[\frac{\Omega_1}{2}(\tau_3 - \tau_0)]} \times \frac{\cos[\frac{\Omega_1}{2}(t - \tau - \tau_1 + \tau_2 + \tau_3)] + \cos[\frac{\Omega_1}{2}(t - \tau + \tau_1 - \tau_2 + \tau_3)] + \cos[\frac{\Omega_1}{2}(t - \tau + \tau_1 + \tau_2 - \tau_3)]}{\cos[\frac{\Omega_1}{2}(\tau_0 + \tau_1 - \tau_2 - \tau_3)] + \cos[\frac{\Omega_1}{2}(\tau_0 - \tau_1 + \tau_2 - \tau_3)] + \cos[\frac{\Omega_1}{2}(\tau_0 - \tau_1 - \tau_2 + \tau_3)]}. \quad (51)$$

The delays must be chosen such that the independence condition (37) be observed. Note that $f(t)$ from (50) is the usual Shannon interpolation kernel, due to our particular choice of the region of support.

Another contribution to sampling of signals whose spectrums contain gaps has relied also on the MSS and involved derivative sampling, this time in a 1D context [02_03_S]. The work has been triggered by the renewed interest on the Papoulis' MSS at that time [sei_00, eld_00].

We have considered this time a signal having the spectrum with the support depicted in Fig.2. We took

the basic (angular) frequency interval $I_0 = \left[-\frac{\Omega}{2}, \frac{\Omega}{2}\right]$, so that the signal spectrum support can be written as $S = \bigcup_{k \in K} (I_0 + k\Omega)$, $k \in K = \{-2, -1, 1, 2\}$.

The general MSS is represented in Fig. 4, so that we should take $N=4$. If the sampled outputs of the MSS, with $H(\omega)=1$, are supplied to the inputs of the system in Fig. 5, the original signal will be reconstructed at its output provided that the following orthogonality condition is observed:

$$\sum_{l=0}^{N-1} H_l(\omega + q\Omega) F_l(\omega + p\Omega) = \delta_p^q \frac{2\pi}{\Omega} H(\omega + p\Omega), \quad p, q \in K, \omega \in I_0. \quad (52)$$

The F_k can be found from the H_k by matrix inversion, using (52).

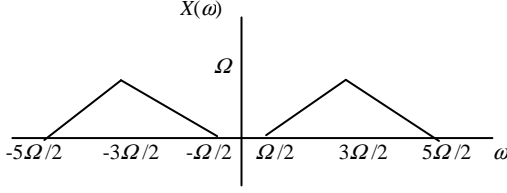


Fig. 2. Spectrum of a bandpass

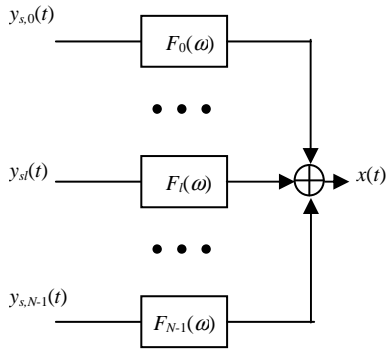


Fig. 4. The general reconstruction diagram. $N=4$ in the example.

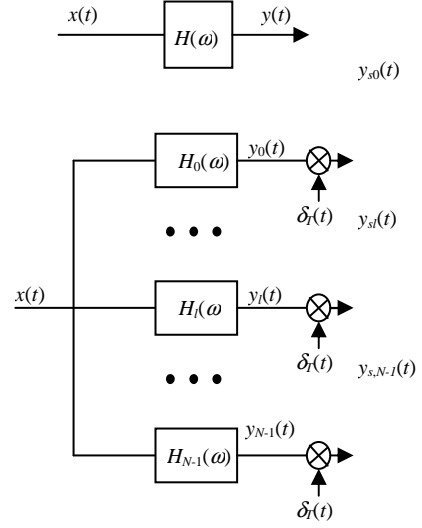


Fig. 3. The Multichannel Sampling Scheme. $N=4$ in the example.

A sampling expansion is of the form

$$x(t) = \sum_{l=0}^{N-1} \sum_{n=-\infty}^{\infty} y_l(nT) f_l(t - nT) \quad (53)$$

where the f_l are the interpolation functions and $T = \frac{2\pi}{\Omega}$ is the sampling period. The following steps are to be done for finding the f_l , as we have shown above (we denote $s = j\omega$, $\sigma = j\Omega$):

1. Solve the system of equations

$$H(s - k\sigma) \exp[(s - k\sigma)t] = \sum_{l=0}^3 \Phi_l(s, t) H_l(s - k\sigma), \quad k \in K. \quad (54)$$

2. Find the f_l from

$$f_l(t) = \frac{1}{\Omega} \int_{-\Omega/2}^{\Omega/2} \Phi_l(s, t) d\omega. \quad (55)$$

In order to find a derivative sampling we take

$$H_l(\omega) = (j\omega)^l, \quad l = 0..3. \quad (56)$$

The matrix of the system (54) can be conveniently factorized as follows

$$\begin{bmatrix} 1 & s-2\sigma & (s-2\sigma)^2 & (s-2\sigma)^3 \\ 1 & s-\sigma & (s-\sigma)^2 & (s-2\sigma)^3 \\ 1 & s+\sigma & (s+\sigma)^2 & (s+\sigma)^3 \\ 1 & s+2\sigma & (s+2\sigma)^2 & (s+2\sigma)^3 \end{bmatrix} = \mathbf{AB}$$

with

$$\mathbf{A} = \begin{bmatrix} 1 & -2 & 4 & -8 \\ 1 & -1 & 1 & -1 \\ 1 & 1 & 1 & 1 \\ 1 & 2 & 1 & 8 \end{bmatrix}, \quad \mathbf{B} = \begin{bmatrix} 1 & s & s^2 & s^3 \\ 0 & \sigma & 2s\sigma & 3s^2\sigma \\ 0 & 0 & \sigma^2 & 3s\sigma^2 \\ 0 & 0 & 0 & \sigma^3 \end{bmatrix}.$$

After performing matrix inversions we get

$$\begin{bmatrix} \Phi_1 \\ \Phi_2 \\ \Phi_3 \\ \Phi_4 \end{bmatrix} = \frac{1}{12} \mathbf{S} \begin{bmatrix} \exp[(s-2\sigma)t] \\ \exp[(s-\sigma)t] \\ \exp[(s+\sigma)t] \\ \exp[(s+2\sigma)t] \end{bmatrix}, \quad (57)$$

where we have denoted

$$\mathbf{S} = \begin{bmatrix} -2 - \frac{s}{\sigma} + 2\frac{s^2}{\sigma^2} + \frac{s^3}{\sigma^3} & \frac{1}{\sigma} - 4\frac{s}{\sigma^2} - 3\frac{s^2}{\sigma^3} & \frac{2}{\sigma^2} + \frac{3s}{\sigma^3} & -\frac{1}{\sigma^3} \\ 8 + 8\frac{s}{\sigma} - 2\frac{s^2}{\sigma^2} - 2\frac{s^3}{\sigma^3} & -\frac{8}{\sigma} + 4\frac{s}{\sigma^2} + 6\frac{s^2}{\sigma^3} & -\frac{2}{\sigma^2} - 6\frac{s}{\sigma^3} & \frac{2}{\sigma^3} \\ 8 - 8\frac{s}{\sigma} - 2\frac{s^2}{\sigma^2} + 2\frac{s^3}{\sigma^3} & +\frac{8}{\sigma} + 4\frac{s}{\sigma^2} - 6\frac{s^2}{\sigma^3} & -\frac{2}{\sigma^2} + 6\frac{s}{\sigma^3} & -\frac{2}{\sigma^3} \\ -2 + \frac{s}{\sigma} + 2\frac{s^2}{\sigma^2} - \frac{s^3}{\sigma^3} & -\frac{1}{\sigma} - 4\frac{s}{\sigma^2} + 3\frac{s^2}{\sigma^3} & \frac{2}{\sigma^2} - \frac{3s}{\sigma^3} & \frac{1}{\sigma^3} \end{bmatrix}^T$$

(T denotes here matrix transposition).

We can perform now the multiplications in (57) and, after reintroducing ω and Ω , we get

$$\begin{aligned} \Phi_1(\omega, t) &= \frac{\exp(j\omega t)}{12} \{4[4\cos(\Omega t) - \cos(2\Omega t)] + j\omega \frac{2}{\Omega} [\sin(2\Omega t) - 8\sin(\Omega t)] \\ &\quad - (j\omega)^2 \frac{4}{\Omega^2} [\cos(2\Omega t) - \cos(\Omega t)] + (j\omega)^3 \frac{2}{\Omega^3} [\sin(2\Omega t) - 2\sin(\Omega t)]\}, \end{aligned}$$

$$\begin{aligned} \Phi_2(\omega, t) &= \frac{\exp(j\omega t)}{12} \left\{ \frac{2}{\Omega} [8\sin(\Omega t) - \sin(2\Omega t)] + j\omega \frac{8}{\Omega^2} [\cos(2\Omega t) - \cos(\Omega t)] \right. \\ &\quad \left. - (j\omega)^2 \frac{6}{\Omega^3} [\sin(2\Omega t) - 2\sin(\Omega t)] \right\}, \end{aligned}$$

$$\Phi_3(\omega, t) = \frac{\exp(j\omega t)}{12} \left\{ \frac{4}{\Omega^2} [\cos(\Omega t) - \cos(2\Omega t)] + j\omega \frac{6}{\Omega^3} [\sin(2\Omega t) - 2\sin(\Omega t)] \right\},$$

$$\Phi_4(\omega, t) = \frac{2\exp(j\omega t)}{12} \frac{1}{\Omega^3} [2\sin(\Omega t) - \sin(2\Omega t)].$$

Now (55) must be applied to these functions in order to find the f_i . Integrals of the form $\int_{-\Omega/2}^{\Omega/2} (j\omega)^l \exp(j\omega t) d\omega, l=0..3$ must be calculated. For $l=0$, the result is $f(t) = \frac{\sin(\Omega t/2)}{\Omega t/2}$. For

$l > 0$ we can apply the derivative theorem [opp_83] for the Fourier transform, and we find that the integrals are equal to $f^{(l)}(t)$. Final expressions for the interpolation functions $f_i(t)$ can now be derived by direct calculation, but we will omit them for brevity. Instead we will study an example.

In order to get some insight in the behavior of the truncation error, we have applied (53) to the signal represented in fig. 1, whose expression is

$$x(t) = \frac{4}{\pi} \cos\left(\frac{3\Omega t}{2}\right) \frac{\sin^2 \frac{\Omega t}{2}}{t^2},$$

and whose maximum value is 1 at $t=0$.

For $\Omega = 2\pi$, that gives the sampling period $T=1$, we have increased 100 times the sampling rate in the interval $[0;1]$. We represented in Fig. 5 the absolute, maximum truncation error in the reconstructed sample points, as a function of the number of terms (the series have been truncated by considering only $2N+1$ terms from $-N$ to N). It can be seen that the result is satisfactory.

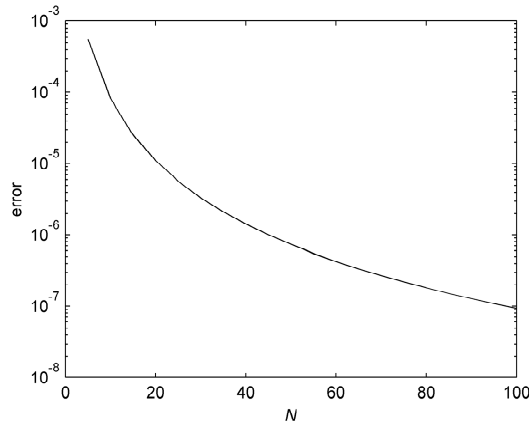


Fig. 5. The truncation error.

C. Sampling Expansion on Lattices for Multidimensional, Multi-Band Signals

We have proposed a sampling theorem for finite energy, multidimensional, multiband signals, with sparse spectral support that does not necessarily tile \mathbb{R}^N under translation [06_03_S]. The spectral support of the signal is generated by translation of a finite number of sets included in a fundamental region of a lattice, whose dual determines the N -dimensional sampling grid, and it is included in a fundamental region of a sublattice of the given lattice. We have used Papoulis' MSS in order to achieve the necessary sampling density. We have calculated bounds for the energy of the aliasing error.

Sampling theorems for multidimensional signals are important in Fourier imaging applications (sensor array imaging, synthetic aperture radar, magnetic resonance imaging), space-time sampling etc. This problem is also extensively covered in literature, for the case of signals having the spectral support included in an N -dimensional parallelepiped. The case of a rectangular sampling lattice [brown_89] is extended to general lattices [cheung_83], by using the MSS, and further extended to periodic/nonperiodic hybrids [izen_05].

We consider complex valued, finite energy, continuous, N -dimensional, multiband signals, whose spectral supports \mathcal{S} result from translations of some finite sets, contained in a fundamental region of a lattice L_U (an N -dimensional parallelepiped). \mathcal{S} is contained in a fundamental region of another lattice, included in L_U , and it does not tile \mathbb{R}^N under translations in general. In order to achieve a sampling density lower than the Nyquist rate, which in this case is equal to the reciprocal of the volume of the parallelepiped containing \mathcal{S} , an N -dimensional MSS is used. We thus generalize to multidimensional MSS the one dimensional multicodet sampling treated in [venk_00, venk_01], and we obtain an N -dimensional smling expansion.

Consider an N -dimensional, complex valued, finite energy, continuous signal, with a spectral support \mathcal{S} included in an N -dimensional parallelepiped. This assumption makes the lattice formalism a natural choice. We will use [izen_05] for definitions and properties of lattices relevant to sampling.

Consider a lattice L_U generated by the column vectors $\mathbf{u}_1, \mathbf{u}_2, \dots, \mathbf{u}_N$ and denote the corresponding matrix $\mathbf{U} = [\mathbf{u}_1 \ \mathbf{u}_2 \ \dots \ \mathbf{u}_N]$. The canonical fundamental region for L_U is

$$\mathcal{C}_0 = U[0,1)^N = \left\{ \mathbf{f} \in \mathbb{R}^N \mid \mathbf{f} = \sum_{i=1}^N v_i \mathbf{u}_i, 0 \leq v_i < 1 \right\}. \quad (58)$$

Consider next M disjoint, connected subsets from \mathbb{R}^N : $\mathcal{G}_m \subset \mathcal{C}_0, m \in \mathcal{M} = \{1..M\}$; each \mathcal{G}_m generates by translations of vectors from L_U a part \mathcal{S}_m of the spectral support:

$$\mathcal{S}_m = \bigcup_{\mathbf{p} \in \mathcal{P}_m} (\mathcal{G}_m \oplus \mathbf{U}\mathbf{p}), \quad \mathcal{P}_m \subset \mathbb{Z}^N \quad (59)$$

(\oplus denotes translation of a set of points by a vector). We suppose \mathcal{P}_m finite and we denote $\text{card}(\mathcal{P}_m) = P_m$.

The spectral support of the signals to be sampled is given by

$$\mathcal{S} = \bigcup_{m \in \mathcal{M}} \mathcal{S}_m. \quad (60)$$

We pack \mathcal{S} as compactly as possible in a fundamental region of a lattice $L_W \subset L_U$, generated by some vectors $\mathbf{w}_i, i=1..N$, and let $\mathbf{W} = [\mathbf{w}_1 \ \mathbf{w}_2 \ \dots \ \mathbf{w}_N]$. Without loss of generality, we can assume that the fundamental region is canonical,

$$\mathcal{C} = W[0,1)^N = \left\{ \mathbf{f} \in \mathbb{R}^N \mid \mathbf{f} = \sum_{i=1}^N v_i \mathbf{w}_i, 0 \leq v_i < 1 \right\}.$$

Two-dimensional examples of this arrangement are presented in Figs. 1 and 2.

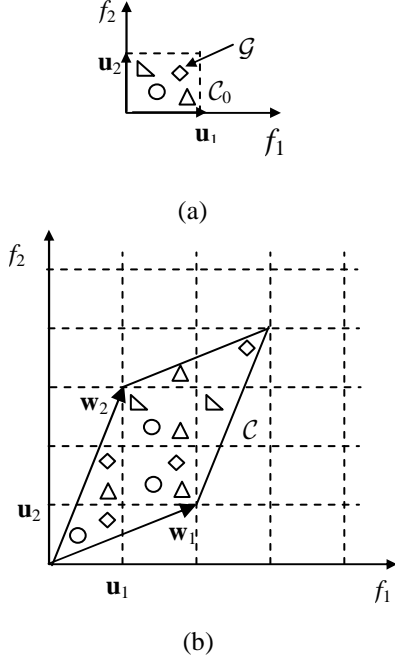


Fig. 6. (a) Fundamental region of the lattice L_U and the sets \mathcal{G}_m . (b) Fundamental region of L_W and the signal's spectrum support in two dimensions.

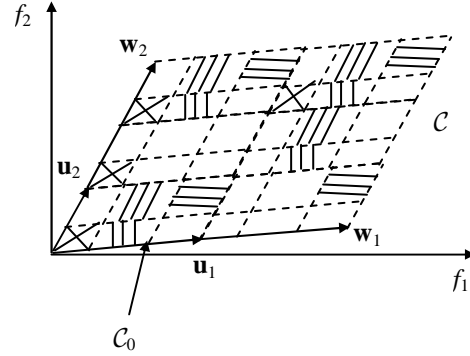


Fig. 7. Spectral support in two dimensions, when the vectors \mathbf{w}_i are parallel to the \mathbf{u}_i . The marked subcells belong to \mathcal{S} . Subcells marked with the same pattern correspond to a given \mathcal{P}_m . \mathcal{C}_0 is the parallelogram determined by \mathbf{u}_1 and \mathbf{u}_2 .

Fig. 7 contains the special case when the vectors \mathbf{w}_i are parallel to the \mathbf{u}_i . It is known [izen_05] that there exists an N -by- N matrix \mathbf{L} with integer elements such that

$$\mathbf{W} = \mathbf{L}\mathbf{U}. \quad (61)$$

Let $L = |\det \mathbf{L}|$, $\mathbf{f}' \in \mathcal{C}_0$, and $A = \{\mathbf{f}' + \mathbf{U}\mathbf{n} \mid \mathbf{n} \in \mathbb{Z}^N\} = L_U \oplus \mathbf{f}'$. Due to the linearity of (61) and to volume conservation, the set $A \cap \mathcal{C}$ has L elements [izen_05], so that $P_m \leq L, m \in \mathcal{M}$.

Consider now a finite energy, complex valued signal, bandlimited to \mathcal{S} , which is sampled with a MSS, as in Fig. 8. The P filters with the frequency responses $H_k(\mathbf{f})$ are known, while the filters with frequency responses $Y_k(\mathbf{f})$, bandlimited to \mathcal{C} , must be determined such that $x_0(\mathbf{t}) = x(\mathbf{t})$ if it is possible, where $x_0(\mathbf{t})$ and $x(\mathbf{t})$ are the output and input signals, having the Fourier transforms $X_0(\mathbf{f})$ and $X(\mathbf{f})$ respectively.

As the sampling signal is $\sum_{\mathbf{n} \in \mathbb{Z}^N} \delta(\mathbf{t} - (\mathbf{U}^{-T})\mathbf{n})$, with $\mathbf{V}^{-T} = (\mathbf{V}^{-1})^T$ denoting the transpose \mathbf{V}^{-1} , i.e. the sampling lattice is the dual of L_U , the sampling density is $(P|\det \mathbf{U}|)^{-1}$. The volume of the signal's

spectral support is $\sum_{i=1}^M P_m V(\mathcal{G}_m)$, where $V(A)$ denotes the N -dimensional volume of a set A . In order to be able to reconstruct the signal, we must take $P \geq \max_{m \in \mathcal{M}} P_m$.

The input-output relation in the frequency domain for the system in Fig. 8 is

$$X_0(\mathbf{f}) = U \sum_{\mathbf{n} \in \mathbb{Z}^N} X(\mathbf{f} - \mathbf{V}\mathbf{n}) \sum_{k=1}^P \hat{H}_k(\mathbf{f} - \mathbf{V}\mathbf{n}) Y_k(\mathbf{f}), \quad (62)$$

where

$$\hat{H}_k(\mathbf{f}) = \begin{cases} H(\mathbf{f}), & \mathbf{f} \in \text{supp}(X(\mathbf{f})) = \mathcal{S} \\ 0, & \text{otherwise} \end{cases}, \quad (63)$$

and U is a shorthand notation for $|\det \mathbf{U}|$, which is equal to the volume of \mathcal{C}_0 .

The condition $X_0(\mathbf{f}) = X(\mathbf{f})$ is true in general if

$$\sum_{k=1}^P \hat{H}_k(\mathbf{f} - \mathbf{U}\mathbf{n}) Y_k(\mathbf{f}) = \frac{1}{U} \delta_{\mathbf{n}}^0, \quad \mathbf{f} \in \mathcal{S}, \quad (64)$$

and, by tacking into account that the Y_k are bandlimited to \mathcal{C} :

$$\sum_{k=1}^P \hat{H}_k(\mathbf{f} - \mathbf{U}\mathbf{n}) Y_k(\mathbf{f}) = 0, \quad \mathbf{f} \in \mathcal{C} \setminus \mathcal{S}. \quad (65)$$

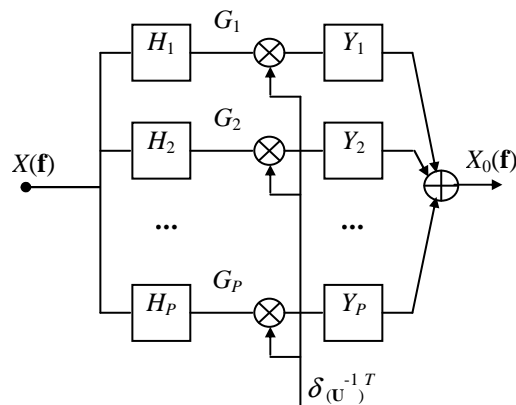


Fig. 8. Multichannel sampling scheme

We begin the analysis by finding some relevant consequences of (64).

It is known that every $\mathbf{f} \in \mathcal{C}$ can be uniquely written as $\mathbf{f} = \mathbf{f}' + \mathbf{U}\mathbf{r}$, $\mathbf{f}' \in \mathcal{C}_0$, $\mathbf{r} \in \mathbb{Z}^N$ [izen_05]. If $\mathbf{f} \in \mathcal{S}$, then $\mathbf{f}' \in \mathcal{G}_m$ and $\mathbf{r} \in \mathcal{P}_m$ for some $m \in \mathcal{M}$. By denoting $\mathbf{r} - \mathbf{n} = \mathbf{p}$ and by taking into account (63), (64) becomes for each $m \in \mathcal{M}$

$$\sum_{k=1}^P \hat{H}_k(\mathbf{f}' + \mathbf{U}\mathbf{p}) Y_k(\mathbf{f}' + \mathbf{U}\mathbf{r}) = \frac{1}{U} \delta_{\mathbf{p}}^{\mathbf{r}}, \quad \mathbf{f}' \in \mathcal{G}_m, \quad \mathbf{p}, \mathbf{r} \in \mathcal{P}_m, \quad (66)$$

where we have used Kronecker's delta.

Consider the matrices

$$\begin{aligned} \mathbf{H}_m(\mathbf{f}') &= [a_{\mathbf{p}k}] = [\hat{H}_k(\mathbf{f}' + \mathbf{U}\mathbf{p})], \\ \mathbf{Y}_m(\mathbf{f}') &= [b_{\mathbf{p}k}] = [Y_k(\mathbf{f}' + \mathbf{U}\mathbf{p})], \\ \mathbf{p} &\in \mathcal{P}_m, k = 1..P, \mathbf{f}' \in \mathcal{G}_m. \end{aligned} \quad (67)$$

For every vector index, the lexicographic order is taken. The dimensions of these matrices are $P_m \times P$ and $P \times P_m$ respectively. The system (66) can be written as:

$$\mathbf{H}_m(\mathbf{f}') \mathbf{Y}_m(\mathbf{f}') = \frac{1}{U} \mathbf{I}_{P_m}. \quad (68)$$

We assume that the \mathbf{H}_m has full row rank for each m , which in the context of the MSS is known as an independence condition.

$$\text{Then } \mathbf{Y}_m(\mathbf{f}') = U^{-1} \mathbf{H}_m^{-1}(\mathbf{f}'), \mathbf{f}' \in \mathcal{G}_m, \quad (69)$$

where \mathbf{H}_m^{-1} is a left inverse for \mathbf{H}_m . Performing (69) for each $m \in \mathcal{M}$, the $Y_k(\mathbf{f})$ result for $\mathbf{f} \in \mathcal{S}$. Since $P_m \leq P$, the solution is generally non unique. In the context of one-dimensional multicoset sampling and reconstruction of multiband signals, an optimization procedure has been applied in order to find the solution that minimizes the reconstruction error [venk_00, venk_01]. Since that situation is a special case of ours, it can be assumed that a similar choice could be performed with the class of signals we have considered.

We study now the consequences of the system (65). There exists of course the trivial solution $Y_k(\mathbf{f}) = 0$, $\mathbf{f} \in \mathcal{C} \setminus \mathcal{S}$, but (65) generally admits other solutions that also could be used as stated above. We remind that, due to linearity and volume conservation, for each $\mathbf{f}' \in \mathcal{C}_0$, there exist L points \mathbf{f} from \mathcal{C} of the shape $\mathbf{f} = \mathbf{f}' + \mathbf{U}\mathbf{n}$ (see (61)). Let these points be characterized by $\mathbf{n} \in \mathcal{L}_m(\mathbf{f}')$, $\text{card}(\mathcal{L}_m) = L$ for $\mathbf{f}' \in \mathcal{G}_m$, $m \in \mathcal{M}$. We divide the points in $\mathcal{C} \setminus \mathcal{S}$ into two categories: the first one, denoted \mathcal{S}^c , consists of points $\mathbf{f} = \mathbf{f}' + \mathbf{U}\mathbf{s}$, $\mathbf{f}' \in \mathcal{G}_m$ for some $m \in \mathcal{M}$, so that $\mathbf{s} \in \mathcal{L}_m(\mathbf{f}') \setminus \mathcal{P}_m$. The second category is $\mathcal{D} = \mathcal{C} \setminus (\mathcal{S} \cup \mathcal{S}^c)$.

For $\mathbf{f} \in \mathcal{S}^c$, by using the substitution $\mathbf{f} = \mathbf{f}' + \mathbf{U}\mathbf{s}$, $\mathbf{f}' \in \mathcal{G}_m$, and by taking into account (63), for every $m \in \mathcal{M}$ (65) becomes

$$\sum_{k=1}^P \hat{H}_k(\mathbf{f}' + \mathbf{U}\mathbf{p}) Y_k(\mathbf{f}' + \mathbf{U}\mathbf{s}) = 0, \quad \mathbf{f}' \in \mathcal{G}_m, \quad \mathbf{p} \in \mathcal{P}_m, \quad \mathbf{s} \in \mathcal{L}_m(\mathbf{f}') \setminus \mathcal{P}_m. \quad (70)$$

We introduce the matrix

$$\mathbf{Y}_m^c(\mathbf{f}') = [c_{ks}] = [\mathbf{Y}_k(\mathbf{f}' + \mathbf{U}\mathbf{s})] \quad (71)$$

of dimensions $P \times (L - P_m)$, where again lexicographic order is taken for the vector index. Then (70) can be written in matrix form for every $m \in \mathcal{M}$:

$$\mathbf{H}_m(\mathbf{f}') \mathbf{Y}_m^c(\mathbf{f}') = \mathbf{0}_{P_m \times L - P_m}. \quad (72)$$

It follows that $\mathbf{Y}_m^c(\mathbf{f}')$ can be any matrix that satisfies (15) and, consequently, we have determined $Y_k(\mathbf{f})$ on \mathcal{S}^c .

If $\mathbf{f} \in \mathcal{D}$, then $\hat{H}_k(\mathbf{f} - \mathbf{U}\mathbf{n}) = 0$ for every $\mathbf{f} \in \mathbb{R}^N$, as $\mathbf{f} - \mathbf{U}\mathbf{n} \notin \mathcal{S}$, so that the $Y_k(\mathbf{f})$ can be arbitrary. The existence of several solutions for the reconstruction filters is due to the fact that the sampling density is generally higher than the reciprocal of the volume of the spectral support. However, if $P_m = P$ for a certain m , then the solution of (68) is unique (provided the independence condition, which becomes $\det(\mathbf{H}_m) \neq 0$, is met).

We remark that, for situations like the one depicted in Fig. 7, the sets $\mathcal{L}_m(\mathbf{f}')$ do not depend on \mathbf{f}' . In order to obtain a sampling expansion for the signal $x(\mathbf{t})$, with Fourier transform $X(\mathbf{f})$, we take the inverse Fourier transform of (62) with $X_0(\mathbf{f}) = X(\mathbf{f})$. Let $g_k(\mathbf{t})$ the inverse Fourier transforms of the signals $G_k(\mathbf{f}) = X(\mathbf{f})H_k(\mathbf{f})$ defined in Fig. 60, and let $*$ denote convolution. We have

$$\begin{aligned} x(\mathbf{t}) &= \mathbb{F}^{-1} \left\{ \sum_{k=1}^P Y_k(\mathbf{f}) \times \left[X(\mathbf{f})H_k(\mathbf{f}) * U \sum_{\mathbf{n} \in \mathbb{Z}^N} \delta(\mathbf{f} - \mathbf{U}\mathbf{n}) \right] \right\} = \\ &= \sum_{k=1}^P y_k(\mathbf{t}) * \left[\sum_{\mathbf{n} \in \mathbb{Z}^N} g_k(\mathbf{t}) \delta(\mathbf{t} - \mathbf{U}^{-T}\mathbf{n}) \right]; \end{aligned}$$

Finally, there results

$$x(\mathbf{t}) = \sum_{k=1}^P \sum_{\mathbf{n} \in \mathbb{Z}^N} g_k(\mathbf{U}^{-T}\mathbf{n}) y_k(\mathbf{t} - \mathbf{V}^{-T}\mathbf{n}). \quad (73)$$

We obtained the following

Theorem. A finite energy, complex valued, continuous signal, defined on \mathbb{R}^N , which has a spectral support in the shape of (60), sampled with the MSS of Fig. 8, with the frequency responses of the reconstruction filters given by (69) and (72), can be interpolated from its samples taken at points $(\mathbf{U}^{-1})^T \mathbf{n}$ according to (73), if the matrix \mathbf{H}_m defined in (67) has full row rank for each $m \in \mathcal{M}$.

We now present bounds for the energy of the energy (L^2 norm) of the aliasing error.

Suppose that, caused by signal mismodeling, there exists some out of band energy in $\mathcal{C}\mathcal{S}$. If we split the Fourier transform of the input signal in two terms: $X(\mathbf{f}) = X_{\mathcal{S}}(\mathbf{f}) + X_{\mathcal{C}\mathcal{S}}(\mathbf{f})$, with the two terms in the right hand side bandlimited to \mathcal{S} and $\mathcal{C}\mathcal{S}$ respectively, then, due to linearity, the output signal can be written as $X_0(\mathbf{f}) = X_{0\mathcal{S}}(\mathbf{f}) + X_{0\mathcal{C}\mathcal{S}}(\mathbf{f})$, where each term in the right hand side is the system output when it is driven by the corresponding term of the input.

Since $X_{0\mathcal{S}}(\mathbf{f}) = X_{\mathcal{S}}(\mathbf{f})$ by definition of the MSS, there results the following expression for the Fourier transform of the aliasing error:

$$E(\mathbf{f}) = \begin{cases} 0, & \mathbf{f} \in \mathcal{S} \\ X_0(\mathbf{f}) - X(\mathbf{f}), & \mathbf{f} \in \mathcal{C} \setminus \mathcal{S} \end{cases} \quad (74)$$

The energy of the aliasing error can be obtained by integration:

$$\mathcal{E} = \int_{\mathcal{C} \setminus \mathcal{S}} |E(\mathbf{f})|^2 d\mathbf{f}. \quad (75)$$

For $\mathbf{f} \in \mathcal{C} \setminus \mathcal{S}$, we write again $\mathbf{f} = \mathbf{f}' + \mathbf{U}\mathbf{n}$ with $\mathbf{n} \in \mathcal{L}(\mathbf{f}') \subset \mathbb{Z}^N$, and $\mathbf{f}' \in \mathcal{C}_0 \setminus \mathcal{G}$, $\mathcal{G} = \bigcup_{m \in \mathcal{M}} \mathcal{G}_m$. As we have shown above, for a given $\mathbf{f}' \in \mathcal{C}_0 \setminus \mathcal{G}$, the cardinality of $\mathcal{L}(\mathbf{f}')$, i.e. the number of corresponding points $\mathbf{f} \in \mathcal{C} \setminus \mathcal{S}$ is

$$\text{card}(\mathcal{L}(\mathbf{f}')) = \begin{cases} L, & \mathbf{f}' \in \mathcal{C}_0 \setminus \mathcal{G} \\ \mathcal{L} - P_m, & \mathbf{f}' \in \mathcal{G}_m \end{cases}. \quad (76)$$

The expression of the Fourier transform of the output signal on $\mathcal{C} \setminus \mathcal{S}$ is similar to (62), except the use of H_k instead of \hat{H}_k . In terms of \mathbf{f}' we have

$$X_0(\mathbf{f}' + \mathbf{U}\mathbf{n}) = U \sum_{k=1}^P \sum_{\mathbf{m} \in \mathcal{L}(\mathbf{f}')} Y_k(\mathbf{f}' + \mathbf{U}\mathbf{n}) \times H_k(\mathbf{f}' + \mathbf{U}\mathbf{n}) X(\mathbf{f}' + \mathbf{U}\mathbf{n}). \quad (77)$$

We introduce the following vectors and matrices, with the vector index in the lexicographic order:

$$\begin{aligned} \mathbf{X}(\mathbf{f}') &= [a_{\mathbf{n}}] = X(\mathbf{f}' + \mathbf{U}\mathbf{n}), \\ \mathbf{X}_0(\mathbf{f}') &= [b_{\mathbf{n}}] = X_0(\mathbf{f}' + \mathbf{U}\mathbf{n}), \\ \mathbf{E}(\mathbf{f}') &= [c_{\mathbf{n}}] = \mathbf{E}(\mathbf{f}' + \mathbf{U}\mathbf{n}), \\ \mathbf{Y}(\mathbf{f}') &= [d_{k\mathbf{n}}] = Y_k(\mathbf{f}' + \mathbf{U}\mathbf{n}), \\ \mathbf{H}(\mathbf{f}') &= [e_{\mathbf{n}k}] = H_k(\mathbf{f}' + \mathbf{U}\mathbf{n}), \\ &\mathbf{n} \in \mathcal{L}(\mathbf{f}'), k = 1..P. \end{aligned} \quad (78)$$

From (77) and (78) the following matrix equations are obtained

$$\mathbf{X}_0(\mathbf{f}') = U\mathbf{Y}(\mathbf{f}')\mathbf{H}(\mathbf{f}')\mathbf{X}(\mathbf{f}') = \mathbf{A}(\mathbf{f}')\mathbf{X}(\mathbf{f}'),$$

and

$$\begin{aligned} \mathbf{E}(\mathbf{f}') &= \mathbf{X}_0(\mathbf{f}') - \mathbf{X}(\mathbf{f}') = \\ &= [\mathbf{A}(\mathbf{f}') - \mathbf{I}]\mathbf{X}(\mathbf{f}') = \mathbf{B}(\mathbf{f}')\mathbf{X}(\mathbf{f}'), \end{aligned} \quad (79)$$

where $\mathbf{A}(\mathbf{f}')$ and $\mathbf{B}(\mathbf{f}')$ have obvious definitions.

We denote by \mathbf{M}^H the hermitian transpose of the matrix or vector \mathbf{M} . We have

$$\mathbf{E}^H(\mathbf{f}')\mathbf{E}(\mathbf{f}') = \mathbf{X}^H(\mathbf{f}')\mathbf{B}^H(\mathbf{f}')\mathbf{B}(\mathbf{f}')\mathbf{X}(\mathbf{f}') = \mathbf{X}^H(\mathbf{f}')\mathbf{R}(\mathbf{f}')\mathbf{X}(\mathbf{f}') \quad (80)$$

The matrix $\mathbf{R}(\mathbf{f}') = \mathbf{B}^H(\mathbf{f}')\mathbf{B}(\mathbf{f}')$ is hermitian, so its eigenvalues are real and positive. Let $\lambda_{\max}(\mathbf{f}')$ the maximum eigenvalue, and let $\lambda_{\max} = \sup_{\mathbf{f}' \in \mathcal{C} \setminus \mathcal{G}} \lambda_{\max}(\mathbf{f}')$. From (80) there results after summation, integration over $\mathcal{C}_0 \setminus \mathcal{G}$, a change of variable to $\mathcal{C} \setminus \mathcal{S}$, and by tacking into account (75):

$$\mathcal{E} \leq \lambda_{\max} \int_{\mathcal{C} \setminus \mathcal{S}} |X(\mathbf{f})|^2 d\mathbf{f}. \quad (81)$$

We obtained an upper bound for the energy of the aliasing error when the spectral support is not band limited to \mathcal{S} , but it is however contained by \mathcal{C} , in terms of the signal's out of band energy. Obviously, a similar lower bound can be obtained based on the smallest eigenvalue of \mathbf{R} .

This concludes both the presentation of selected results in Sampling Theory and the Section dedicated to technical contributions.

2.6. Development

The planning of future research relies on two directions: Applied Electromagnetics and Solar Energy and on the interference between the two, namely antennas powered by solar energy.

The field of Applied Electromagnetics is planned to be developed within the Department of Measurement and Optical Electronics, Faculty of Electronics and Telecommunications of Timișoara by extending capabilities and assets of the Laboratory of Microwaves, Antennas and Electromagnetic Compatibility, by further cooperation with partners and finding new ones, by attracting new qualified personnel and by involving students in research.

Following personal efforts in attracting funding, the Laboratory has been equipped with a high performance 24 GHz Vector Network Analyzer, a high performance and two average performance Spectrum Analyzers, a high performance Signal Generator and a wide range of general purpose electronic equipment: signal generators, power supplies, measuring instrumentation and laboratory tools. This assets, together with general purpose computers allowed for designing and measuring performances of the metamaterial based devices we have devised and reported in a large number of publications in the last three years. For the near future, a TEM cell or an anechoic chamber and laboratory manufacturing facilities for microstrip boards are planned to be purchased. This will allow for independent development of passive structures, since, at the present time, measurements can be performed in our laboratory but manufacturing is realized within the facilities of our partners.

The future research directions in Applied Electromagnetics are planned to continue in finding new structures inspired from metamaterials having unusual and useful properties and applying this structures in filter design and realization, in sensor development and in finding new designs for power distribution networks of high speed digital or mixed signal integrated circuits and printed-circuit boards. However, the palette of applications of metamaterial inspired devices we intend to tackle is not supposed to be limited to the above listed ones, which we have already approached. Electronically controlled beam steering, holographic surfaces, dispersion engineering applications and new control techniques will also be considered. As the literature reviewed in the previous sections reveals, this research is still performed in university-based laboratories. Patents owned by large international corporations have been issued only in the last two or three years and industrial applications are still a mater of future. However, the same literature reveals that the interest in industry is constantly growing for metamaterial-based solutions.

On the other hand, scientific interest in metamaterials is growing due to the unusual properties that allow for propagation control of electromagnetic waves. Super-prism and super-lens effects and cloaking are other topics that attracted the interest of researchers who published their results in non-engineering oriented journals. Nevertheless, engineers involved in research played an important role in discovering and revealing these effects. This growing field of dispersion engineering is therefore very promising. Our contribution consisting of the creation of a periodic structure with electromagnetic band-gap between every two modes of propagation within the first eight ones is a very good start for this field. In order to be appropriately controlled, waves should be carried by a single mode. Our structure provides a wide variety of single mode propagation, at a wide range of frequencies. Furthermore, techniques such as scaling, use of multiple patches and vias and altering of geometry can be used for modifying the dispersion diagram in frequency in order to devise structures that meet specific frequency requirements.

It is our intention to tackle the phenomena related to wave propagation control. This involves considering interfaces between various periodic, quasi-periodic and homogeneous media. Since periodic and quasi-periodic media are man-made, finding such metamaterials with good properties is a generous subject of research. It is also a new subject, if viewed from our perspective. However, engineering applications are the reason for our research. Therefore we will target finding new engineering solutions, such as new designs for passive beam splitters, microwave lenses and holographic surfaces.

Devising new structures for power planes in high speed circuits in view of mitigation of parallel-plate noise is another interesting research field, with connection to signal integrity issues and Electromagnetic Compatibility in general. As shown in the previous sections, we had good results related to this topic. Modern high-speed circuits are stacks of several metal planes separated by dielectric materials, which may be different, so may have different constitutive parameters. The metal

planes are connected by vias. The pins of the mounted devices can be connected to the metal planes equally through vias with metal walls. When a fast signal switch occurs at one pin, the transient current density in the metal walls of the vias generates an electromagnetic wave that propagates through the parallel-plate waveguide created by the metal walls. With many almost simultaneous switches, the resulting electromagnetic signals have the character of a broad-band noise, although it is essentially deterministic. This kind of noise is also called "simultaneous switching noise" or "ground bounce noise" and it can cause alteration of the power supply of the circuit, since modern MOS devices require low voltages.

An obvious solution for mitigation of the parallel-plate noise consists of embedding a metamaterial-based high impedance surface having an electromagnetic band-gap in the frequency range of the noise. Devising such a surface requires careful research for finding an optimum because several factors concur. First, the spectrum of the noise is low-pass. The electromagnetic band-gap can start from DC only if the power planes are electrically connected together, which is clearly not an option in this case. Therefore, the electromagnetic band-gap can only expand between two frequencies, the first one being required to be as low as possible and the second one sufficiently high to cover the whole spectrum of the noise. A periodic surface with such feature can be obtained by selecting large dimensions for the unit cell. However, the whole surface is of finite size due to small dimensions of modern circuits, so that the size of the unit cell must be as small as possible since a large number of unit cells are necessary in order to approximate the behavior of an infinite surface. Therefore, other solutions must be considered such as new designs of the metallic patches and number and placements of vias.

A second problem in design of periodic surfaces intended for mitigation of parallel-plate noise is coupling of signals between vias. A signal having a frequency comprised in the electromagnetic band-gap range has an imaginary propagation constant and therefore is evanescent. However, such a signal can couple between vias if sufficiently close and badly positioned. The influence of vias placement is subject of current research.

Another direction in current development of devices based on metamaterials is filter construction, with the two alternatives: fixed and switchable or tunable. Both possibilities have been explored and several multi-band filters have been proposed in view of applications, especially for modern wireless systems. We have also tackled this field, devised new structures and performed parametric studies in view of meeting application dependent specifications. However, much work has to be done in the future in order to match the level of flexibility in design of classical solutions. Closely related is the problem of signal coupling. Although solutions exist, new designs are necessary for improvement.

We have also approached the problem of switched filters. We have proposed several structures that allow switching between different frequency responses, e.g. from band-pass to low-pass. Switching is accomplished by means of electronic control elements, such as MEMS, FETs, varactor diodes or *pin* diodes that alter the geometry of the surface and consequently the frequency response. A further extension consists of tunable filters that rely on modification of capacitance of varactor diodes through the biasing network. We have introduced novel biasing techniques and assessed the impact of the bias on the frequency characteristics and we intend to further develop these studies and propose new practical realizations.

Up to this moment we have not approached applications of periodic surfaces as open structures. We intend to do that in the future, again in both solutions: fixed and tunable. The field of applications extends from leaky-wave antennas to electronically steerable ones and up to holographic surfaces.

Successful research activity is not possible without cooperation. Up to now, we have cooperated in the field of Applied Electromagnetics with a team from the Budapest University of Engineering and Economics, with a team from the Laboratory of Antennas and Electromagnetic Compatibility (LACE) from the Politecnico di Torino, Italy and with the Research Group in Magnetic Fluids with the "Politehnica" University of Timișoara. The first one involved setting up a waveguide measuring systems of constitutive parameters of seeds (such as e.g. wheat) in X band in view of optimization of microwave heating process. The cooperation with LACE has both a teaching side and a research side. On one hand, within the teaching side we have sustained eight hour-courses for several years with topics from the *S* parameters applications at the Politecnico and a colleague from Italy taught eight hour-courses with topics from Smith chart applications and constitutive parameters. This teaching cooperation is in the framework of the Socrates / Erasmus European program and is continuing and

planned to be developed with undergraduate students and PHD students exchange. On the other hand, the research cooperation in the field of metamaterials had as a result the publication of more than 20 scientific papers in refereed journals and proceedings of international conferences in the last three years. This very good start is supposed to be continued also in a formal framework. Besides applications of metamaterials listed above, the field of metamaterial-based sensors will be approached in the next future. Furthermore, an enlarged cooperation is planned between the two parts and the Research Group in Magnetic Fluids, based on preliminary results on X-band waveguide measurement of constitutive parameters of materials containing nano-sized magnetite particles. Since the material is planar, embedding such slabs in the periodic surfaces we have studied may lead to interesting engineering consequences.

The presented research directions and topics in metamaterials and magnetic fluids, together with existing equipment and computing facilities constitute a sufficiently large field to accommodate full-time researchers, doctoral students and diploma students. Funding can be ensured through national and European grants and contracts with economic partners in the geographical area, where automotive industry now uses microwave systems, transmission lines and components and is interested in signal integrity issues.

Education in the field of Applied Electromagnetics (High Frequency Techniques, Antennas and Propagation and Electromagnetic Compatibility) takes place both at an undergraduate and at a graduate level. Students are provided with specially written teaching material and an experimental equipment for laboratory training consisting of X band devices and measuring instruments. A normal enhancement of teaching facilities is expected in the future. However, technical knowledge acquired at the first two levels in the field of high frequency applications is not enough for performing research activities. Therefore additional courses must be planned at the doctoral school level. At least two courses have to be introduced in order to ensure a smooth transition from school activity towards research: 1. Microwaves, Antennas and Propagation – Advanced Topics and 2. Microwave Measurements. Various teaching material, existing laboratories and equipment and experience gained by the personnel working in the field ensures the possibility to perform this teaching activity. After finishing the introductory courses, doctoral students are supposed to gain experience and obtain results by working in the research laboratory under the supervision of and interacting with the doctoral supervisor and with his/her colleagues in a team-work environment.

Besides working with doctoral students, constant cooperation with other research teams and laboratories will be considered. Our experience shows that large research structures are not efficient in our particular situation. We will rather consider formation of small ad-hoc groups or teams created for solving problems and for application for grants in specific research targets.

From the above presentation, it is clear that the main research topics are planned to belong to the field of Applied Electromagnetics. However our experience in the other two fields where we have worked and obtained results, namely Signal Processing and Solar Energy will have an important impact on our future development. Signal Processing is ubiquitous in modern applications of Electronics and expertise gained in working in this field is planned to be applied in sensor construction. Moreover, filtering applications we planned to develop using metamaterials are not conceivable without solid knowledge and experience in Signal Processing.

The Solar Energy field is still in development at the "Politehnica" University of Timișoara. As shown in Part II, mainly practical applications have been considered. Since we are still involved in the team following a fruitful cooperation, we will participate to measurements and feasibility studies. A particular topic we have the intention to tackle provides a connection between Microwaves and Solar Energy: construction of Solar Energy powered equipment. Current interest is in solar energy powered antennas, but other systems might also be considered for this type of powering if intended to be placed in remote locations. In fact, this problem might be tackled from a more general point of view: find specific requirements and design constraints for solar energy based power supplies to be used in powering remote microwave systems.

3. References

3.1. General References

- [abhari_03] R. Abhari, G. V. Eleftheriades, "Metallo-dielectric electromagnetic band-gap structures for suppression and isolation of the parallel-plate noise in high-speed circuits," *IEEE Trans. Antennas Propag.*, vol. 51, no. 6, pp. 1629-1639, June 2003
- [abr_64] M. Abramowits, I. A. Stegun, *Handbook of Mathematical Functions*, National Bureau of Standards, Applied Mathematics Series 55, Nov., 1964.
- [ahn_01] D. Ahn, J.-S. Park, C.-S. Kim, J. Kim, Y. Qian, T. Itoh, "A design of the low-pass filter using the novel microstrip defected ground structure," *IEEE Trans. Microwave Theory Tech.*, vol. 49, no. 1, pp. 86-93, Jan. 2001.
- [ant_87] I. Anton, I. De Sabata, L. Vekas, et al., "Magnetic fluid seals – some design problems and applications", *J. Magn. Mater.*, 65 (2-3), pp. 379-381, Mar. 1987
- [ant_90] I. Anton, I. De Sabata, L. Vekas, "Application oriented researches on magnetic fluids", *J. Magn. Mater.*, 85 (1-3), pp. 219-226, Apr. 1990.
- [baya_09] F. Bayatpur, and K. Sarabandi, "A tunable metamaterial frequency-selective surface with various modes of operation," *IEEE Trans. Microwave Theory Tech.*, vol. 57, no. 6, pp. 1433-1438, June 2009.
- [ber_81] B. N. Berkovskii, A. N. Vislovich, *Desiatoe Rijkoe Sovesc po Magn. Ghidrodin.*, vol. III, Riga, pp. 97-98, 1981.
- [bla_88] C. Blaj, *Doctoral Thesis*, "Politehnica" University of Timisoara, 1988.
- [bri_53] L. Brillouin, *Wave Propagation in Periodic Structures; Electric Filters and Crystal Lattices*, 2nd ed., New York: Dover, 1953.
- [brown_85] J. L. Brown Jr., "Sampling expansions for multiband signals", *IEEE Trans. Acoust., Speech, Signal Proc.*, vol. ASSP-33, pp. 312-315, 1985.
- [brown_89] J. L. Brown Jr., K. Sa,ngasri, "Sampling reconstruction of N -dimensional images after multi-linear filtering", *IEEE Trans. Circuits Syst.*, vol. 36, no. 7, pp. 1035-1038, July, 1989.
- [brown_91], J. L. Brown Jr., S. D. Cabrera, "On well-posedness of the Papoulis generalized sampling expansion", *IEEE Trans. Circuits Syst.*, vol. 38, no. 5, pp. 554-556, May, 1991.
- [chang_11] W.-S. Chang, C.-Y. Chang, "Novel microstrip periodic structure and its application to microwave filter design," *IEEE Microwave Wireless Comp. Lett.*, vol. 21, no. 3, pp. 124-126, March 2011.
- [chan_03] K. W. Chan and H. C. So, "An Exact Analysis of Pisarenko's Single-Tone Frequency Estimation Algorithm", *Signal Processing*, vol. 83, pp. 685-690, 2003.
- [cheung_93] K. F. Cheung, "A multidimensional extension of Papoulis' generalized sampling expansion with applications in minimum density sampling", in R. J. Marks II ed. *Advanced Topics in Shannon Sampling and Interpolation Theory*, New York: Springer Verlag, 1993, pp. 85-119.
- [con_78] J. B. Conway, *Functions of One Complex Variable*, Second Edition, New York: Springer-Verlag, 1978.

- [costa_08] F. Costa, A. Monorchio, S. Talarico, and F. M. Valori, "An active high impedance surface for low profile, tunable and steerable antennas," *IEEE Antennas Wireless Propag. Lett.*, vol. 7, pp. 676-680, 2008.
- [costa_11] F. Costa, A. Monorchio, "Tunable high-impedance surface with a reduced number of varactors," *IEEE Antennas Wireless Propag. Lett.*, vol. 10, pp. 11-13, 2011.
- [collin_92] R. E. Collin, *Introduction to Microwave Engineering*, N.Y.: IEEE Press, 1992.
- [CST] Microwave Studio, Computer Simulation Technology, 2009, 2011.
- [das_96] N. K. Das, "Methods of suppression or avoidance of parallel-plate power leakage from conductor-backed transmission lines," *IEEE Trans. Microw. Theory Tech.*, vol. 44, no. 2, pp. 169-181, Feb. 1996.
- [des_89] I. De Sabata, I. Vekas, "On the restoring force of magnetic fluid bearings", *Rev. Roum. Sci. Tech. – Méc. Appl.*, **34**, 1, pp. 13-20, 1989.
- [des_92] I. De Sabata, N. C. Popa, I. Potencz, et al. "Inductive transducers with magnetic fluids", *Sensor Actuat A-Phys*, 32 (1-3), pp. 678-681, Apr. 1992.
- [dong_12] Y. Dong, T. Itoh, "Promising future of metamaterials," *IEEE Microwave Magazine*, vol. 13, no. 2, pp. 39-56, March/April 2012.
- [eld_00] Y. C. Eldar, A. V. Oppenheim, "Filterbank Reconstruction of Bandlimited Signals from Nonuniform and Generalized Samples", *IEEE Transactions on Signal Processing*, Vol. 48, No. 10, October 2000, pp. 2864-2875.
- [elef_12_a] G. V. Eleftheriades, "Metamaterials: the first ten years," *IEEE Microwave Magazine*, vol. 13, no. 2, pp. 8-10, March/April 2012.
- [elef_12_b] G. V. Eleftheriades, "Transforming Electromagnetics using metamaterials," *IEEE Microwave Magazine*, vol. 13, no. 2, pp. 27-38, March/April 2012.
- [elef_02] G. V. Eleftheriades, A. K. Iyer, P. C. Kremer, "Planar negative refractive index media using periodically L-C loaded transmission lines," *IEEE Trans. Microwave Theory Tech.*, vol. 50, no. 12, pp. 2702-2712, Dec. 2002.
- [elek_04] F. Elek, G. V. Eleftheriades, "Dispersion analysis of the shielded Sievenpiper structure using multiconductor transmission-line theory," *IEEE Microw. Wireless Comp. Lett.*, vol. 14, no. 9, Sept. 2004.
- [enoch_03] S. Enoch, G. Tayeb, B. Gralak, "The richness of the dispersion relation of electromagnetic bandgap materials", *IEEE Trans. Antennas and Propagat.*, vol.51, no.10, pp.2659-2666, Oct. 2003.
- [erh_90] J. C. Erhard, "MR data acquisition and reconstruction using efficient sampling schemes", *IEEE Trans. on Medical Imaging*, vol. 9, No. 3, pp. 305-309, 1990.
- [erik_93] A. Eriksson, P. Stoica, "On statistical analysis of Pisarenko tone frequency estimator", *Signal Process.*, vol. 31, no. 3, pp. 349-353, Apr. 1993.
- [fang_99] L. Fang-Lih and W. Ruey-Beei, "Computations for radiation and surface-wave losses in coplanar waveguide bandpass filters," *IEEE Trans. Microw. Theory Tech.*, vol. 47, no. 4, pp. 385-389, Apr. 1999.

- [fertig_96] L. B. Fertig, J. H. McClellan, "Instantaneous frequency estimation using linear prediction with comparisons to the DESAs", *IEEE Signal Processing Lett.*, vol. 3, pp. 54–56, Feb. 1996.
- [fitz_94] M. P. Fitz, "Further Results in the Fast Estimation of a Single Frequency", *IEEE Trans. Comm.*, vol. 42, No. 2/3/4, pp. 862-864, Feb./Mar./Apr. 1994.
- [fu_07] H. Fu, P. Y. Kam, "MAP/ML Estimation of the Frequency and Phase of a single Sinusoid in Noise", *IEEE Trans. Signal Processing.*, vol. 55, No. 3, pp. 834-845, Mar. 2007.
- [gao_06] C. Gao, Z. N. Chen, Y. Y. Wang, N. Yang, and X. M. Qing, "Study and suppression of ripples in passbands of series/parallel loaded EBG filters," *IEEE Trans. Microwave Theory Tech.*, vol. 54, no. 4, pp. 1519-1525, April, 2006.
- [gous_06] G. Goussetis, A. P. Feresidis, P. Kosmas, "Efficient analysis, design, and filter applications of EBG waveguide with periodic resonant loads," *IEEE Trans. Microwave Theory Tech.*, vol. 54, no. 11, pp. 3885-3892, Nov. 2006.
- [gre_03] M. Greconici, *Doctoral Thesis*, "Politehnica" University of Timisoara, 2003.
- [gupta_02] K. C. Gupta, T. Itoh, A. A. Oliner, "Microwave and RF education – past, present and future", *IEEE Trans. Microwave Theory Tech.*, vol. 50, no. 3, pp. 1006-1014, March, 2002.
- [hao_09] Z.-C. Hao, J.-S. Hong, J. P. Parry, P. Hand, "Ultra-wideband bandpass filter with multiple notch bands using nonuniform periodical slotted ground structure," *IEEE Trans. Microwave Theory Tech.*, vol. 57, no. 12, pp. 3080-3088, Dec. 2009.
- [hig_87] J. R. Higgins, "Some gap sampling series for multiband signals", *Signal Processing*, No. 12., pp. 313-319, 1987.
- [kam_05] T. Kamgaing, O. M. Ramahi, "Desin and modelling of high-impedance electromagnetic surfaces for switching noise suppression in power planes," *IEEE Trans. Electromagn. Compat.*, vol. 47, no. 3, pp. 479-489, Aug. 2005.
- [kam_08] T. Kamgaing, O. M. Ramahi, "Multiband electromagnetic bandgap structures for applications in small form-factor multichip module packages," *IEEE Trans. Microw. Theory Tech.*, vol. 56, no. 10, pp. 2293-2300, Oct. 2008.
- [karm_03] N. C. Karmakar, and M. N. Mollah, "Investigation into nonuniform photonic band-gap microstripline low-pass filters," *IEEE Trans. Microwave Theory Tech.*, vol. 51, no. 2, pp. 564-572, February 2003.
- [kay_81] S. M. Kay and S. L. Marple Jr., "Spectrum Analysis – A Modern Perspective", *Proc. of the IEEE*, Vol. 69, No. 11, pp. 1360-1419, Nov. 1981.
- [kay_88] . S. M. Kay, *Modern Spectral Estimation: Theory and Application*, Englewood Cliffs, NJ: Prentice Hall, 1988.
- [kay_89] S. A. Kay, "A Fast and Accurate Single Frequency Estimator", *IEEE Trans. ASSP*, vol. 37, No. 12, pp. 1987-1989, Dec. 1989.
- [kay_93] S. M. Kay, *Fundamentals of Statistical Signal Processing: Estimation Theory*, Englewood Cliffs, NJ: Prentice Hall, 1993.

- [ken_87] R. J. Kenefic and A. H. Nuttall, "Maximum Likelihood Estimation of the Parameters of a Tone Using Real Discrete Data", *IEEE J. Oceanic Eng.*, vol. OE-12, No. 1, pp. 279-280, Jan. 1987.
- [kim_08] K. H. Kim, J. E. Schutt-Ainé, "Analysis and modelling of hybrid planar-type electromagnetic-bandgap structures and feasibility study on power distribution networks applications," *IEEE Trans. Microw. Theory Tech.*, vol. 56, no. 1, pp. 178-186, Jan. 2008.
- [kim_96] D. Kim, M. J. Narashima, "An Improved Single Frequency Estimator", *IEEE Signal Processing Letters*, vol. 3, no. 7, pp. 212-214, July 1996.
- [kittel_96] Charles Kittel, *Introduction to Solid State Physics*, John Wiley & Sons, 1996.
- [kuo_06] T.-N. Kuo, S.-C. Lin, and C. H. Chen, "Compact ultra-wideband bandpass filters using composite microstrip-coplanar-waveguide structure," *IEEE Trans. Microwave Theory Tech.*, vol. 54, no. 10, pp. 3772-3777, October 2006.
- [lapine_07] M. Lapine, S. Tretyakov, "Contemporary notes on metamaterials," *IET Microw. Antennas Propag.*, 1 (1), pp. 3-11, 2007.
- [lim_05] S. Lim, Ch. Caloz, T. Itoh, "Metamaterial-Based Electronically Controlled Transmission-Line Structure as a Novel Leaky-Wave Antenna with Tunable Radiation Angle and Beamwidth," *IEEE Trans. Antennas Propag.*, vol. 53, no. 1, pp. 161-173, Jan. 2005.
- [lui_08] K. W. K. Lui, H. C. So, "Modified Pisarenko harmonic decomposition for single-tone frequency estimation", *IEEE Trans. Signal Processing.*, vol. 56, no. 7, pp. 3351-3356, July 2008.
- [luise_95] M. Luise, R. Reggiannini, "Carrier Frequency Recovery in All-Digital Modems for Burst-Mode Transmissions", *IEEE Trans. Comm.*, vol. 43, No. 2/3/4, pp. 1169-1178, Feb./Mar./Apr. 1995.
- [matek_08] L. Matekovits, G. C. Vietti Colomé, M. Orefice, "Controlling the bandlimits of TE-surface wave propagation along a modulated microstrip-line-based high impedance surface," *IEEE Trans. Ant. Prop.*, vol. 56, no. 8, pp. 2555-2562, Aug. 2008.
- [matek_09] L. Matekovits, M. Heimlich, K. Esselle, "Tunable periodic microstrip structure on GaAs wafer," *Progress In Electromagnetics Research*, PIER 97, pp. 1-10, 2009.
- [matek_10] L. Matekovits, "Analytically Expressed Dispersion Diagram of Unit Cells for a Novel Type of Holographic Surface", *IEEE Antennas and Wireless Propagat. Letters*, Vol. 9, pp. 1251 - 1254, 2010.
- [matek_11] L. Matekovits, M. Heimlich, K. P. Esselle, "Metamaterial-based millimeter-wave switchable leaky wave antennas for on-chip implementation in GaAs technology," *Journal of Electromagnetic Waves and Applications (JEMWA)*, Vol. 25, pp. 49-61, Jan. 2011.
- [matt_07] A. F. Matthews, S. K. Morrison, Y.S. Kivshar, "Self-collimation and beam splitting in low-index photonic crystals", *Optics Communications*, vol. 279, no 2, pp. 313-319, Nov., 2007.
- [menzel_03] W. Menzel, L. Zhu, K. Wu, and F. Bögelsach, "On the design of novel compact broadband planar filter," *IEEE Trans. Microwave Theory Tech.*, vol. 51, no. 2, pp. 364-369, February 2003.
- [mcvay_04] J. McVay, N. Engheta, A. Hoorfar: "High Impedance Meta-material Surfaces Using Hilbert-Curve Inclusions", *IEEE Microwave and Wireless Components Lett.*, vol. 14, no. 3, pages 130-132, March 2004.

- [mcvay_05] J. McVay, A. Hoorfar, N. Engheta, "Peano high-impedance surfaces," *Radio Sci.*, 40, RS6S03, 2005.
- [mitsa_90] T. Mitsa, K. J. Parker, W. E. Smith, A. M. Tekalp, J. Szumowski, "Correction of motion artifacts along the slice selection axis in MRI", *IEEE Trans. on Medical Imaging*, vol. 9, No. 3, pp. 310-317, 1990.
- [noj_08] S. Nojima and Y. Kamakura, "Irreducible first Brillouin-zone for twodimensional binary-compound photonic crystals," *J. Phys. Soc. Jpn.*, vol. 77, no. 3, p. 034403, Mar. 2008
- [notomi_00] M. Notomi, "Theory of light propagation in strongly modulated photonic crystals: Refraction like behavior in the vicinity of the photonic band gap", *Physical Review B*, vol. 62, no. 16, Oct. 2000
- [opp_83] A. V. Oppenheim, A. Wilsky, I. T. Young, *Signals and Systems*, N. J.:Prentice Hall, 1983.
- [pau_09] F. de Paulis, A. Orlandi, "Signal integrity analysis of single-ended and differential striplines in presence of EBG planar structures," *IEEE Microwave Wireless Comp. Lett.*, vol. 19, no. 9, pp. 554-556, Sept. 2009.
- [pau_10] F. de Paulis, L. Raimondo, A. Orlandi, "Impact of shorting vias placement on embedded planar electromagnetic bandgap structures within multilayer printed circuit boards," *IEEE Trans. Microw. Theory Tech.*, vol. 58, no. 7, pp. 1867-1876, July 2010
- [park_01] Y.-J Park, A. Herschlein, W. Wiesbeck, "A photonic bandgap structure for guiding and suppressing surface waves in millimeter wave antennas," *IEEE Trans. Microw. Theory Tech.*, vol. 49, no. 10, pp. 1854-1859, Oct. 2001.
- [park_06] J. Park, A. C. W. Lu, K. M. Chua, L. L. Wai, J. Lee, J. Kim. "Double-stacked EBG structure for wideband suppression of simultaneous switching noise in LTCC-based SiP applications," *IEEE Microwave Wireless Comp. Lett.*, vol. 16, no. 9, pp. 481-483, Sept. 2006.
- [pap_81] A. Papoulis, *Systems and Transforms with Applications in Optics*, Malabar Fl.: Krieger Pub., 1981.
- [pendry_99] J. B. Pendry, A. J. Holden, D. J. Robbins, W. J. Stewart, "Magnetism from conductors and enhanced nonlinear phenomena," *IEEE Trans. Microwave Theory Tech.*, vol. 47, no. 11, pp. 2075-2084, Nov. 1999.
- [pis_73] V. F. Pisarenko, "The retrieval of harmonics by linear prediction", *Geophys. J. R. Astron. Soc.*, vol. 33, pp. 347-366, 1973
- [popa_97] N. C. Popa, I. De Sabata, "Numerical simulation for electrical coils of inductive transducers with magnetic liquids", *Sensor Actuat A-Phys*, 59 (1-3), pp. 272-276, Apr. 1997.
- [popa_99] N. C. Popa, I. De Sabata, I. Anton, L. Potencz, L. Vékas, "Magnetic fluids in aerodynamic measuring devices", *J. Magn. Mater.*, 201, pp. 385-390, 1999.
- [qui_91] B. G. Quinn, J. M. Fernandes, "A fast efficient technique for the estimation of frequency", *Biometrika*, 78, 3, pp. 489-497, 1991.
- [rao_11] P. H. Rao, M. Swaminathan, "A novel compact electromagnetic bandgap structure in power plane for wideband noise suppression and low radiation," *IEEE Trans. Electromagn. Compat.*, vol. 53, no. 4, pp. 996-1004, Nov. 2011.

- [rajo_07] E. Rajo-Iglesias, M. Caiazzo, L. Inclán-Sánchez, and P.-S. Kildal, "Comparison of bandgaps of mushroom-type EBG surface and corrugated and strip-type soft surfaces," *IET Microw. Antennas Propag.*, 1, (1), pp. 184-189, 2007.
- [rajo_09] E. Rajo-Iglesias, P.-S. Kildal, "Cut-off bandwidth of metamaterial-based parallel plate gap waveguide with one textured metal pin surface," *Proc. 3rd European Conference on Antennas and Propagation EUCAP09*, pp. 33-36, March 2009.
- [rif_74] D. C. Rife and R. R. Boorstyn, "Single-Tone Parameter Estimation from Discrete-Time Observations", *IEEE Trans. Inf. Theory*, vol. 20, No. 5, pp. 591-598, Sept. 1974.
- [rogers_05] S. D. Rogers, "Electromagnetic-bandgap layers for broad-band suppression of TEM modes in power planes," *IEEE Trans. Microw. Theory Tech.*, vol. 53, no. 8, pp. 2495-2505, Aug. 2005.
- [ros_78] R. E. Rosensweig, in *Thermomechanics of Magnetic Fluids*, B. Berkovskii (ed), Washington: Hemisphere, pp. 231-254, 1978.
- [ros_06] E. Rosnes, A. Vahlin, "Frequency Estimation of a Complex Sinusoid Using a Generalized Kay Estimator", *IEEE Trans. Comm.*, vol. 54, No. 3, pp. 407-415, Mar. 2006.
- [sak_84] . H. Sakai, "Statistical analysis of Pisarenko's method for sinusoidal frequency estimation", *IEEE Trans. Acoust., Speech, Signal Processing*, vol. ASSP-32, pp. 95-101, Feb. 1984.
- [sav_03] S. M. Savaresi, S. Bittanti, H. C. So, "Closed-form unbiased frequency estimation of a noisy sinusoid using notch filters", *IEEE Trans. Automat. Contr.*, vol. 48, no. 7, pp. 1285-1292, July 2003.
- [sanz_09] B. Sanz-Izquierdo, E. A. Parker, J.-B. Robertson, J. C. Batchelor, "Tuning technique for active FSS arrays," *Electronic Letters*, vol. 45, no. 22, pp. 1-2, oct. 2009.
- [sei_00] D. Seidner, "Vector Sampling Expansion", *IEEE Transactions on Signal Processing*, Vol. 48, No. 5, May 2000, pp. 1401-1416.
- [she_05] W. H. She, Z. N. Wing, J. W. Halloran, W. J. Chappell, "Variable dielectric constants by structured porosity for passive ceramic components," *Digest of 2005 IEEE MTT-S International Microwave Symposium*, pp. 865-869, 12-17 June 2005.
- [shelby_01] R. A. Shelby, D. R. Smith, S. Schultz, "Experimental verification of a negative index of refraction," *Science*, vol. 292, pp. 77-79, Apr. 2001.
- [shum_99] J. D. Shumpert, W. J. Chappell, L. B. Katehi, "Parallel-plate mode reduction in conductor-backed slots using electromagneyic bandgap structures," *IEEE Trans. Microw. Theory Tech.*, vol. 47, no. 11, pp. 2099-2104, Nov. 1999.
- [siev_98] D. Sievenpiper, E. Yablonovitch, "Circuit and method for eliminating surface currents on metals," U.S. patent 60/079953, Mar. 30., 1998.
- [siev_99_a] D. Sievenpiper, L. Zhang, R. F. Jimenez Broas, N. G. Alexópolous, E. Yablonovitch, "High-impedance electromagnetic surfaces with a forbidden frequency band," *IEEE Trans. Microwave Theory Tech.*, vol. 47, no. 11. pp. 2059-2074, Nov. 1999.
- [siev_99_b] D. Sievenpiper, "High-impedane electromagnetic surfaces," Ph.D. dissertation, Dept. Elect. Eng., Univ. California at Los Angeles, Los Angeles, CA, 1999.

- [siev_02] D. Sievenpiper, J. Schaffner, J. J. Lee, "A steerable leaky-wave antenna using a tunable impedance ground plane," *IEEE Antennas Wireless Propag. Lett.*, vol. 1, pp. 179-182, 2002.
- [siev_03] D. Sievenpiper, J. H. Schaffner, H. Jae Song, R. Y. Loo, G. Tangonan, "Two-dimensional beam steering using an electrically tunable impedance surface," *IEEE Trans. Antennas Propag.*, vol. 51, no. 10, pp.2713-2722, Oct. 2003.
- [siev_05_a] D. Sievenpiper, J. Colburn, B. Fong, J. Ottusch, J. Vishar, "Holographic artificial impedance surfaces for conformal antennas," in *Proc. Digest IEEEAPS/URSI Symp., Washington DC*, vol. 1B, pp. 256-259, Jul. 2005.
- [siev_05_b] D. Sievenpiper, "Forward and backward leaky wave radiation with large effective aperture from an electronically tunable textured surface," *IEEE Trans. Antennas Propag.*, vol. 53, no. 1, pp. 236-247, Jan. 2005.
- [so_02_a] H. C. So, "A closed form frequency estimator for a noisy sinusoid", in *45th IEEE Midwest Symp. Circuits Systems*, Tulsa, OK, 2002.
- [so_02_b] . H. C. So, S. K. Ip, "A novel frequency estimator and its comparative performances for short record lengths", in *11th Eur. Signal Processing Conf.*, Toulouse, France, 2002.
- [so_04] H. C. So and K. W. Chan, "Reformulation of Pisarenko harmonic decomposition method for single-tone frequency estimation", *IEEE Trans. Signal Process.*, vol. 52, no. 4, pp. 1128–1135, April 2004.
- [spat_87] A. Spataru, *Fondements de le théorie de la transmission de l'information*, Lausanne, Switzerland: Presses polytechniques romandes, 1987.
- [stoica_93] P. Stoica, "List of references on spectral line analysis", *Signal Process.*, vol. 31, no. 3, pp. 329–340, Apr. 1993.
- [stoica_97] P. Stoica, R. L. Moses, *Introduction to Spectral Analysis*, Prentice Hall, New Jersey, 1997.
- [tav_07] A. Tavallae, R. Abhari, "2-D characterisation of electromagnetic bandgap structures employed in power distribution networks," *IET Microw. Antennas Propag.*, **1**, (1), pp. 204-211, 2007.
- [teix_07] F. L. Teixeira, "Closed-form metamaterials blueprints for electromagnetic masking of arbitrarily shaped convex PEC objects," *IEEE Antennas Wireless Propag. Lett.*, vol. 6, pp. 163-164, 2007.
- [thala_11] D. Thalakituna, L. Matekovits, M. Heimlich, K. P. Esselle, S. G. Hay, "Active switching devices in a tunable EBG structure: placement strategies and modelling", *J. of Electromagn. Waves and Appl.*, vol. 25, pp. 1740-1751, 2011.
- [tre_85] S. A. Tretter, "Estimating the Frequency of a Noisy Sinusoid by Linear Regression", *IEEE Trans. Inf. Theory*, vol. 31, No. 6, pp. 832-835, Nov. 1985.
- [tufts_96] D. W. Tufts, P. D. Fiore, "Simple effective estimation of frequency based on Prony's method", in *Proc. Int. Conf. Acoust., Speech, Signal Process.*, Atlanta, GA, vol. 5, pp. 2801–2804, , May 1996.
- [vall_09] A. Vallecchi, M. Albani and F. Capolino, "Planar Metamaterial Transverse Equivalent Network and Its Application to Low-Profile Antenna Designs," *Proc. 3rd European Conference on Antennas and Propagation EUCAP09*, Berlin, Germany, pp. 861-865, March, 2009.

- [vau_91] R. G. Vaughan, N. L. Scott, D. R. White, "The theory of bandpass sampling", *IEEE Trans. Signal Proc.*, vol. 39, no. 9, 1991.
- [veselago_68] V. G. Veselago, "The electrodynamics of substances with simultaneously negative values of ϵ and μ ," *Soviet Physics Usphekhi*, vol. 10, no. 4, pp. 509-514, 1968.
- [weil_77] T. Weiland, "A discretization method for the solution of Maxwell's equations for sixcomponents fields," *Electronics and Communication (AEÜ)*, vol. 31, pp. 116-120, 1977.
- [weil_08] T. Weiland, M. Timm, I. Munteanu, "A practical guide to 3-D simulation," *Microwave Magazine*, vol. 9, no. 6, pp. 62-75, Dec. 2008.
- [wu_05] T.-L. Wu, Y.-H. Lin, T.-K. Wang, C.-C. Wang, S.-T. Chen, "Electromagnetic bandgap power/ground planes for wideband suppression of ground bounce noise and radiated emission in high-speed circuits," *IEEE Trans. Microw. Theory Tech.*, vol. 53, no. 9, pp. 2935-2942, Sept. 2005.
- [xu_11] R. Feng Xu, B. Sanz Izquierdo, P. R. Young, "Switchable substrate integrated waveguide," *IEEE Microwave Wireless Comp. Lett.*, vol. 21, no. 4, pp. 194-196, April 2011.
- [yang_05] Li Yang, M. Fan, F. Chen, "A novel compact electromagnetic-bandgap structure and ist applications for microwave circuits", *IEEE Trans. Microw. Theory Tech.*, vol. 53, no. 1, pp. 183-190, Jan. 2005.
- [zhang_07] M.-S. Zhang, Y.-S. Li, C. Jia, L.-P. Li, "A power plane with wideband SSN suppression using a multi-via electromagnetic bandgao structure," *IEEE Microwave Wireless Comp. Lett.*, vol. 17, no. 4, pp. 307-309, April 2007.
- [zhang_08] L.-J. Zhang, C.-H. Liang, L. Liang, L. Chen, "A novel design approach for dual-band electromagnetic band-gap structure," *Progress in Electromagnetic Research (PIER)*, vol. 4, pp. 81-91, 2008.

3.2. List of Publications 1993-2012

2012

[12_01_M] Aldo De Sabata, Ladislau Matekovits, "Electromagnetic Band-Gap Solution for Mitigation of Parallel-Plate Noise in Power Distribution Networks", *Microwave and Optical Technology Letters*, vol. 54, no. 7, pp. 1689-1692, 2012, ISSN 0895-2477, DOI: 10.1002/mop.

[12_02_M] Aldo De Sabata, Ladislau Matekovits, "Unit cell geometry in stripline technology featuring sequential band-gaps between every two consecutive modes", *IEEE Antennas and Wireless Propagation Letters*, vol. 11, pp. 97-100, 2012, ISSN 1536-1225, DOI: 10.1109/LAWP.2012.2183848.

[12_03_M] Ladislau Matekovits, Aldo De Sabata, "Some design parameters for high Q filters built in metamaterial technology", *6th European Conference on Antennas and Propagation, EUCAP 2012*, Prague, Czech Republic, March 26-30, pp. 1-4, 2012.

[12_04_M] Ladislau Matekovits, Aldo De Sabata, "Highly selective multiband metamaterial bandpass filter", *IEEE International Workshop on Antenna Technology, IWAT 2012*, March 5-7, Tucson Arizona, pp. 40-43, 2012.

[12_05_M] Ladislau Matekovits, Aldo De Sabata, "Parametric assessment of properties of a periodically patterned surface with non-uniform rectangular spiral metallization in the unit cell", *IEEE International Symp. on Antennas and Propag. and USNC-URSI National Radio Science Meeting, APS-URSI 2012*, July 8-14, Spokane, Ill., to appear, 2012.

[12_06_M] Aldo De Sabata, Ladislau Matekovits, "On scaling properties of the dispersion diagram of a multi-scale printed surface embedded in a parallel-plate waveguide", *IEEE 7th International Symp. on Appl. Computational Intelligence and Informatics, SACI 2012*, May 24-26, Timișoara, pp. 411-414 2012.

[12_07_M] Aldo De Sabata, Ladislau Matekovits, Marius Silaghi, Ulrich L. Rhode, "Investigation on the scaling properties of a novel electromagnetic band-gap structure for application to parallel-plate noise suppression", *EMC Europe*, Roma 2012, Sept. 17-21, to appear, 2012.

[12_08_E] Ioan Luminosu, Aldo De Sabata, Coleta De Sabata, Traian Jurca, "Solar collectors for recyclable materials", *Journal of Environmental Protection and Ecology*, vol. 13, no. 1, pp. 300-306, 2012, ISSN 1311-5065.

2011

[11_01_M] Ladislau Matekovits, Aldo De Sabata, Karu P. Esselle, "Effects of a coplanar waveguide biasing network built into the ground plane on the dispersion characteristics of a tunable unit cell with an elliptical patch and multiple vias", *IEEE Antennas and Wireless Propagation Letters*, vol. 10, pp. 1088-1091, 2011, ISSN 1536-1225, DOI: 10.1109/LAWP.2011.2170653.

[11_02_M] Ladislau Matekovits, Aldo De Sabata, "Photonic band-gap with electronically reconfigurable geometry", *EUROCON - International Conference on Computer as a Tool*, Lisbona, April 11-14, pp. 1-4, ISBN: 978-142447486-8, DOI: 10.1109/EUROCON.2011.5929163, www.eurocon2011.it.pt, 2011.

[11_03_M] Aldo De Sabata, Ladislau Matekovits, "Characteristics of a switchable metamaterial based parallel plate waveguide derived by electromagnetic simulation", *6th IEEE International Symposium on Applied Computational Intelligence and Informatics (SACI)*, May 28-29, Timișoara, Romania, DOI: 10.1109/SACI.2011.5872990, ISSN, pp. 151-154, <http://www.ac.upt.ro/saci2009/index.RO.html>, 2011.

[11_04_M] Ladislau Matekovits, Aldo De Sabata, "Novel multiband wideband filter relying on metamaterial technology", *Final Program and Book of Abstracts - IWAT 2011: 2011 IEEE International Workshop on Antenna Technology: Small Antennas, Novel Structures and Innovative Metamaterials*, Article number 5752369, pp. 372-375, DOI: 10.1109/IWAT.2011.5752369 ISSN <http://www.iwat2011.hk/index.php>, 2011.

[11_05_M] Ladislau Matekovits, Aldo De Sabata, Ildiko Peter, "Variation of characteristics of a microwave photonic band gap structure versus the dielectric constant in inhomogeneous parallel plate waveguide", *2011 IEEE International Symposium on Antennas and Propagation and USNC/URSI National Radio Science Meeting*, Spokane, Washington, USA, July 3-8, pp. 1836-1839, DOI: 10.1109/APS.2011.5996854, ISBN: 978-1-4244-9561-0, 2011, <http://www.apursi2011.org/>.

[11_06_M] Aldo De Sabata, Ladislau Matekovits, Ildiko Peter, "Electronically switched multiband high-impedance surface with circular and annular patches", *International Symposium on Signals, Circuits and Systems, ISSCS 2011*, June 30-July 1, Iași, Romania, DOI: 10.1109/ISSCS.2011.5978759 , ISSN: 978-1-61284-943-0/11/\$26.00, pp. 1-4 , 2011, <http://scs.etc.tuiasi.ro/isscs2011>.

[11_07_M] Ladislau Matekovits, Karu P. Esselle, Aldo De Sabata, Mario Orefice, "Some issues on the constructive constraints and their effects in the design of active periodic leaky-wave antennas", *12th Australian Symposium on Antennas, Sydney, Australia*, February 16-17, Invited Talk, Abstracts, p. 8, 2011, ISBN 978 0 643 10168 5, <http://research.ict.csiro.au/conferences/asa/12th-asa>.

[11_08_M] Ladislau Matekovits, Aldo De Sabata, "Analysis of the gap bandwidth of some high impedance surfaces in the microwave range", *Materials Science Forum*, vol. 670, pp. 497-503, DOI: 10.4028/www.scientific.net/MSF.670.497, ISSN: 1662-9752, 2011.

[11_09_M] Aldo De Sabata, Ladislau Matekovits, Ulrich L. Rhode, Marius A. Silaghi, "Multiband passive filter built with metamaterial in a parallel-plate waveguide", *Journal of Electrical and Electronics Engineering*, vol. 4, nr. 1, pp. 49-52, May, 2011, DOI ISSN 1844-6035 (Oradea, CNCSIS B+), <http://electroinf.uoradea.ro/reviste%20EEE/default.htm>.

[11_10_M] Ladislau Matekovits, Aldo De Sabata, Ildiko Peter, "Influence of magnetic permeability on dispersion diagrams of a parallel-plate waveguide built with metamaterials", *Proc. of Asia-Pacific Microwaves Conference, Melbourne, Australia, 5-8 December, 2011*, pp. 1746-1749, 2011, ISBN: 978-0-85825-974-4 (fără DOI pe IEEE), <http://www.apmc2011.com/>.

[11_11_M] Aldo De Sabata, Ladislau Matekovits, "Parallel-plate waveguides based on metamaterials with fixed and electronically reconfigurable geometry", *Scientific Bulletin of "Politehnica" University of Timisoara, Transactions on Automatic Control and Computer Science*, Vol. 56(70), No. 4, pp. 161-166, Dec. 2011, ISSN 1224-600X.

[11_12_M] Aldo De Sabata, Ladislau Matekovits, Ulrich L. Rhode, Marius A. Silaghi, "Metamaterial based microwave band-pass filter", *Annals of DAAAM for 2011 & Proceedings of the 22nd International DAAAM Symposium "Intelligent Manufacturing & Automation: Power of Knowledge and Creativity"*, 23-26th November, 2011, pp. 1267-1268, ISBN 978-3-901509-83-4, ISSN 1726-9679, Ed. Branko Katalinic, Vienna, Austria, 2011.

[11_13_E] Coleta De Sabata, Floricica Barvinschi, Aldo De Sabata, Ioan Luminosu, Traian Jurca, "Ecological wastewater cleaning of swine farms using solar energy", *Journal of Environmental Protection and Ecology*, vol. 12, no. 3A, pp. 1510-1516, 2011, ISSN 1311-5065.

[11_14_E] Ioan Luminosu, Coleta de Sabata, Aldo De Sabata, "Solar Energy Based Industrial Applications at the "Politehnica" University of Timișoara", *Thermal Science*, vol. 15, no. 3, pp. 587-598, 2011, DOI: 10.2298/TSCI100127026L ISSN 0354-9836.

[11_15_E] Ioan Luminosu, Aldo De Sabata, Coleta De Sabata, Marius Silaghi, "Impact of Using Tracking Surfaces on Necessary Solar Radiation Collecting Area in Stock Raising Applications", *Journal of Electrical and Electronics Engineering*, vol. 4, no. 2, pp.61-64, 2011, ISSN 1844-6035 (Oradea, CNC SIS B+), <http://electroinf.uoradea.ro/reviste%20EEE/default.htm>.

[11_16_E] Traian Jurca, Eugenia Tulcan-Paulescu, Ciprian Dughir, Mihaela Lascu, Paul Gavrilă, Aldo De Sabata, Ioan Luminosu, Coleta De Sabata, Marius Paulescu, "Global solar irradiation modeling and Measurements in Timișoara", Physics Conference TIM-10, 3 Oct. 2011, AIP Conf. Proc 1387, pp. 253-258, 2011, DOI: 10.1063/1.3647083, 978-0-7354-0951-4, <http://link.aip.org/link/?APCPCS/1387/253/1>

2010

[10_01_M] Ladislau Matekovits, Aldo De Sabata, Mario Orefice, "Parametric study of a unit cell with elliptical patch for periodic structures with variable number of grounding vias", *Proc. of the Fourth European Conf. on Antennas and Propagation, EUCAP, Barcelona*, April 12-16, Spain, pp. 1-3, 2010, ISBN: 978-847653472-4, <http://www.eucap2010.org/>

[10_02_M] Aldo De Sabata, Ladislau Matekovits, "Design charts for grounded, elliptically shaped microstrip periodic structures featuring electromagnetic band-gap", *8th International Conference on Communications (COMM)*, București, Romania, June 10-12, pp. 239-242, ISBN 978-1-4244-6362-6, DOI: 10.1109/ICCOMM.2010.5509010, <http://comm2010.ncit.pub.ro/>

[10_03_M] Aldo De Sabata, Ladislau Matekovits, "Numerical exploration of filtering properties of some switched high impedance surfaces", *9th International Symposium on Electronics and Telecommunications ISETC*, Timișoara, Romania, Nov. 11-12, pp. 73-76, 2010, ISBN 978-1-4244-8458-4, DOI 10.1109/ISETC2010.5679246, <http://www.etc.upt.ro/other/isetc2010/home.php>

[10_04_M] Ladislau Matekovits, Aldo De Sabata, Karu P. Esselle, "Effects of the Biasing Network in a Parallel Plate Waveguide Periodic Unit Cell Featuring Switched Electromagnetic Band Gap", *Proceedings of Asia-Pacific Microwave Conference 2010*, Yokohama, Japan, Dec. 7-10, pp. 1122-1125, ISBN 978490233921 5, <http://www.apmc2010.org/>

[10_05_M] Aldo De Sabata, Ladislau Matekovits, "A New High Impedance Surface Featuring Several Electromagnetic Band-Gaps", *Bul. Șt. UPT, Seria Electronică și Telecomunicații, Trans. on Electronics and Telecommunications*, Tom 55(69), Fasc. 2, pp. 3-6,2010, ISSN 1583-3380, <http://shannon.etc.upt.ro/bulletin/index.html>

[10_06_E] Ioan Luminosu, Aldo De Sabata, Coleta De Sabata, *Applications Oriented Research on Solar Collectors at the "Politehnica" University of Timișoara*, in Reccab M. Ochieng Ed., *Solar Collectors and Panels, Theory and Applications*, Rijeka, Croatia: Sciyo, pp. 379-404, ISBN 978-953-307-142-8, www.sciyo.com.

Available from: <http://www.intechopen.com/articles/show/title/applications-oriented-research-on-solar-collectors-at-the-politehnica-university-of-timi-oara>

[10_07_E] Ioan Luminosu, Coleta De Sabata, Aldo De Sabata, "Research in Solar Energy at the "Politehnica" University of Timișoara", *Thermal Science*, vol. 14, no. 1, Jan. 2010, pp. 157-169, DOI: 10.2298/TSCII0011571, ISSN 0354-9836.

[10_08_E] Coleta De Sabata, Ioan Luminosu, Aldo De Sabata, *Tradiție și perspective în energetica solară la Universitatea "Politehnica" din Timișoara*, Timișoara: Excelsior Art, 2010, 214 pagini, ISBN 978-973-592-248-1, www.excelsiorart.ro.

[10_09_E] Ioan Luminosu, Aldo De Sabata, Coleta De Sabata, "Education in Solar Energy at the "Politehnica" University of Timișoara", *Banat Journal of Biotechnology*, I(2), pp. 83-87, 2010, ISSN 2068-4673 (Print), ISSN 2068-4738 (CDROM), <http://dse.usab-tm.ro/en/bjb.html>

[10_10_E] Ioan Luminosu, Coleta De Sabata, Aldo De Sabata, "Operation model for a simple solar thermal installation", *Buletinul AGIR*, nr. 2-3, apr.-sept., pp. 93-97, 2010, ISSN 1224-7928.

[10_11_E] Ioan Luminosu, Aldo De Sabata, Coleta De Sabata, Traian Jurca, "Educație în Energie Solară la Universitatea "Politehnica" din Timișoara", *Știință și Inginerie, A X-a Conferință Națională Multidisciplinară "Profesorul Dorin Pavel – fondatorul hidroenergeticii românești"*, vol. 17, pp. 525-532, 2010, Ed. AGIR, ISSN 2067-7138.

2009

[09_01_M] Aldo De Sabata, Ladislau Matekovits, Andrei Silaghi, Ulrich Rhode, Marius Silaghi, "Investigation on surface waves related properties of some periodic structures", *Proc. of the 12th International Conference on Microwave and High Frequency Heating, Ampere 2009*, 7-10 Sept. 2009, Karlsruhe, Germany, pp. 364-367, 2009.

[09_02_M] Cosmin Sinescu, Meda Negrutiu, Dana Pop, Lavinia Cuc, Aldo De Sabata, Radu Negru, Mihai Hluscu, Mihai Rominu, Corina Marcauteanu, Eniko Demjan, Adrian Bradu, Iulian Antoniac, George Dobre, Adrian Podoleanu, "The importance of holograms in dentistry", *Conference on Holography - Advances and Modern Trends, Prague, Czech Republic, Apr 21-23, 2009*, in *Holography: Advances and Modern Trends, Book Series: Proceedings of SPIE*, Vol. 7358, Article Number: 73580J, DOI: 10.1117/12.821545, Published: 2009

[09_03_S] Liviu Toma, Aldo De Sabata, Robert Pazsitka, "Iterative procedure for real single-tone frequency estimation", *Revue Roumaine De Sciences Techniques, Electrotechnique Et Energetique*, 54, 3, pp. 253-260, 2009, ISSN 0035-4066.

[09_04_S] Aldo De Sabata, Liviu Toma, "Analysis of an Algorithm for Real Tone Frequency Estimation", *Proc. of the Int. Symp. on Signals, Circuits and Systems ISSCS 2009*, July 9-10 2009, vol. 1, pp. 113-116, ISBN 978-1-4244-3784-9.

[09_05_S] Aldo De Sabata, Liviu Toma, "Application of Bandpass Filtering in Real Tone Frequency Estimation", *5th International Symposium on Applied Computational Intelligence and Informatics* May 28–29, 2009 – Timișoara, Romania, pp. 429-433, ISBN: 978-1-4244-4478-6.

[09_06_E] Ioan Luminosu, Coleta De Sabata, Aldo De Sabata, Traian Jurca, "On the use of magnetic fluids in solar energy installations", *Buletinul AGIR*, anul XIV, nr. 2-3, pp. 66-69, apr.-sept. 2009, ISSN 1224-7928.

[09_07_E] Coleta De Sabata, Ioan Luminosu, Aldo De Sabata, Traian Jurca, "Cercetări experimentale și realizări industriale privind preîncălzirea bitumului cu ajutorul energiei solare", *Buletinul AGIR*, anul XIV, nr. 2-3, pp. 70-75, apr.-sept. 2009, ISSN 1224-7928.

[09_08_E] Ioan Luminosu, Aldo De Sabata, Coleta De Sabata, "Thermally Autonomous Residence in the Western Part of Romania", *5th International Symposium on Applied Computational Intelligence and Informatics (SACI)*, May 28–29, 2009 – Timișoara, Romania, pp. 229-234, DOI: 10.1109/SACI.2009.5136247, ISBN: 978-1-4244-4478-6, Library of Congress: 2009903350

2008

[08_01_S] Liviu Toma, Aldo De Sabata, Robert Pazsitka, Ladislau Matekovits, "A Hybrid Single Tone Frequency Estimator, *Bul. St. Univ. "Politehnica" din Timisoara*", *Bul. St. Univ. "Politehnica" din Timisoara, Trans. on Electronics and Telecomm., International Symposium on Electronics and Telecommunications, ISETC2008*, Tom 53(67), Fasc. 2, 2008, pp. 50-52, ISSN 1583-3380.

[08_02_S] Aldo De Sabata, Liviu Toma, Robert Pazsitka, Ladislau Matekovits, "Real single tone frequency estimation by PHD and filtering", *Bul. St. Univ. "Politehnica" din Timisoara, Trans. on Electronics and Telecomm. International Symposium on Electronics and Telecommunications, ISETC2008*, Tom 53(67), Fasc. 2, pp 53-54, ISSN 1583-3380.

[08_03_E] Ioan Luminosu, Aldo De Sabata, Coleta De Sabata, Mariana Nagy, "An energetic study of a small solar residence", *bul. PAMM*, cxii (BAM–2370), pp. 171-180, Budapesta, 2008, ISSN 0133-3526.

[08_04_E] Ioan Luminosu, Aldo De Sabata, Coleta De Sabata, Mariana Nagy, "Statistics on the availability of solar energy on the 45th Northern parallel". *Bul. PAMM*, no. cxii (BAM – 2369), pp. 161-170, Budapesta, 2008, ISSN 0133-3526.

[08_05_E] Coleta De Sabata, Ioan Luminosu, Aldo De Sabata, Traian Jurca, "Summer Climatization Based on Solar Energy: Considerations and Experimental Results", *Bul. St. Univ. "Politehnica" din Timisoara, Trans. on Mechanics*, Tom 53(67), Fasc. 3, pp. 65-68, 2008, ISSN 1224-6077.

[08_06_E] Ioan Luminosu, Aldo De Sabata, Coleta De Sabata, Traian Jurca, "Simularea numerică a funcționării unui boiler solar în condiții cvasireale", *"Știință și Inginerie"*, vol. 14, *Lucrările celei de-a VIII-a Conferințe naționale multidisciplinare - cu participare internațională - "Profesorul Dorin Pavel - fondatorul hidroenergeticii românești"*, Sebeș, 30-31 mai 2008, pp. 121-128, Ed. Agir, București, 2008, ISBN 973-8130-82-4, 978-973-720-198-0.

2007

[07_01_M] Alimpie Ignea, Aldo De Sabata, "Hysteresis Distorsions for Two-Tone Signals", *Proc. of 15th IMEKO Symposium on Novelties in Electrical Measurements and Instrumentation*, Iași, România, sept. 2007, pp. 61-63, ISBN 978-973-667-260-6, 978-973-667-261-3.

[07_02_S] Liviu Toma, Aldo De Sabata, Gabriel VasIU, "Two-step procedure decreases variance in tone frequency estimation", *Revue Roumaine de Sciences Techniques, Électrotechnique et Énergetique*, 52, 4, pp. 463-474, 2007, ISSN 0035-4066.

[07_03_S] Liviu Toma, Aldo De Sabata, Septimiu Mischie, "A new two-step single tone frequency estimation algorithm", *International Journal of Circuits, Systems and Signal Processing*, Issue 2, vol. 1, pp. 105-108, 2007, ISSN 1998-0140, on line <http://www.naun.org/journals/circuitssystemsignal>

[07_04_S] Aldo De Sabata, Liviu Toma, Septimiu Mischie, "Two-step Pisarenko harmonic decomposition for single tone frequency estimation", *7th WSEAS/IASME Int. Conf. on Power Systems, High Voltages, Electric Machines*, Venice, Italy, Nov. 21-23, pp. 243-246, 2007.

[07_05_E] Coleta De Sabata, Ioan Luminosu, Aldo De Sabata, Alina Palea, "On the Design of a Solar, Partially Energetically Independent House in the Region of Banat", *Bul. St. Univ. "Politehnica" din Timisoara, Trans. on Mechanics*, Tom 52(66), Fasc. 4, pp. 82-87, 2007, ISSN 1224-6077.

[07_06_E] Ioan Luminosu, Coleta De Sabata, Aldo De Sabata, "Cercetări teoretice și experimentale asupra posibilității de realizare a unei case solare parțial autonome termoenergetic", *Revista AGIR*, anul XII, nr. 3, pp. 31-44, iul.-sept. 2007, ISSN 1224-7928.

[07_07_E] I. Luminosu, A. De Sabata, C. De Sabata, M. Nagy, "Heat and warm water for a small residence produced by means of solar energy" *Proc. of Panonian Applied Mathematics and Mechanics Conference*, Arad, Nov. 26, 8 pagini (comunicată), 2007.

2006

[06_01_M] Alimpie Ignea, Traian Jurca, Aldo De Sabata, Ciprian Dughir, Adrian Mihăiuti, *Aspecte privind monitorizarea perturbațiilor dintr-un site*, Timișoara: Waldpress, 2006, ISBN 973-7878-22-1, 100 p.

[06_02_M] Ladislau Matekovits, Aldo De Sabata, Paola Pirinoli, Mario Orefice, "Broadband measurement of the refractive index using microstrip lines", *Bul. Șt. Univ. "Politehnica" din Timișoara, Trans. on Electronics and Telecomm.*, Tom 51(65), Fasc. 1, pp. 44-48, 2006, ISSN 1583-3380.

[06_03_S] Aldo De Sabata, Alimpie Ignea, "Sampling expansions on lattices for multidimensional, multiband signals", *WSEAS Transactions on Signal Processing*, Issue 1, Vol. 2, Jan. 2006, pp. 60-66 ISSN 1790-5022.

[06_04_S] Aldo De Sabata, Liviu Toma, Septimiu Mischie, "Closed-form variance formula of the rphd single-tone frequency estimator", *Facta Universitatis (Nis), Ser.: Elec. Energ.*, vol. 19, no. 3, Dec. 2006, pp. 453-464, ISSN 0353-3670

2005

[05_01_M] Ioan De Sabata, Aldo De Sabata, "Thermodynamic derivation of the expressions of the force and energy in the maxwell-hertz theory", *Bul. Șt. Univ. "Politehnica" din Timișoara, Trans. on Power Engineering*, Tom 50(64), Fasc. 1,2, PP. 185-194, 2005, ISSN 1583-3380.

[05_02_S] Aldo De Sabata, "Sampling theorem for multidimensional, multiband signals", *WSEAS Transactions on Signal Processing*, Issue 3, vol. 1, dec. 2005, pp. 458-461, ISSN 1790-5022 (apărută și în 2005 *WSEAS int. Conf. on Dynamical Systems and Control*, Venice, Italy, 2005, pp. 405-408).

[05_03_S] Aldo De Sabata, *S Parameters*, suport de curs, Politecnico di Torino, www.polito.it, 70 p.

2004

[04_01_M] Aldo De Sabata, Ladislau Matekovits, "Scattering parameters for symmetrical networks", *Bul. Șt. Univ. "Politehnica" din Timișoara, Trans. on Electronics and Telecomm.*, Tom 49(63), Fasc. 2, pp. 317-322, 2004, ISSN 1583-3380.

2003

[03_01_M] Ioan De Sabata, Aldo De Sabata, "Magnetic fluid bearings with poles on the shaft", *Rev. Roum. Sci. Techn. - Électrotechn. et Énerg.*, 48, 2/3, 381-391, 2003, ISSN 0035-4066.

[03_02_S] Robert Pazsitka, Liviu Toma, Dan Stoiciu, Aldo De Sabata, "Derivation of the Sampling Theorem for Bandpass Signals", *Bul. Șt. Univ. "Politehnica" Timișoara, Electronică și Telecom.*, Tom 48(62), fasc. 2, pp. 14-15, 2003, ISSN 1583-3380.

2002

[02_01_M] Ioan De Sabata, Aldo De Sabata, "On magnetic fluid bearings with alternating poles", *Rev. Roum. Sci. Techn. - Électrotechn. et Énerg.*, 47, 3, pp. 295-306, 2002, ISSN 0035-4066.

[02_02_M] Alimpie Ignea, Eugen Mârza, Aldo De Sabata, *Antene și propagare*, Timișoara: Ed. de Vest, 2002, ISBN 973-36-0351-1, 310 p.

[02_03_S] Aldo De Sabata, "Generalized derivative band-pass sampling", *Bul. Șt. Univ. "Politehnica" Timișoara, Electronică și Telecom., Proc. of the Symp. on Electronics and Telecommunications "ETc 2002"*, Tom 47(61), fasc.1- 2, vol. I, pp. 168-170, 2002, ISSN 1224-6034.

2001

[01_01_M] Ioan De Sabata, Marian Greconici, Aldo De Sabata, "Restoring force acting on a rotor with alternating poles in a magnetic fluid", *Rev. Roum. Sci. Techn. - Électrotechn. et Énerg.*, 46, 1, pp. 79-88, 2001, ISSN 0035-4066.

[01_02_M] Aldo De Sabata, *Tehnica frecvențelor înalte*, Timișoara: Ed. "Orizonturi Universitare", 2001, ISBN 973-8109-57-4, 117 p.

[01_03_M] Ioan De Sabata, Aldo De Sabata, "O sinteză asupra acțiunilor ponderomotoare din lichide magnetice și două aplicații ale acestora", *Analele Universității din Oradea*, Fasc. Ing. Elect., pp. 64-73, 2001.

[01_04_M] Géczi Gábor, Sembery Péter, Váczy Gábor, Aldo De Sabata, "Termények dielektromos állandójának meghatározása 2.45 GHz frekvencián, csötápvonalas módszerek segítségével", *Műszaki Kémiai Napok '01, Veszprém, Április 24-26*, pp. 82-87, 2001, ISBN 963-00-6467-7.

[01_05_M] Ioan De Sabata, Marian Greconici, Aldo De Sabata, "Force that acts on a rotor with alternating poles", *Proc. of 11th Int. Symp. on Power Electronics*, Oct. 31-Nov. 2, Novi Sad, Yugoslavia, pp. 337-340, 2001.

[01_06_S] Aldo De Sabata, *Metode adaptive în tehnica măsurării*, Timișoara: Ed. "Politehnica", 2001, ISBN 973-8247-40-3, 108 p.

2000

[00_01_M] Bernhard Rothenstein, Aldo De Sabata, "Special Relativity with light signals but from Galilean postulate", *Hadronic J.*, vol. 23, Issue 6, pp. 607-617, Dec. 2000, ISSN 0162-5519.

[00_02_M] Gabor Geczi, Paul Sembery, Aldo De Sabata, "Dielectric constant measurement for wheat", *Bul. Șt. Univ. "Politehnica" Timișoara, Tom 45(59), Fasc. 1, Proc. of the Symp. on Electronics and Telecommunications "ETc 2000"*, vol. II, pp. 198-200, 2000, ISSN 1224-6034.

1999

[99_01_M] Bernhard Rothenstein, Aldo De Sabata, *Teoria Relativității Speciale*, Timișoara: Ed. Eurobit, 1999, ISBN 973-9336-10-8, 124 p.

[99_02_M] Bernhard Rothenstein, Aldo De Sabata, "Relativistic Derivation of the Electric and Magnetic Fields of an Electric Point Charge and of a Line Charge Moving with a Constant velocity, Built on Retardation of Space-Time Coordinates", *Bul. Șt. Univ. "Politehnica" Timișoara, Matematică-Fizică*, Tom 44(58), Fasc. 1, pp. 38-43, 1999, ISSN 1224-6069.

[99_03_M] Aldo De Sabata, Ioan De Sabata, "Some Curiosa as Opportunities for Making More Attractive Lectures in Electrical Engineering", *Proc. of the 10th EAIEE Annual Conference, Capri, Italy*, pp. 249-251, 1999.

1998

[98_01_M] Bernhard Rothenstein, Aldo De Sabata, "Frequency shifts for accelerated sources and observers: an illustration of non-locality in frequency measurement", *Eur. J. Phys.*, **19** (6), 569-574, 1998, 0143-0807, DOI: 10.1088/0143-0807/19/6/010.

[98_02_S] Aldo De Sabata, Anton Policec, Diego Bravar, Paolo Giribona, "Partial Fourier MR imaging", *Bul. Șt. Univ. "Politehnica" Timișoara, Electrotehnică, Electronică și Telecomunicații*, Tom 43(57), Fasc. 1, pp. 191-198, 1998, ISSN 1583-3380.

[98_03_S] Aldo De Sabata, Alimpie Ignea, "Sampling and Reconstruction of Sparse Images-An Information Theory Approach", *Proc. of the Int. Symp. on Electronics and Telecommunications (ETC 98)*, Timișoara, vol I, pp. 35-38, 1998.

1997

[97_01_M] Bernhard Rothenstein, Aldo De Sabata, "An uncommon way to Special relativity", *Eur. J. Phys.*, **18** (4), pp. 263-266, 1997, 0143-0807, DOI: 10.1088/0143-0807/18/4/003.

[97_02_S] Aldo De Sabata, Carmen De Sabata, "On the Discrete Fourier Transform for a Class of Digital Signals", *Bul. Șt. Univ. "Politehnica" Timișoara, Electrotehnică, Electronică și Telecomunicații*, Tom 42(56), Fasc. 1, pp. 105-110, 1997, ISSN 1583-3380.

[97_03_S] Aldo De Sabata, "Sampling expansions for general band-pass signals", *Proc. of the Int. Conf. "Analysis and Numerical Computation of Solutions of Nonlinear Systems Modelling Physical Phenomena"*, West University of Timișoara and EOARD (USA), Ed. Mirton Timișoara, pp. 494-500, 1997, ISBN 973-578-267-7.

1996

[96_01_M] Aldo De Sabata, *Măsurări cu microunde și optoelectronice*, Timișoara: Lit. Univ. "Politehnica", 1996, 210 p.

[96_02_M] Bernhard Rothenstein, Aldo De Sabata, "Relativistic Dynamics Via the Doppler Effect in the de Broglie Wave", *Bul. Șt. Univ. "Politehnica" Timișoara, Matematică-Fizică*, Tom 41(55), fasc. 2, pp. 81-87, 1996, ISSN 1224-6069.

[96_03_M] Bernhard Rothenstein, Aldo De Sabata, Sorin Bălan, "Addition Law of Relativistic Velocities: An Uncommon Way to Special Relativity", *Analele Univ. de Vest, Timișoara, seria Fizică*, no. 5, pp. 3-13, 1996.

[96_04_M] Bernhard Rothenstein, Aldo De Sabata, Sorin Bălan, Erwin Lovasz, "Doppler effect in a spherical wave", *Bul. Șt. Univ. "Politehnica" Timișoara, Matematică-Fizică*, Tom 41(55), Fasc. 1, pp. 95-102, 1996, ISSN 1224-6069.

[96_05_S] Aldo De Sabata, "Sampling Expansions for Harmonic Limited, Multiband Signals", *Bul. Șt. Univ. "Politehnica" Timișoara, Electrotehnică, Electronică și Telecomunicații*, Tom 41(55), Fasc. 1, vol. II, pp. 29-34, 1996.

1995

[95_01_S] Aldo De Sabata, "Gap sampling series for finite energy signals", *Bul. Șt. Univ. "Politehnica" Timișoara, Electrotehnică, Electronică și Telecomunicații*, Tom 40(54), pp. 121-126, 1995.

[95_02_S] Aldo De Sabata, "Finite gap sampling expansions", *Bul. Șt. Univ. "Politehnica" Timișoara, Electrotehnică, Electronică și Telecomunicații*, Tom 40(54), , pp. 115-120, 1995.

[95_03_S] Alexandru Isar, Corina Botoca, Aldo De Sabata, *Semnale, circuite și sisteme, culegere de probleme*, Timișoara: Lit. Univ. "Politehnica", 120 p.

1994

[94_01_S] Aldo De Sabata, "Extension of a finite version of the sampling theorem", *IEEE Transactions on Circuits and Systems II*, vol. 41, no. 12, pp. 821-823, Dec. 1994, ISSN1 1549-7747, ISSN21057-7130, ISSN3 1559-3791 (ARC), DOI: 10.1109/82.338625.

[94_02_S] Aldo De Sabata, Claude Iung, Jean-François Aubry, "A variable-scale DWT", *Proc. of the Int. Symp. on Electronics and Tech. Informatics*, Timișoara, sept. 29-30, vol. III, pp. 43-49, 1994.

1993

[93_01_S] Alimpie Ignea, Aldo De Sabata, "A New Echo Signal Processing Method for Ultrasonic Distance Measurement", *Buletinul Științific al Universității Tehnice Timișoara, Electrotehnică, Electronică și Telecomunicații*, Tom 38(52), pp. 183-186, 1993.

[93_02_S] Aldo De Sabata, "Adaptive Sampling of Signals with Additive Noise", *Rev. Acad. Th. Mil., număr special*, anul III, pp. 26-30, 1993.

[93_03_S] Aldo De Sabata, "Aproximarea derivatei în cazul interpolării Hermite a semnalelor de bandă limitată", *Analele Univ. Oradea, fasc. Ing. Elect.*, pp. 172-179, 1993.

[93_04_S] Aldo De Sabata, "O generalizare a teoremei lui Papoulis", *Analele Univ. Oradea, fasc. Ing. Elect.*, pp. 167-171, 1993.

[93_05_S] Aldo De Sabata, "Undersampling and Reconstruction of Finite-Duration Signals through Hilbert Transform", *Proc. of Int. Symp. on Signals, Circuits and Systems, Iași, Nov. 4-5*, pp. 140-143, 1993.

[93_06_S] Aldo De Sabata, "Undersampling Finite-Duration Signals through Multilinear Filtering", *Proc. of Int. Symp. on Signals, Circuits and Systems, Iași, Nov. 4-5*, pp. 136-139, 1993.

Note: The letter in the reference identifies the domain as follows:

"M" – Applied Electromagnetics

"S" – Signal Processing

"E" – Solar Energy